UNIVERSITÀ
DEGLI STUDI
DI BRESCIA

DOTTORATO DI RICERCA IN INGEGNERIA MECCANICA E INDUSTRIALE

ING-IND/13 - MECCANICA APPLICATA ALLE MACCHINE

CICLO XXXV

STUDY OF STRATEGIES FOR AN OPTIMAL ENERGY MANAGEMENT ON ELECTRIC AND HYBRID VEHICLES

Dottoranda:

Giulia Sandrini

Matricola n° 86113

Supervisore: Chiar.mo Prof. Marco Gadola

Co-supervisori: Ing. Daniel Chindamo

Dr. Pier Luigi Porta (ENEA)

STUDY OF STRATEGIES FOR AN OPTIMAL ENERGY MANAGEMENT ON ELECTRIC AND HYBRID VEHICLES

TABLE OF CONTENTS

STUDY OF STRATEGIES FOR AN OPTIMAL ENERGY MANAGEMENT ON ELECTRIC AND HYBRID VEHICLES

ABSTRACT

This PhD thesis is focused on identifying energy management strategies on board electric and hybrid vehicles, to optimize energy management and thus allow for resource savings. In fact, vehicle's operational phase optimisation through a more efficient energy management allows main components downsizing, such as battery pack.

First of all, a simulation tool called TEST (Target-speed EV Simulation Tool), is presented. This tool allows to carry out longitudinal dynamics simulations on pure electric or hybrid-electric vehicles, and therefore monitoring all the relevant data needed to carry out a proper powertrain sizing, including the electric motor(s) and the battery pack. Furthermore, several powertrain layouts can be also tested, including those using fuel cells.

Then a regenerative braking strategy, suitable for FWD, RWD and AWD vehicles, is presented. Its main target is to recover the maximum possible braking energy, while keeping the vehicle stable with good braking performance. The strategy has been tested both through a state-of-art vehicle dynamics simulation software (VI-CarRealTime) and through driver-in-the-loop simulations using a driving simulator. Furthermore, the proposed strategy has been integrated into TEST to evaluate its influence on vehicle range and consumptions.

The above-mentioned tools have been used to evaluate a real-world case scenario to assess the feasibility of using a methane fuel cell powered fleet to carry out door to door waste collection activities. Results show high feasibility in terms of vehicle range compared to standard waste collection missions, provided that components are properly sized. Components sizing has been done through iterations using different components on the same missions.

Finally, an in-depth analysis of the LCA (Life Cycle Assessment) studies related to electric vehicles has been reported, with particular focus to the battery pack, highlighting some environmental critical issues. This LCA study therefore emphasizes the importance of a correct energy management to minimize the environmental impact associated with energy consumption.

1 INTRODUCTION

In this thesis document, several strategies for an optimal energy management on electric and hybrid vehicles are presented. The necessity of such strategies is related to problems of environmental impact (aspect that will be deepened in this thesis, in Section 6 [1]), to problems associated with the low range of the electric traction (in particular of the battery pack), to the need to save resources in the production phase of the traction batteries; aspects that will be presented in more detail below.

Nowadays, the automotive sector is facing the challenge of improving its environmental sustainability. Because of that, car manufacturers are trying to increase the market share of electric and hybrid vehicles [2]. As a matter of fact, due to the stringent emission laws from governments from all over the world, diesel vehicles are being replaced by hybrid vehicles [2]. In this regard, it is interesting to mention the law of 16 January 2019 (formal adoption on 3 April 2019) [3,4], as the European Parliament voted for the further reduction of carbon dioxide (CO_2) emissions for the newly registered vehicles. In particular, cars and light commercial vehicles (vans) registered from 2025 will have to emit 15% less CO_2 and by 2030 cars will have to emit 37.5% less CO_2, while light commercial vehicles will have to emit 31% less. Furthermore, the most recent regulation 2021/1119/EU [5], in force since 29 July 2021, mandates a reduction in greenhouse gas emissions by 55% compared to 1990 levels by 2030. This law also provides for a series of actions that must lead to climate neutrality by 2050. Furthermore, the European Parliament voted on Wednesday, 2022 June 8, to ban sales of new internal combustion engine cars and vans in the European Union from 2035 onward (ordinary legislative procedure 2021/0197(COD)).

Furthermore, the problem of traditional vehicles is not only linked to environmental problems, i.e., global warming associated with the emission of large quantities of CO_2 and pollution linked to the emission of pollutants such as unburnt substances and nitrogen oxides (NOx) contained in the exhaust gases of thermal engines, but it is also associated with the noninfinite availability of fossil

fuels [6]. For all the above reasons, the automotive market is pushing more and more electrified, hybrid or fully electric vehicles.

However, the spread of these alternative powertrains (especially full electric) is being slowed down by their range as it is still not comparable to a traditional liquid fuel-powered vehicle. In fact, despite the considerable step forward in battery technology, energy density (energy to weight ratio) of lithium batteries is still far from being competitive with gasoline or diesel [6].

Therefore, to reduce this gap a hybrid and/or electric powertrain must be well designed in order to minimize energy loss and ultimately, increase its range without increasing battery weight. To reduce design time and costs, a model-based design approach can be used instead of the traditional prototype-based approach [7]. By means of virtual models, most of the common test procedures can be carried on since the very early design phase. This allows designers to adjust their efforts as a function of the simulation results obtained. This method has been proven to be much more efficient than the traditional one [8,9].

In this thesis a new simulation tool (named TEST, Target-speed EV Simulation Tool) will be presented in Section 2 and this work was also published on "MDPI - Energies" journal [10]. The main target of this tool is to obtain shorter calculation times and perform closed-loop simulation in a more efficient way comparing to other tools reported in literature. Such a tool should be reliable, robust and numerically stable. It also has to be intuitive and easy to use for people with no specific training. The graphical user interface should be simple and straightforward. The TEST model has been written in MATLAB/Simulink; a programming environment widely used in the automotive world. The simulation tool presented in this work allows for the simulation of both mechanical and electrical behaviour of a full electric or hybrid APU (Auxiliary Power Unit) vehicle, considering longitudinal dynamics only. This approach makes the whole system more flexible, versatile, and suitable to model any sort of EV-HEV powertrain, making it a true multipurpose simulation tool. It is worth highlighting that the design of new EV or HEV powertrain is carried out using a "modular" approach; therefore, the use of this kind of simulation tool during the design and development process becomes a necessity, hence leading to a more efficient vehicle design in terms of costs and time saved. The modularity of the model also allows you to easily make changes to the tool, or add additional modules, in order to simulate other types of hybrid vehicles and test different energy management strategies on board the vehicle.

As already mentioned, for reasons of pollution, non-infinite availability of fossil fuels and for issues related to exhaust emissions, the automotive market is

progressively switching to electrification, i.e., to hybrid electric vehicles and fully electric vehicles. However, as already mentioned, a strong limitation of these vehicles (especially for fully electric vehicles) is imposed by the limited range of electric drive when compared to traditional internal combustion engine vehicles. In fact, despite their continuous technological development, the energy density of lithium batteries is still far from being competitive with petrol or diesel [6].

Therefore, in order to maximize the range of electric vehicles with the same nominal capacity in the battery pack, it is necessary to better manage the energy on board the vehicle, in particular, by maximizing energy recovery during the deceleration and braking phases.

In fact, as stated in [11], regenerative braking technology can increase the driving range by 10 to 20% when the electric vehicle travels in urban road traffic with frequent stop and start events (American Electric Power Research Institute data) [12].

The goal of efficient regenerative braking logic is to increase the vehicle range, thus making it possible to reduce the weight and size of the battery pack in the design phase and, therefore, to reduce the consumption of natural resources in the battery production phase. All this results in a less severe environmental impact, both in the production phase of the battery pack and in the use phase of the vehicle [1] (Section 6 explores this aspect further).

In this thesis, a regenerative braking logic is presented in Section 3 (and in the publication [13] in "MDPI - Energies" journal), to be implemented in the vehicle control unit, which aims at minimizing the use of dissipative braking and to achieve the maximum possible energy regeneration by means of the braking torque provided by the electric motor(s) while preserving vehicle stability even in emergency braking events. During the development phase of this logic, it was useful and important to use a compact simulator to carry out some qualitative tests and tests related to the driver's perception.

As already mentioned, nowadays, climate change is the main critical issue that citizens and governments face. This has led many countries to sign climate agreements to tackle this problem, such as the Paris agreement [14]. It can be seen by analysing the environmental impacts of different anthropogenic activities that fossil fuel usage is particularly significant for energy production, domestic heating, and the transportation sector [15].

Renewable energy is considered an ideal replacement for these fossil products, and it could also be used to charge EV vehicles [1,16]. However, a critical issue of renewable sources is that they are non-controllable sources. Then

new forms of energy storage have been introduced (e.g., green hydrogen) to face the dependence of the power from the environmental conditions [17]. The use of hydrogen in the transport sector can help to overcome problems related to the uncertainty of renewable energy. Hydrogen has been introduced as a power vector in the transport sector thanks to the introduction of fuel cells (FCs) [18,19]. Furthermore, fuel cell vehicles make it possible to solve the demanding problems associated with fully electric vehicles (traction guaranteed by the battery pack alone), that is, the low range and long battery recharging times.

In this thesis, a model of a hybrid electric/FC vehicle powered by hydrogen will be presented in Section 4. The fuel cell model was also integrated into the TEST model, for the simulation of the entire vehicle and, in particular, for the estimation of energy and hydrogen consumption. This work has also been published on "MDPI - Energies" journal [20].

To promote the development of new technologies that allow an increasingly frequent and wide use of renewable "green" energies and that make it possible to overcome the problem of the lack of range of full electric vehicles, an interesting energy source is also, for example, that of biomethane.

The latest generation technologies, as anticipated, include the "Fuel Cells" (FC) systems, benefiting from high efficiency and zero emissions, provided that, by extending the analysis to the entire production process, the hydrogen necessary for their operation is obtained thanks to renewable energies. An alternative may be precisely that of studying fuel cell vehicles powered not by hydrogen, but by biomethane, to exploit a renewable energy source.

Furthermore, one of the main problems related to hydrogen FC is the current weak network of infrastructures necessary for the supply of hydrogen itself. For this reason, a solution that includes a FC powered by biomethane (or methane) would also solve this problem.

The type of fuel cells that lends itself to a methane (or therefore biomethane) power supply is that of solid oxide FC (SOFC). Initially, a study of the state of the art of SOFC (Solid Oxide Fuel Cell) systems was carried out and once the necessary information was collected, the aim was to create a model of a solid oxide fuel cell vehicle, which could become functional and bring advantages, taking into account all the limitations and criticalities foreseen for the SOFCs. Furthermore, the SOFC model has also been integrated into the TEST model.

As will be shown during the discussion of Section 5 of this thesis, the problems of solid oxide cells are different. The slow transient linked to the

chemical reactions that take place inside them make the SOFCs unsuitable for use on the vehicle as a primary energy source, the choice therefore necessarily fell on their use as a generator that recharges the battery pack during the use of the vehicle. For this reason, the sector that best lends itself to this type of FC is that of vehicles operating on a fleet, the study presented in this thesis will in fact concern the creation of a vehicle model equipped with SOFC, and the sizing of the FC itself and battery pack, for a waste collection vehicle, whose mission is known, which is therefore predefined.

Another important criticality of SOFCs is that of fragility, which means that the work carried out in this area is suitable for any future studies and designs, which involve a solution to this problem, the barrier of the fragility of solid oxide cells must therefore be overcome before the actual realization of a vehicle with SOFC on board.

Finally, the last topic covered in this thesis, in Section 6, concerns the environmental performance of traction batteries for electric vehicles, from a life cycle perspective [1]. Section 6 is proposed to investigate the various aspects related to the impacts associated with the life cycle of traction batteries for electric vehicles, carried out through a review of the available literature, with particular attention to LCA (Life Cycle Assessment) studies. This is in order to better understand the usefulness of an energy optimization on board the vehicle, which allows to reduce consumption in the use phase and to allow the sizing of a reduced battery pack in the design phase, which therefore allows to save resources in the production phase of the pack itself.

Much of the work presented in this thesis was partly supported by the "BIOMASS HUB" project [ID 1165247, PORFESR 2014–2020, and Regione Lombardia (IT)]. In particular the models exposed in the Section 2 (TEST model, for the simulation of the longitudinal dynamics of electric and hybrid electric vehicles, for energy consumption estimation), in the Section 4 (Hydrogen Fuel Cell model with hybrid electric/FC vehicle configuration) and in Section 5 (biomethane fuel cell vehicle model, with FC that acts as a generator to recharge the battery pack).

2 LONGITUDINAL DYNAMICS SIMULATION TOOL FOR HYBRID APU AND FULL ELECTRIC VEHICLE (TEST MODEL)

Due to problems related to environmental pollution and fossil fuels consumption that have not infinite availability, the automotive sector is increasingly moving towards electric powertrains. The most limiting aspect of this category of vehicles is certainly the battery pack, regarding the difficulty in obtaining high range with good performance and low weights. The aim of the work presented in this chapter is to provide a simulation tool, which allows for the analysis of the performance of different types of electric and hybrid powertrains, concerning both mechanical and electrical aspects. The first version of this model (named TEST, Target-speed EV Simulation Tool) is presented in [10], published in "MDPI - Energies" journal, after the publication of the paper the tool has undergone changes and improvements that have led to the version exposed in this doctoral thesis. Through this model it is possible to test different vehicle configurations before prototype realization or to investigate the impact that subsystems' modifications may have on a vehicle under development. This will allow to speed-up the model-based design process typical for fully electric and hybrid vehicles.

The main approach adopted in the TEST model is the "Backward-Facing" [21] as all variables are computed starting from the target speed profile (therefore from the vehicle wheels) to the motor (or motors). Then, the simulation tool checks the vehicle's performance limitations, such as the maximum performance of the motor (or motors) and the maximum battery current during both discharging and charging phases. Only if one or more limitations criteria are not met, the "Forward-Facing" approach is adopted to obtain the actual vehicle speed (which will deviate from the target one), considering the maximum vehicle performance. The tool, despite considering many variables concerning the vehicle is remarkably simple in terms of calculations made. Therefore, the computational burden required is limited and the simulation tool is decidedly efficient in this sense. The model aims to be at the same time complete but simple enough to lower the simulation time and computational burden so that it can be used in real-time applications, such as driving simulators. All this reduces the time and costs of vehicle design. Validation is also provided, based on a real vehicle and comparison with another consolidated simulation tool. Maximum error on mechanical quantities is proved to be within 5% while on electrical quantities it is always lower than 10%.

An extremely intuitive graphical user interface was also created for using the TEST program. The interface has been developed through MATLAB's APP Designer tool, which allows one to change all the variables input to the model quickly and easily. Through this approach it is also possible to use the program as a black box, without necessarily having to be aware of the specific mathematical background implemented in the simulation tool. It also offers the possibility to manage a large and complex array of output variables.

This chapter is organized as follows.

- In Section 2.1 a literature review is carried out, to highlight the differences and advantages of the TEST model compared to models already present in the literature.
- In Section 2.2 the general layout of this tool will be presented as well as the mathematical background. In particular, details of each submodel will be given.
- In Section 2.3 a graphical user interface will be presented. This interface is useful for using the program and for setting all the necessary inputs.
- In Section 2.4 the validation process will be described. The validation was carried out both through the comparison with the results of another consolidated simulation tool, and through the comparison with real-world experimental data.
- In Section 2.5 conclusion remarks are given. The utility and the featured application of this simulation tool will be highlighted as well.

2.1 LITERATURE REVIEW

Before presenting the TEST model in detail, it is interesting to analyse the literature, comparing the characteristics of this tool, highlighting its improvements, with those of existing models.

As an example, a consolidated simulation tool for innovative powertrains is reported in [22] and named PROPS (Powertrain ROad Performance Simulation); it covers both fully electric and hybrid powertrains, but the computational burden required is too large. In [23] a similar work is proposed with the addition of an algorithm to maximize powertrain efficiency and range. Both above-mentioned simulation tools have been successfully used to investigate which is the most representative driving cycle to estimate vehicles emissions [24]. Some other works have been found in the literature, but they are focused on a specific powertrain system or subsystem (battery pack for instance)

or vehicles categories (i.e., buses), instead of being generalized and multipurpose [25–29]. The calculation approach proposed in [30] is similar to that of this work and both models have been built in MATLAB/Simulink environment. However, the model presented in [30] is much simpler. For instance, the inertia of the wheels and the various transmission components are not taken into account (only the motor inertia can be taken into account). Moreover, this model only allows simulation of BEVs (Battery Electric Vehicles) with a single electric motor. The only approach adopted is the "Forward-Facing" one, and the eventual limitations imposed by the motor and the battery pack are not taken into consideration. The tool described in [31] has approximately the same structure as that described in [30], but it is built using Scilab. Both use a completely "Forward-Facing" approach, allowing the simulation only on BEVs equipped with a single electric motor and single ratio gear box. Both, compared to the tool proposed in this thesis, are more simplified. Finally, the method proposed in [32] is the most similar to what is proposed in this thesis. However, it is not up to date as it goes back to 1999 and consequently it is not in line with current technologies and developments.

The vehicle being simulated by the TEST model can have multiple powertrain configurations: front wheel drive, rear wheel drive, all-wheel drive, single electric motor or multi-motor. Generators and APUs can be single or multiple as well, and they can be connected in many ways to the virtual DC power bus. This simulation tool is therefore very flexible and open to various configurations/layouts. Furthermore, one of the main advantages of this tool compared to other tools [22,23,26,27] is that it does not involve any PID (or PI) controllers to perform closed-loop simulation with a target speed profile, hence avoiding complex calibration procedures. While most of the similar work from literature use a "Forward-Facing" model, i.e., the flow of calculation of quantities such as torques, forces, speeds, etc. goes from the motor (or motors) to the wheels, the TEST includes a "Backward-Facing" and "Forward-Facing" hybrid model, allowing for better computational efficiency.

2.2 SIMULATION TOOL

The model allows for the simulation of both the mechanical part (forces, torques, speeds, accelerations, etc.) and the electric part (electric powers, electric resistances, battery parameters) of a full electric vehicle or APU hybrid vehicle (see figures from Figure 2.1 to Figure 2.4).

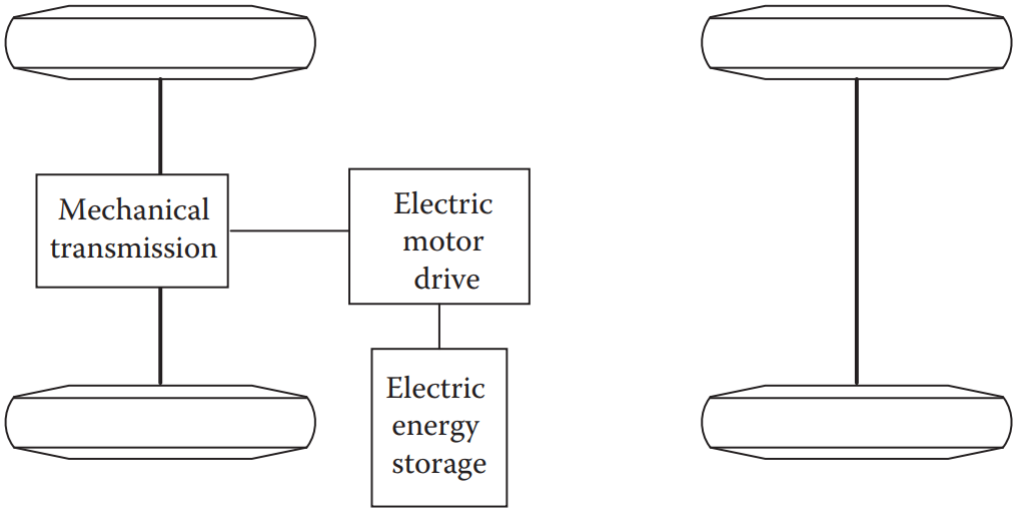

Figure 2.1. *Full electric vehicle powertrain* [33]. *In particular, the figure shows a vehicle with front or rear wheel drive only (depending on whether the left axle represents the front or rear axle respectively). The TEST model can simulate both configurations. In addition, it can also simulate full electric vehicles with all-wheel drive. For the latter, the diagram in the figure presents the components "Mechanical transmission" and "Electric motor drive" also on the other axle and this last motor is also connected to the "Electric energy storage". The TEST model can also simulate APU hybrid vehicles. The latter have one of the powertrain configurations described, but in addition have a generator or more generators that recharge the battery pack ("Electric energy storage ").*

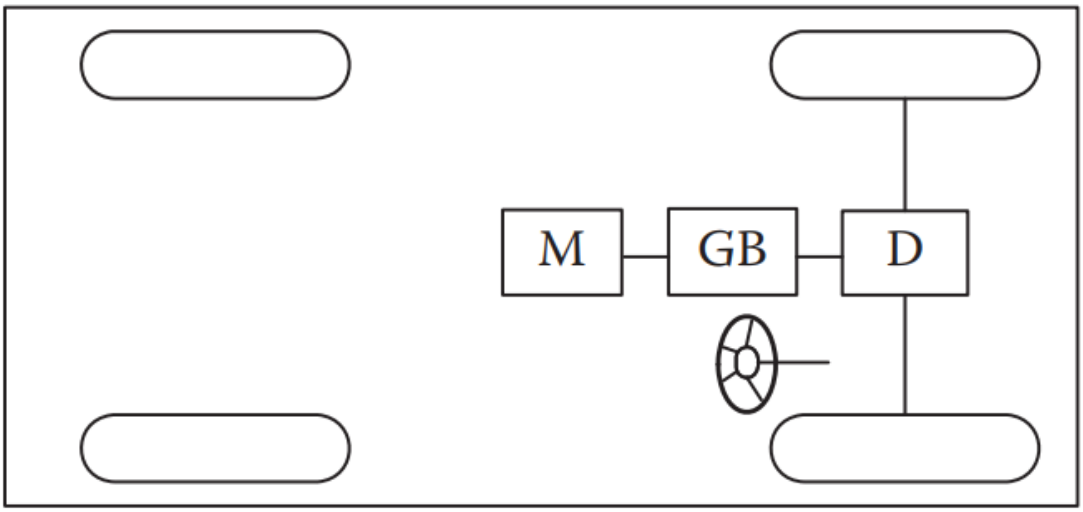

Figure 2.2. *Motor and transmission configuration of each driving axle. In particular: "M" represents the electric motor, "GB" represents a fixed gearing and "D" represents the differential* [33,34].

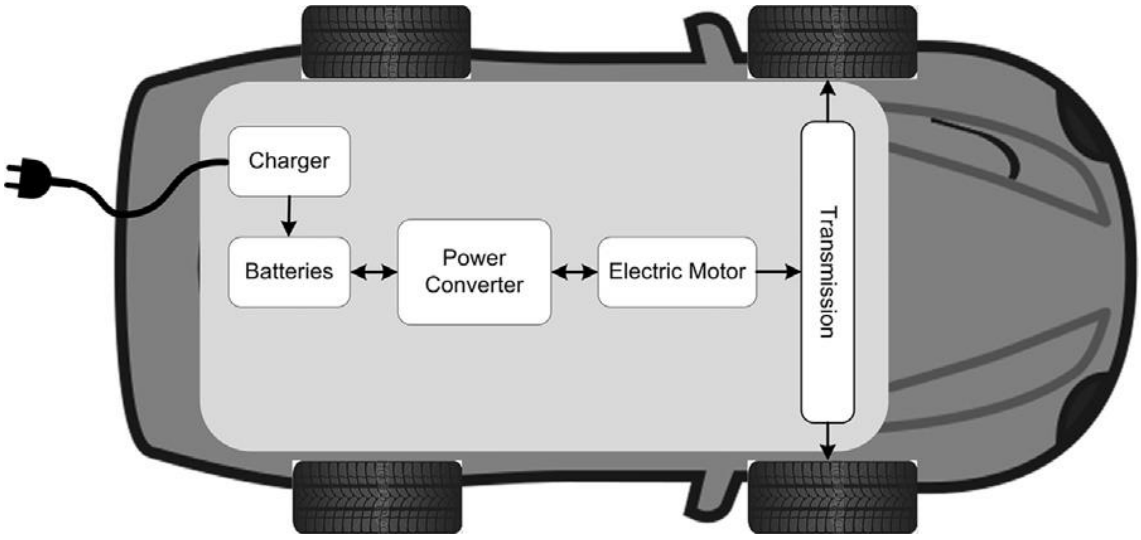

Figure 2.3. *Full electric vehicle powertrain* [35]. *In particular, the figure shows a vehicle with front wheel drive only. In addition, TEST model can also simulate full electric vehicles with rear wheel drive and all-wheel drive. For rear-wheel drive vehicles the diagram shown in the figure is the same, but with the transmission connected to the rear axle. For all-wheel drive vehicles, the powertrain is made up of two electric motors, each with its own transmission (with a single reduction ratio), acting on each axle. The charger shown in the figure has not been implemented in the TEST model.*

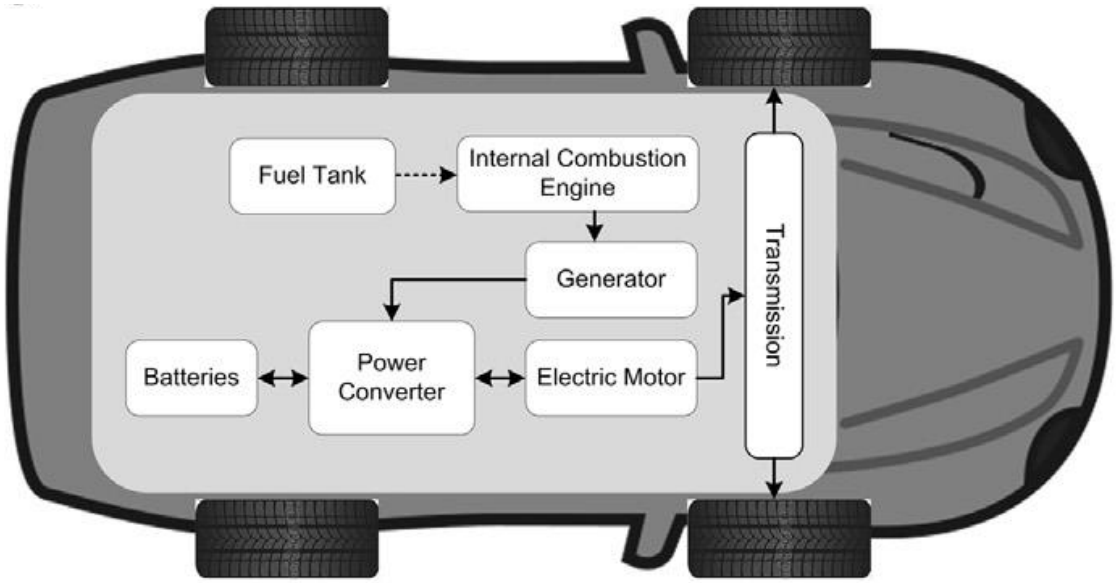

Figure 2.4. *Range extender vehicle (APU electric vehicle) powertrain* [35]. *In particular, the figure shows a vehicle with front wheel drive only. In addition, TEST model can also simulate APU electric vehicles with rear wheel drive and all-wheel drive. For rear-wheel drive vehicles the diagram shown in the figure is the same, but with the transmission connected to the rear axle. For all-wheel drive vehicles, the powertrain is made up of two electric motors, each with its own transmission (with a single reduction ratio), acting on each axle. The charger and the fuel tank shown in the figure have not been implemented in the TEST model. The internal combustion engine represented in the scheme could also represent a gas turbine.*

To lighten the model, it was chosen not to use the Simulink library blocks relating to the powertrain, apart from possibly the battery block ("Datasheet Battery"). The program works in fixed steps and the operating logic ensures that the model lends itself to discrete operation, obviously with the appropriate precautions, for example, by replacing the Simulink blocks of the derivatives and integrals with similar calculations obtained using only blocks that allow for discreet operation.

In this regard, following the same logic, the "Datasheet Battery" block has been reworked, to obtain one that works discreetly but following the same logic. The following paragraphs explain the operating logic of the entire program. Furthermore, Figure 2.5 shows a schematic illustration of the operation of the program.

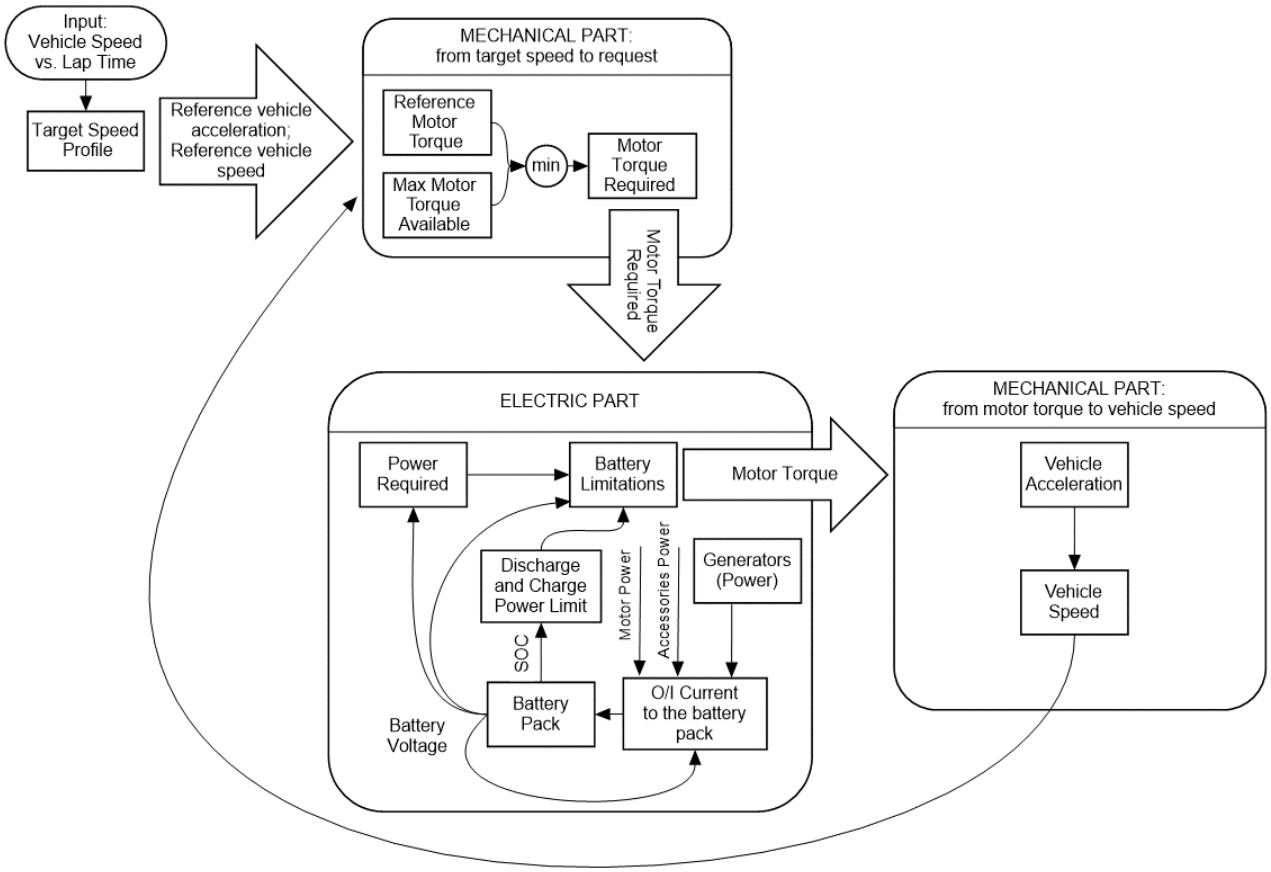

Figure 2.5. *Conceptual scheme of the Simulink model developed for the simulation of the longitudinal dynamics of an electric or hybrid vehicle that follows a target speed profile.*

2.2.1 Power Longitudinal Dynamics Modelling: From Target Speed to Request

Different speed profiles (different Laps) can be supplied as inputs to the model, once the profile to be followed is chosen, it is possible to filter it by defining a constant k. The model considers as the input speed profile the moving average of k values of the chosen speed profile. If you do not want to filter the profile, then simply set k equal to 1.

The reference acceleration a_{ref} is obtained from the filtered speed profile using the following equation (2.1):

$$a_{ref} = \frac{\left(v_{ref} - v_{prev}\right)}{t_s} \tag{2.1}$$

where v_{ref} is the target speed of the filtered speed profile, corresponding to the instant of calculation considered, v_{prev} is the actual vehicle speed of the instant of calculation preceding that considered and t_s is the sample time of the simulation.

Considering the wheel radius and the reduction ratios, the model calculates the angular speeds of the wheels and the rotation speed of the electric motors, not taking into account any slippages, as in equations from (2.2) to (2.5).

$$\omega_{wheel\_ref\_F} = \frac{v_{ref}}{R_{wheelF}} \tag{2.2}$$

$$\omega_{wheel\_ref\_R} = \frac{v_{ref}}{R_{wheelR}} \tag{2.3}$$

$$\omega_{mot\_ref\_F} = \omega_{wheel\_ref\_F} \cdot \tau_{diffF} \cdot \tau_{redF} \tag{2.4}$$

$$\omega_{mot\_ref\_R} = \omega_{wheel\_ref\_R} \cdot \tau_{diffR} \cdot \tau_{redR} \tag{2.5}$$

where $\omega_{wheel\_ref\_F}$ and $\omega_{wheel\_ref\_R}$ are the angular velocities of the wheels, front and rear respectively, if the vehicle faithfully follows the imposed speed profile (and without slippages), while R_{wheelF} is the rolling radius of the front wheels and R_{wheelR} that of the rear wheels. $\omega_{mot\_ref\_F}$ is the angular velocity of the motor that acts on the front axle and is calculated only in the presence of this motor, otherwise it is set equal to zero, the same is true for $\omega_{mot\_ref\_R}$ which is the angular velocity of the motor that acts on the rear axle. τ_{diffF} and τ_{diffR} are respectively the overall reduction ratios of the differential and transmission on the wheel side (with respect to the gearbox) of the front and rear drive chain, while τ_{redF} and τ_{redR} are the reduction ratios of the reduction/gearbox front and rear.

In addition to the speed target, it is also possible to impose, for each Lap, a temperature profile of the battery pack, linked to the speed profile, obtained for example experimentally, by detecting the temperature of the pack on a real vehicle that travels the imposed speed profile. The space travelled by the vehicle is obtained by integrating the speed of the profile, if the vehicle faithfully follows the imposed cycle. The model, through the space travelled and using a one-dimensional Lookup Table, detects the altitude of the road at the point considered on the track. The slope of the road surface is obtained from the distance on the track and from the elevation profile, the slope is expressed as an angle in degrees (θ), as follows (2.6):

$$\theta = asin\left(\frac{dz}{dx}\right) \tag{2.6}$$

where dz is the difference between the altitude of the road at the point considered and the altitude of the point of the instant of calculation preceding that considered, while dx is the difference in distance travelled, between the current instant and the previous calculation instant, with the imposed speed profile. In addition, if the vehicle is stationary, θ is imposed equal to that of the previous calculation instant.

The calculation of the resistant forces (additional resistant or traction force due to the slope, rolling resistance force and aerodynamic resistance) is essential for the functioning of the model. The additional force given by the presence of the slope of the ground F_θ, positive if it acts as a resistant force, negative if it is in favour of acceleration, agrees with the speed vector and acts as a traction force) is considered through the following relationship (2.7):

$$F_\theta = \left(m_{vehicle} + m_{driver} + m_{fuel} + m_{cargo}\right) \cdot g \cdot \sin(\theta) \tag{2.7}$$

g is the gravity acceleration, $m_{vehicle}$ is the unladen mass of the vehicle, m_{driver} is the driver's mass (plus the mass of any passengers), m_{fuel} is the mass of the fuel (considered constant during the simulation, in this version of the model), necessary for powering the any generators, and, finally m_{cargo} is the mass of the load carried by the vehicle, given as a function of time as input data.

The rolling resistance F_r is calculated using equation (2.8) as reported in [36] and in [37], also taking into account the downforce contribution, for nonzero speeds (and set zero for zero speed).

$$F_r = \left[\left(m_{vehicle} + m_{driver} + m_{fuel} + m_{cargo}\right) \cdot g + \frac{1}{2} \cdot WHF \cdot \rho \cdot {v_{ref}}^2\right] \cdot f \cdot \cos(\theta) \quad (2.8)$$

where WHF is the vertical aerodynamic coefficient, ρ is the air density and f is the rolling resistance coefficient calculated as in equation (2.9). In particular, the equation (2.9) predicts the values of f with acceptable accuracy for speeds up to approximately 130 km/h, as mentioned in [37].

$$f = f_r \cdot \left(1 + v_{ref} \cdot f_{r\_2}\right) \quad (2.9)$$

where f_r is the static rolling resistance coefficient and f_{r_2} is the coefficient which allows to consider the rolling resistance coefficient as a linear function of speed.

The equation (2.10) used to calculate the aerodynamic resistance F_{aero} is:

$$F_{aero} = \frac{1}{2} \cdot \rho \cdot C_x \cdot A_f \cdot \left(v_{ref}\right)^2 \quad (2.10)$$

where A_f is the frontal area of the vehicle and C_x is the longitudinal aerodynamic coefficient, considered constant. Therefore, in this version of this model, no aerodynamic map has been considered yet, which would still be easy to implement.

In the "Reference Motor Torque" block, the motor torques required to follow the target speed profile are calculated. There is in output from this block also the traction force required by the wheels (including the contribution given by the inertia of the wheels themselves), necessary in different blocks to distinguish the cases in which a positive traction force is required (to accelerate or to partially overcome the resisting forces and decelerate less intensely compared to the absence of traction force) from cases in which a negative one is required (to have greater deceleration than that given only by the resisting forces).

Moreover, a balance of forces acting on the vehicle (in the centre of gravity) is carried out in order to identify the traction force F_{tr} necessary for the vehicle to travel with acceleration equal to that of reference, as in the following equation (2.11):

$$F_{tr} = a_{ref} \cdot \left(m_{vehicle} + m_{driver} + m_{fuel} + m_{cargo}\right) + F_{aero} + F_r + F_\theta \quad (2.11)$$

Adding the inertia contributions to the traction force, the total traction force at wheels F_{ref_wheels} must be recalculated. The inertia contributions, respectively of the front ($F_{inertiaF}$) (2.12) and rear ($F_{inertiaR}$) (2.13) wheels, are obtained through the following equations:

$$F_{inertiaF} = 2 \cdot \frac{J_{wheelF}}{R_{wheelF}} \cdot \frac{\Delta(\omega_{wheel\_ref\_F})}{\Delta t} \tag{2.12}$$

$$F_{inertiaR} = 2 \cdot \frac{J_{wheelR}}{R_{wheelR}} \cdot \frac{\Delta(\omega_{wheel\_ref\_R})}{\Delta t} \tag{2.13}$$

where the "2" coefficient is used to consider both wheels of the axle. J_{wheelF} and J_{wheelR} are the front and rear wheel moment of inertia, respectively. The total traction force, including contributions due to the inertia of the wheels, is multiplied by $TractRatio_{acc}$ if the electric motors are used for traction or by $TractRatio_{brak}$ if the motors are used as generators to recharge the batteries during braking, to obtain the portion of traction force F_{tr_motF} which must be guaranteed by the front motor. $TractRatio_{acc}$ is the distribution of torque between the two electric motors (towards the front) in the case of the accelerator pedal pressed, $TractRatio_{brak}$ is the distribution in the event that the brake pedal is pressed. Using these distribution values to divide the traction force between the two axles, an approximation is therefore being made. Obviously, if only the front electric motor is present on the vehicle, both distributions will have to be set equal to 1, vice versa, if the vehicle has only rear motor, both distributions will be null.

Finally, the motor torques required at the front T_{ref_F} and at the rear T_{ref_R} are calculated, using relationships (2.14) and (2.15), only if the motor is present, considering the contributions of input and output inertia to the gearbox, the motors inertia and a general transmission efficiency for transmission on each of the two axles.

$$T_{ref\_F} = \frac{\frac{F_{tr\_motF} \cdot R_{wheelF} + J_{outF} \frac{\Delta(\omega_{wheel\_ref\_F})}{\Delta t}}{\tau_{diffF} \cdot \tau_{redF}} + (J_{inF} + J_{motF}) \frac{\Delta(\omega_{mot\_ref\_F})}{\Delta t}}{{\eta_{transF}}^{X}} \tag{2.14}$$

$$T_{ref\_R} = \frac{\frac{(F_{tr\_motF} - F_{ref\_wheels}) \cdot R_{wheelR} + J_{outR} \frac{\Delta(\omega_{wheel\_ref\_R})}{\Delta t}}{\tau_{diffR} \cdot \tau_{redR}} + (J_{inR} + J_{motR}) \frac{\Delta(\omega_{mot\_ref\_R})}{\Delta t}}{{\eta_{transR}}^{X}} \tag{2.15}$$

where X is equal to 1 in the case of motors that produce traction force and −1 in the case of motors that act as generators; J_{outF} and J_{outR} are the moment of inertia of the transmission before respectively the front and rear motor reducer; J_{inF} and J_{inR} are the moment of inertia of the transmission after respectively the front and rear motor reducer; J_{motF} is the moment of inertia of the front electric motor, while J_{motR} of the rear one; η_{transF} and η_{transR} are the general efficiencies of the entire transmission, front and rear respectively.

Once the torques that the electric motors must supply or absorb in the case of braking (and in the absence of traditional brakes) have been obtained, it is necessary to compare them with the maximum available torques of the two motors to check whether the target mission can be met or not. The calculation of the maximum torque available for each motor (front or rear) is obviously carried out only if the motor in question is present on the vehicle, otherwise the maximum torque value is set at zero. To obtain the maximum torque of the motors, the angular speeds (in RPM) of the previous instant are considered. This is done as an approximation since the rotation speed of the motors at the instant considered is not yet known, the vehicle may in fact, due to limitations of the motors or batteries, fail to follow the target speed profile.

In the Simulink model the maximum motor torques are obtained thanks to the Lookup Tables containing information regarding the torque curves of the motors in the condition of maximum admission. The reference torque T_{ref_F} and the maximum available torque at the front are compared and the torque T_{req_F}, which will in turn be compared with the limits imposed by the battery pack, is the lowest in modulus between the first two. The same approach can be adopted for the rear motor, for the calculation of T_{req_R}. Alternatively, for one or both motors, it is possible to define a maximum torque for regenerative braking, which has a trend that grows linearly, with slope m_{RB_F} for the front motor and m_{RB_R} for the rear one, as a function of the time elapsed since the start of the braking, and which then reaches a predefined maximum value (in module, T_{RBmax_F} for the front motor and T_{RBmax_R} for the rear one), as can be seen in Figure 2.6. This is what was done in the model, in the "Motor Torque Required" block.

Starting from the latter regenerative braking configuration, it is possible to return to the first described, simply by setting an absolute maximum braking torque equal to or greater than the maximum motor torque and an infinite angular coefficient for the equation of the straight line that binds time elapsed since start of braking and maximum regeneration torque at the instant considered. For the instant considered, it can now be considered that the rotation speed of the front and rear motor respectively, $\omega_{mot\_req\_F}$ and $\omega_{mot\_req\_R}$, is equal to the reference rotation speed of the relative motor (closely related to the target speed profile) if there is no limitation given by the maximum performance of the motor in question. While, if the motor is unable to guarantee the torque required by the target, its rotation speed is approximated to that of the previous instant.

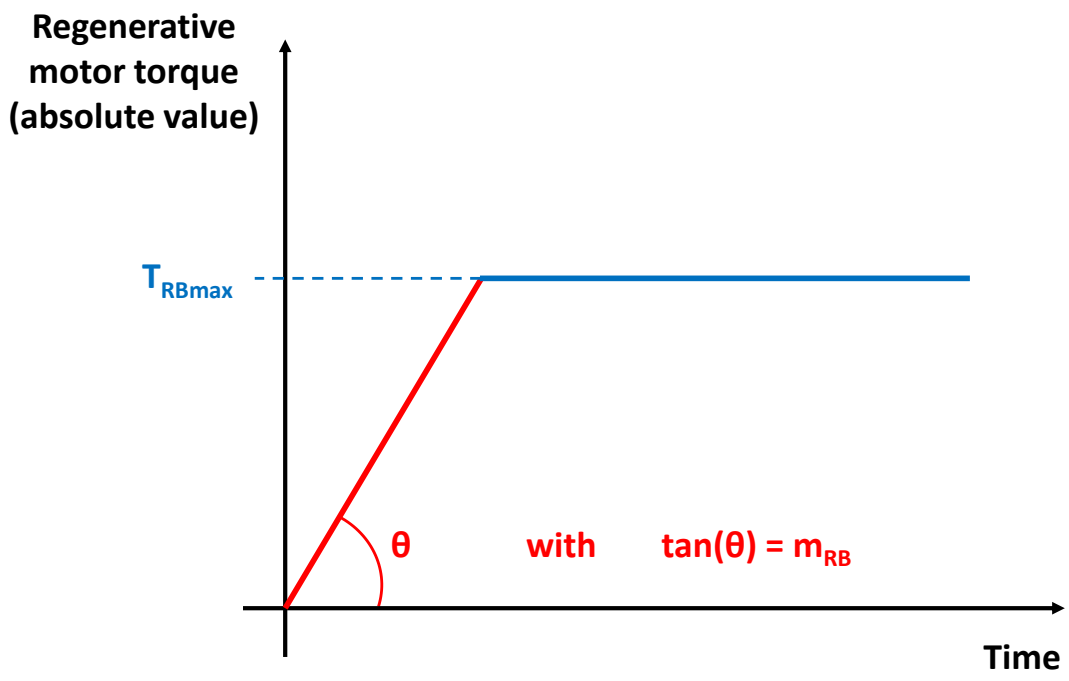

Figure 2.6. *Maximum regenerative motor torque trend implemented in the TEST model, where "T_{RBmax}" and "m_{RB}" are equivalent to* $\boldsymbol{T_{RBmax\_F}}$ *for the front motor and* $\boldsymbol{T_{RBmax\_R}}$ *for the rear one, and* $\boldsymbol{m_{RB\_F}}$ *for the front motor and* $\boldsymbol{m_{RB\_R}}$ *for the rear one respectively.*

Furthermore, it is possible to define a speed (one for the front motor, v_{RBmin_F} and one for the rear, v_{RBmin_R}) up to which the regenerative braking action by the electric motor will not intervene. Regenerative braking will therefore only activate after exceeding this limit speed. If no limit speed is desired, simply set the relative value to zero.

In the "Motor Torque Required" block, binary values (1 or 0) are also obtained as output depending on whether or not there are torque limitations due to the maximum performance of the motors, in the pressed accelerator condition ($Limit_{mot\_acc}$) and in the braking condition ($Limit_{mot\_brak}$). The question is whether this limitation, respectively in the accelerator or brake pedal pressed phase, that is present on only one motor, is enough to trigger the variable $Limit_{mot\_acc}$ or $Limit_{mot\_brak}$ the unit value.

2.2.2 Power Electronics and BMS Modelling

Once the requests of the mechanical part have been defined, it is necessary to consider the electrical part to take into account any limitations given by the batteries and for the calculation of the power, current, voltage and SOC (State of Charge) parameters of the battery pack.

2.2.2.1 Battery Limitations

To know the power that the electric motors must request from the batteries (or the power that thanks to the motors recharge the batteries) it is necessary to know the powers lost due to the Joule effect due to the resistances of the electric cables that connect the motors and batteries themselves. Obviously, the connection cables are present only in the presence of the relative motor; therefore, in the absence of the latter the related resistance is considered null. The connection cables' resistances between batteries and front R_{cableF} and rear R_{cableR} motor are calculated as follows, in equations (2.16) and (2.17):

$$R_{cableF} = \rho_{Cu} \cdot \frac{L_{cableF}}{\frac{\pi}{4}(\Phi_{cableF})^2} \tag{2.16}$$

$$R_{cableR} = \rho_{Cu} \cdot \frac{L_{cableR}}{\frac{\pi}{4}(\Phi_{cableR})^2} \tag{2.17}$$

where ρ_{Cu} is the resistivity of copper (or any other material the electrical cables under consideration can be made), L_{cableF} and L_{cableR} are the total lengths of the connection cables of the front and rear motor respectively, $\frac{\pi}{4}(\Phi_{cableF})^2$ and $\frac{\pi}{4}(\Phi_{cableR})^2$ are the cross-sectional areas of the front and rear cables while Φ_{cableF} is the diameter of the front cables and Φ_{cableR} is the diameter of the rear cables.

Within the "Power Required" block, the total power required of the batteries by the electric motors (or that the motors could guarantee as input to the batteries) is calculated, instant by instant. This power is the result of an approximation as no voltage drop is considered as regards the resistance of cables and electric motors. In particular, the total power required P_{tot_req} is equal to the sum of the power required by the front motor P_{reqF} and that required by the rear motor P_{reqR}. The calculation of the latter two quantities is represented in equations (2.18) and (2.19).

$$P_{reqF} = \frac{T_{req\_F} \cdot \omega_{mot\_req\_F}}{\eta_{mot\_ref\_F}{}^{Y}} + R_{cableF} \cdot \left(\frac{T_{req\_F} \cdot \omega_{mot\_req\_F}}{V}\right)^2 \tag{2.18}$$

$$P_{reqR} = \frac{T_{req\_R} \cdot \omega_{mot\_req\_R}}{\eta_{mot\_ref\_R}{}^{Z}} + R_{cableR} \cdot \left(\frac{T_{req\_R} \cdot \omega_{mot\_req\_R}}{V}\right)^2 \tag{2.19}$$

where Y and Z are worth 1 if the motors require energy from the batteries, -1 if the motors act as generators by sending energy to the battery pack. V is the voltage of the battery pack and is calculated in the Simulink "Battery Pack" block of the model, $\eta_{mot\_ref\_F}$ and $\eta_{mot\_ref\_R}$ are the electrical efficiencies of the front and rear motor and they are obtained through a special block, which is present

inside the "Power Required" block. The electrical efficiencies of the motors are calculated by the model only if the considered motor is present, otherwise the relative efficiency is set to zero. In particular, the efficiency of each motor is obtained thanks to a two-dimensional Lookup Table that receives in input the motor torque and motor speed and returns the efficiency.

In the equations (2.18) and (2.19), implemented in the TEST model, the electrical efficiency of the motor has been neglected for the calculation of the power dissipated to Joule effect, without affecting the final results. For the sake of accuracy, the two equations should be rewritten as equations (2.22) and (2.23). In a version of the TEST model following the one described in this thesis (from Section 2 to Section 5), the equations (2.18) and (2.19) will therefore be replaced by equations (2.22) and (2.23).

$$P_{reqF} = \frac{T_{req\_F} \cdot \omega_{mot\_req\_F}}{{\eta_{mot\_ref\_F}}^{Y}} + R_{cableF} \cdot \left(\frac{T_{req\_F} \cdot \omega_{mot\_req\_F}}{{\eta_{mot\_ref\_F}}^{Y} \cdot V} \right)^2 \tag{2.20}$$

$$P_{reqR} = \frac{T_{req\_R} \cdot \omega_{mot\_req\_R}}{{\eta_{mot\_ref\_R}}^{Z}} + R_{cableR} \cdot \left(\frac{T_{req\_R} \cdot \omega_{mot\_req\_R}}{{\eta_{mot\_ref\_R}}^{Z} \cdot V} \right)^2 \tag{2.21}$$

To calculate the overall power input or output from the battery pack, it is also necessary to know the power supplied by the generators (if they are present). In this version of the model, the possibility of integrating the vehicle with a number of generators N_{gen} that is zero or greater than zero was considered, where all the generators installed on the vehicle are identical and all have the same operation instant by instant.

Furthermore, no resistance of the connection cables between generators and batteries was considered, considered negligible. In particular, the generators have a constant rotation speed and a constant rated power output over time, unless the need to cut power due to the limitations imposed by the maximum performance of the battery pack.

In the "Generators" subassembly, the electrical efficiency of the single generator is obtained starting from the nominal power (P_{gen_nom}, positive) of the single generator and its rotation speed ω_{gen}, through a two-dimensional Lookup Table. Multiplying the efficiency by the rated power and by the number of generators gives the total maximum power value (P_{gen_th}, positive) that the generators can supply as input to the battery pack.

For the comparison of the balance of the power required, entering or leaving the battery pack, with the limitations of the pack itself, it is also necessary to consider the contribution of the power lost inside the cells due to their electrical

resistance. First of all, the model, starting from the total power entering or leaving the battery pack and the voltage of the pack, calculates the theoretically required current I_{req} if there are no limitations given by the batteries, as in equation (2.22).

$$I_{req} = \frac{P_{tot\_req} + P_{acc} - P_{gen\_th}}{V} \tag{2.22}$$

where P_{acc} is the total power consumed by the vehicle accessories, considered constant. A Lookup Table, which receives the temperature of the battery pack and the SOC at the input, returns the resistance R_i of the single cell to the output.

Finally, the calculation (2.23) of the total power $P_{battI2R}$ of all cells, dissipated by Joule effect in the entire battery pack is:

$$P_{battI2R} = N_s \cdot R_i \left(\frac{I_{req}}{N_p}\right)^2 \tag{2.23}$$

where N_s corresponds to the number of cells arranged in series inside the battery pack, while N_p the number of those arranged in parallel. The power dissipated by the Joule effect thus obtained is relative to the case in the absence of limitations given by the maximum performance of the battery pack, but will be used, as an approximation, even in the cases in the presence of such limitations. In this way, in limited condition, an approximation of the power lost due to the internal resistance of the cells is made for excess. In the "Battery Limitations" block, the discharging and charging limitations of the batteries are considered. These limitations can be expressed as powers or as currents.

In particular, these limits are defined in function of the SOC of the pack and they are obtained in a dedicated subassembly which will be described later. The power balance shown below, in inequalities (2.24) and (2.25), allows one to distinguish the case of discharge from that of recharging the batteries.

Discharge of the battery pack:

$$P_{tot\_req} + P_{acc} + P_{gen\_th} \geq 0 \tag{2.24}$$

Charge of the battery pack:

$$P_{tot\_req} + P_{acc} + P_{gen\_th} < 0 \tag{2.25}$$

Depending on whether the power balance mentioned above is positive (or null) or negative, one passes to considering an "if" subassembly or another in the Simulink model. In the case that the previous power balance is positive or null, the desired variables are the output from the "if" subassembly "Battery

Discharge". In this case, the generators can work by supplying the entire rated power as output, without the need for limitations.

In this block there are in turn two further "if" checks that divide the case in which there is no limitation imposed by the battery pack from that in which the power absorbed by the electric motors must be limited. The available power $P_{available}$, which can be taken from the battery pack, is calculated as in equation (2.26):

$$P_{available} = \left(V \cdot I_{dischrg\_limit}\right) \cdot \eta_{inv\_disch} - P_{buffer} - P_{battI2R} + P_{gen} \tag{2.26}$$

where η_{inv_disch} is the efficiency of the inverter in discharge and which is valid in the event that the discharge limit of the battery pack is supplied as a limit current (positive, $I_{dischrg\_limit}$), if it is expressed as a power (positive, $P_{dischrg\_limit}$) the previous relationship must be reconstructed as follows, in equation (2.27):

$$P_{available} = P_{dischrg\_limit} \cdot \eta_{inv\_disch} - P_{buffer} - P_{battI2R} + P_{gen} \tag{2.27}$$

where P_{buffer} is simply a constant power that is used to keep within the discharge and charge limits with a defined tolerance, equal to the value of this constant and P_{gen} is the "real" power supplied to the batteries by the generators, which in case of discharge is equal to the maximum power P_{gen_th}, without the need for any limitation. The power to be taken from the battery pack consists of the sum of the power absorbed by the vehicle accessories (P_{acc}, considered constant) and the total power required by the electric motors P_{tot_req}. By subtracting the contribution of these two powers from the maximum available, it is therefore possible to ascertain whether this is actually available and therefore no limitation is necessary or vice versa (i.e., if the result of this subtraction is positive or negative).

The losses associated with the inverter were considered by means of two constant efficiency values (in charge and in discharge). However, if a more precise implementation is needed, it would be good to consider the losses associated with the inverter as the sum of the conduction losses (proportional to the square of the current) and the commutation losses (which are a function of the commutation frequency and the speed of the motor).

In the event that there are no limitations given by the battery pack being discharged, the required quantities will actually be the "real" ones of the vehicle, at the instant considered (remembering that the limitations of maximum drive torque have already been considered), and they will be taken as output from the first "if" block.

A binary control variable is also defined, $Limit_{batt\_acc}$, defined in this case equal to 0, defined instead equal to 1 in the condition of limitation of the motors during traction due to the maximum performance of the batteries. The calculations are carried out in the second "if" block if it is necessary to impose limitations during the discharge phase. In the case with limitation in the discharge phase, if the available power is not enough even to power the accessories, obviously the electric motors will be turned off and it is necessary to define the ΔP_{acc} variable to keep track of the amount of power missing for the power supply of the accessories. ΔP_{acc} is defined equal to the difference between available power and power that should be absorbed by the accessories. On the other hand, if after the part of available power supplied to the accessories is considered, a part of power remains available; the latter will be used to power the electric motors.

In the presence of both motors, this power will be divided between front P_{battF} and rear P_{battR} through the distribution constant $TractRatio_{acc}$. Below are the calculations of the front drive torque T_{mot_F}, in equation (2.28), and rear T_{mot_R}, in equation (2.30).

$$T_{mot\_F} = \frac{\left[P_{battF} - R_{cableF} \cdot \left(\frac{P_{battF}}{V}\right)^2\right] \cdot \eta_{mot\_F}}{\omega_{motF}} \tag{2.28}$$

$$\omega_{motF} = \omega_{mot\_prev\_F} \tag{2.29}$$

$$T_{mot\_R} = \frac{\left[P_{battR} - R_{cableR} \cdot \left(\frac{P_{battR}}{V}\right)^2\right] \cdot \eta_{mot\_R}}{\omega_{motR}} \tag{2.30}$$

$$\omega_{motR} = \omega_{mot\_prev\_R} \tag{2.31}$$

For the calculation of both motors torques, it is taken into account the resistance of the cables (but the relative voltage drop is neglected), the electrical efficiency of the motors (η_{mot_F} and η_{mot_R}, obtained by means of the Lookup Table, starting from the efficiency map of the motors) and the equality of the instantaneous rotation speed of the motor (ω_{motF} and ω_{motR}) is set as an approximation to the rotation speed relative to the previous instant of calculation ($\omega_{mot\_prev\_F}$ and $\omega_{mot\_prev\_R}$) as show in the equations (2.29) and (2.31).

The foregoing is valid in the event that the electric motors must absorb power from the battery pack, but it could fall into the limit case in which the motors act as generators ($P_{tot\_req} < 0$), but the power absorbed by the accessories is still sufficient to ensure that the batteries are being discharged. In this case, no

limitation is required for the motors torque and the ΔP_{acc} will be calculated as follows (2.32).

$$\Delta P_{acc} = P_{available} - P_{tot\_req} - P_{acc} \tag{2.32}$$

The $Limit_{batt\_acc}$ control variable is defined for both motors and the output variable to the "if" block will be equal to 1 if that relating to at least one motor is unitary (i.e., if at least one of the motors is limited by the maximum performance of the battery pack), equal to zero vice versa. If a motor (front or rear) is not present on the vehicle in question, all the relevant quantities are defined as null, including the $Limit_{batt\_acc}$ variable. In case that the battery pack is in a recharging condition, the desired variables are output from the "Battery Charge" "if" subassembly, contained in the "Battery Limitations" block. In the "Battery Charge" block there are in turn two further "if" blocks that divide the case in which there is no limitation imposed by the battery pack from that in which it is necessary to implement limitations. The maximum power that the battery pack can absorb $P_{absorbable}$ is calculated using the following equation (2.33):

$$P_{absorbable} = \frac{\left(V \cdot I_{chrg\_limit}\right)}{\eta_{inv\_ch}} + P_{buffer} - P_{battI2R} - P_{acc} \tag{2.33}$$

where η_{inv_ch} is the efficiency of the inverter in charge. equation (2.33) is valid if the discharge limit of the battery pack is supplied as a limit current (negative, I_{chrg_limit}), if it is expressed as a power (always negative, P_{chrg_limit}) the previous relationship must be reconstructed as follows, as in equation (2.34):

$$P_{absorbable} = \frac{P_{chrg\_limit}}{\eta_{inv\_ch}} + P_{buffer} - P_{battI2R} - P_{acc} \tag{2.34}$$

It is therefore possible to understand if it is necessary to make limitations or not, considering the power contributions of generators and electric motors. The outputs are obtained from the "if" subassembly relating to the absence of limitations if the inequality (2.35) is valid, from the "if" subassembly relating to the presence of limitations vice versa.

$$P_{absorbable} + P_{gen\_th} - P_{tot\_req} \leq 0 \tag{2.35}$$

When no limitation is required during the battery discharge, the system variables are considered equal to those resulting from the comparison with the maximum performance of the electric motors. $Limit_{batt\_brak}$ binary control variable is also defined, null in the absence of limitations of the electric motors when braking (and also even if the motors participate in traction), set equal to 1

in the case of motor limitation during regenerative braking, due to battery limitations. $Limit_{gen}$ is instead a binary quantity useful for checking that the generators have been limited (when it is equal to 1) or less (equal to zero).

The "if" subassembly relating to the presence of current limitations is in turn divided into two "if" subassembly, "Without Motor Power Restrictions" and "With Regenerative Braking Restriction". The model recovers the variables of interest from the first "if" block if the maximum $P_{absorbable}$ that the battery can absorb (negative) is less than or equal to the required power P_{tot_req} (input or output to the battery pack) from the motors, vice versa from the second "if" subassembly. The logic adopted is to limit the generators first, so as to be able to guarantee the regenerative braking of the motors within the limits (so as to be able to exploit the traditional brakes of the vehicle to a minimum) and only in case of need for further limitation also limit the electric motors. If it is sufficient to implement the limitation to the generators only, the only new quantity to be calculated is precisely the "real" power that the generators supply to the battery input P_{gen}, equal to the difference between the total power of the motors P_{tot_req} and the maximum absorbable power battery $P_{absorbable}$. The difference has been structured in this way to ensure that the power of the generators is positive. If it is also necessary to limit the power of the electric motors, the generators will be turned off and all the power supplied as input to the battery will be guaranteed by the electric motors $P_{mot\_tot} = P_{absorbable}$. In this case, the control variables will assume the following binary values, represented in equations (2.36) and (2.37).

$$Limit_{mot\_brak} = logical(1) \tag{2.36}$$

$$Limit_{gen} = \begin{cases} logical(1), & N_{gen} \neq 0 \\ logical(0), & N_{gen} = 0 \end{cases} \tag{2.37}$$

The total power supplied by the motors P_{mot_tot} is divided between the front P_{battF} and the rear P_{battR} by means of the distribution constant $TractRatio_{brak}$. The new quantities of the system are obtained by means of the equations from (2.38) to (2.41).

$$T_{mot\_F} = \frac{\left[P_{battF} - R_{cableF} \cdot \left(\frac{P_{battF}}{V}\right)^2\right]}{\eta_{mot\_F} \cdot \omega_{mot\_prev\_F}} \tag{2.38}$$

$$\omega_{motF} = \omega_{mot\_prev\_F} \tag{2.39}$$

$$T_{mot\_R} = \frac{\left[P_{battR} - R_{cableR} \cdot \left(\frac{P_{battR}}{V}\right)^2\right]}{\eta_{mot\_R} \cdot \omega_{mot\_prev\_R}} \tag{2.40}$$

$$\omega_{motR} = \omega_{mot\_prev\_R} \tag{2.41}$$

Again, the motors' efficiencies are obtained by means of Lookup Tables and the voltage drops caused by the resistances of the electric cables are neglected. Furthermore, the rotation speed of the motors is approximated to that of the previous calculation instant. This part of the Simulink model, which includes the limitations of the battery pack, represents part modelling of the BMS. The logic of the BMS is strongly linked to the type of battery and the strategies adopted by the vehicle manufacturer. For this reason, these logics can vary greatly depending on the type of vehicle and its mission.

2.2.2.2 Battery Parameters

Once the requests for electric motors and generators have been defined, after applying the necessary limitations, it is necessary to know the input or output current to the battery pack. The calculation of the current (I) is very simple, and it is represented by the equation number (2.42) if there is a discharge condition of the battery pack, otherwise, in charge condition, it is represented by the equation (2.44).

$$I = \frac{P_{mot\_tot} + P_{acc} + \Delta P_{acc} - P_{gen}}{V \cdot \eta_{inv\_disch}} \tag{2.42}$$

$$I = \frac{\left(P_{mot\_tot} + P_{acc} + \Delta P_{acc} - P_{gen}\right) \cdot \eta_{inv\_ch}}{V} \tag{2.43}$$

where the total battery power deriving from the electric motors P_{mot_tot} is the sum of the front contribution P_{battF} and rear contribution P_{battR}.

Considering the current passing through the battery pack, relative to the previous calculation instant with respect to the one considered, it is possible to obtain all the battery values of interest, including the voltage of the pack, used for the calculations inside the blocks previously exposed.

In the model, the thermal balances are not taken into account, the temperature can therefore be assumed constant or supplied as input starting from experimental values measured according to the target speed profile.

Furthermore, by multiplying the current and voltage between them, it is possible to obtain the incoming (negative) or outgoing (positive) power from the battery pack, starting from the current of the previous calculation instant (I_{prev})

and the instantaneous temperature of the battery pack, it is possible, through the "Datasheet Battery" (Figure 2.7) block of the Simulink library, to obtain battery state of charge $BattSoc$ and voltage (V) of the pack. The battery block of the Simulink library is an internal resistance battery model [29] and it is easily replicable for its discreet use if there is the need to perform this type of simulation.

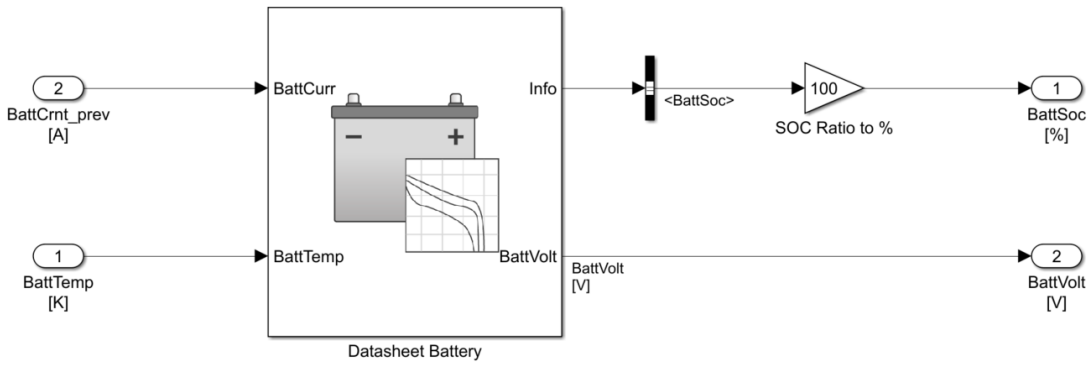

Figure 2.7. *The "Datasheet Battery" block and its connections with model parameters. The "Datasheet Battery" block is present in the "Simulink Library Browser" in the "Powertrain Blockset". The model parameters "BattCrnt_prev" represents* $\boldsymbol{I_{prev}}$ *, "BattTemp" is the temperature of the battery pack (average temperature of the battery cells measured by the BMS) expressed in Kelvin, "BattSoc" is the battery state of charge, and "BattVolt" is the voltage* $\boldsymbol{V}$ *of the battery pack.*

Finally, to conclude the discussion concerning the electrical part of the model, the origin of the discharge and charge limits of the battery pack, obtained starting from the state of charge of the battery pack, is described. Both limits are obtained using Lookup Tables which contain information about the link between SOC and limit in discharge and the link between SOC and limit in charge.

2.2.2.3 "Datasheet Battery" block

This subsection shows the parameters to be set in the "Datasheet battery" block in detail. The Figure 2.8 shows these parameters.

The "Rated capacity at nominal temperature" (C_{batt}) in the mask of the "Datasheet Battery" block is the rated capacity of a single cell of the battery pack. In the TEST model it has been chosen to give the tool user the possibility to decide whether to set the capacity value of the single cell or to supply the capacity of the entire battery pack as input data (see Section 2.3, in particular Figure 2.16). The value of the type of capacity chosen (of the cell or of the pack) is written by the

tool in the MATLAB® "Workspace" as variable `BattChargeMax`. The "Rated capacity at nominal temperature" in the mask is then calculated using the equation (2.44).

$$C_{batt} = \texttt{BattChargeMax/Batt\_Np\_2} \tag{2.44}$$

where `Batt_Np_2` is equal to 1 if C_{batt} defined by the user corresponds to the capacity of the single cell, otherwise, if it corresponds to the capacity of the entire battery pack, `Batt_Np_2` is set by the tool equal to N_p.

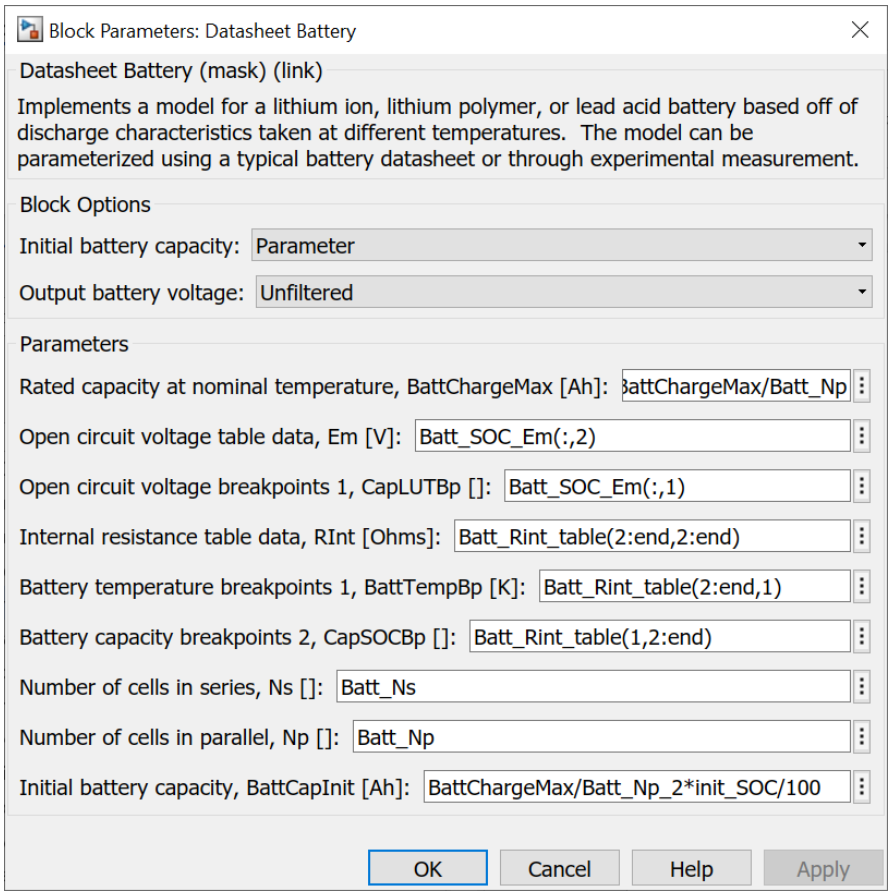

***Figure 2.8**. "Mask" window "Block Parameters" of the "Datasheet Battery" block, in the Simulink model TEST.*

The "Datasheet Battery" block wants the open circuit voltage as input data. `Batt_SOC_Em` is a vector that reports the values of the open circuit voltage of the single cell as a function of the SOC. The first column reports the SOC values ("Open circuit voltage breakpoints 1") and the second column reports the corresponding values of open circuit voltage ("Open circuit voltage table data").

The mask wants also the internal resistance of a single cell in function of temperature and SOC. `Batt_Rint_table` is a table where the first column reports the temperature values ("Battery temperature breakpoints 1"), the first row the SOC values ("Battery capacity breakpoints 2") and at the centre the corresponding internal resistance data ("Internal resistance table data").

The "Number of cells in series" (`Batt_Ns`) is simply N_s and the "Number of cells in parallel" (`Batt_Np`) is N_p.

Finally, the mask wants the "Initial battery capacity" (C_{batt_init}) expressed in Ah. In the TEST model it was chosen to provide the SOC of the battery pack at the start of the simulation (`init_SOC`), in percentage, as input data, so the initial capacity is calculated using the following equation (2.45).

$$C_{batt\_init} = \texttt{BattChargeMax/Batt\_Np\_2*init\_SOC/100} \tag{2.45}$$

2.2.3 Power Longitudinal Dynamics Modelling: From Motor Torque to Vehicle Speed

Once the limitations given by the electrical part have also been considered, it is necessary to define how the vehicle responds to the set speed target, faithfully following it or departing from it due to the limitations.

In the "Vehicle Acceleration" block, a balance of forces (see equation (2.46)) is carried out again, as in the case of the "Reference Motor Torque" block, but this time to find the "real" acceleration (a) of the vehicle, starting from the limited motors torques (if necessary).

$$a = \frac{F_{trF} + F_{trR} - F_{wheels\_inertia\_F} - F_{wheels\_inertia\_R} - F_{brake} - F_d - F_r - F_\theta}{m_{vehicle} + m_{driver} + m_{fuel} + m_{cargo}} \tag{2.46}$$

Thanks to the motor torque and the rotation speed of each of the electric motors, it is possible to obtain the front F_{trF} and rear F_{trR} traction force provided by the motors (positive if it is really a traction force, negative in the case of regenerative braking). If there is an electric motor that acts on the front axle, the related traction force is calculated as in (2.47), while it is imposed null in the absence of this motor. It is the same with regards to the electric motor that acts on the rear axle (2.48).

$$F_{trF} = \frac{\left[T_{mot\_F} \cdot \eta_{transF}{}^{T} - (J_{motF} + J_{inF})\frac{\Delta(\omega_{motF})}{\Delta t}\right] \cdot (\tau_{diffF} \cdot \tau_{redF}) - J_{outF}\frac{\Delta\left(\frac{\omega_{motF}}{\tau_{diffF} \cdot \tau_{redF}}\right)}{\Delta t}}{R_{wheelF}} \tag{2.47}$$

with $T = 1$ for $T_{mot\_F} \geq 0$, otherwise $T = -1$.

$$F_{trR} = \frac{\left[T_{mot\_R} \cdot \eta_{transR}{}^{U} - (J_{motR} + J_{inR}) \frac{\Delta(\omega_{motR})}{\Delta t}\right] \cdot (\tau_{diffR} \cdot \tau_{redR}) - J_{outF} \frac{\Delta\left(\frac{\omega_{motR}}{\tau_{diffR} \cdot \tau_{redR}}\right)}{\Delta t}}{R_{wheelR}} \quad (2.48)$$

with $U = 1$ for $T_{mot\_F} \geq 0$, otherwise $U = -1$.

The contributions given by the inertia of the front ($F_{wheels\_inertia\_F}$) and rear ($F_{wheels\_inertia\_F}$) wheels are calculated as follows using equations from (2.49) to (2.52).

If the front electric motor is present:

$$F_{wheels\_inertia\_F} = 2\frac{J_{wheelF}}{R_{wheelF}} \cdot \frac{\Delta\left(\frac{\omega_{motF}}{\tau_{diffF} \cdot \tau_{redF}}\right)}{\Delta t} \quad (2.49)$$

If the front electric motor is absent:

$$F_{wheels\_inertia\_F} = 2\frac{J_{wheelF}}{R_{wheelF}} \cdot \frac{\Delta\left(\frac{\omega_{motR}}{\tau_{diffR} \cdot \tau_{redR}} \cdot \frac{R_{wheelR}}{R_{wheelF}}\right)}{\Delta t} \quad (2.50)$$

If the rear electric motor is present:

$$F_{wheels\_inertia\_R} = 2\frac{J_{wheelR}}{R_{wheelR}} \cdot \frac{\Delta\left(\frac{\omega_{motR}}{\tau_{diffR} \cdot \tau_{redR}}\right)}{\Delta t} \quad (2.51)$$

If a rear electric motor is not included:

$$F_{wheels\_inertia\_R} = 2\frac{J_{wheelR}}{R_{wheelR}} \cdot \frac{\Delta\left(\frac{\omega_{motF}}{\tau_{diffF} \cdot \tau_{redF}} \cdot \frac{R_{wheelF}}{R_{wheelR}}\right)}{\Delta t} \quad (2.52)$$

The F_{brake} braking force of traditional brakes must be that necessary to integrate regenerative braking, if necessary, to allow the vehicle to follow the speed target when braking, unless there is any limitation given by the maximum permissible braking of the braking system. In the "Traditional Brakes" block, located inside the "Vehicle Acceleration" assembly, the balance of forces reported in (2.53) is carried out to obtain the braking force required (F_{brake_req}, defined positive) from the brake system.

$$F_{brake\_req} = F_{trF} + F_{trR} - F_{aero} - F_r - F_\theta - \left(m_{vehicle} + m_{driver} + m_{fuel} + m_{cargo}\right) \cdot a_{ref} \quad (2.53)$$

This force must be compared with the maximum force that can be generated by the braking system (F_{brake_max}, defined positive). The effective F_{brake} will be equal to the smaller of the two. The following equation (2.54) shows the calculation of F_{brake_max}:

$$F_{brake\_max} = 2 \cdot \frac{p_{brake\_max} \cdot Bias_{brakeF} \cdot A_{pistonF} \cdot \mu_{padF} \cdot R_{discF}}{R_{wheelF}} + 2 \cdot \frac{p_{brake\_max} \cdot (1 - Bias_{brakeF}) \cdot A_{pistonR} \cdot \mu_{padR} \cdot R_{discR}}{R_{wheelR}} \quad (2.54)$$

where p_{brake_max} is the maximum pressure that can be generated inside the master cylinder of the brake system; $Bias_{brakeF}$ represents the pressure portion, compared to that of the master cylinder, which acts on the front brakes; $A_{pistonF}$ and $A_{pistonR}$ are the total action areas of the brake pistons of the front and rear callipers respectively; μ_{padF} and μ_{padR} are the dynamic coefficients of friction between brake pads and brake callipers, front and rear; R_{discF} and R_{discR} are respectively the average radii of application of the braking force on the front and rear discs. In the "Traditional Brakes" block a further control parameter called $Limit_{trad\_brak}$ is defined, which is set to 1 if there is a limitation of traditional braking or equal to 0 instead.

The aerodynamic drag force F_d is equal to F_{aero} calculated previously on the basis of the target speed if in the instant considered there are no limitations to the motors caused by the maximum performance of the motors themselves or by the maximum performance of the battery pack and if there is no limitation of the traditional brakes. Otherwise, F_d is calculated using, as an approximation, the vehicle speed of the instant of calculation preceding the one considered. To avoid incurring approximation errors during the calculations, the "real" vehicle acceleration output from block "Vehicle Acceleration" is that calculated using equation (2.46) if there are limitations that lead to the failure to follow the target speed, otherwise a is defined equal to a_{ref}.

A further block relating to the mechanical part with limitations is the one called "Vehicle Speed", which outputs the "real" vehicle speed. The logical scheme adopted to obtain the "real" speed followed instant by instant by the vehicle is shown in Figure 2.9. As can be seen, appropriate measures have been taken to prevent the propagation of the approximation errors, inevitable during the calculations and due to different approximations adopted in the model. The sign of the F_{ref_wheels} variable is used to distinguish the case of the accelerator pedal pressed from the case of the brake pedal pressed.

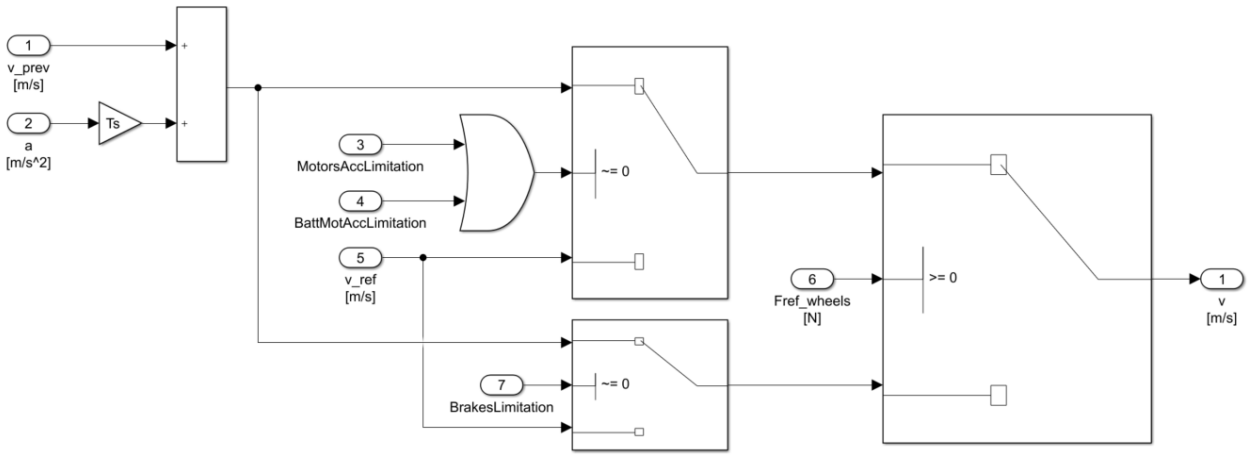

Figure 2.9. *Simulink logical scheme adopted to obtain the instantaneous vehicle speed. In the Simulink model shown in this figure,* `v` *is the variable* $\boldsymbol{v}$, `v_prev` *is the variable* $\boldsymbol{v_{prev}}$, `a` *is* $\boldsymbol{a}$ *variable,* `v_ref` *is* $\boldsymbol{v_{ref}}$, `Fref_wheels` *is* $\boldsymbol{F_{ref\_wheels}}$, `MotorsAccLimitation` *is* $\boldsymbol{Limit_{mot\_acc}}$, `BattMotAccLimitation` *is* $\boldsymbol{Limit_{batt\_acc}}$, *and* `BrakesLimitation` *is* $\boldsymbol{Limit_{trad\_brak}}$.

For the calculation of the speed (v), where necessary, a uniformly accelerated motion between one instant of calculation of the simulation and the next was considered, see equation (2.55).

$$v = v_{prev} + a \cdot t_s \tag{2.55}$$

Finally, from the speed it is also possible to obtain the space travelled by the vehicle (x) during the execution of the actual driving cycle, once again considering motion uniformly accelerated between two successive calculation steps, as in the following equation (2.56):

$$x = x_{prev} + v \cdot t_s + \frac{a}{2} \cdot t_s^2 \tag{2.56}$$

where x_{prev} is the space covered by the vehicle from the start of the simulation until the calculation step preceding the one considered.

2.2.4 Outputs

Once the simulation is completed, all variables will be saved in MATLAB® workspace. Therefore, the outputs are completely "customizable by the user" based on the variables he wants to analyse. In Section 2.4.1.6, and, in particular, in Figure 2.23, an example layout will be shown for the outputs with the most relevant quantities.

2.3 GRAPHIC USER INTERFACE

For easier and simpler management of the Simulink model, a graphic user interface has been created, using the "App Designer" tool of MATLAB®, which allows for the control and modification of all the inputs of the model and starts the simulation. In particular, it is possible to save, for a specific vehicle, six different simulations (from Lap 0 to Lap 5), relating to six different speed profiles, or use a standard driving cycle: WLTC (Worldwide Harmonized Light-Duty Vehicles Test Cycle) relating to WLTP procedure (Worldwide Harmonized Light-Duty Vehicles Test Procedure) [38], SFTP-US06-regulated cycle, described in the EPA Supplemental Federal Test Procedure (SFTP) or J227a cycle (Figure 2.10).

For the WLTC speed profile it is possible, through a special drop-down menu, to choose the class of the cycle according to the classification of the WLTP standard [38] and, through a specific switch, to set the simulation of the relative urban or non-urban cycle (Figure 2.10). For the J227a cycle it is instead possible, through the appropriate drop-down menu (Figure 2.10), to choose between the simulation of the J227a Schedule B, C or D standard profile.

All speed profile (including regulated driving cycles) can be edited by clicking on the "Define Speed Profile" button shown in Figure 2.10, each can also be filtered through the average of k elements. It is also possible to define an altimetric profile (clicking on the "Define Elevation Profile"), a temperature profile of the battery pack (clicking on the "Define Battery Temperature Profile"), a fixed sample time of simulation (t_s) and an initial state of charge of the battery pack (variable `init_SOC`, used in the "Datasheet Battery" block, see Section 2.2.2.3) for each Lap (speed profile). k, the altimetric profile, the temperature profile, t_s, and the initial SOC can differ between a Lap and the other (Figure 2.10). The elevation profile can be provided as the elevation in function of the space travelled by the vehicle or the time elapsed since the simulation began, the choice is declared to the software by means of the appropriate switch shown in Figure 2.10 ("Elevation profile vs. Space/Time").

It is also possible to choose, through the appropriate switch (Figure 2.10), whether, during the simulation, to repeat the set driving cycle until the SOC falls below a certain value (defined in "Minimum SOC [%]" in the panel of Figure 2.10) or whether to set a number of repetitions (defined in "N° of driving cycle repetitions" in the panel shown in Figure 2.10) of the driving cycle.

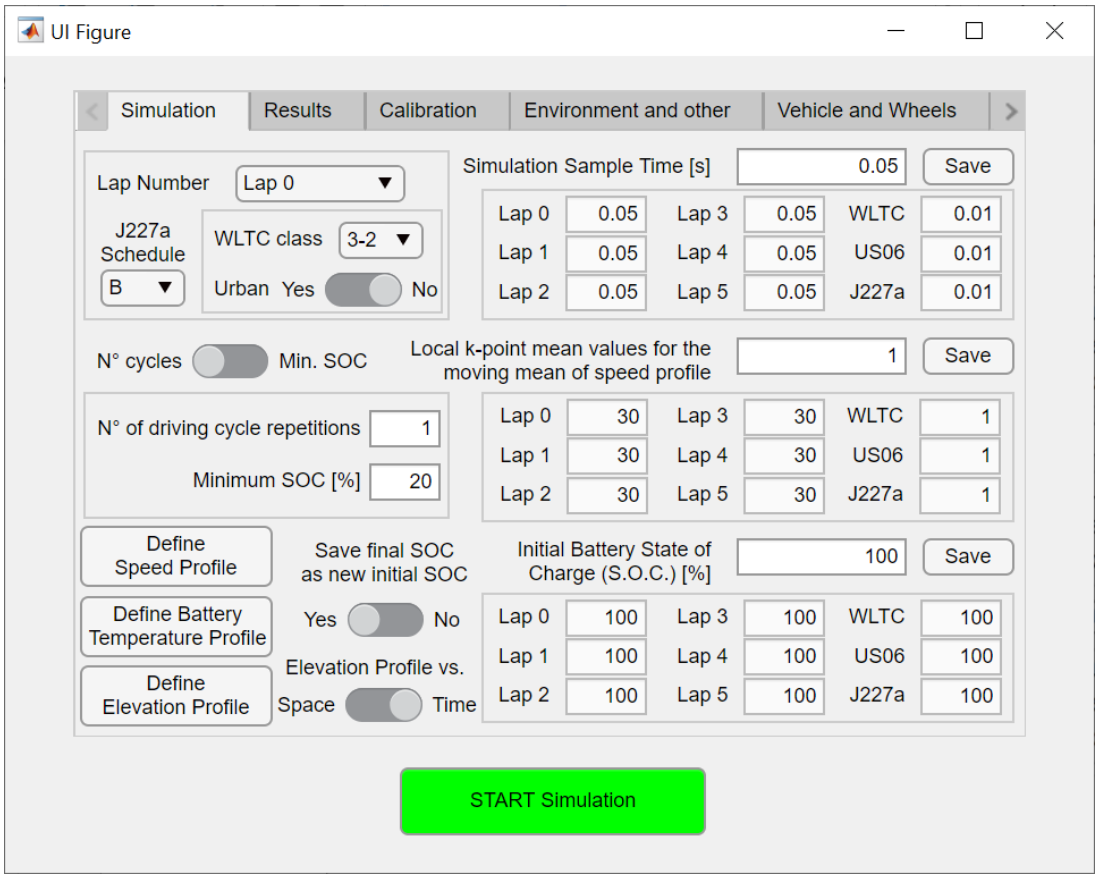

Figure 2.10. *"Simulation" panel of the Graphic User Interface. In particular, the "Simulation" panel allows you to enter the inputs regarding the simulation parameters.*

Finally, always in the "Simulation" panel (Figure 2.10) it is possible, by means of an appropriate switch, to decide whether at the end of the simulation to save the final SOC value as the new initial SOC value of the battery pack (for the Lap in question, to be used in a subsequent simulation).

Through the "Results" panel (Figure 2.11) it is possible to save 3 different sets of data that will be graphically compared with the results of the simulation of the TEST model, these data concern the following parameters as a function of time: battery current voltage and SOC, and front and rear motor torque.

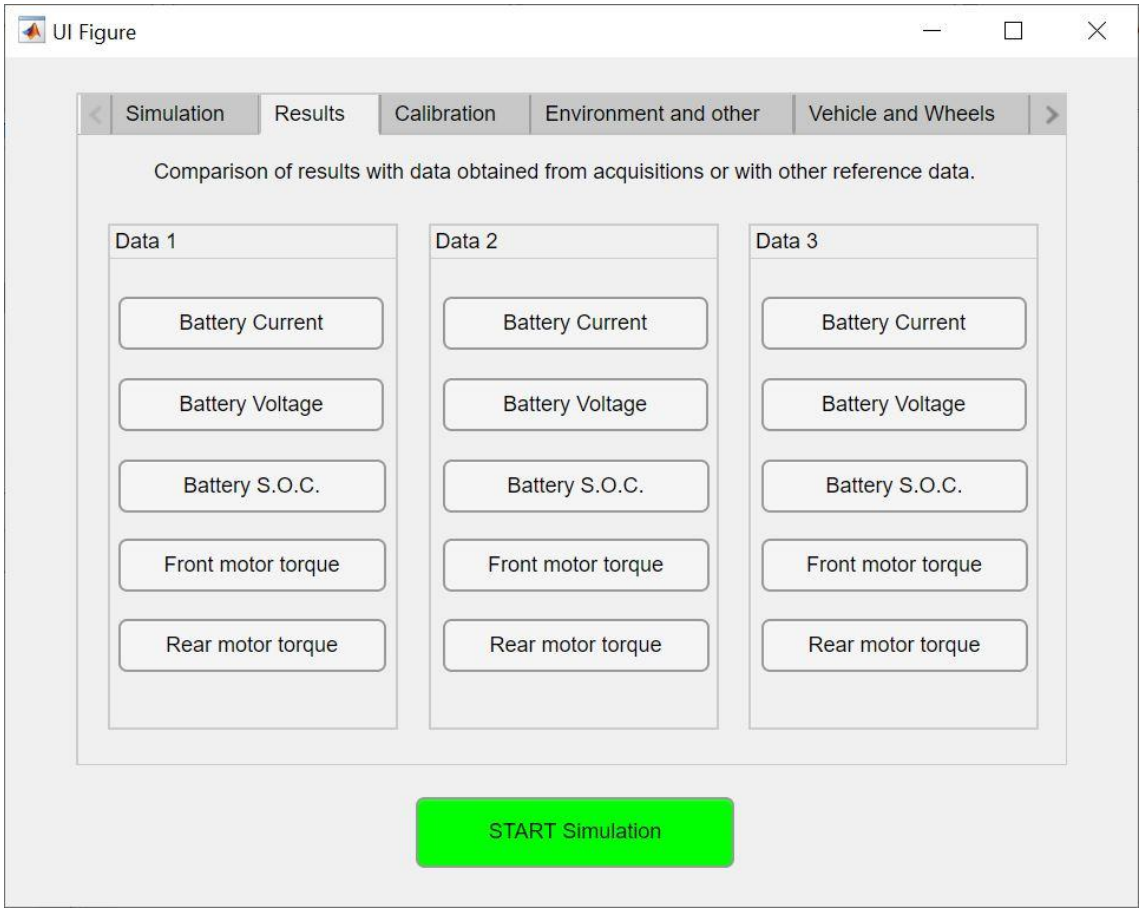

Figure 2.11. *"Results" panel of the Graphic User Interface. In particular, the "Results" panel allows you to save 3 sets of data that will be graphically compared with the results of the simulation of the TEST model.*

During the validation phase, the need for calibration of the mechanical part of the TEST model was found. This is particularly true for high-performance vehicles (see Section 2.4.2). The possibility of doing this calibration has therefore been integrated into the TEST model, through the "Calibration" panel (Figure 2.12) of the Graphic User Interface.

In particular, it is possible to calibrate the total motor torque (sum between the torque of the front and rear electric motor, if both present, otherwise it is the torque of the only motor present) as a function of the vehicle speed v (see Section 2.4.2.6). Below, in equation (2.57), the function used for calibration is shown.

$$y = c_N \cdot v^N + \cdots + c_2 \cdot v^2 + c_1 \cdot v + c_0 \tag{2.57}$$

with $N \geq 0$ and where y is the ratio between the TEST total motor torque and the "real" total motor torque. $c_N, \cdots, c_2, c_1, c_0$ are the calibration coefficient, which can

be defined by pressing the "Define Calibration Coefficient" button in the panel "Calibration" shown in Figure 2.12.

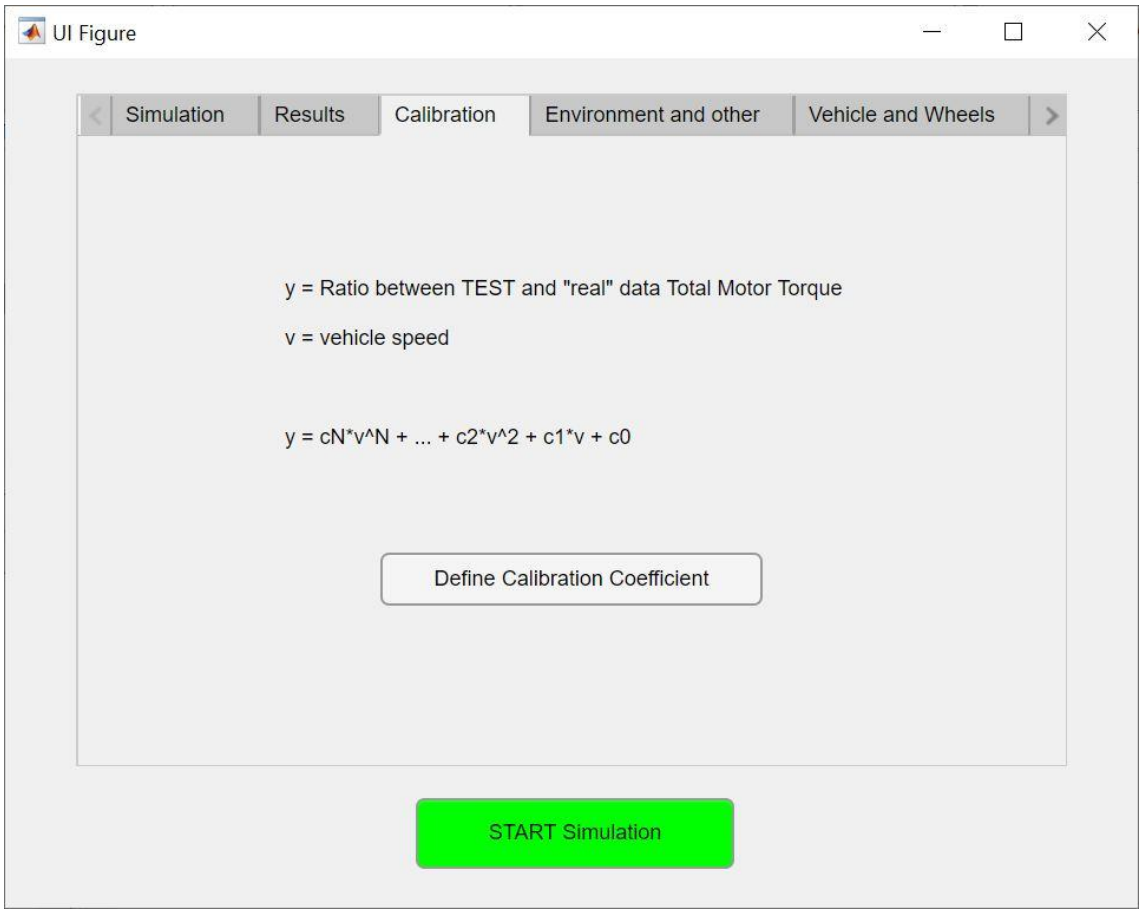

Figure 2.12. *"Calibration" panel of the Graphic User Interface. In particular, the "Calibration" panel allows you to calibrate the model, in particular the motor torque resulting from the simulation.*

Furthermore, it is possible to define all the environmental parameters (air density ρ, gravity acceleration g) and other parameters such as the resistivity (ρ_{Cu}) of the conductor cable material (for example copper), the driver's weight (m_{driver}), the weight of fuel on board (m_{fuel}), necessary to power any generators, and the mass of the cargo carried by the vehicle (Figure 2.13). The latter can be variable during the simulation and must be supplied as input to the model according to the time elapsed from the start of the simulation. It is then possible to define as input all the parameters relating to the vehicle in general and the wheels (Figure 2.14), and the traditional braking system (Figure 2.15).

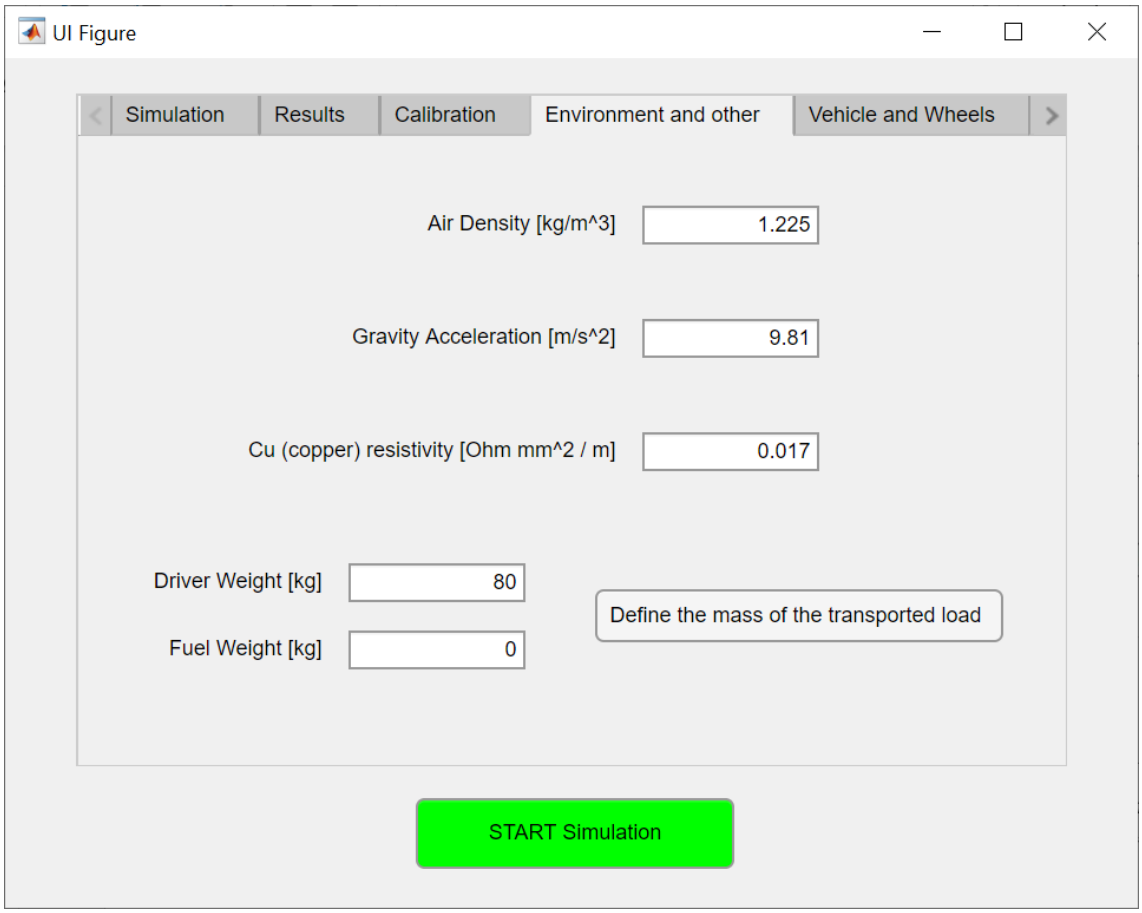

Figure 2.13. *"Environment and other" panel of the Graphic User Interface. In particular, this panel allows you to enter the inputs regarding the environmental (and other) parameters.*

In the "Vehicle and Wheels" panel (Figure 2.14) you can define the total mass of the empty vehicle ($m_{vehicle}$), the frontal area of the vehicle (A_f), the downforce coefficient (WHF), the drag coefficient (C_x), the front (R_{wheelF}) and rear (R_{wheelR}) wheels loaded rolling radius, the rolling friction coefficients (f_r and f_{r_2}), the moment of inertia of the front (J_{wheelF}) and rear (J_{wheelR}) wheel, the power absorbed by the vehicle accessories (P_{acc}) and the distribution of motor torque to the front axle in acceleration ($TractRatio_{acc}$) and in braking ($TractRatio_{brak}$) phases.

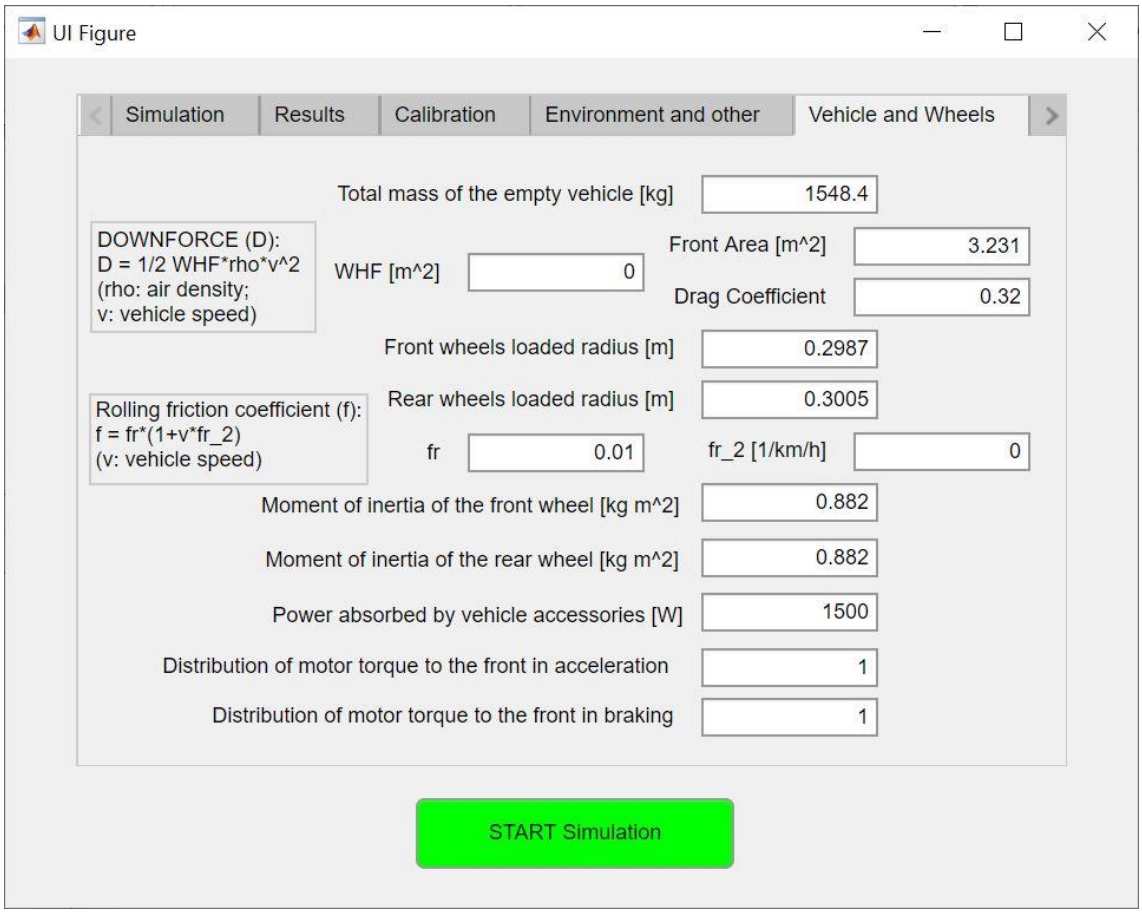

Figure 2.14. *"Vehicle and Wheels" panel of the Graphic User Interface. In particular, this panel allows you to enter the inputs regarding the vehicle and wheels parameters.*

In the "Brakes" panel (Figure 2.15) you can define the following quantities relating to the braking system: the maximum brake pressure in the master cylinder (p_{brake_max}), the pressure distribution to the front braking system in the master cylinder ($Bias_{brakeF}$), the total action area of the front ($A_{pistonF}$) and rear ($A_{pistonR}$) brake pistons, the dynamic friction coefficient of the front (μ_{padF}) and rear (μ_{padR}) brake callipers, and the operating average radius of the front (R_{discF}) and rear (R_{discR}) brake callipers.

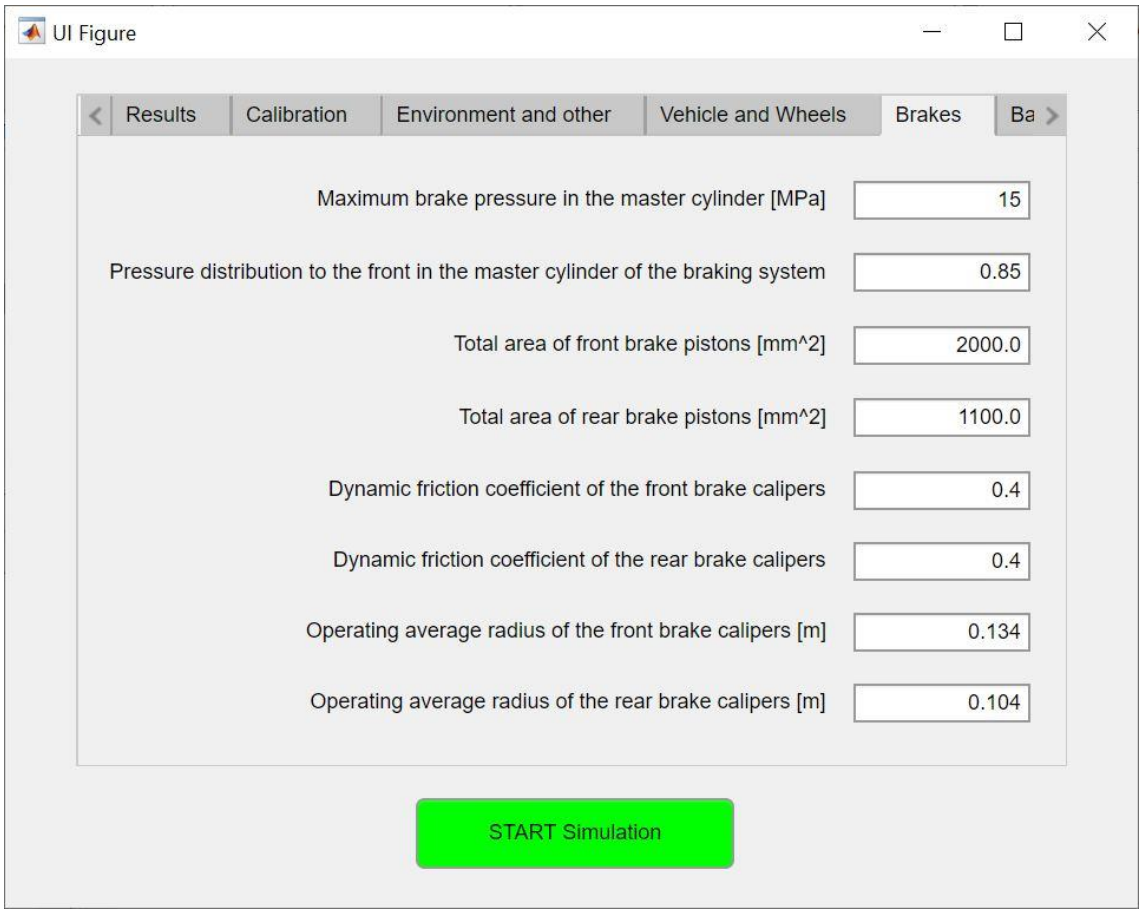

Figure 2.15. *"Brakes" panel of the Graphic User Interface. In particular, this panel allows you to enter the inputs regarding the traditional braking system parameters.*

The APP also allows you to set all the parameters relating to the batteries (Figure 2.16), with the option of choosing, through appropriate switches, to enter information regarding the charging and discharging limitations in Ampere or Watt and whether to refer the limitations provided to the entire battery pack or to the single battery module (limitations to be set by clicking the "Define Battery Limitations" button in the panel of Figure 2.16).

These parameters include the number of cells in series (N_s) and in parallel (N_p) in the battery pack, the rated capacity of the pack or of the single cell (to be chosen using the appropriate switch shown in the panel of Figure 2.16) at nominal temperature, the power buffer for discharge and charge limits (P_{buffer}), and the inverter efficiency in discharge (η_{inv_disch}) and in charge (η_{inv_ch}). Through the "Define Open Circuit Voltage" button it is also possible to define the open circuit voltage as a vector that reports the values of the open circuit voltage of the single cell as a function of the SOC (`Batt_SOC_Em`, used in the

"Datasheet Battery" block, see Section 2.2.2.3): the first column reports the SOC values, and the second column reports the corresponding values of open circuit voltage. Through the "Define Internal Resistance Table" button it is also possible to define the internal resistance of a single cell in function of temperature and SOC (`Batt_Rint_table`, used in the "Datasheet Battery" block, see Section 2.2.2.3): a table where the first column reports the temperature values, the first row the SOC values, and at the centre the corresponding internal resistance data.

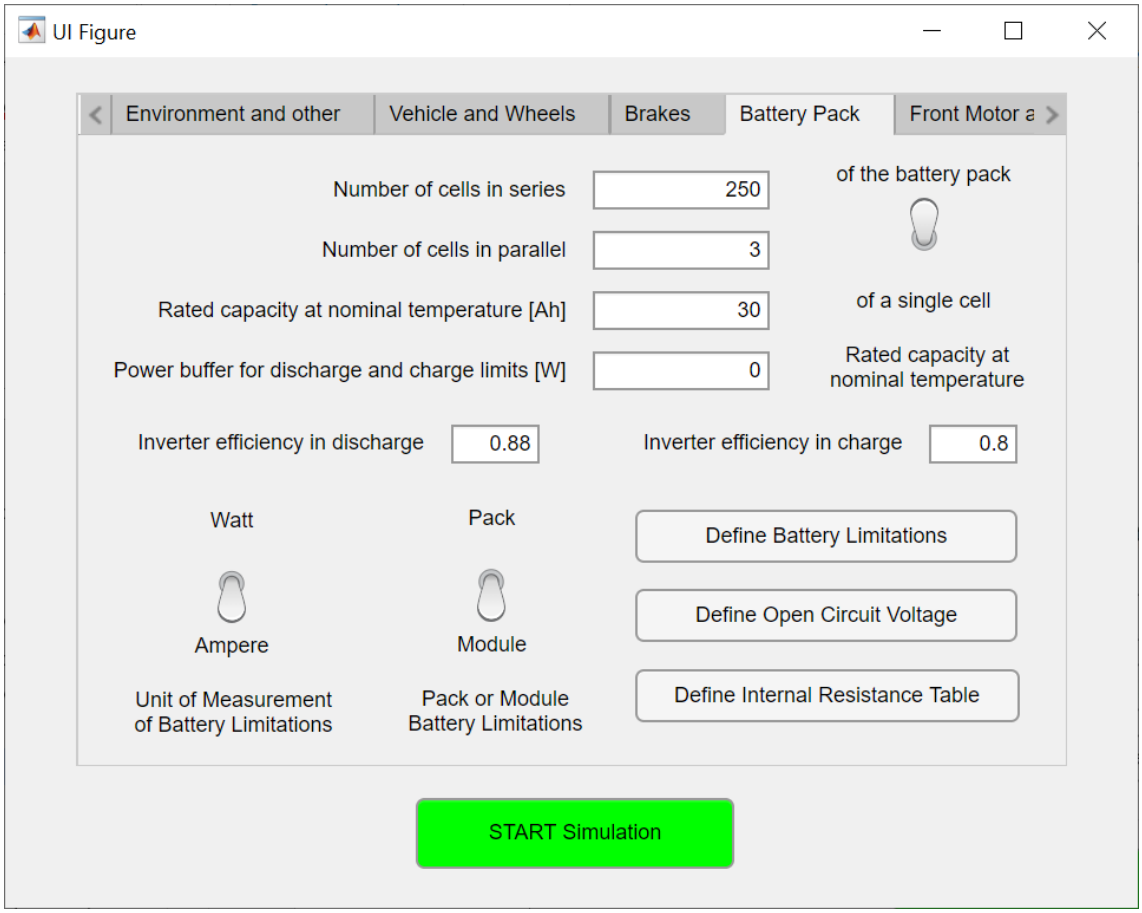

Figure 2.16. *"Battery Pack" panel of the Graphic User Interface. In particular, this panel allows you to enter the inputs regarding the battery pack parameters.*

The Graphic User Interface also allows you to set all the parameters relating to the two electric motors, front (Figure 2.17) and rear (Figure 2.18). For each motor it is possible to define both the continuous (by clicking the "Continuous Front Motor Torque" and "Continuous Rear Motor Torque" buttons, defining the torque as a function of the RPM) and peak (by clicking the "Peak Front Motor Torque" and "Peak Rear Motor Torque" buttons, again defining the torque as a function of the RPM) torque curve and choose which one

to use during the simulation (by means of a special switch shown in panels "Front Motor and Transmission" and "Rear Motor and Transmission"), as can be seen from Figure 2.17 and Figure 2.18. Therefore, there is still no implementation in the model of an automatic management of the peak torque for the maximum allowed time and then an automatic transition to the maximum continuous torque. Through "Motor Efficiency Map" buttons of Figure 2.17 and Figure 2.18 it is also possible to define the efficiency map of each electric motor: a table where the first column reports the motor torque values, the first row the motor RPM values, and at the centre the corresponding motor efficiencies (in percentage) data.

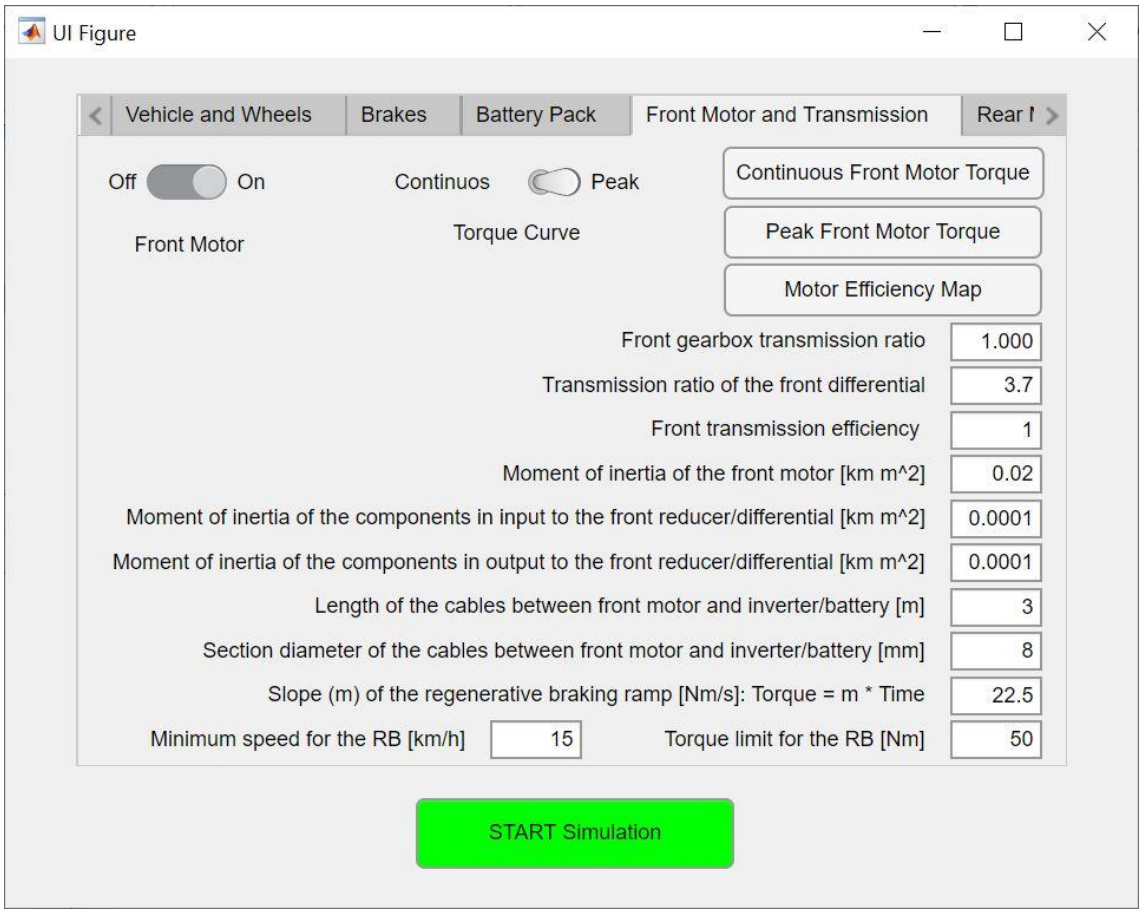

Figure 2.17. *"Front Motor and Transmission" panel of the Graphic User Interface. In particular, this panel allows you to enter the inputs regarding the front motor and front transmission parameters.*

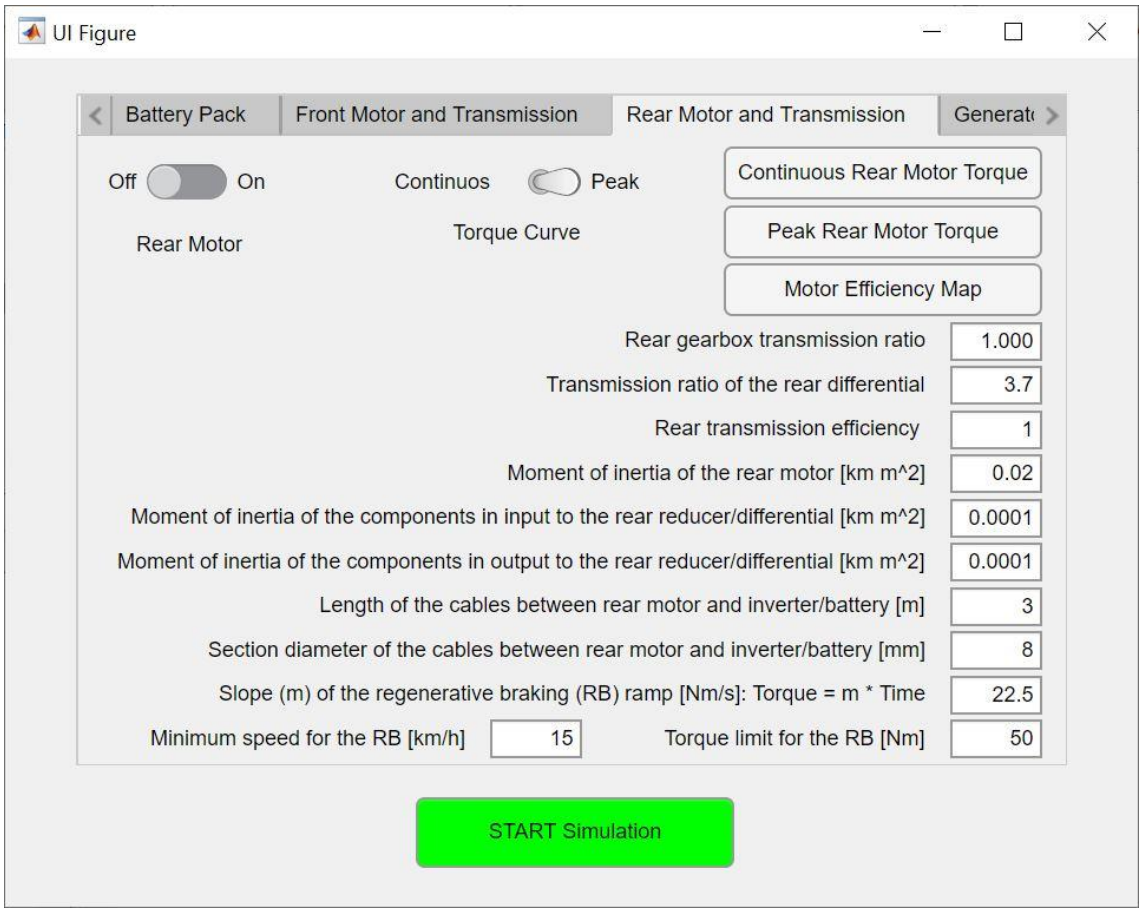

Figure 2.18. *"Rear Motor and Transmission" panel of the Graphic User Interface. In particular, this panel allows you to enter the inputs regarding the rear motor and rear transmission parameters.*

In the panels of Figure 2.17 and Figure 2.18 you can also define the following quantities relating to the electric motors: the front (τ_{redF}) and rear (τ_{redR}) gearbox transmission ratio, the transmission ratio of the front (τ_{diffF}) and rear (τ_{diffR}) differential, the moment of inertia of the components in input to the front (J_{inF}) and rear (J_{inR}) reducer/differential, the moment of inertia of the components in output to the front (J_{outF}) and rear (J_{outR}) reducer/differential, the length of the front (L_{cableF}) and rear (L_{cableR}) electrical conductor cables (i.e. between motor and inverter/batteries), the section diameter of these front (Φ_{cableF}) and rear (Φ_{cableR}) cables, the slope of the regenerative braking ramp of the front (m_{RB_F}) and rear (m_{RB_R}) motor, the torque limit for the regenerative braking of front (T_{RBmax_F}) and rear (T_{RBmax_R}) motor, and the minimum speed for the activation of the front (v_{RBmin_F}) and rear (v_{RBmin_R}) regenerative braking.

Furthermore, through the On/Off switch shown in Figure 2.17 and Figure 2.18, you can set whether the motors (front and rear) are present ("On") or not ("Off") in the vehicle powertrain layout.

Finally, it is possible to modify all the input parameters concerning any generators in parallel installed on the vehicle (Figure 2.19): the generator nominal power (P_{gen_nom}), the turbine rotation nominal speed (ω_{gen}), the torque curve and the efficiency map. The torque curve can be defined by pressing "Generator Torque" button of Figure 2.19 and setting the torque values as a function of the rotation speed of the generators. Clicking on the "Generator Efficiency Map" button of the panel of Figure 2.19 it is possible to define the efficiency map: a table where the first column reports the generator torque values, the first row the generator RPM values, and at the centre the corresponding generator efficiencies (in percentage) data.

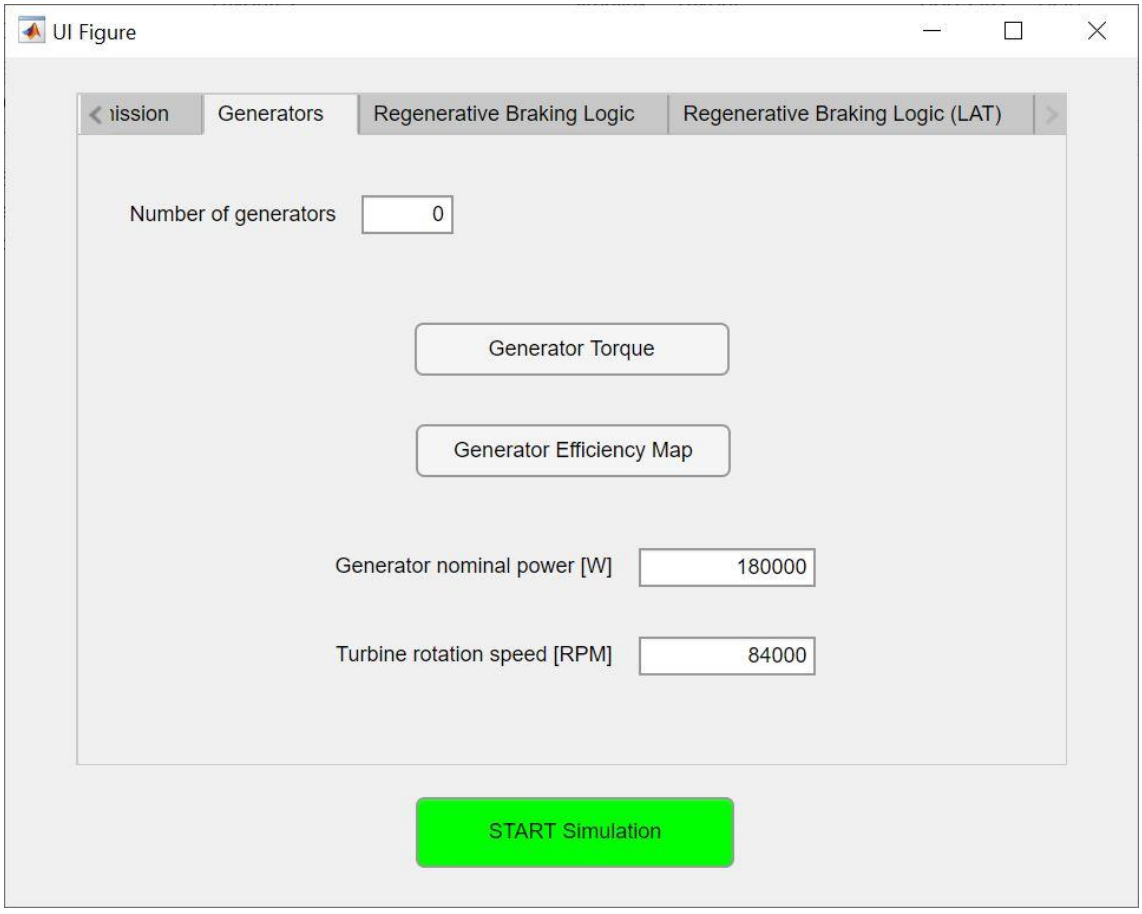

Figure 2.19. *"Generators" panel of the Graphic User Interface. In particular, this panel allows you to enter the inputs regarding the generators' parameters. In this figure, you can also see the Tabs of panels relating to a regenerative braking logic that was subsequently integrated into the TEST model, see Section 3.*

Using the "START Simulation" button (shown in figure from Figure 2.10 to Figure 2.19), simulation is started, and the graphic results are shown. The information regarding the simulation and some variables of the simulation itself are also automatically saved in the workspace, such as the electric motors torques, the voltage current and SOC of the battery pack, the space travelled by the vehicle, etc. It is however possible to save any other quantity and display any other graph as long as they represent variables calculated in some branch of the Simulink model described in Section 2.2, entitled "Simulation Tool".

2.4 MODEL VALIDATION

The validation of the model was carried out by comparing two borderline cases: a low-performance vehicle in terms of traction performance and a very high-performance hypercar. In the first case the validation was carried out through the comparison between model results and experimental data acquired through the VCU (Vehicle Control Unit) installed on a vehicle in the prototyping phase. In the second case the validation was carried out through the comparison between TEST and PROPS [22] results.

Furthermore, the driving missions of the two vehicles are also very different, in the first case an urban driving context is considered, in the second case the driving mission is of the Motorsport type, on the track.

2.4.1 Validation with Low Performance Vehicle

For the validation of the model under conditions of common driving cycles used in the public roads, the results of the model (obtained by setting the appropriate data concerning the specific vehicle) were compared with the data obtained experimentally from the VCU (Vehicle Control Unit) of a waste collection vehicle in the prototyping phase.

2.4.1.1 Powertrain

The prototype being simulated has a purely electric powertrain and it is a rear-wheel drive, with a single electric motor powered by a lithium battery pack. The configuration of this vehicle does not include any type of generator that recharges the battery pack, the only charging function in the simulation is the use of the electric motor as a generator during regenerative braking.

In particular, when the accelerator is released, there is a regenerative torque which increases linearly with the time from the beginning of the release up to a maximum value, later this value remain constant until the accelerator pedal is pressed. In the same way, regenerative braking also intervenes with the brake pedal pressed.

2.4.1.2 *Traction Motor*

The electric motor is three-phase with an assembly mass of 57.2 kg and a rotational inertia of 0.086 kg·m². It is characterized by the peak and continuous torque curves shown in Figure 2.20. In particular, the maximum peak torque is 380 Nm, while the maximum continuous torque is 304.3 Nm. Finally, Figure 2.21 shows the motor efficiency map.

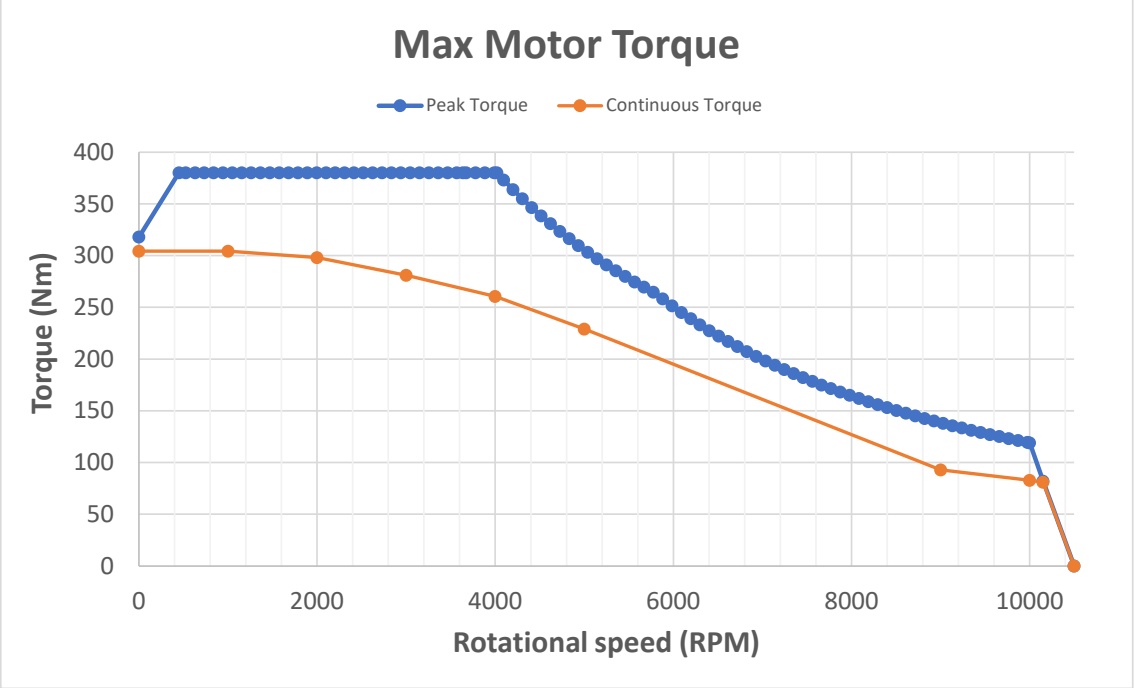

Figure 2.20. *Peak torque and the continuous torque (in Nm) of the traction motor vs. the speed of rotation of the electric motor itself (in RPM).*

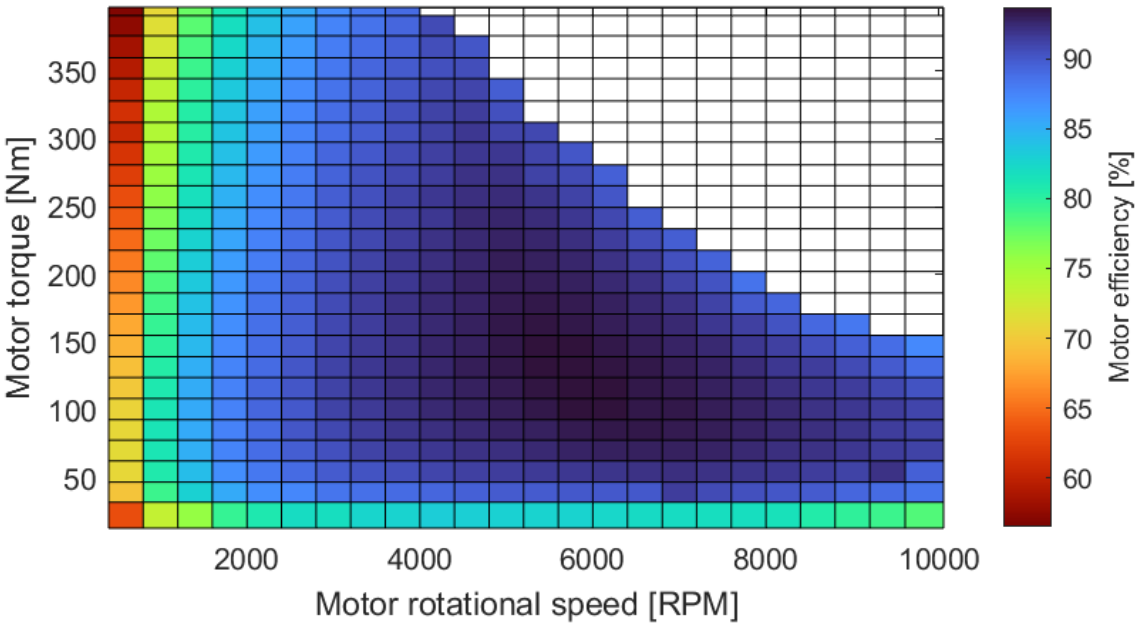

Figure 2.21. *Motor efficiency map.*

2.4.1.3 Battery Pack

The battery pack consists of 108 lithium cells arranged in series which give it a maximum nominal capacity of 120 Ah. Regarding the outgoing current (positive) and incoming current (negative), the battery pack has the limits shown in Figure 2.22, depending on the state of charge.

The open circuit voltage (OCV) and the internal resistance (RES) of the battery pack were considered constant, in fact the average temperature of the cells detected by the BMS is constant during the test and the SOC does not vary significantly. OCV and RES were derived from the experimental data and their values are represented in the Table 2.1, together with the other main data of the vehicle.

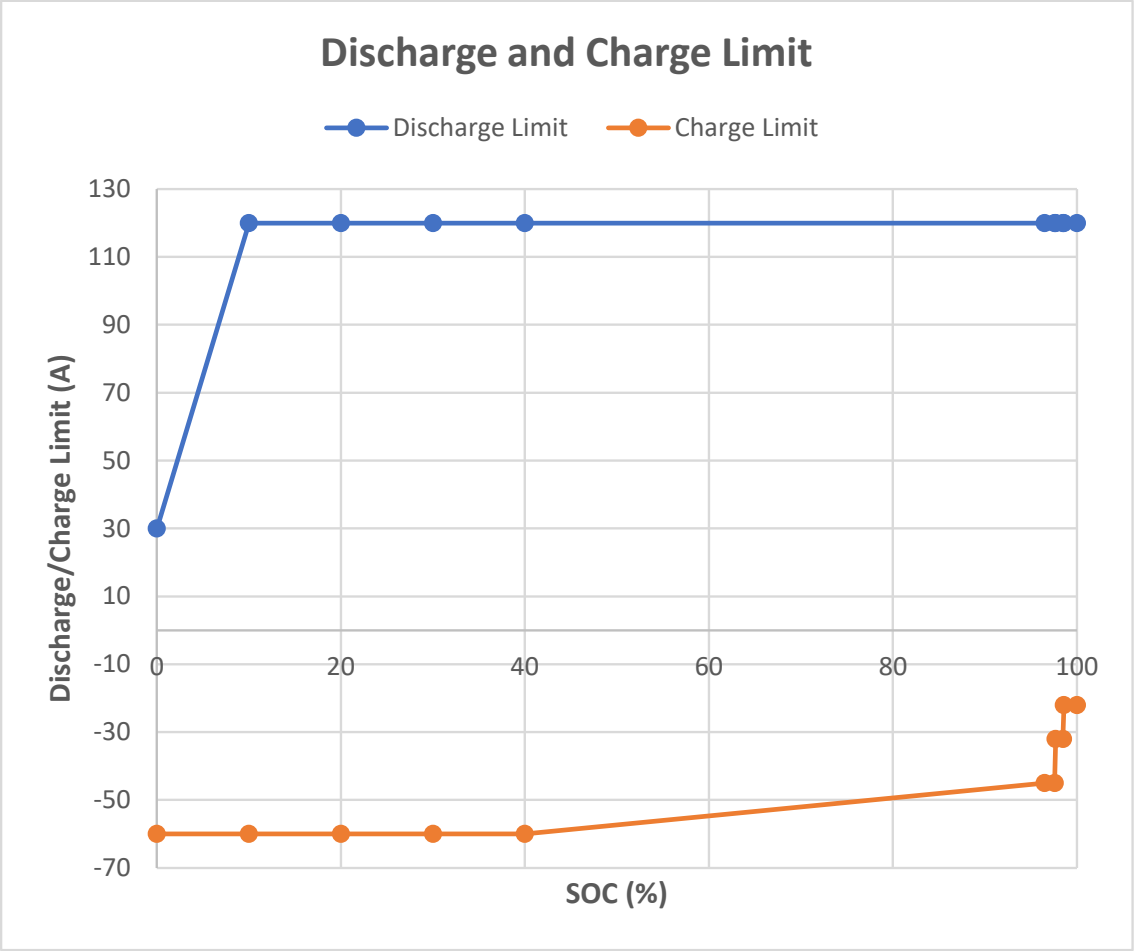

Figure 2.22. *Discharge and charge current limits (in Ampere) vs. the State of Charge (SOC, in percentage) of the battery pack.*

Table 2.1. *Main data of the waste collection vehicle.*

Parameter	Value	Unit
Vehicle weight	3450	kg
Front area of the vehicle	3	m^2
Drag coefficient	0.7	-
Wheels loaded radius	0.35	m
Maximum motor power	160	kW
Maximum motor torque	380	Nm
Torque limit for the regenerative braking	50	Nm
Gearbox transmission ratio	21.5385	-
Battery rated capacity at nominal temperature	120	Ah
Number of battery cells in series	108	-
Number of battery cells in parallel	1	-
OCV (Open Circuit Voltage)	356.1	V
RES (internal resistance of the battery pack)	0.097	Ω
Power absorbed by vehicle accessories	620	W

2.4.1.4 Data Acquisition System

The data needed for comparison with the program results was acquired through the vehicle control unit. The VCU installed on the prototype is an Ecotrons VCU, model EV2274A. A speed profile followed by the vehicle was used for the simulation and the corresponding motor torque and battery SOC, current, voltage and power were used for the comparison with the model results.

2.4.1.5 Target Speed Profile

The mission of the waste collection vehicle object of this model validation is a public road driving cycle. The target speed profile for validation was obtained thanks to road tests carried out with a vehicle prototype, acquiring all the data of interest from the VCU. Table 2.2 shows the main data of the target speed profile considered.

Table 2.2. *Main information of the waste collection vehicle driving cycle.*

Parameter	Value	Unit
Lap time	600	s
Space travelled	2395	m
Maximum speed	31.1	km/h
Minimum speed	0	km/h
Medium speed	14.4	km/h
Maximum acceleration	1.8	m/s^2
Maximum deceleration	−2.4	m/s^2

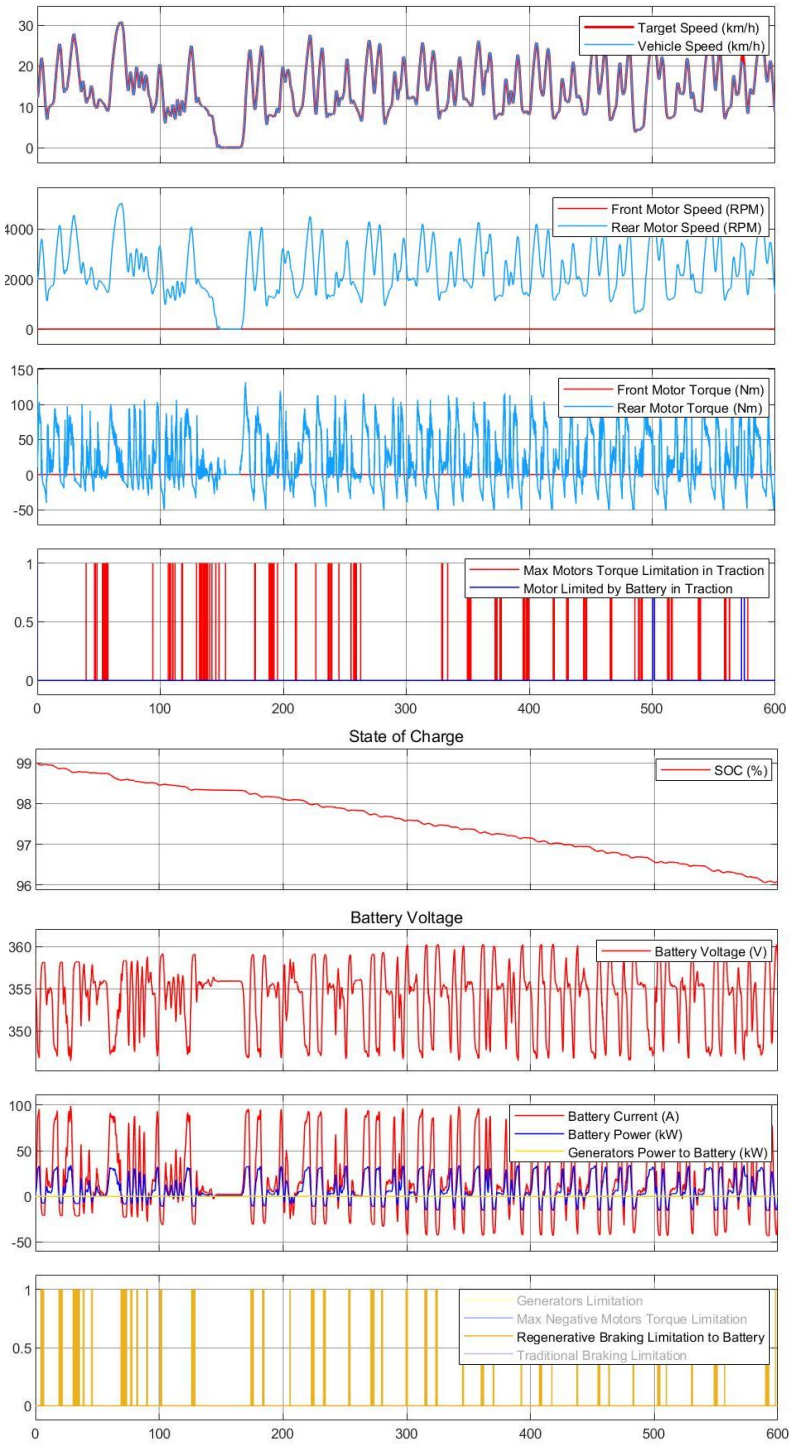

Figure 2.23. *General overview of the results screen, where the abscissa axes show the time expressed in seconds. The units of measure and the parameters of the ordinate axes are shown in the legends. In the two graphs showing the acceleration and deceleration limitations, the value of the limitation is equal to one if this has intervened, 0 vice versa. In particular, "Max Motors Torque Limitation Traction" correspond to* $\boldsymbol{Limit_{mot\_acc}}$ *variable, "Motor Limited by Battery in Traction" corresponds to* $\boldsymbol{Limit_{batt\_acc}}$*, "Generators Limitation" is* $\boldsymbol{Limit_{gen}}$*, "Max Negative Motors Torque Limitation" is* $\boldsymbol{Limit_{mot\_brak}}$*, "Regenerative Braking Limitation to Battery" is* $\boldsymbol{Limit_{batt\_brak}}$*, and, finally, "Traditional Braking Limitation" corresponds to* $\boldsymbol{Limit_{trad\_brak}}$ *binary variable.*

2.4.1.6 Comparison between Model Results and Experimental Data

Figure 2.23 shows a general overview of the results screen. The most important model results for validation will be analysed in more detail later.

The mechanical part of the model works well, as can be seen in Figure 2.24, which shows the comparison between the motor torque obtained from the model and the experimental motor torque.

The motor torque values obtained in output from the model are much noisier than the real torque values (acquired through the VCU). This is because the model does not consider transients; it calculates the quantities considering only the calculation instant in question (and the previous). The quantities of the model (such as the motor torque and the battery power) can therefore theoretically vary instantly abruptly.

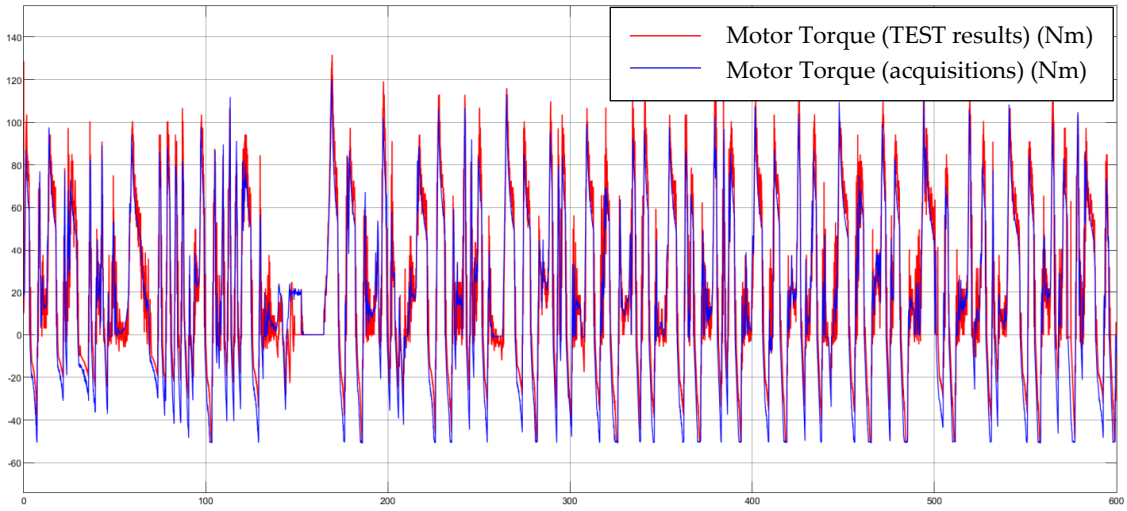

Figure 2.24. *Motor torque (in Nm) vs. lap time expressed in seconds. In particular, in the figure, there are the motor torque resulting from the model (in red) and the motor torque acquired through the Vehicle Control Unit (VCU) of the waste collection vehicle prototype (in blue).*

For the electrical part of the model, it was necessary to adjust the power required at the battery terminals resulting from the TEST model, calibrating the two inverter efficiencies, one for the discharge case (η_{inv_disch}) and one for the charging case (η_{inv_ch}). These efficiencies represent the power dissipations in the inverters and in the BMS. Figure 2.25 shows the comparison between the power obtained experimentally and the battery power resulting of the calibrated model while Figure 2.26 shows the comparison regarding current and voltage of the battery pack.

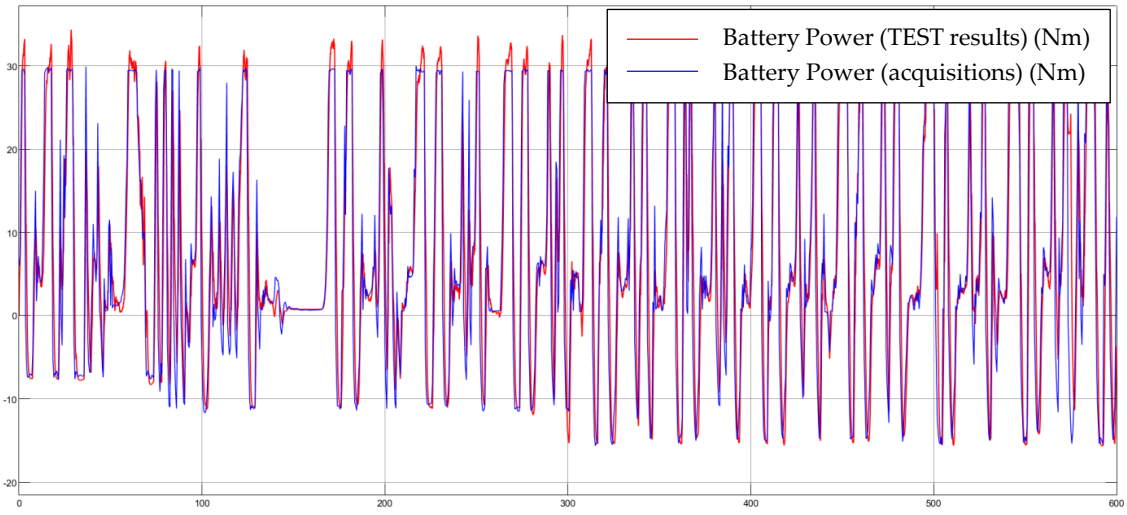

Figure 2.25. *Battery power (in kW) vs. lap time expressed in seconds. In particular, in the figure, there are the battery power resulting from the calibrated model (in red) and the battery power acquired through the VCU of the waste collection vehicle prototype (in blue).*

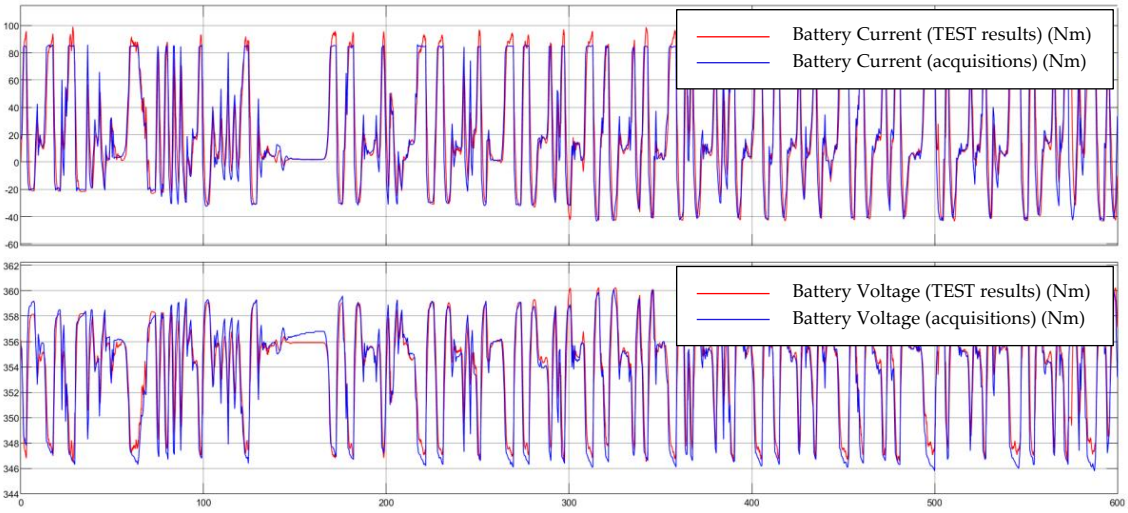

Figure 2.26. *Battery current (in Ampere, first graph) and the battery voltage (in Volt, second graph) vs. lap time expressed in seconds. In particular, in the figure, there are the battery current and voltage resulting from the calibrated model (in red) and the battery current, and voltage acquired through the VCU of the waste collection vehicle prototype (in blue).*

The differences between battery current and voltage obtained through simulation and acquired by the BMS (real data) are partly due to the fact that the battery model ("Datasheet Battery") does not consider transients. For example, between 100 and 200 seconds elapsed from the start of the test there are about 20 seconds in which the vehicle is stationary, the current outgoing from the battery

pack is constant and equal to about 2 Amperes and the battery voltage in output from the model is constant and equal to about 356 Volts. The current is not zero since, even when the vehicle is stationary, the auxiliaries must be powered. In real data it is possible to observe that the battery voltage does not remain constant in these 20 seconds but gradually increases. This is an effect due to the transient, in fact the Open Circuit Voltage (OCV) of a battery pack at rest tends to increase until it stabilizes at a maximum value.

Finally, the Figure 2.27 shows the comparison between the SOC obtained experimentally thanks to the BMS (Battery Management System) and the SOC resulting of the model. The SOC acquired through the VCU has a sensitivity of only 0.5% of variation, for this reason the SOC curve represented in the graph of the Figure 2.27 is piecewise linear, it was obtained by joining the points where the BMS has detected a change in SOC. To obtain the performance indices of the model (shown in Table 2.3), the error was obtained (calculated as the difference between the output parameter of the model and the parameter acquired through the VCU prototype) and its mean and standard deviation were calculated. The mean and the standard deviation (std) were also calculated for the absolute value (abs) of the error. The differences between the model results and the experimental data can be considered negligible; the model is thus validated.

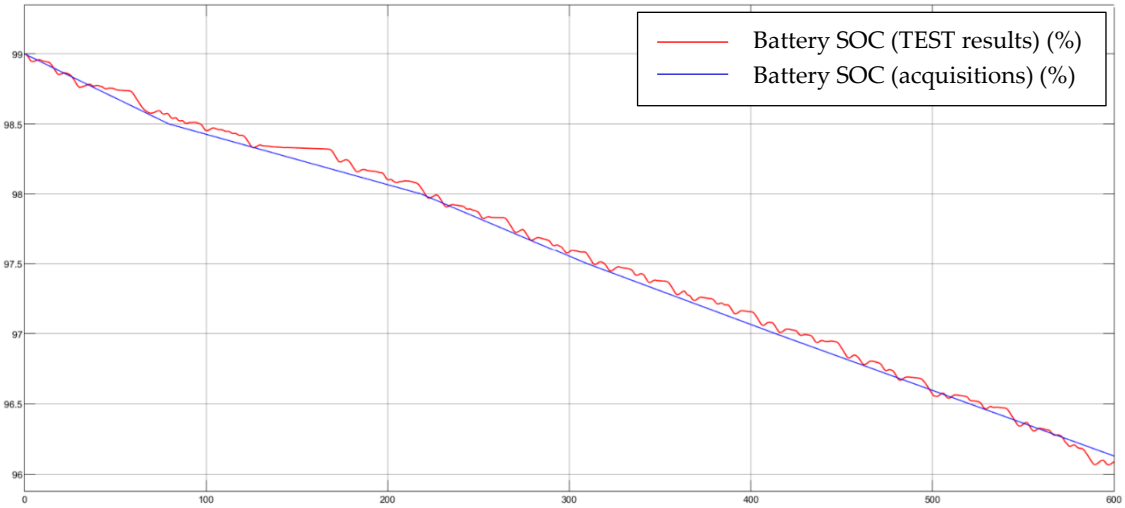

Figure 2.27. *Battery SOC (in percentage) vs. lap time expressed in seconds. In particular, in the figure, there are the battery SOC resulting from the calibrated model (in red) and the battery SOC acquired through the VCU (in particular from the BMS) of the waste collection vehicle prototype (in blue).*

Table 2.3. *Performance indices of the waste collection vehicle simulation.*

Parameter	mean error	std	abs mean error	std (abs)
Motor torque	4.44 Nm	13.96 Nm	11.30 Nm	9.33 Nm
Battery power	0.58 kW	4.18 kW	2.66 kW	3.28 kW
Battery current	1.54 A	12.01 A	7.58 A	9.43 A
Battery voltage	0.18 V	1.41 V	0.91 V	1.10 V

2.4.2 Validation with High-Performance Hypercar

For the validation of the model with data and operation typical of a high-performance vehicle, the data of an ultra-high performance hypercar, which is in the design stage, were considered. The speed profile adopted was obtained through a best lap time test of the car in question on the Nürburgring circuit, implemented in VI-CarRealTime® (VI-Grade®). The results from the TEST model were compared with those coming from a different simulation tool (PROPS) as reported in [22] and the comparison allowed for the performance of a correct calibration of the program.

2.4.2.1 Powertrain

The simulated hypercar is an APU (Auxiliary Power Unit) hybrid car, equipped with two electric motors, one acting on the front axle and one acting on the rear axle. Electric motors are powered by a lithium battery pack and they provide (or absorb) the same power at all times. Two generators are also installed on the vehicle, represented by two turbines powered by a liquid fuel, in particular by petrol. These generators are used to recharge the battery pack at constant power, unless limited by the battery pack itself. The generators are therefore always active while driving, rotating at constant speed, and their power is cut where the maximum charging limits (depending on the SOC) of the battery pack require it.

2.4.2.2 Traction Motor

The two electric motors of the car are identical, and they present the torque curve in maximum admission condition represented in Figure 2.28. The maximum torque of the motors is equal to 530 Nm and the rotation speed is limited to 23000 RPM.

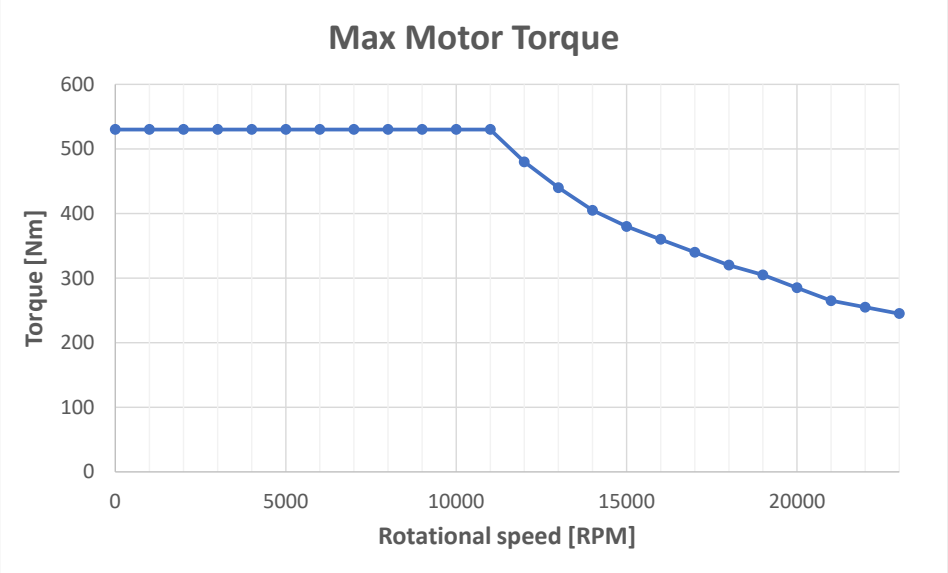

Figure 2.28. *Maximum motor torque vs. motor RPM. The graph is relating to the hypercar electric motors in maximum admission condition.*

2.4.2.3 Battery Pack

The battery pack configuration consists of 226 cells in series and 4 in parallel, for a total of 904 cells, with a maximum capacity of 6.55 Ah. The operating temperature of the cells must remain around 60 °C and the maximum charge and discharge limits must not be exceeded, limits that depend on the SOC and they are represented in the Figure 2.29, where the positive powers refer to the discharge and the negative ones to the charge of the battery pack.

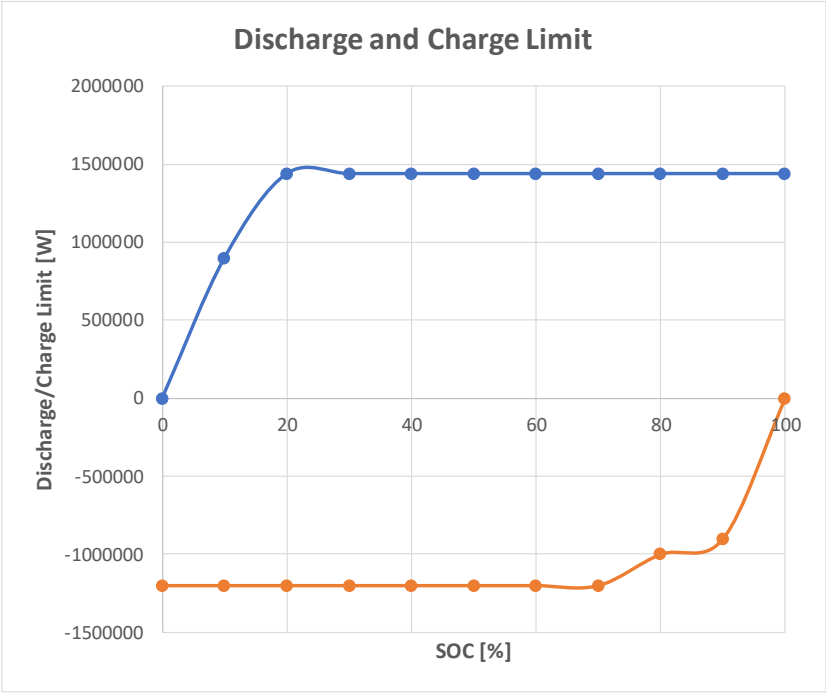

Figure 2.29. *Discharge (positive) and charge (negative) current limits (in Watt) vs. the SOC of the battery pack (in percentage).*

In order not to exceed the maximum limits it was defined to remain within the limits with a buffer of 1500 Watts. From Figure 2.30 it is possible to observe how the Open Circuit Voltage (OCV) varies according to the SOC of the battery pack. The internal resistance of each cell varies as a function of SOC and temperature, as can be seen from Table 2.4. Furthermore, in Table 2.5 main vehicle data is reported.

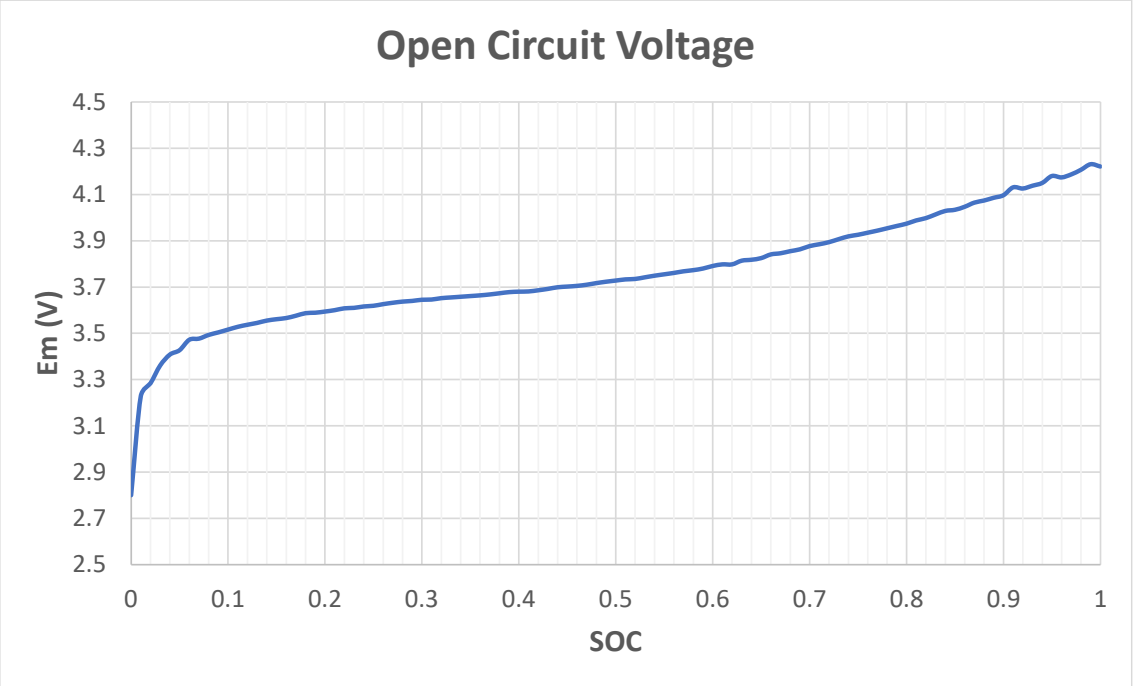

Figure 2.30. *OCV (Open Circuit Voltage, "Em" expressed in Volt) vs. the SOC of the battery pack.*

Table 2.4. *Internal resistance (expressed in Ohm) of each cell in function to the SOC (from 0 to 1, first row of the table) and to the temperature in Kelvin (from 243.1 K to 313.1 K, first column of the table).*

	0	**0.2**	**0.4**	**0.6**	**0.8**	**1**
243.1	0.00442	0.00466	0.00451	0.00424	0.00516	0.00657
253.1	0.00319	0.00328	0.00278	0.00276	0.00302	0.00390
263.1	0.00218	0.00205	0.00203	0.00173	0.00192	0.00226
273.1	0.00102	0.00128	0.00127	0.00123	0.00136	0.00152
283.1	0.00072	0.00091	0.00090	0.00089	0.00096	0.00112
298.1	0.00028	0.00036	0.00034	0.00038	0.00037	0.00051
313.1	0.00051	0.00067	0.00050	0.00077	0.00077	0.00139

Table 2.5. *Main data of the hypercar.*

Parameter	Value	Unit
Vehicle weight	900	kg
Front area of the vehicle	1.752	m^2
Drag coefficient	0.518	-
Wheels loaded radius	0.3517	m
Maximum motor power	610.5	kW
Maximum motor torque	530	Nm
Front and rear gearbox transmission ratio	2	-
Transmission ratio of the front and rear differential	3.9	-
Maximum brake pressure in the master cylinder	30	MPa
Pressure distribution to the front in the master cylinder	0.6	-
Total area of front brake pistons	5058	mm^2
Total area of rear brake pistons	4084	mm^2
Dynamic friction coefficient of the front brake callipers	0.4	-
Operating average radius of the brake callipers	0.141	m
Battery rated capacity at nominal temperature	6.55	Ah
Operating temperature of the battery	333.15	K
Number of battery cells in series	226	-
Number of battery cells in parallel	4	-
Battery pack weight	118	kg
Power absorbed by vehicle accessories	400	W

2.4.2.4 Generators

The vehicle in question is equipped with two generators for recharging the battery pack. Each generator can deliver a nominal power of 180 kW and a maximum torque of 530 Nm, thanks to the relative turbine which rotates at a constant speed of 84 thousand RPM. These values are shown in Table 2.5, which summarizes the main quantities of interest of the hypercar used for the validation of the model.

2.4.2.5 Target Speed Profile

The mission of the hypercar object of this model validation is of the MotorSport type. The target speed profile for validation was obtained thanks to a maximum performance test in VI-CarRealTime® on the Nordschleife variant of Nürburgring racetrack as shown in Figure 2.31 while

Table 2.6 shows the main data of the target speed profile obtained (Figure 2.32) and Figure 2.33 shows the elevation profile of the track.

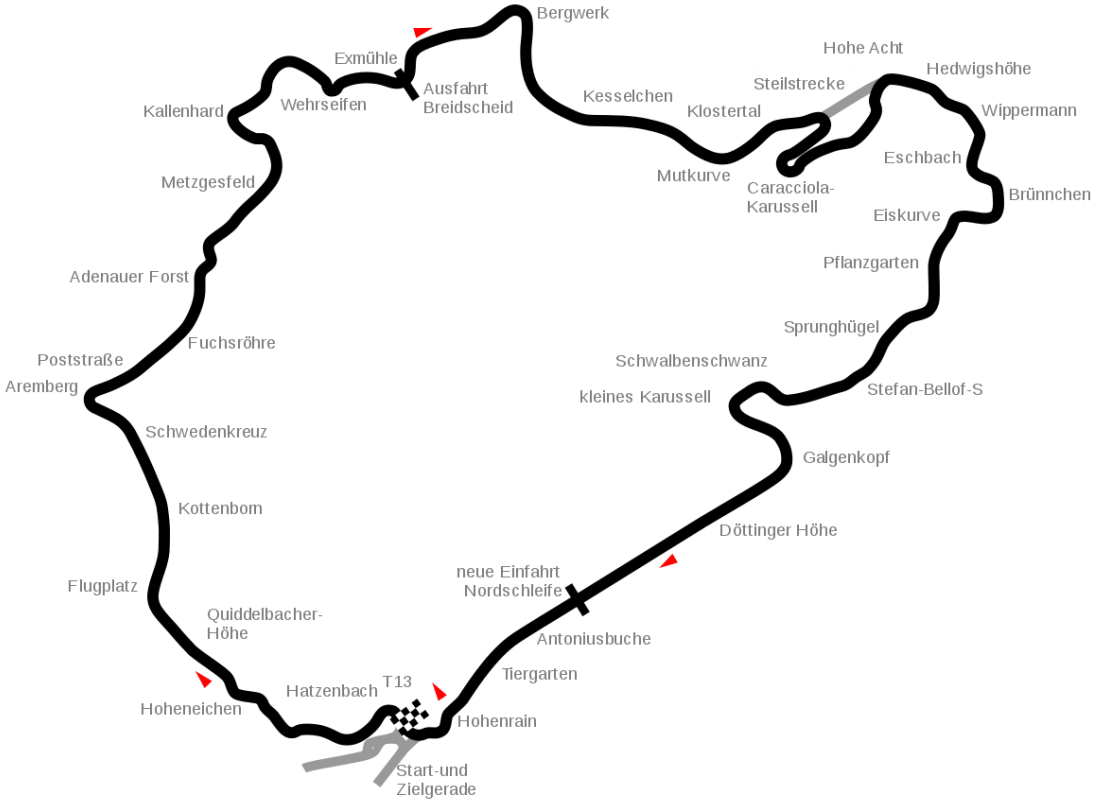

Figure 2.31. *Nürburgring track, in its Nordschleife variant.*

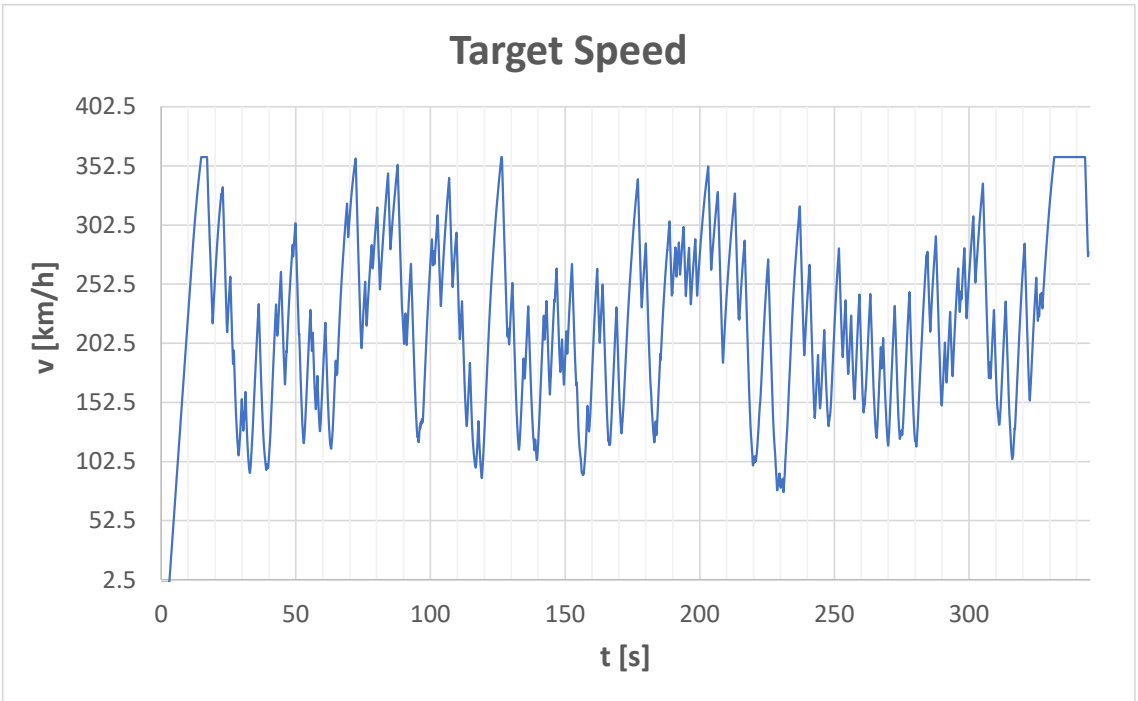

Figure 2.32. *Target speed profile obtained thanks to a maximum performance test in VI-CarRealTime® on the Nordschleife variant of Nürburgring racetrack.*

Table 2.6. *The table shows the main information of the hypercar driving cycle.*

Parameter	Value	Unit
Lap time	319.951	s
Space travelled	21.1	km
Maximum speed	389.7	km/h
Minimum speed	0	km/h
Medium speed	237.2	km/h
Maximum acceleration	22.2	m/s^2
Maximum deceleration	-41.1	m/s^2

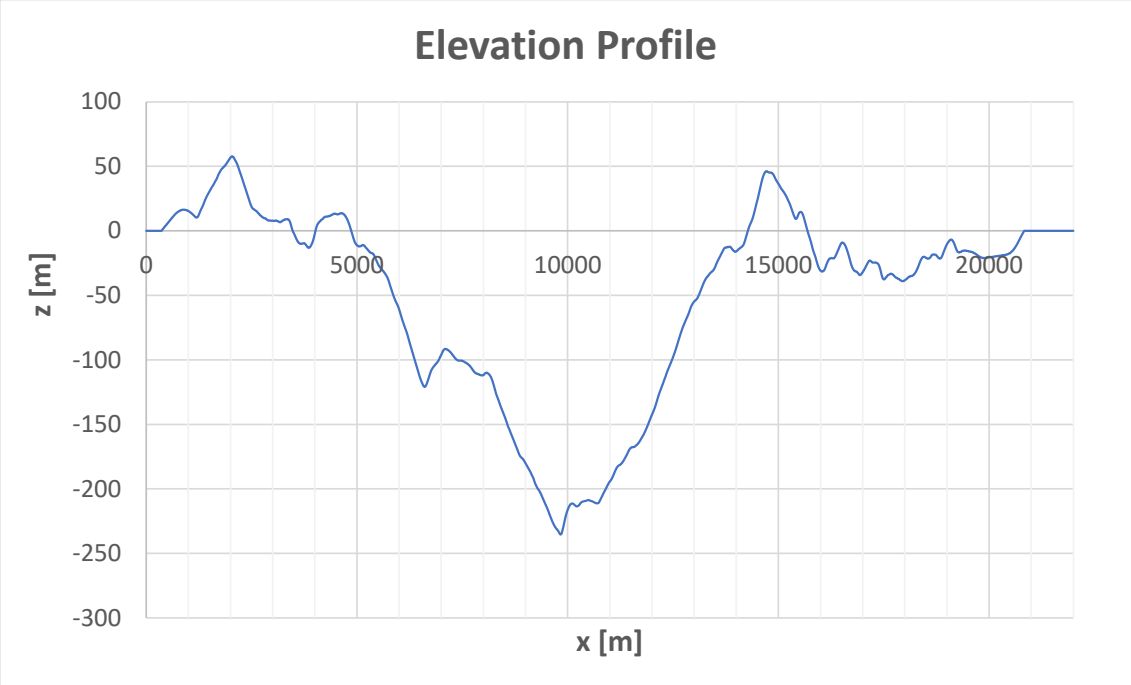

Figure 2.33. *Elevation profile of the Nordschleife circuit. In particular, the graph shows the elevation ("z") vs. the "longitudinal" position ("x") of the hypercar on the track (the space travelled by the hypercar on the Nordschleife circuit).*

2.4.2.6 Model Calibration

Once the results of TEST and PROPS [22] were compared, a deviation was noted between the torques required (required by the electric motors) to perform the same speed profile imposed. By isolating blocks of the program gradually, it was found that the problem arises with the balance of forces, in the TEST

program the resisting forces are overestimated at low speeds, for the vehicle in question, due to the various approximations of the model. The latter therefore requires calibration. The calibration was carried out by studying the acceleration phase, imposing a speed ramp, with constant acceleration, from 50 to 380 km/h in 30 seconds. The ramp starts from 50 km/h and not from zero speed for a correct comparison with the results of the PROPS [22] program, which presents problems at low speeds (speeds close to zero).

Furthermore, to allow the PROPS [22] results to stabilize, a 30-second interval at a constant speed of 50 km/h is taken before the ramp. The speed profile imposed for the simulations of TEST and PROPS [22], necessary for the calibration of the model, is shown in Table 2.7 and in Figure 2.34. For the comparison of the results between TEST and PROPS [22], the total motor torque was considered, equal to the sum of the torque delivered by the electric motor acting on the front axle with that delivered by the rear electric motor. The torques necessary for the execution of the ramp, obtained from the TEST (without calibration) and PROPS [22] programs, are shown in Figure 2.35.

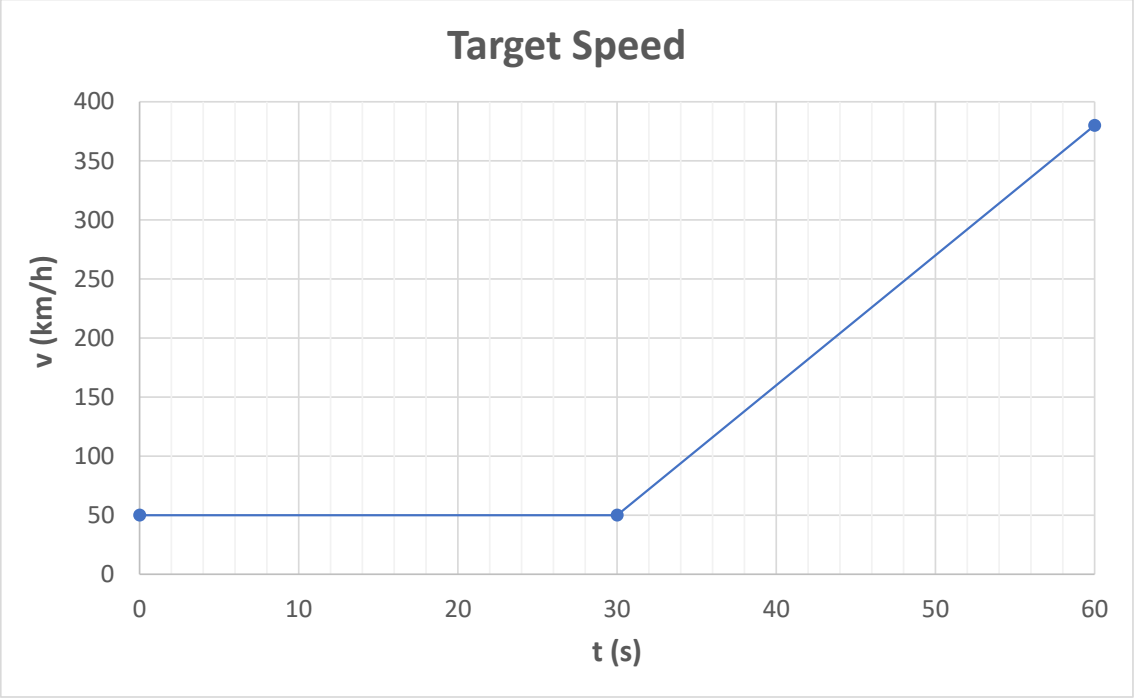

Figure 2.34. *Speed profile imposed for the calibration of the model, for the simulation of the hypercar.*

Table 2.7. *Speed profile imposed for the calibration of the model, for the simulation of the hypercar.*

Time (s)	Vehicle speed (km/h)
0	50
30	50
60	380

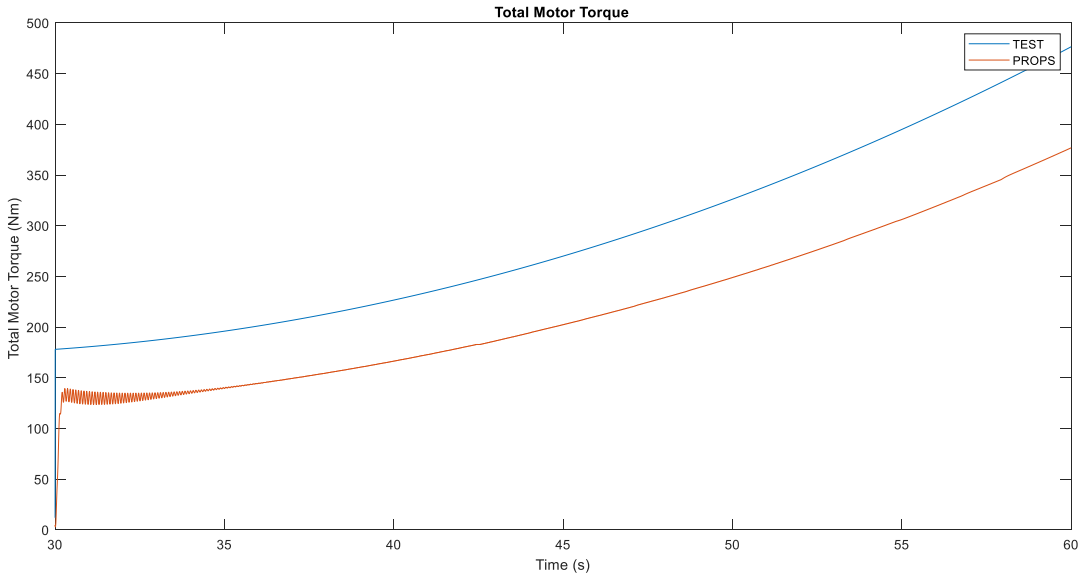

Figure 2.35. *Comparison between TEST (without calibration), in blue, and PROPS, in orange, total torques during the execution of the calibration speed profile.*

From Figure 2.35 it is possible to see the difference between the two torque trends. In particular, the behaviour of the ratio between the TEST and PROPS [22] torque result was analysed, represented in the Figure 2.36 as a function of the vehicle speed. To obtain "clean" results, the results were analysed starting from the 35 seconds elapsed from the start of the simulation. In this way the results of the PROPS [22] model have time to stabilize. The coefficients of the second-order polynomial equation that approximate the ratio between the torques were found. The result of the approximation function is shown in red in Figure 2.37. The function (y) identified for the approximation is expressed unction identified for the approximation is expressed by equation (2.58).

$$y = 5.5 \cdot 10^{-7}\, v^2 - 0.0007\, v + 1.4668 \tag{2.58}$$

The polynomial coefficient $5.5 \cdot 10^{-7}$, 0.0007 and 1.4668 were obtained through the "polyfit" function of MATLAB®. The lower order coefficient of the

squared speed indicates that the ratio between the torques has an approximately linear trend as a function of the speed, in particular the results of TEST and PROPS [22] tend to realign for high vehicle speeds. Equation (2.58) mentioned above was then used to perform the TEST calibration for the hypercar described in Section 2.4.2.

Figure 2.36. *Ratio between the TEST and PROPS torques vs. vehicle speed.*

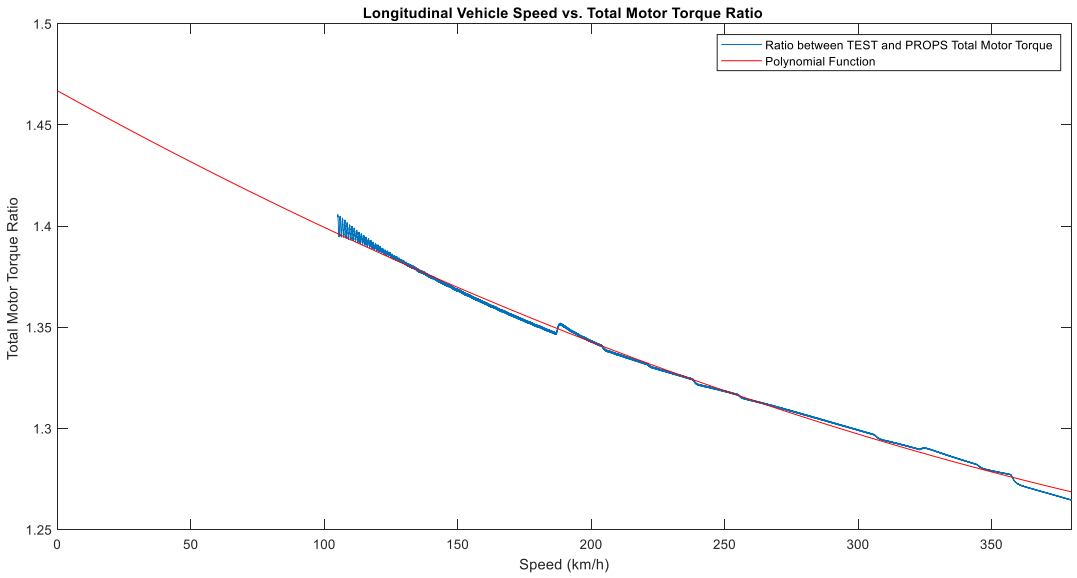

Figure 2.37. *Second degree polynomial (in red) that approximate the ratio between the TEST and PROPS torques (in blue).*

2.4.2.7 *Conditions for Validation of the Model*

For the validation of the TEST model equipped with calibration, a comparison was made once again with the PROPS [22] results, this time on the speed profile of the Nürburgring obtained with VI-CarRealTime®. The version of the PROPS [22] adopted does not allow to cut power to the generators if the limitations of the batteries require it, they provide constant power throughout the simulation. Therefore, in order to also validate the electrical part of the model, it was decided to turn off both generators for the entire TEST and PROPS [22] simulations, to obtain comparable SOC, current, voltage and power data of the battery pack. Furthermore, the same braking logic of the TEST model has also been adopted for the PROPS [22].

2.4.2.8 *Comparison between TEST and PROPS Results*

Towards the end of the simulation the battery pack is completely discharged, as can be seen from the Figure 2.38. To make a comparison, it is therefore better to focus on the first 150 seconds that have passed since the start of the simulation. In fact, in these first 150 seconds the battery pack has a SOC higher than about 20% and therefore there are no problems of excessively discharged pack. The results of state of charge as a function of time in TEST and PROPS [22] model are not perfectly aligned, but the difference between the two can still be considered acceptable. In the first 150 seconds the total torque results of TEST and PROPS [22] are comparable, as can be seen in Figure 2.39.

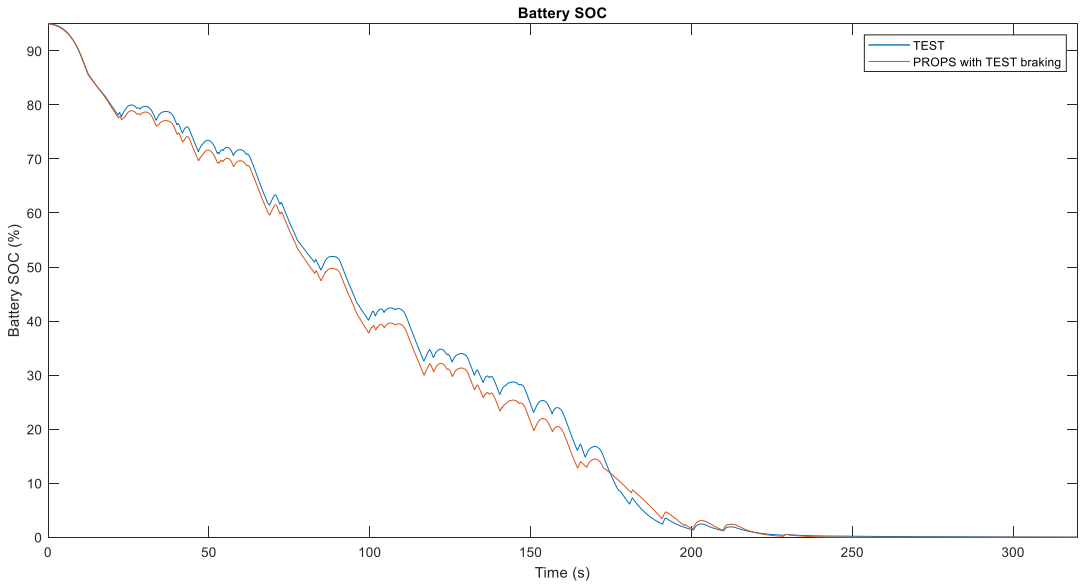

Figure 2.38. *TEST (in blue) and PROPS (in red) battery SOC (in percentage) vs. Lap Time (in seconds).*

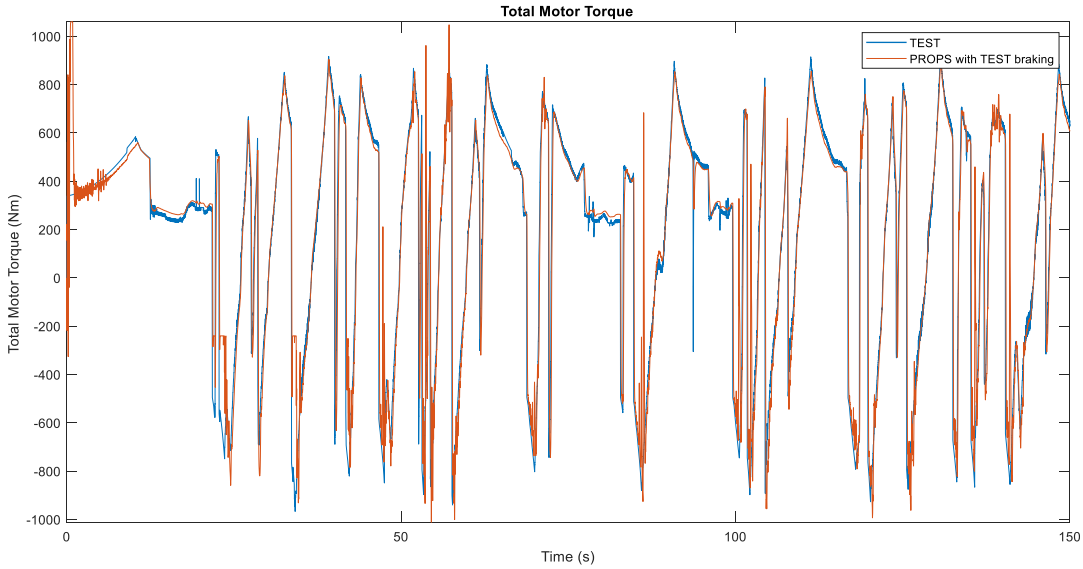

Figure 2.39. *This graph shows TEST (in blue) and PROPS (in red) total motor torque (in Nm) vs. Lap Time (in seconds).*

Returning to the parameters of the battery pack, also the results of power, input (negative) or output (positive) current from the pack and voltage at the battery terminals can be considered consistent between the two analysed models (always focusing on the first 150 seconds from the start of the simulation). It is possible to compare the results by observing the graphs shown in Figure 2.40, Figure 2.41, and in Figure 2.42.

As can be seen from the graphs of figure from Figure 2.39 to Figure 2.42, the results of the PROPS [22] program are more fluctuating. This is due to the presence of PI controller, which is absent in the TEST model.

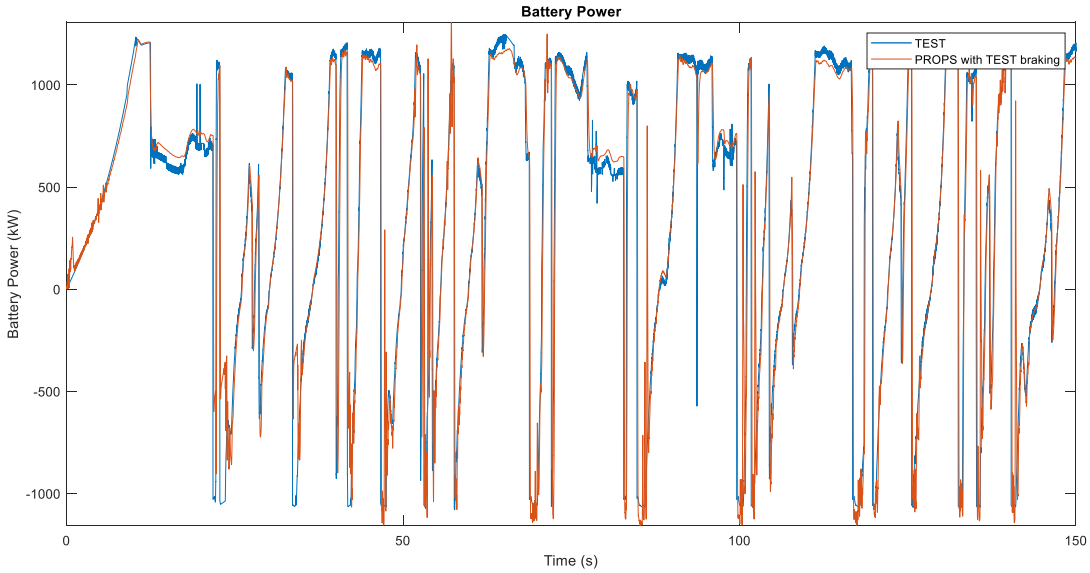

Figure 2.40. *TEST (in blue) and PROPS (in red) battery power (in kW) vs. Lap Time (in seconds).*

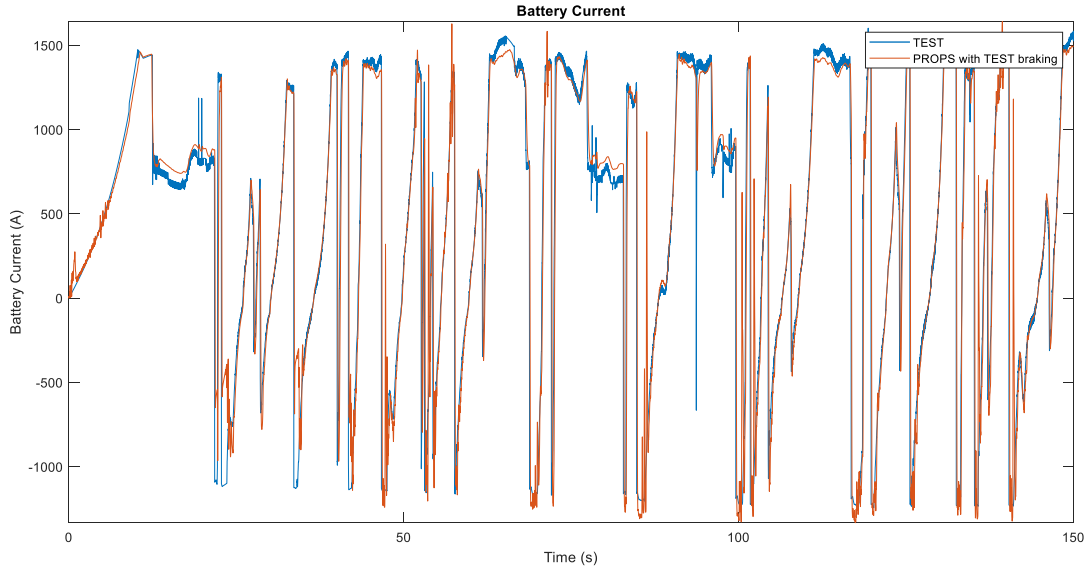

Figure 2.41. *TEST (in blue) and PROPS (in red) battery current (in Ampere) vs. Lap Time (in seconds).*

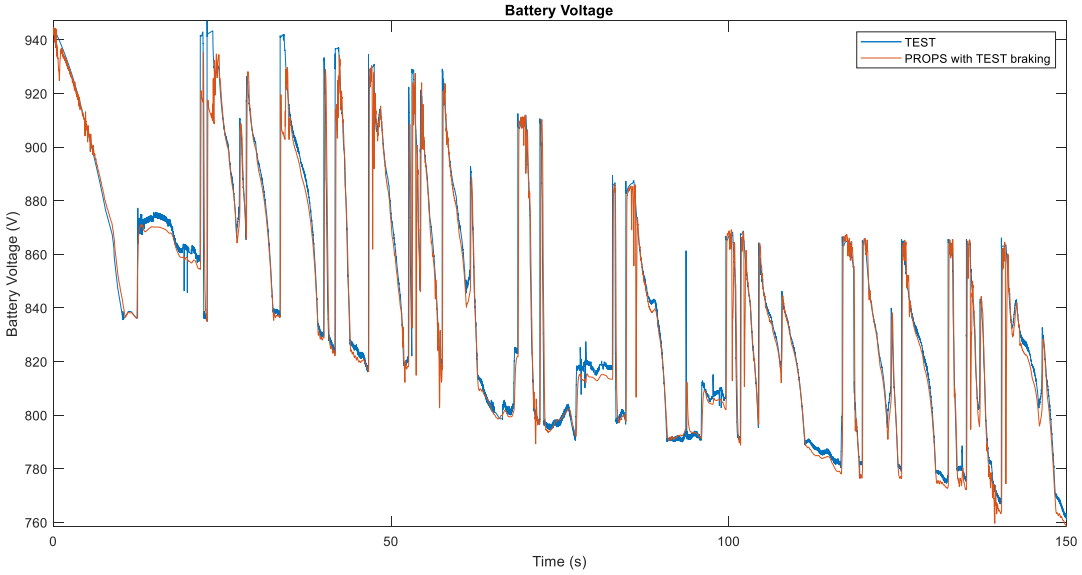

Figure 2.42. *TEST (in blue) and PROPS (in red) battery voltage (in Volt) vs. Lap Time (in seconds).*

To obtain the performance indices of the TEST model (shown in Table 2.8), the error was obtained (calculated as the difference between the output parameter of the TEST model and the output parameter of the PROPS model, which has been validated with real-world data [22]) and its mean and standard deviation were calculated. The mean and the standard deviation (std) were also calculated for the absolute value (abs) of the error.

It is worth highlighting that both tools have on average the same accuracy and estimation capabilities as shown in Table 2.8; however, the proposed method requires a lower computational burden as it is designed using the "Backwards-Facing" technique as mentioned in Section 2, which has been proved to be more efficient. This makes this simulation tool suitable for real time applications such as driving simulators [39–42]. The same applies if compared with [27,29].

Furthermore, it is key to note that sampling time t_s plays an important role on simulation performance, so that a sensitivity analysis has been carried out to assess its influence. In fact, when t_s is too big the computation is faster, but the final accuracy is poor due to aliasing effect, especially when t_s is lower or close to the sampling rate of the input target speed profile. On the other hand, when t_s is too small the computational burden grows exponentially without being justified by a substantial increase in accuracy. In general, using a sampling time between 0.05 s and 0.01 s is recommended.

Table 2.8. *Performance indices of the hypercar simulation with the TEST model.*

Parameter	mean error	std	abs mean error	std (abs)
Total motor torque	−15.80 Nm	187.50 Nm	80.00 Nm	170.31 Nm
Battery power	−18.35 kW	277.44 kW	110.15 kW	255.30 kW
Battery current	−20.03 A	314.31 A	125.50 A	288.87 A
Battery voltage	3.22 V	12.39 V	5.41 V	11.60 V
Battery SOC percentage	1.88	0.96	1.89	0.94

2.5 FINAL CONSIDERATIONS AND FUTURE DEVELOPMENTS

The main target of TEST tool was to obtain shorter calculation times and perform closed-loop simulation in a more efficient way comparing to other tools reported in literature. Such tool is reliable, robust and numerically stable. It is also intuitive and easy to use for people with no specific training, thanks to a specifically designed graphical user interface. Moreover, it features the possibility to avoid any PID (or PI) controllers to perform closed-loop simulation with a target speed profile, hence avoiding complex calibration procedures. This is possible due to the "Backwards-Facing" design technique adopted for its development. The TEST simulation tool allows also to simulate performance of a multitude of hybrid or full electric powertrains with low computational burden, short simulation time and good accuracy of results. Due to the approximations adopted in the calculation of the forces, the model may require a calibration as function of the vehicle speed (in particular for high-performance cars). The electrical part of the model requires the knowledge of all the electrical efficiencies, for calculating the power at the battery terminals. If some of these efficiencies are unknown it is possible to consider them as calibration coefficients.

Furthermore, the program is made up of several blocks, thus resulting in a program that is modular, flexible and open to simple modifications. By making the appropriate modifications to the blocks, replacing some blocks or integrating the program with additional modules, it is possible to use the model for the simulation of other types of vehicles, for example fuel cell vehicles, or to test different on-board energy management strategies, for example regenerative braking logics. This allows for high flexibility in the simulations.

Validation is also provided, based on a comparison with real data (VCU acquisitions) and with another consolidated simulation tool [22]. Maximum error on mechanical quantities is proved to be within 5% while it is always lower than 10% on electrical quantities.

Further developments of the model will concern, as already anticipated, the replacement of equations (2.18) and (2.19) with equations (2.20) and (2.21), which allow the electrical efficiency of the motors to be taken into account also for the calculation of losses due to the Joule effect, and further improvements reported by following.

The current at the motor terminals is an alternating electric current (AC), while the electric current supplied by the battery pack is a direct electric current (DC). Between the motor and the battery pack there is an inverter, a DC/AC converter in the simplest architecture and an inverter plus a booster DC/DC converter in the most complex, but realistic, architecture. When calculating a direct current from an alternating power, the power factor $cos(\varphi)$ should be considered.

Another improvement that can be made to the TEST model relates to the losses associated with the inverter. In the version of the TEST model described in this chapter (Section 2), the losses associated with the inverter have been considered by means of a constant efficiency value. In a future development of the model, these losses could be implemented in a more precise way, as the sum of the conduction losses (proportional to the square of the current) and the commutation losses (which are a function of the commutation frequency and the motor speed).

In the TEST model, the presence of the electric connection cables between the generator/s and the battery pack was not considered. The power dissipated due to the Joule effect in these cables was in fact considered negligible. In a future version of the model, it could therefore, for greater accuracy, take into account the resistance of these cables and therefore implement the calculation of the losses due to the Joule effect also in these cables, as done for the electric connection cables between the motor/s and the battery pack.

3 REGENERATIVE BRAKING LOGIC THAT MAXIMIZES ENERGY RECOVERY ENSURING THE VEHICLE STABILITY (RB LOGIC)

This chapter presents a regenerative braking logic that aims to maximize the recovery of energy during braking without compromising the stability of the vehicle. This model of regenerative braking, called "RB logic" and presented in [13], published in "MDPI - Energies" journal, ensures that the regenerative torque of the electric motor (for front- and rear-wheel drive vehicles) or electric motors (for all-wheel drive vehicles equipped with one motor for each axle) is exploited to the maximum, avoiding the locking of the driving wheels and, subsequently, if necessary, integrating the braking with the traditional braking system. The priority of the logic is that of maximizing energy recovery under braking, followed by the pursuit of optimal braking distribution. This last aspect in particular occurs when there is an integration of braking and, for vehicles with all-wheel drive, also when choosing the distribution of regenerative torque between the two electric motors. The logic was tested via simulation on a front-, rear-, and all-wheel drive compact car, and from the simulations, it emerged that, on the WLTC driving cycle, the logic saved between 29.5 and 30.3% in consumption compared to the same vehicle without regenerative recovery, and 22.6–23.5% compared to a logic commonly adopted on the market. On cycle US06, it saves 23.9–24.4% and 19.0–19.5%, respectively.

Model validation was carried out by means of the VI-CarRealTime® simulation package by VI-Grade® and the TEST (Target-speed EV Simulation Tool) model described in Section 2 [10,22,23].

This chapter is organized as follows:

- In Section 3.1 a literature review is carried out, to highlight the differences and advantages of the RB logic compared to logics already present in the literature.
- In Section 3.2, the general layout of this logic is presented together with the related mathematical background. In particular, the logic is modular, and the details of each submodel are provided. This section begins with the definition of the model's inputs and outputs, including an explanation of how the logic interprets the brake demand signal and a calculation of the optimal braking distribution. The calculation of the electric motor' torque requests, which also prevents wheel locking, is then shown. Subsequently,

various situations are considered that may make it necessary to limit these motor torques, that is, the maximum braking torques available from the electric motor/s and the battery pack limitations. Finally, once these torques have been calculated, taking into account all the limitations, the logic will calculate pressures in the front and rear braking systems in order to guarantee the amount of braking required by the brake demand.

- In Section 0, the results achieved through this logic are presented. In particular, results based on standard driving cycles (to validate energy savings) and test outcomes (aimed at showing how the logic does not impair vehicle stability) are shown.
- In Section 3.4, the results obtained in Section 0 are discussed, some future developments for the logic object of this thesis are presented, and some future fields of application are proposed (the context in which it is possible to know the road friction coefficient, for example, in the context of smart roads).
- Section 3.5 explains how the RB logic has been integrated into the TEST model (described in Chapter 2).
- In Section 3.7 concluding remarks are provided, and the most important information in Section 3.4 is summarized.

3.1 LITERATURE REVIEW

Before presenting the regenerative braking model in detail, it is interesting to analyse the literature, comparing the characteristics of this logic, highlighting its improvements, with those of existing logics.

In [43], a strategy was proposed for the distribution of braking torques according to ECE regulations [44] and the so-called fold lines. Such a strategy meets the requirements of braking regulations and aims at maximizing the recovery energy, but, on the other hand, it may occasionally result in reduced stability and braking efficiency due to the fold lines deviating from the ideal curve [12]. The logic of regenerative braking (RB logic) presented in this thesis solves the problem of stability, as the logic not only maximizes energy recovery but also restores the system to the condition of optimal braking distribution if the vehicle is in critical conditions and at the limit of wheel locking. Once this last condition has been reached, the vehicle will then lock the wheels in conditions of optimal braking distribution, as it would in the absence of RB logic. Therefore, it is appropriate to associate RB logic with a correct ABS logic, which also takes the contribution of the electric motor into account in braking. In this regard, it is interesting to mention article [45]. In [46] a method to maximize regenerative

braking is proposed, where the braking torques on the front and rear axles are distributed according to the ideal curve and the motor ensures braking torque demand through the driving wheels according to its regenerative braking torque capabilities; otherwise, the friction braking torque comes into play in order to supplement the braking torque [12]. By always following the ideal curve for braking distribution, energy recovery is not fully maximized. The RB logic, by bringing the system back to optimum braking distribution conditions only when it is close to critical conditions, allows for the maximization of regenerative recovery in standard conditions by moving the braking distribution toward the axle driven by the electric motor (in the case of vehicles with front- or rear-wheel drive only). The approach adopted for the RB logic is therefore a hybrid of those exposed in articles [43,46]. In this way, the resulting problems are solved for both logics, and the related advantages are exploited.

In [47], a distribution control law for regenerative braking torque and hydraulic braking torque is proposed, but in this control, the various constraint factors on energy recovery are not considered [12]. Unlike the latter regenerative braking logic, the RB logic object in this document takes into account not only the limitations imposed by the maximum torque in the motors but also the limitations on energy recovery imposed by the maximum currents that the battery pack can accept at the input of the considered operating point. Furthermore, if limitations occur, the model outputs can be corrected by suitably integrating braking with traditional brakes.

In [48,49], a fuzzy control strategy distributing the regenerative braking torque and the hydraulic braking torque is presented. An ABS logic is already integrated into these two strategies. This can be an advantage over RB logic. On the other hand, not having an ABS strategy already integrated in the regenerative braking logic can allow for the adoption of, downstream of the RB logic, a specific one according to the needs, provided that the latter takes into account the intervention of the electric motors during braking, such as the logic presented in article [45]. In the studies cited above, the vertical load variation on the front and rear axles due to longitudinal load transfer is not considered; therefore, the stability of the vehicle cannot be fully guaranteed. However, as stated in [50], the aim of the regeneration control strategy is to ensure the maximum recovery of braking energy while also ensuring braking stability; therefore, this aspect must be taken into consideration for the sake of active safety.

Paper [51] describes a method for improving the braking stability of the vehicle. An optimal braking torque distribution, front to rear, is achieved by controlling the longitudinal slip ratio of each tire; see also [12]. The load transfer

between the wheels is also considered in the RB logic, both due to longitudinal and lateral accelerations, but the logic object of this thesis is suitable for use on vehicles where electric motors act on the axles and not on a single wheel. The motor torques are then managed for the axles and not for each individual wheel.

In [52], the regenerative braking strategy takes into account the ideal braking torque distribution, but the characteristics of the battery pack are not considered, unlike in the RB logic proposed in this chapter.

In [12], a braking torque distribution algorithm is presented: calculation of the optimal braking torque distribution is based on the ECE braking regulation [44], and the motor and battery limitations are taken into account together with various limitations, as with the RB logic, but the strategy is mainly based on the concept of optimal braking distribution. Conversely, the RB logic causes the system to deviate from the latter in order to maximize energy recovery whenever dynamic conditions allow it without compromising the stability of the vehicle.

A recent comprehensive literature review (year, 2021) on energy management issues when using braking controllers is presented in [53]. In this study, the literature analysis is carried out according to different categories [54]:

- For gradual braking and emergency braking;
- With or without the estimation of the road surface friction coefficient;
- With fixed or allocated torque distribution;
- By tools used for simulation (MATLAB/Simulink®, AMESim®, CARSim®, or co-simulation);
- By the type of model validation (without validation, with physical imitators, or with real vehicles).

The controllers for regenerative braking can be classified into conventional and intelligent controllers. Conventional controllers are basically the proportional–integral–differential controllers (PIDC), threshold controllers (TC), and sliding-mode controllers (SMC). Intelligent controllers are fuzzy logic controllers (FLC), neural network-based controllers (NNC), and model reference controllers (MRC) [53].

The regenerative braking strategy presented in this article can be considered to be a conventional controller. It is based on a modular and flexible Simulink® model. It can be implemented in the vehicle control unit (VCU) of front-, rear-, or all-wheel drive vehicles equipped with electric traction only (full electric vehicles, hybrid APU vehicles, and fuel cell electric vehicles). In

particular, the vehicle in question can have an electric motor acting on the front or rear axle or on two electric motors, one for each axle.

The model combines several characteristics considered by the different studies cited above, in particular:

- Various vehicle, driveline, electric motor(s), and brake system data are considered;
- The model calculates the brake force request, starting from the brake demand i.e., from driver force acting on the brake pedal;
- The optimal braking distribution between front and rear axles is obtained considering the load transfer due to longitudinal acceleration/deceleration;
- The logic aims at maximizing energy recovery under braking considering various limitations that can come into play;
- The limitations related to tire grip are considered;
- Motor and battery limitations are also considered;
- Finally, traditional brakes integrate regenerative braking to ensure the braking torque request is met in all conditions while keeping the system closer to the optimal braking distribution.

3.2 REGENERATIVE BRAKING MODEL

The regenerative braking logic object of this chapter was modelled in the MATLAB/Simulink® software. Indeed, the Simulink® environment is very popular in the programming of automotive control units.

The model can be set for use on an electric vehicle equipped with a single motor, both front- and rear-wheel drive, or for an all-wheel drive vehicle with an electric motor for each axle. The vehicle braking system must be equipped with two master cylinders, allowing for the separate management of front and rear brake pressures.

Figure 3.1 summarizes the structure of the regenerative braking logic. Model inputs are the brake demand from the driver, the vehicle acceleration, the rotation speed of the motor or motors, and of the wheels and battery characteristics. Both load transfer and optimal braking distribution between front and rear axles are calculated based on vehicle acceleration.

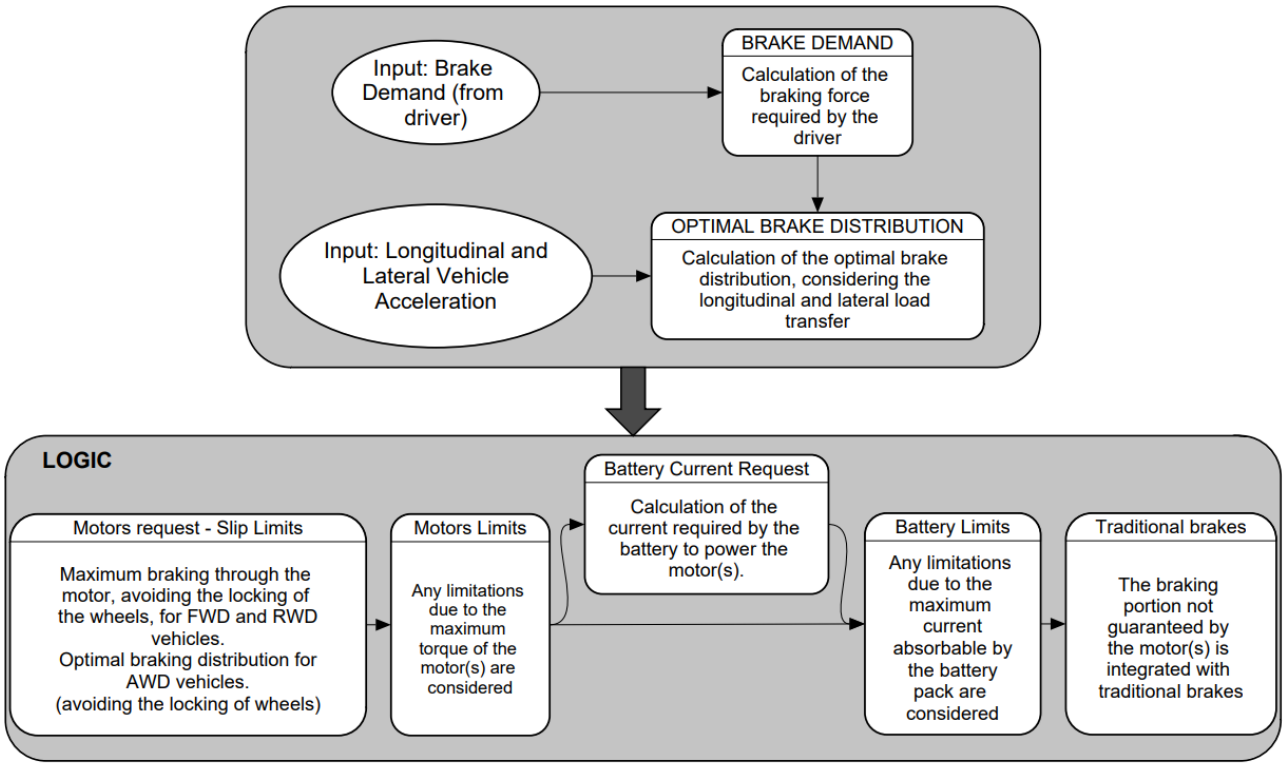

Figure 3.1. *Structure of the regenerative braking logic.*

Regenerative motor torques are calculated based on brake demand in order to optimize energy recovery considering the optimal brake distribution if there are two motors and ensuring the stability of the vehicle by considering its slip limits. Then, it is also necessary to consider the limitations imposed by the maximum performance of the motors and batteries. Finally, traditional brakes can be integrated with the electric motor brake in order to ensure the deceleration intensity requested by the driver. All this while keeping the system close to optimal braking conditions.

The next subsections show the equations and logics implemented in the Simulink® model for deploying a regenerative braking logic aimed at maximizing energy recovery.

3.2.1 Model Inputs and Outputs

The Simulink® model inputs are listed below.

- Brake demand ($BrakeDemand$): value from 0 to 1, proportional to the force imposed by the driver on the brake pedal.
- Longitudinal vehicle deceleration (j): positive value for vehicle deceleration.

- Lateral vehicle acceleration (a_y): absolute value.
- Vehicle speed (v): longitudinal vehicle speed.
- Angular velocity of the front wheels (ω_{wheelF}): average value between left and right front wheels.
- Angular velocity of the rear wheels (ω_{wheelR}): average value between left and right front wheels.
- Angular velocity of the front electric motor (ω_{motF}): if the front motor is present.
- Angular velocity of the rear electric motor (ω_{motR}): if the rear motor is present.
- Battery voltage (V).
- Maximum charging current of the battery pack ($Crnt_{MAX}$): maximum current that the battery is able to accept in input from the motors at the moment considered.

The model outputs are listed below.

- Front brake pressure ($Pres_{brakeF}$): signal required for the control logic of the front braking system.
- Rear brake pressure ($Pres_{brakeR}$): signal required for the control logic of the rear braking system.
- Front motor torque (T_{motF}): output torque of the front electric motor.
- Rear motor torque (T_{motR}): output torque of the rear electric motor.

3.2.2 Brake Demand

The "BRAKE DEMAND" module receives the brake signal from the driver as an input and associates the required braking force to this signal.

The $BrakeDemand$ signal range is a value from 0 to 1, proportional to the master cylinder pressure and, hence, to the force imposed by the driver on the brake pedal, and the required braking force is imposed proportional to the maximum traditional brake force. Therefore, the $BrakeDemand = 1$ value represents the maximum braking pressure, which is set a priori in the vehicle model.

The maximum force ($F_{MAXbrakeF}$) that the traditional front brakes can generate at the tire contact patch is calculated in equation (3.1):

$$F_{MAXbrakeF} = 2 \cdot \frac{Pres_{MAXbrakeF} \cdot A_{pistonF} \cdot \mu_{padF} \cdot R_{discF}}{R_{wheelF}} \tag{3.1}$$

$Pres_{MAXbrakeF}$ is the maximum pressure that can be generated inside the master cylinder of the front brake system, $A_{pistonF}$ is the total area of the brake pistons in the front callipers, μ_{padF} is the dynamic coefficient of friction between the front brake pads and brake discs, R_{discF} is the average radius of application of the braking force on the front discs, and R_{wheelF} is the nominal rolling radius of the front wheels.

The maximum force ($F_{MAXbrakeR}$) that the traditional rear brakes can generate at the tire contact patch is calculated in equation (3.2):

$$F_{MAXbrakeR} = 2 \cdot \frac{Pres_{MAXbrakeR} \cdot A_{pistonR} \cdot \mu_{padR} \cdot R_{discR}}{R_{wheelR}} \tag{3.2}$$

$Pres_{MAXbrakeR}$ is the maximum pressure that can be generated inside the master cylinder of the front brake system, $A_{pistonR}$ is the total area of the brake pistons in the front callipers, μ_{padR} is the dynamic coefficient of friction between the front brake pads and brake discs, R_{discR} is the average radius of application of the braking force on the front discs, and R_{wheelR} is the nominal rolling radius of the front wheels.

The maximum disc brake force ($F_{MAXbrake}$) is the sum of the maximum front braking force ($F_{MAXbrakeF}$) and the maximum rear braking force ($F_{MAXbrakeR}$).

The total braking force associated with the brake demand ($F_{brakeReq}$) is calculated in equation (3.3).

$$F_{brakeReq} = BrakeDemand \cdot F_{MAXbrake} \tag{3.3}$$

3.2.3 Optimal Brake Distribution

The "OPTIMAL BRAKE DISTRIBUTION" module calculates the optimal brake distribution between the front and rear axle, taking the longitudinal (j) and lateral (a_y) vehicle acceleration as inputs. The braking distribution guarantees the correct stability of the vehicle during braking events.

The optimal braking distribution is calculated by taking into account the load transfer and the road friction coefficient to consider the road–tire adhesion limit that leads to locking the front and rear wheels at the same time.

The load on the front axle (W_f), considering only the static weight and the longitudinal load transfer, is calculated in (3.4):

$$W_f = \frac{M \cdot g}{L} \cdot \left(L_b + h_g \cdot \frac{j}{g} \right) \tag{3.4}$$

M is the vehicle mass, g is the gravitational acceleration equal to 9.81 m/s^2, L is the wheelbase, h_g is the centre of gravity height, and L_b is the longitudinal distance between the rear axle and the centre of gravity of the vehicle, which is the difference between the wheelbase and the longitudinal distance between the front axle and the centre of gravity (L_a), as in equation (3.5):

$$L_b = L - L_a \tag{3.5}$$

The load on the rear axle (W_r), considering only the static weight and the longitudinal load transfer, is calculated in (3.6):

$$W_r = \frac{M \cdot g}{L} \cdot \left(L_a + h_g \cdot \frac{j}{g} \right) \tag{3.6}$$

The load transfer, due to lateral acceleration, depends on the roll stiffness distribution and the roll angle.

The roll stiffness (k_{rollF}) of the front axle is calculated in equation (3.7):

$$k_{rollF} = \left(k_{springF} + 2 \cdot k_{ARBf} \cdot \frac{{track_F}^2}{2} \right) \tag{3.7}$$

$k_{springF}$ is the stiffness of the front suspension springs, k_{ARBf} is the stiffness of the front anti-roll bar, and $track_F$ is the front track of the vehicle.

The roll stiffness (k_{rollR}) of the rear axle is calculated in equation (3.8):

$$k_{rollR} = \left(k_{springR} + 2 \cdot k_{ARBr} \cdot \frac{{track_R}^2}{2} \right) \tag{3.8}$$

$k_{springR}$ is the stiffness of the rear suspension springs, k_{ARBr} is the stiffness of the rear anti-roll bar, and $track_R$ is the rear track of the vehicle.

The roll angle, ϑ_{ROLL}, is calculated in equation (3.9):

$$\vartheta_{ROLL} = \frac{(m_{sF} + m_{sR}) \cdot h_g - m_{sF} \cdot h_{CRf} - m_{sR} \cdot h_{CRr}}{k_{rollF} + k_{rollR}} \cdot a_y \tag{3.9}$$

m_{sF} is the front sprung mass of the vehicle, msR is the rear sprung mass, h_{CRf} is the height of the front roll centre, and h_{CRr} is the height of the rear roll centre.

Finally, the front (ΔF_{zF}) and rear (ΔF_{zR}) load transfers, due to lateral acceleration, are calculated, respectively, in equations (3.10) and (3.11):

$$\Delta F_{zF} = \frac{k_{rollF} \cdot \vartheta_{ROLL} + m_{sF} \cdot a_y \cdot h_{CRf}}{track_F} + \frac{2 \cdot m_{nsF} \cdot a_y \cdot R_{wheelF}}{track_F} \tag{3.10}$$

$$\Delta F_{zR} = \frac{k_{rollR} \cdot \vartheta_{ROLL} + m_{sR} \cdot a_y \cdot h_{CRr}}{track_R} + \frac{2 \cdot m_{nsR} \cdot a_y \cdot R_{wheelR}}{track_R} \tag{3.11}$$

Considering a single-wheel assembly, m_{nsF} is half the front unsprung mass of the vehicle and m_{nsR} is half the rear unsprung mass.

In the end, the reference loads on the front (W_{refF}) and rear (W_{refR}) axles, considering the inner wheel when cornering, is imposed, respectively, in equations (3.12) and (3.13).

$$W_{refF} = 2 \cdot \left(\frac{W_f}{2} - \Delta F_{zF}\right) \tag{3.12}$$

$$W_{refR} = 2 \cdot \left(\frac{W_r}{2} - \Delta F_{zR}\right) \tag{3.13}$$

The model calculates the maximum forces on the front and rear axles considering the reference forces above.

The front total maximum braking force (F_{bfMAX}) is expressed in equation (3.14), where μ is the road–tire friction coefficient.

$$F_{bfMAX} = \mu \cdot W_{refF} \tag{3.14}$$

The rear total maximum braking force (F_{brMAX}) is expressed in equation (3.15):

$$F_{brMAX} = \mu \cdot W_{refR} \tag{3.15}$$

In the end, the optimal braking distribution (BD) is defined as follows (3.16):

$$BD = \frac{F_{bfMAX}}{F_{brMAX}} \tag{3.16}$$

3.2.4 Motors Request – Slip Limits

The Simulink® model includes three different logics for a front-wheel drive vehicle (FWD) with a single electric motor acting on the front axle, a rear-wheel drive vehicle (RWD) equipped with an electric motor acting on the rear axle, and for all-wheel drive vehicle (AWD) equipped with an electric motor for each axle.

3.2.4.1 FWD

For the FWD vehicle, the braking force required from the motor (F_{reqF}) is imposed as the minimum between the total braking force requested by the driver ($F_{brakeReq}$) and the front total maximum braking force (F_{bfMAX}), multiplied by a safety coefficient (SC_F).

The front electric motor torque required (T_{reqF}) is calculated in equation (3.17), taking into account the front wheel radius, the inertia of the wheels, the inertia of the differential, the inertia of the motor, and the transmission ratios [13].

$$T_{reqF} = \left[\frac{F_{reqF} \cdot R_{wheelF} + (2 \cdot J_{wheelF} + J_{outF}) \cdot \frac{\Delta(\omega_{wheelF})}{\Delta t}}{\tau_{diffF} \cdot \tau_{redF}} + (J_{inF} + J_{motF}) \cdot \frac{\Delta(\omega_{motF})}{\Delta t} \right] \cdot \eta_{transF} \quad (3.17)$$

$\frac{\Delta}{\Delta t}$ is the time derivative; J_{wheelF} is the moment of inertia for a single front wheel; J_{outF} and J_{inF} are the moments of inertia of the transmission before and after the front motor reducer, respectively; J_{motF} is the moment of inertia of the front electric motor; τ_{diffF} is the gear ratio of the front differential; τ_{redF} is the gear ratio of the front motor reducer; and η_{transF} is the general efficiency of the whole front transmission.

3.2.4.2 RWD

For the RWD vehicle, the braking force required from the motor (F_{reqR}) is imposed as the minimum between the total braking force requested by the driver ($F_{brakeReq}$) and the rear total maximum braking force (F_{brMAX}), multiplied by a safety coefficient (SC_R).

The rear electric motor torque required (T_{reqR}) is calculated in equation (3.18), taking into account, as in the FWD case, the wheel radius, the inertia of the wheels, the inertia of the differential, the inertia of the motor, and the transmission ratios [13].

$$T_{reqR} = \left[\frac{F_{reqR} \cdot R_{wheelR} + (2 \cdot J_{wheelR} + J_{outR}) \cdot \frac{\Delta(\omega_{wheelR})}{\Delta t}}{\tau_{diffR} \cdot \tau_{redR}} + (J_{inR} + J_{motR}) \cdot \frac{\Delta(\omega_{motR})}{\Delta t} \right] \cdot \eta_{transR} \quad (3.18)$$

J_{wheelR} is the moment of inertia for a single rear wheel; J_{outR} and J_{inR} are the moments of inertia for the transmission before and after the front motor reducer, respectively; J_{motR} is the moment of inertia for the rear electric motor; τ_{diffR} is the gear ratio of the rear differential; τ_{redR} is the gear ratio of the rear motor reducer; and η_{transR} is the general efficiency of the whole rear transmission.

3.2.4.3 AWD

For the AWD vehicle, the rear braking force associated with the driver demand ($F_{brakeReqR}$) is calculated in equation (3.19):

$$F_{brakeReqR} = \frac{F_{brakeReq}}{BD + 1} \tag{3.19}$$

The front braking force associated with the driver demand ($F_{brakeReqF}$) is instead the difference between $F_{brakeReq}$ and $F_{brakeReqR}$.

The braking force required from the front motor (F_{reqF}) is imposed as the minimum between the front total braking force requested by the driver ($F_{brakeReqF}$) and the front total maximum braking force (F_{bfMAX}), multiplied by a safety coefficient (SC_F). Similarly, the braking force required from the rear motor (F_{reqR}) is imposed as the minimum between the rear total braking force requested by the driver ($F_{brakeReqR}$) and the rear total maximum braking force (F_{brMAX}), multiplied by a safety coefficient (SC_R).

The equations (3.17) and (3.18) are also used for the calculation of the required driving torques for the AWD case but they are calculated starting from the values of F_{reqF} and F_{reqR} calculated as explained in this subsection.

3.2.5 Motors Limits

In the subsystem called "Motors Limits" in Figure 3.1, the electric motor torques required under braking, front (T_{reqF}) and rear (T_{reqR}), are compared with the maximum regenerative motor torques available at the motor RPM of the considered instant.

Outputs from this subsystem are the minimum value of torque, front (T_{refF}) and rear (T_{refR}), between the maximum available and the required torque (both considered in absolute value).

The maximum value of available torque for each motor (front and rear) is obtained by means of Simulink® lookup tables containing the torque curves of the motors as a function of the RPM of the motors themselves.

3.2.6 Battery Current Request

The "Battery Current Request" subsystem calculates the current that the motors should send to the battery if they provided the output braking torque from the "Motor Limits" subsystem.

The charging current of the front motor ($Crnt_{reqF}$), if present, is obtained with Relationship (3.20):

$$Crnt_{reqF} = \frac{\left(T_{refF} \cdot \omega_{motF}\right) \cdot \eta_{motF} - R_{cableF} \cdot \left(\frac{T_{refF} \cdot \omega_{motF}}{V}\right)^2}{V} \tag{3.20}$$

η_{motF} is the efficiency of the front motor at the point of operation considered, and it is obtained through the use of a two-dimensional Simulink® lookup table. This lookup table contains the front motor efficiency map; it receives the motor torque, T_{refF}, and the RPM of the motor in input and returns the efficiency at the operating point in output. R_{cableF} is the electric resistance of the front connection cables, and it is calculated as in equation (2.16).

Similarly, the charging current of the rear motor ($CrntreqR$), if present, is obtained through Relationship (3.21):

$$Crnt_{reqR} = \frac{\left(T_{refR} \cdot \omega_{motR}\right) \cdot \eta_{motR} - R_{cableR} \cdot \left(\frac{T_{refR} \cdot \omega_{motR}}{V}\right)^2}{V} \tag{3.21}$$

η_{motR} is the efficiency of the rear motor at the point of operation considered, and it is obtained using a two-dimensional Simulink® lookup table that receives the motor torque T_{refR} and the RPM of the motor in input and returns the efficiency at the operating point in output. R_{cableR} is the electric resistance of the rear connection cables, and it is calculated as in equation (2.17).

In the equations (3.20) and (3.21), implemented in the RB logic, the electrical efficiency of the motor has been neglected for the calculation of the power dissipated to Joule effect, without affecting the final results. For the sake of accuracy, the two equations should be rewritten as equations (3.24) and (3.25). In a version of the RB logic following the one described in this chapter (Section 3), the equations (3.20) and (3.21) will therefore be replaced by equations (3.24) and (3.25).

$$Crnt_{reqF} = \frac{\left(T_{refF} \cdot \omega_{motF}\right) \cdot \eta_{motF} - R_{cableF} \cdot \left(\frac{T_{refF} \cdot \omega_{motF} \cdot \eta_{motF}}{V}\right)^2}{V} \tag{3.22}$$

$$Crnt_{reqR} = \frac{\left(T_{refR} \cdot \omega_{motR}\right) \cdot \eta_{motR} - R_{cableR} \cdot \left(\frac{T_{refR} \cdot \omega_{motR} \cdot \eta_{motR}}{V}\right)^2}{V} \tag{3.23}$$

Finally, the total current that the motors should send to the battery ($Crnt_{req}$) is provided by the sum of $Crnt_{reqF}$ and $Crnt_{reqR}$.

3.2.7 Battery Limits

In the "Battery Limits" subsystem, the limits of the battery pack are considered; in particular, it is checked if the current that the motors should send to the battery does not exceed the maximum that can be absorbed by the battery pack at the moment ($Crnt_{MAX}$). If this limit is not respected, it is necessary to limit the regenerative motor torques.

In case the motors do not need to be limited due to restrictions due to the battery pack, the following equations apply (equations from (3.24) to (3.26)):

$$Crnt_{mot} = Crnt_{req} \tag{3.24}$$

$$T_{motF} = T_{refF} \tag{3.25}$$

$$T_{motR} = T_{refR} \tag{3.26}$$

$Crnt_{mot}$ is the charging current of the battery pack generated by the motor or motors, T_{motF} is the braking torque of the front motor, and T_{motR} is the braking torque of the rear motor.

In case of battery limitations, equations from (3.24) to (3.26) are not valid. The current generated by the motor or motors is obtained through equation (3.27) and the other two quantities are calculated as shown in the following sections, depending on the type of vehicle: FWD, RWD, or AWD.

$$Crnt_{mot} = Crnt_{MAX} \tag{3.27}$$

3.2.7.1 FWD

For FWD vehicles, in the event of battery limitations, the regenerative front motor torque is recalculated from the maximum charging current, as in equation (3.28):

$$T_{motF} = \frac{V \cdot Crnt_{MAX} + R_{cableF} \cdot {Crnt_{MAX}}^2}{\eta_{FWD} \cdot \omega_{motF}} \tag{3.28}$$

η_{FWD} is the actual efficiency of the front electric motor (in the case of an FWD vehicle), calculated with a Simulink® lookup table containing an efficiency map of the front motor.

3.2.7.2 RWD

Similar to the case of FWD vehicles, for RWD vehicles, in the event of battery limitations, the regenerative rear motor torque is recalculated based on the maximum absorbable current, as in equation (3.29):

$$T_{motR} = \frac{V \cdot Crnt_{MAX} + R_{cableR} \cdot {Crnt_{MAX}}^2}{\eta_{RWD} \cdot \omega_{motR}} \tag{3.29}$$

η_{RWD} is the actual efficiency of the rear electric motor (in the case of an RWD vehicle), calculated with a Simulink® lookup table containing an efficiency map of the rear motor.

3.2.7.3 AWD

For AWD vehicles, the maximum power that can be sent to the battery by the motors is divided between the front (P_{AWDf}) and rear (P_{AWDr}) motors by means of the optimal braking distribution ratio, as in equations (3.30) and (3.31):

$$P_{AWDr} = \frac{V \cdot Crnt_{MAX}}{BD + 1} \tag{3.30}$$

$$P_{AWDf} = V \cdot Crnt_{MAX} - P_{AWDr} \tag{3.31}$$

By applying the optimal distribution to the power, the optimal distribution between the braking forces of the two axles is obtained, with an approximation due to losses related, in turn, to the resistance of the connection cables. In fact, the power is provided by the product between the force and the speed, and the longitudinal speed can be considered constant between the two axles; therefore, distributing the power in a certain way between the two axles means distributing the braking forces in the same way.

The maximum regenerative torque (T_{AWD_MAXf}) that can be obtained from the front motor, exploiting the absorbable power, P_{AWDf}, of the battery pack, is provided by Relation (3.32).

$$T_{AWD\_MAXf} = \frac{P_{AWDf} + R_{cableF} \cdot \left(\frac{P_{AWDf}}{V}\right)^2}{\eta_{AWDf} \cdot \omega_{motF}} \tag{3.32}$$

η_{AWDf} is the electrical efficiency of the front motor at the operating point characterized by the parameters P_{AWDf} and ω_{motF}, obtained thanks to Simulink® lookup tables containing efficiency maps of the front motor.

At this point of the model, a further check is carried out: it is verified that T_{AWD_MAXf} is not greater than T_{refF}, calculated as an output by the "Motors Limits" subsystem.

If T_{AWD_MAXf} is not greater than T_{refF}, the hypothetical front regenerative torque (T_{AWD_HYPf}) is equal to T_{AWD_MAXf}; vice versa, it is equal to T_{refF}.

Moreover, if T_{AWD_MAXf} is not greater than T_{refF}, the hypothetical charging power provided by the rear motor (P_{AWD_HYPr}) is equal to P_{AWDr}; otherwise, P_{AWD_HYPr} is calculated with equation (3.33):

$$P_{AWD\_HYPr} = \left(Crnt_{MAX} - Crnt_{refF}\right) \cdot V \tag{3.33}$$

$Crnt_{refF}$ is the current that the front motor sends to the battery pack when it produces a regenerative motor torque equal to T_{refF}.

$Crnt_{refF}$ is calculated as follows in Relation (3.34):

$$Crnt_{refF} = \frac{T_{refF} \cdot \omega_{motF} \cdot \eta_{refF} - R_{cableF} \cdot \left(\frac{T_{refF} \cdot \omega_{motF}}{V}\right)^2}{V} \tag{3.34}$$

η_{refF} is the electrical efficiency of the front motor at the operating point characterized by the parameters T_{refF} and ω_{motF}, obtained thanks to a Simulink® lookup table containing an efficiency map of the front motor.

The hypothetical rear regenerative torque (T_{AWD_HYPr}) is calculated using the equation (3.35), starting from the power P_{AWD_HYPr}.

$$T_{AWD\_HYPr} = \frac{P_{AWD\_HYPr} + R_{cableR} \cdot \left(\frac{P_{AWD\_HYPr}}{V}\right)^2}{\eta_{AWD\_HYPr} \cdot \omega_{motR}} \tag{3.35}$$

η_{AWD_HYPr} is the electrical efficiency of the rear motor at the operating point characterized by the parameters P_{AWD_HYPr} and ω_{motR}, obtained thanks to Simulink® lookup tables containing efficiency maps of the rear motor.

Now, a further check is carried out: it is verified that T_{AWD_HYPr} is not greater than T_{refR}, calculated as output by subsystem "Motors Limits".

If T_{AWD_HYPr} is not greater than T_{refR}, the actual rear regenerative torque (T_{motR}) is equal to T_{AWD_HYPr}, and T_{motF} is equal to T_{AWD_HYPf}; vice versa, T_{motR} is equal to T_{refR}, and, in this case, it is necessary to recalculate the regenerative front motor torque as in equation (3.36).

$$T_{motF} = \frac{P_{AWD\_NEWf}}{\eta_{AWD\_NEWf} \cdot \omega_{motF}} \tag{3.36}$$

η_{AWD_NEWf} is the electrical efficiency of the front motor at the operating point characterized by the parameters P_{AWD_NEWf} and ω_{motF}, obtained thanks to Simulink® lookup tables containing efficiency maps of the front motor.

P_{AWD_NEWf} is calculated in equation (3.37):

$$P_{AWD\_NEWf} = \left(Crnt_{MAX} - Crnt_{refR}\right) \cdot V + R_{cableF} \cdot \left(Crnt_{MAX} - Crnt_{refR}\right)^2 \quad (3.37)$$

$Crnt_{refR}$ is the current that the rear motor sends to the battery pack when it produces a regenerative motor torque equal to T_{refR}.

$Crnt_{refR}$ is calculated as follows in equation (3.38):

$$Crnt_{refR} = \frac{T_{refR} \cdot \omega_{motR} \cdot \eta_{refR} - R_{cableR} \cdot \left(\frac{T_{refR} \cdot \omega_{motR}}{V}\right)^2}{V} \quad (3.38)$$

η_{refR} is the electrical efficiency of the rear motor at the operating point characterized by the parameters T_{refR} and ω_{motR}, obtained thanks to a Simulink® lookup table containing an efficiency map of the front motor.

3.2.8 Traditional Brakes

The "Traditional Brakes" subsystem calculates the pressure on the front ($Pres_{brakeF}$) and rear ($Pres_{brakeR}$) master cylinders of the brake system necessary to integrate the braking forces provided by the motor or motors in such a way as to guarantee the total braking force requested by the driver. Moreover, the integration of braking through the traditional brake system ensures that the system comes as close as possible to the condition of optimal braking distribution to guarantee vehicle stability.

If only the motor (or motors) is able to guarantee the braking request from the driver, the pressures $Pres_{brakeF}$ and $Pres_{brakeR}$ are imposed equal to the null value; vice versa, the model must calculate the two pressure values. In this second case, $Pres_{brakeF}$ is calculated as in equations (3.39) if the value resulting from (3.39) is smaller than $Pres_{MAXbrakeF}$; otherwise, $Pres_{brakeF}$ is imposed equal to $Pres_{MAXbrakeF}$, while $Pres_{brakeR}$ is calculated as in equations (3.40) if the value resulting from (3.40) is smaller than $Pres_{MAXbrakeR}$; otherwise, $Pres_{brakeR}$ is imposed equal to $Pres_{MAXbrakeR}$.

$$Pres_{brakeF} = \frac{\left[\left(F_{brakeReq} - \frac{F_{brakeReq}}{BD+1}\right) - \frac{T_{motF} \cdot \tau_{diffF} \cdot \tau_{redF}}{R_{wheelF}}\right] \cdot R_{wheelF}}{A_{pistonF} \cdot \mu_{padF} \cdot R_{discF}} \quad (3.39)$$

$$Pres_{brakeR} = \frac{\left[\frac{F_{brakeReq}}{BD+1} - \frac{T_{motR} \cdot \tau_{diffR} \cdot \tau_{redR}}{R_{wheelR}}\right] \cdot R_{wheelR}}{A_{pistonR} \cdot \mu_{padR} \cdot R_{discR}} \quad (3.40)$$

3.3 MODEL VALIDATION

This section reports the results of simulation tests carried out with VI-CarRealTime® on an FWD, an RWD, and an AWD car to check the braking efficiency and stability of a vehicle equipped with the logic presented in this chapter.

Finally, through the Simulink® TEST model [10], the energy saving obtained through this regenerative braking logic is estimated.

3.3.1 Reference Vehicles

Three fully electric compact cars were taken as reference vehicles: one with front-wheel drive with an electric motor acting on the front axle, one with rear-wheel drive with an electric motor acting on the rear axle, and one with all-wheel drive with an electric motor for each axle.

The three vehicles share the characteristics shown in Table 3.1.

Table 3.1. *Reference vehicles characteristics.*

Dimension	Value	Unit
Total weight	1548.38	kg
Front suspended mass	835.50	kg
Rear suspended mass	548.15	kg
Front unsprung mass (of a single wheel group)	44.21	kg
Rear unsprung mass (of a single wheel group)	38.15	kg
Wheelbase	2577.4	mm
Front track	1506.3	mm
Rear track	1476.9	mm
Centre of gravity height	563.92	mm
CG longitudinal front wheel distance	1021.55	mm
Frontal area of the vehicle	3.23	m^2
Drag coefficient	0.32	-
Front rolling wheel radius	298.7	mm
Rear rolling wheel radius	300.5	mm
Rolling friction coefficient of the wheels	0.01	-
Transmission ratio	1	-
Drive ratio of differential [1]	3.7	-
Power absorbed by vehicle accessories	1500	W

[1] Drive ratio of front differential for an FWD vehicle, of rear differential for an RWD vehicle, and of front and rear differentials for an AWD vehicle.

Figure 3.2 represents the torque and power curves of the motor for both the FWD and RWD vehicles and for the two motors of the AWD vehicle.

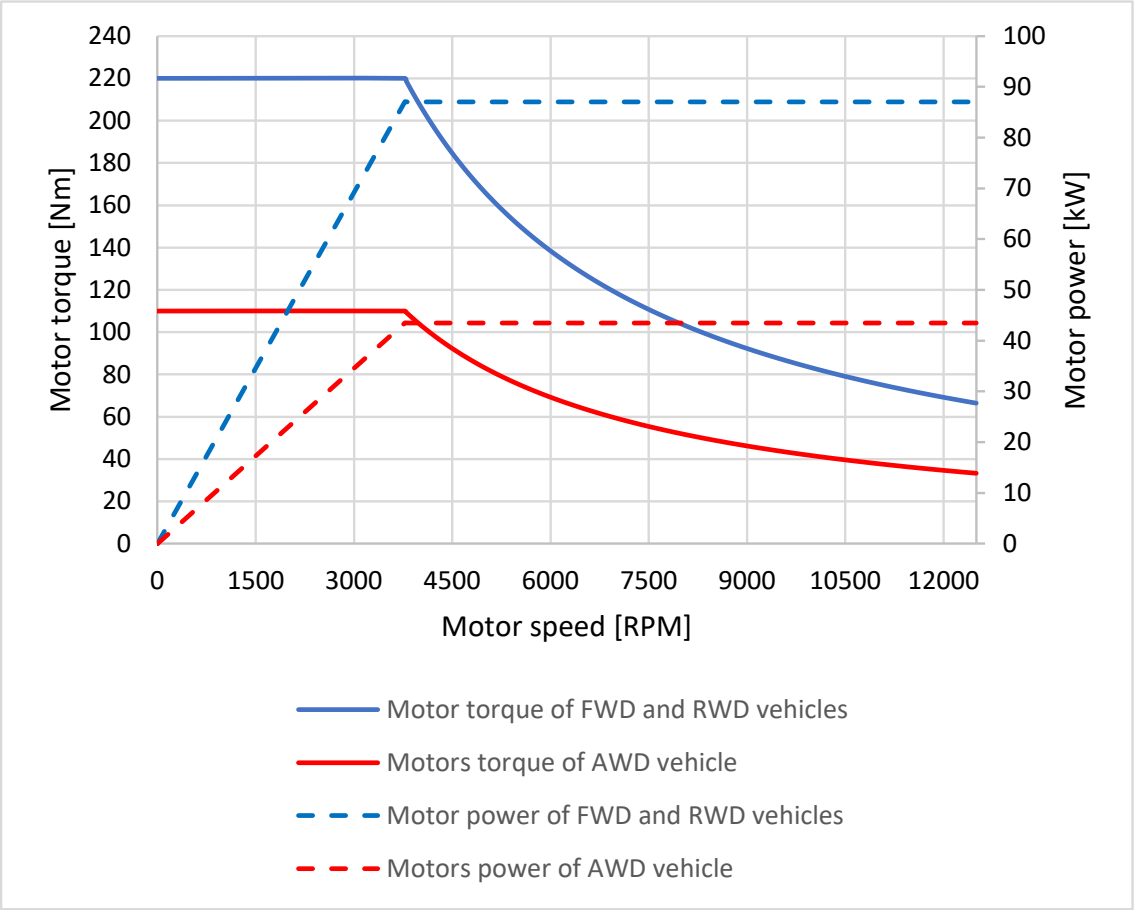

Figure 3.2. *Torque and power of electric motors of FWD, RWD, and AWD vehicles.*

Table 3.2 shows the characteristics of the braking system of the three vehicles. If the vehicles are equipped with the regenerative braking logic, the front and rear master cylinders should be controlled by the logic independently; otherwise, there is a master cylinder controlled by the force input on the brake pedal, which distributes the pressure (total pressure equal to 15 MPa) between the front and rear cylinders with a bias on the front equal to 0.65.

Table 3.2. *Braking system characteristics.*

Dimension	Value	Unit
Maximum front brake pressure	9.75	MPa
Maximum rear brake pressure	5.25	MPa
Front pistons area	2000	mm^2
Rear pistons area	1100	mm^2
Front effective piston radius	134	mm
Rear effective piston radius	104	mm

Table 3.3 shows the main suspension characteristics of the three vehicle models, useful for defining the constant parameters of the regenerative logic. The three vehicles do not feature anti-roll bars for simplicity.

Table 3.3. *Suspension characteristics.*

Dimension	Value	Unit
Front centre roll height	39.20	mm
Rear centre roll height	128.84	mm
Front spring stiffness	25	N/mm
Rear spring stiffness	27	N/mm

Table 3.4 shows the characteristics of the battery pack of the reference vehicles.

Table 3.4. *Battery pack characteristics.*

Dimension	Value	Unit
Number of cells in series	96	-
Number of cells in parallel	2	-
Nominal capacity of the pack	105	Ah
Nominal capacity of the pack	42	kWh
Available battery capacity	37.5	kWh
Operating temperature	23	°C
Maximum deliverable power in discharge	87	kW
Maximum absorbable power in charge	85	kW
Open Circuit Voltage of a single cell	4.17	V

The available capacity of the battery pack is the portion of capacity that can actually be used during vehicle operation. It differs from the nominal capacity, which is instead the real battery capacity, without considering that, during the operation of the vehicle, there will be limitations that will ensure that this capacity is not fully used in order to preserve the battery from premature decay.

When the three vehicles are equipped with the regenerative braking logic described in this thesis, a minimum speed equal to 15 km/h is defined for the

activation of regenerative recovery, and the safety coefficients SC_F and SC_R are both set equal to 0.9; finally, the road–tire friction coefficient, μ, considered in the logic is set to constant.

Furthermore, none of the vehicles analysed are equipped with an ABS system.

3.3.2 Test of Regenerative Braking Logic

In this section, straight braking tests performed with VI-CarRealTime® are presented to show how the regenerative braking logic object of this thesis acts on the regenerative motor torque and on the pressure in the traditional brake system.

The tests are carried out for the three vehicle types (FWD, RWD and AWD), equipped with RB logic with the μ coefficient constant equal to 1.

Table 3.5 shows the parameters of the tests; in particular, the initial vehicle speed is set equal to 108 km/h (30 m/s). At the start of the test ("Start time" equal to zero seconds), 100% brake demand is achieved linearly in 10 s ("Ramp up time"). The test ends when the vehicle stops. Therefore, a brake demand equal to 1 may not be reached during the test. The braking imposed was specifically chosen not to be very intensive so as not to lead to wheel locking or vehicle instability.

Table 3.5. *Parameters of straight braking test.*

Dimension	Value	Unit
Initial vehicle speed	108	km/h
Final vehicle speed	0	km/h
Start time	0	s
Ramp up time	10	s
Brake demand	1	-
Road friction coefficient	1	-

Figure 3.3 shows the speed of the three vehicles (FWD, RWD, and AWD) featuring the RB logic, as well as the brake demand during the straight braking test. Figure 3.3 also shows the motor torque and the brake pressure during the tests. Only the brake pressures on the left side of the vehicle are graphically represented because the left and right pressures are the same.

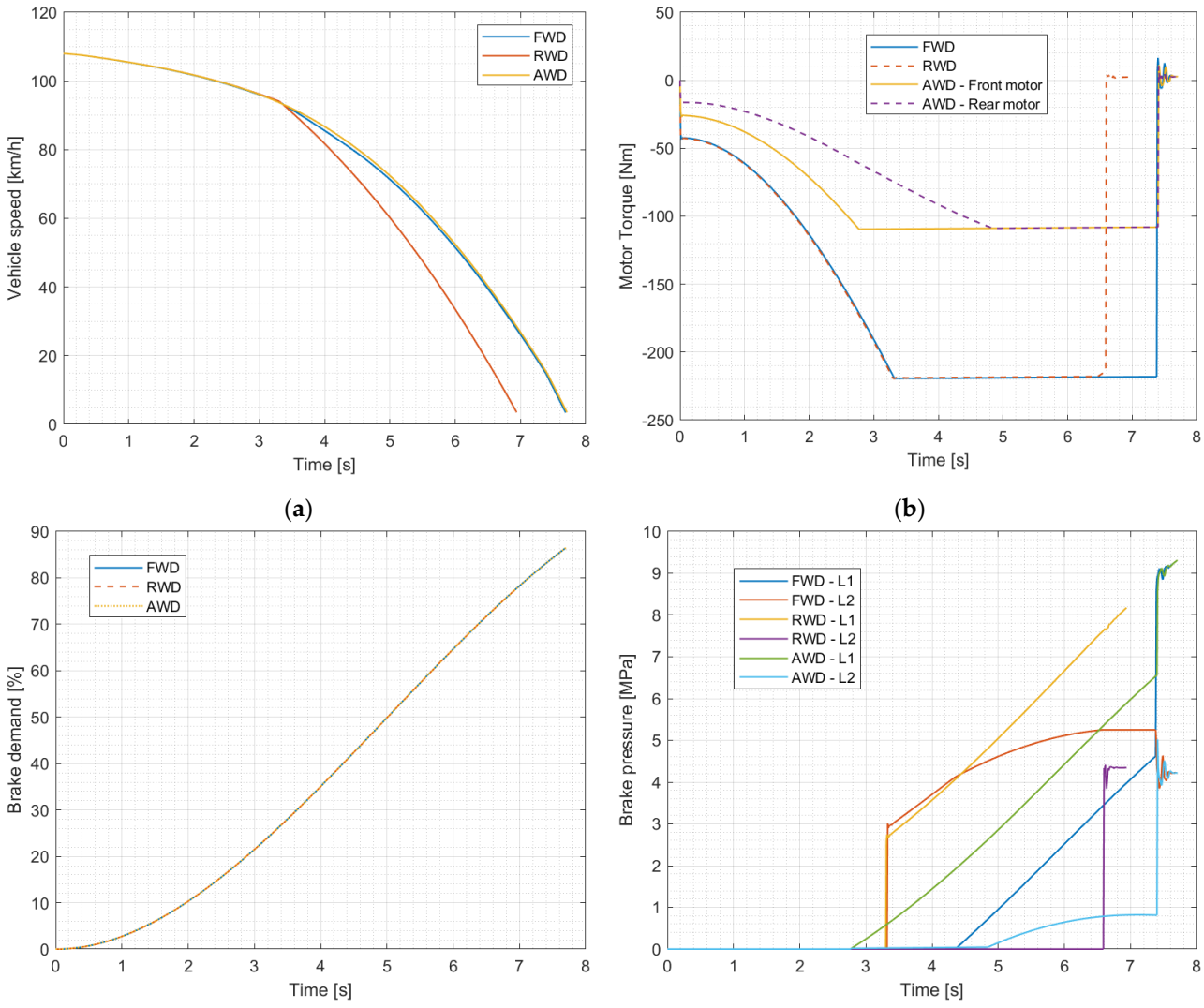

Figure 3.3. *Straight braking tests. (**a**) Vehicle speed; (**b**) motor torque; (**c**) brake demand; (**d**) brake pressure at the front left wheel (L1) and at the rear left wheel (L2).*

Figure 3.3 shows that, in the initial stage of braking, only the braking torque of the motor (or motors) intervenes, while when braking becomes more intensive, the contribution of the traditional brakes integrates the regenerative braking.

3.3.3 Braking Performance and Handling

In this section, tests performed with the VI-CarRealTime® software are presented to check the performance and handling of vehicles equipped with RB logic.

3.3.3.1 Straightline Panic Brake

First of all, a panic braking test on a straightline is carried out via VI-CarRealTime® to verify the braking effectiveness of the vehicle equipped with RB

logic. The behaviour of the latter is compared with that of the same vehicle without regenerative braking.

The tests are carried out for the three vehicle types, as stated before (FWD, RWD, and AWD), and with two different coefficients of road surface friction (1 for dry tarmac; 0.7 for a wet surface), remembering that the μ model coefficient in the RB logic is defined as a constant value because it is not possible to know the real road friction coefficient on board the vehicle.

In the RB logic, the μ model coefficient is normally set equal to 1. The tests with a road friction coefficient of 0.7 for vehicles equipped with regenerative braking logic, are also repeated with a μ model coefficient set to 0.7 to verify the influence of the correct definition of this parameter for panic braking performance.

These tests are used to verify that the RB logic performs well in comparison with a standard vehicle (i.e., without any regenerative braking), even in the case of a low friction coefficient. For this reason, no tests were carried out below the value of 0.7: as a matter of fact, any standard vehicle without an anti-lock braking system (ABS) performs poorly in a panic stop manoeuvre on wet pavement because wheel locking occurs immediately; therefore, it makes no sense to take its behaviour as a reference. The same goes for the tests of the next subsection. Braking in turn manoeuvres can be carried out successfully only if an appropriate ABS logic is implemented on the vehicle, either with or without a regenerative braking logic. An appropriate ABS strategy, downstream of the RB logic, also considering the contribution of the electric motors during braking, is therefore required. An example of ABS logic suitable for the purpose, as already anticipated, is presented in [45].

Table 3.6 shows the test parameters: the initial vehicle speed is set to 90 km/h; this speed is maintained for 1 s ("Start time"), then 100% brake demand is achieved linearly in 1 s ("Ramp up time").

Table 3.6. *Parameters of straight panic braking test.*

Dimension	Value	Unit
Initial vehicle speed	90	km/h
Final vehicle speed	0	km/h
Start time	1	s
Ramp up time	1	s
Brake demand	1	-

Figure 3.4 shows the results of various panic brake tests carried out on a straightline.

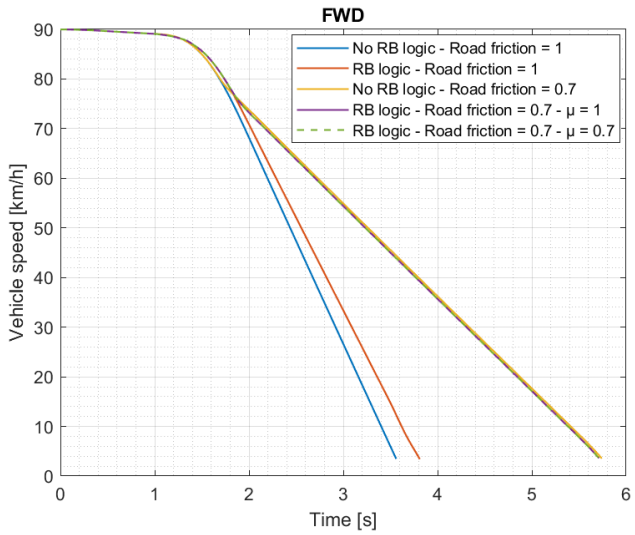

(**a**)

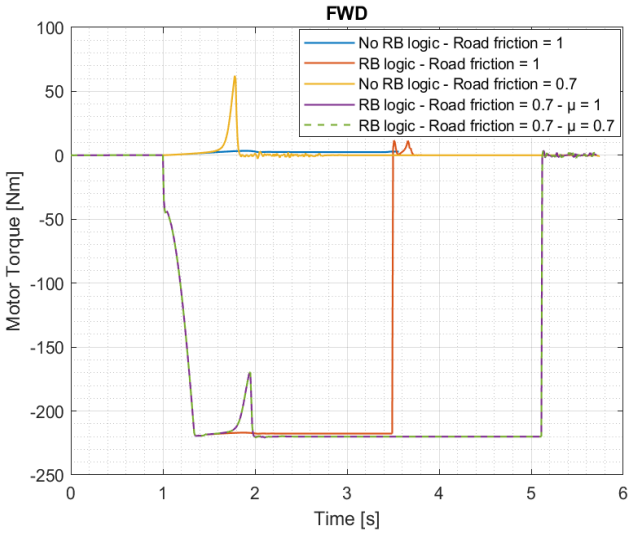

(**b**)

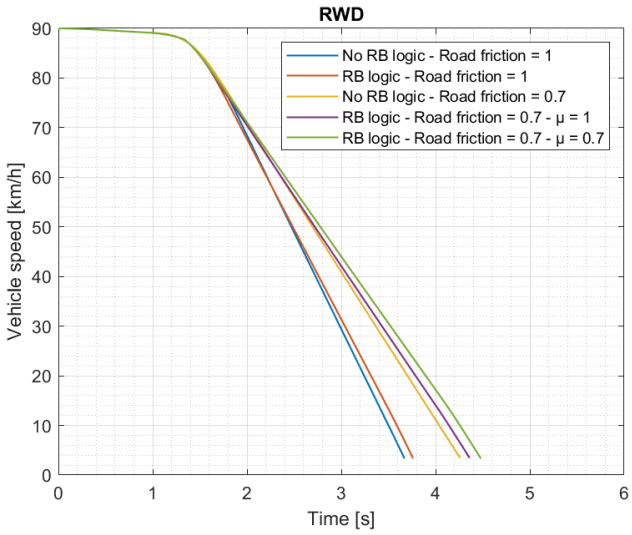

(**c**)

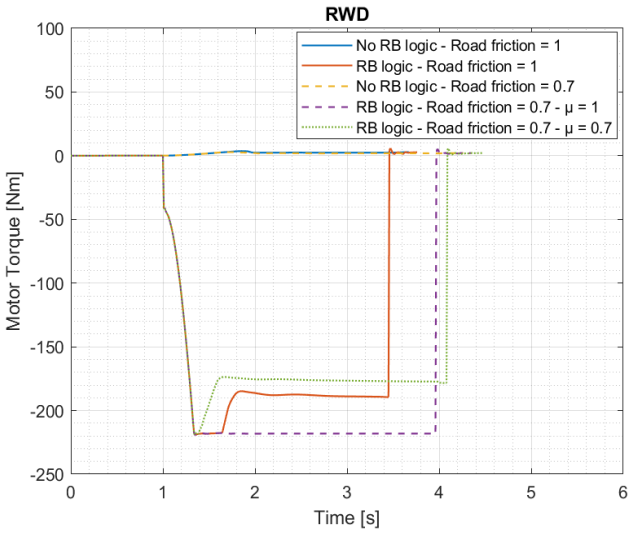

(**d**)

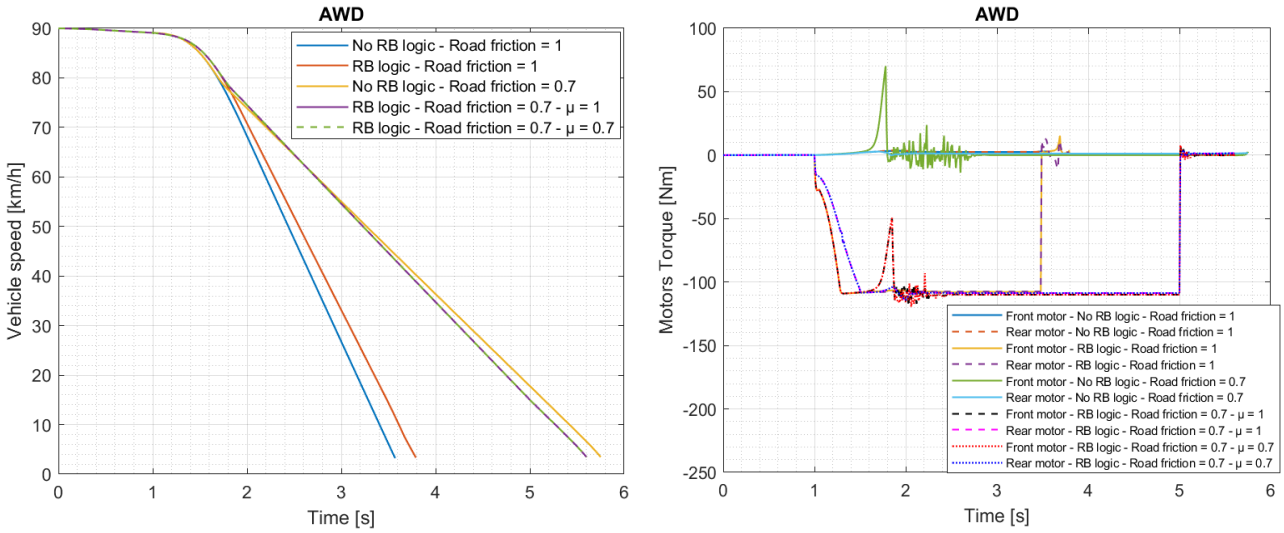

(**e**) (**f**)

Figure 3.4. *Vehicle speeds and motor torques during the straightline panic brake tests. In particular: (**a**) vehicle speed in tests with FWD vehicles (with and without RB logic) on surfaces with road friction coefficients equal to 1 and 0.7; (**b**) motor torque in tests with FWD vehicles (with and without RB logic) on surfaces with road friction coefficients equal to 1 and 0.7; (**c**) vehicle speed in tests with RWD vehicles (with and without RB logic) on surfaces with road friction coefficients equal to 1 and 0.7; (**d**) motor torque in tests with RWD vehicles (with and without RB logic) on surfaces with road frictions coefficient equal to 1 and 0.7; (**e**) vehicle speed in tests with AWD vehicles (with and without RB logic) on surfaces with road friction coefficients equal to 1 and 0.7; (**f**) motor torque in tests with AWD vehicles (with and without RB logic) on surfaces with road friction coefficients equal to 1 and 0.7.*

As shown by Figure 3.4, panels (**a**), (**c**), and (**e**), the RB logic leads to a slight deterioration of the panic braking performance of all three vehicles (FWD, RWD, and AWD) on road surfaces with a friction coefficient equal to 1. As for surface tests with a μ model coefficient of friction equal to 0.7, the FWD vehicles equipped with RB logic behave like the vehicle without the regenerative braking; the RWD vehicles equipped with RB logic have slightly lower performance in the panic brake test compared with the RWD vehicle without regenerative braking; and, finally, the RB logic in AWD vehicles leads to an improvement in panic braking compared to the same vehicle not equipped with RB logic.

In these tests, the contribution of the variation of the μ model coefficient assumed that the RB logic does not lead to substantial variations in the behaviour of the cars.

It can be said that effective panic braking has been achieved through RB logic even without an ABS system.

Furthermore, unlike what happens on vehicles equipped with classic regenerative braking logics in the literature, the RB logic object of this chapter also allows for an intensive intervention of electric motors in generator mode for panic braking, as can be seen from panels (**b**), (**d**), and (**f**) in Figure 3.4.

Figure 3.5 shows the mean between the angular speeds of the left and right front wheels and the mean between the angular speeds of the left and right rear wheels for all the FWD vehicles in the panic brake tests (with road friction coefficients equal to 1 and 0.7): the vehicle without RB logic, the vehicle with RB logic with a μ model coefficient equal to 1, and the vehicle with RB logic with a μ model coefficient equal to 0.7.

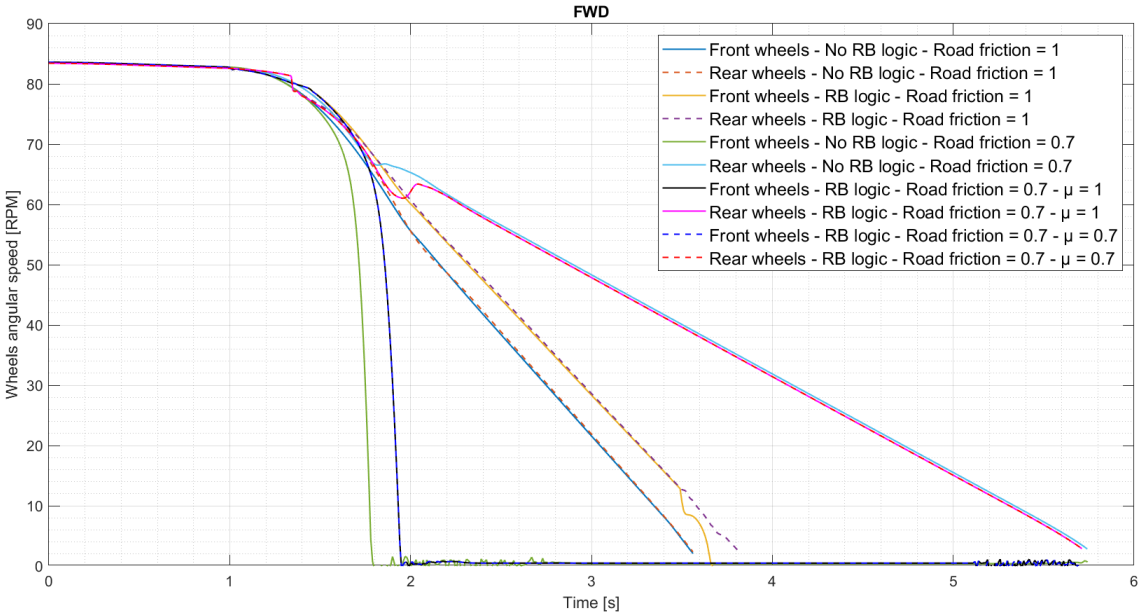

Figure 3.5. *Mean between the angular speeds of the left and right wheels (front mean and rear mean) of the FWD vehicles (with and without RB logic) during the straight panic brake tests on road surfaces with friction coefficients equal to 1 and 0.7.*

As shown by the graph in Figure 3.5, in the tests with a road friction coefficient equal to 0.7, all the vehicles lock the front wheels and not the rear wheels, even those equipped with RB logic; this is positive to ensure stability, as it is necessary to avoid locking the rear wheels or, in any case, to assure the front wheels lock before the rear ones.

Figure 3.6 shows the mean between the angular speeds of the left and right front wheels and the mean between the angular speeds of the left and right rear wheels for all the RWD vehicles in the panic brake tests.

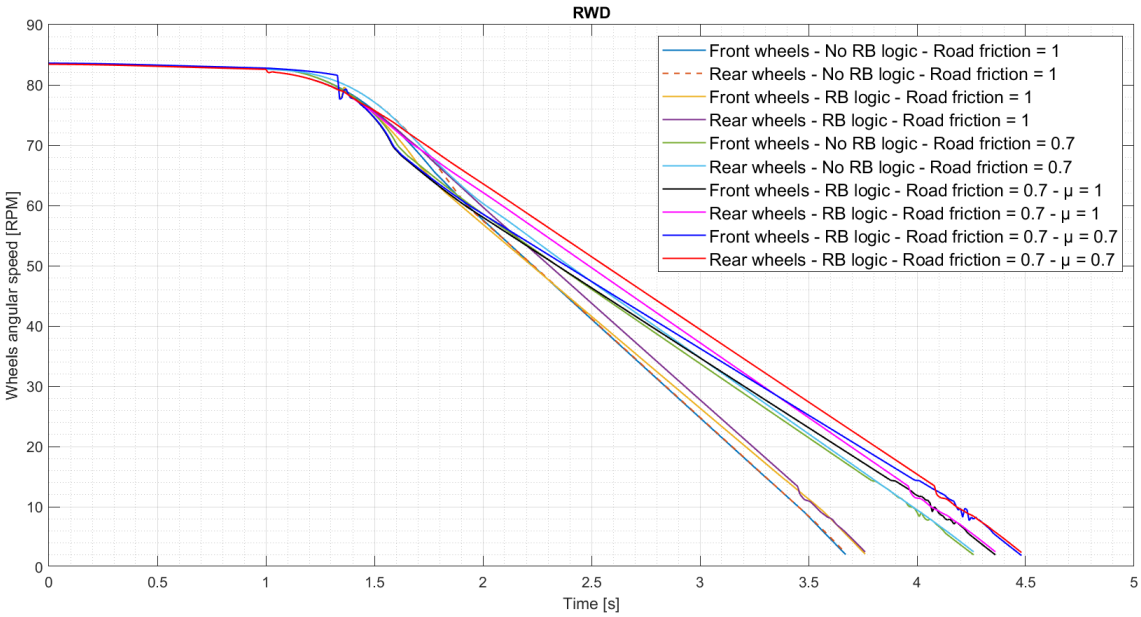

Figure 3.6. *Mean between the angular speed of the left and right wheels (front mean and rear mean) of the RWD vehicles (with and without RB logic) during the straight panic brake tests on road surfaces with friction coefficients equal to 1 and 0.7.*

As shown in Figure 3.6, in all the tests (with road friction coefficients equal to 1 and 0.7), all the vehicles lock the front and rear wheels almost simultaneously. The tests with RWD vehicles, therefore, achieved excellent results.

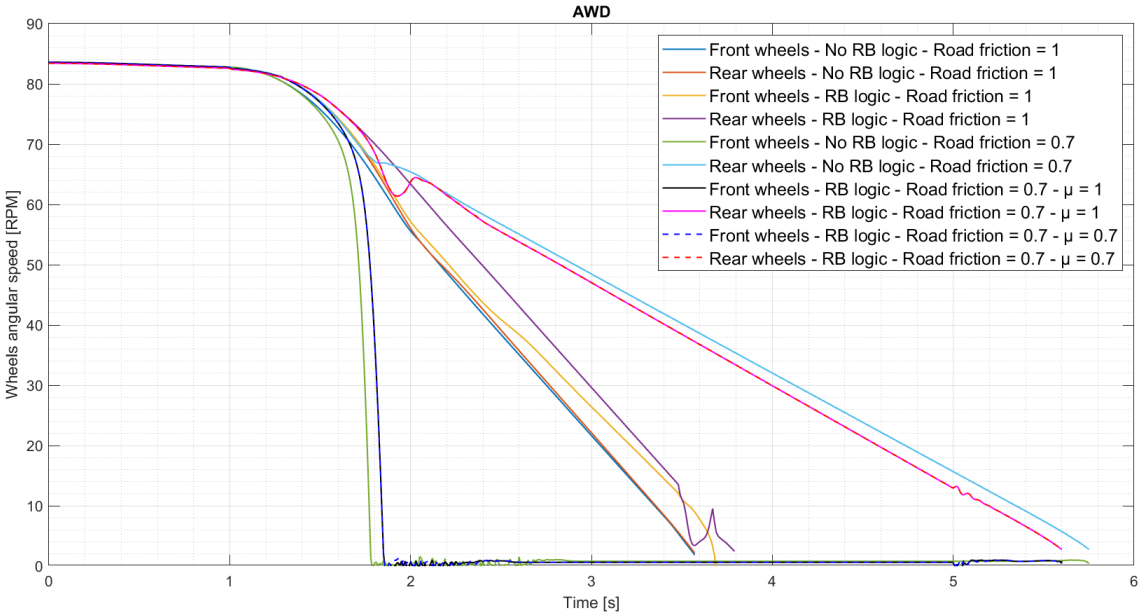

Figure 3.7. *Mean between the angular speeds of the left and right wheels (front mean and rear mean) of the AWD vehicles (with and without RB logic) during the straight panic brake tests on road surfaces with friction coefficients equal to 1 and 0.7.*

Finally, Figure 3.7 shows the mean between the angular speeds of the left and right front wheels and the mean between the angular speeds of the left and right rear wheels for all the AWD vehicles in the panic brake tests.

As shown in Figure 3.5 and Figure 3.7, the tests with AWD vehicles obtained similar results to those of the FWD vehicles; in fact, even for AWD vehicles, in the case of a road friction coefficient equal to 0.7, front-wheel locking occurs before the rear, thus ensuring yaw stability.

3.3.3.2 Braking in Turn

The "braking in turn" test consists of driving along a constant radius curve at a predetermined speed and then braking with a target deceleration. Table 3.7 shows the related parameters.

Table 3.7. *Parameters of the "braking in turn" test.*

Dimension	Value	Unit
Initial vehicle speed	35	m/s
Final vehicle speed of the test	0	m/s
Constant deceleration in braking	10	m/s²
Turn radius	300	m
Turn direction	right	-
Start time of the braking	5	s
Distance traveled before the start of the maneuver	5	m

In this test, the vehicle, traveling at 126 km/h, turns into a circular trajectory with a radius of 300 m. After 5 s, the braking phase begins with target deceleration equal to 10 m/s². The simulation ends when the vehicle reaches zero speed.

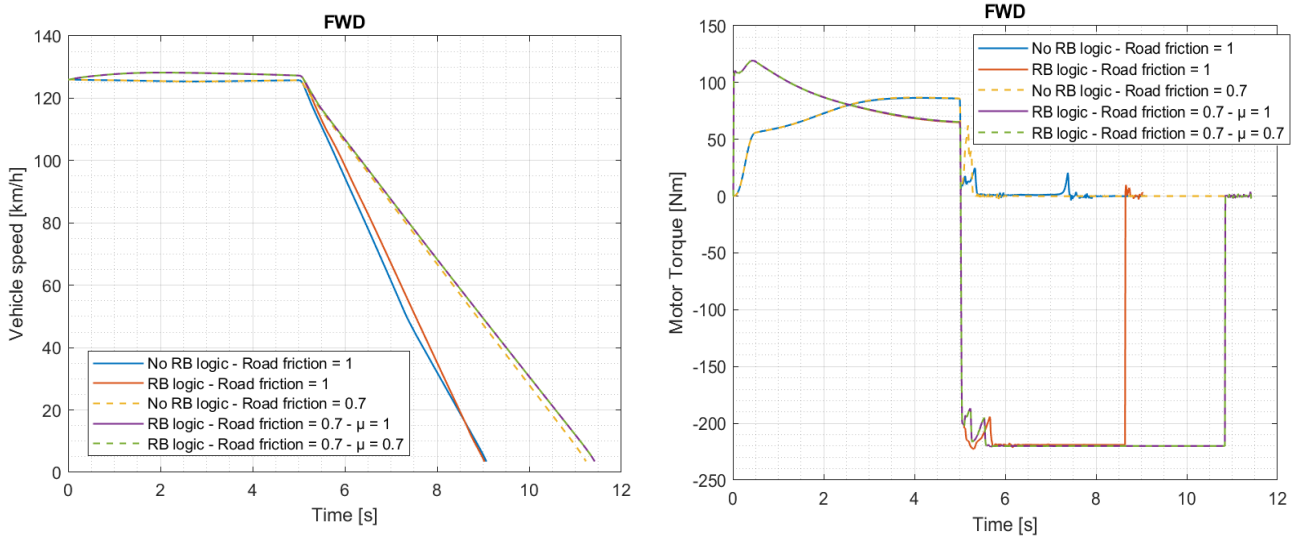

(**a**) (**b**)

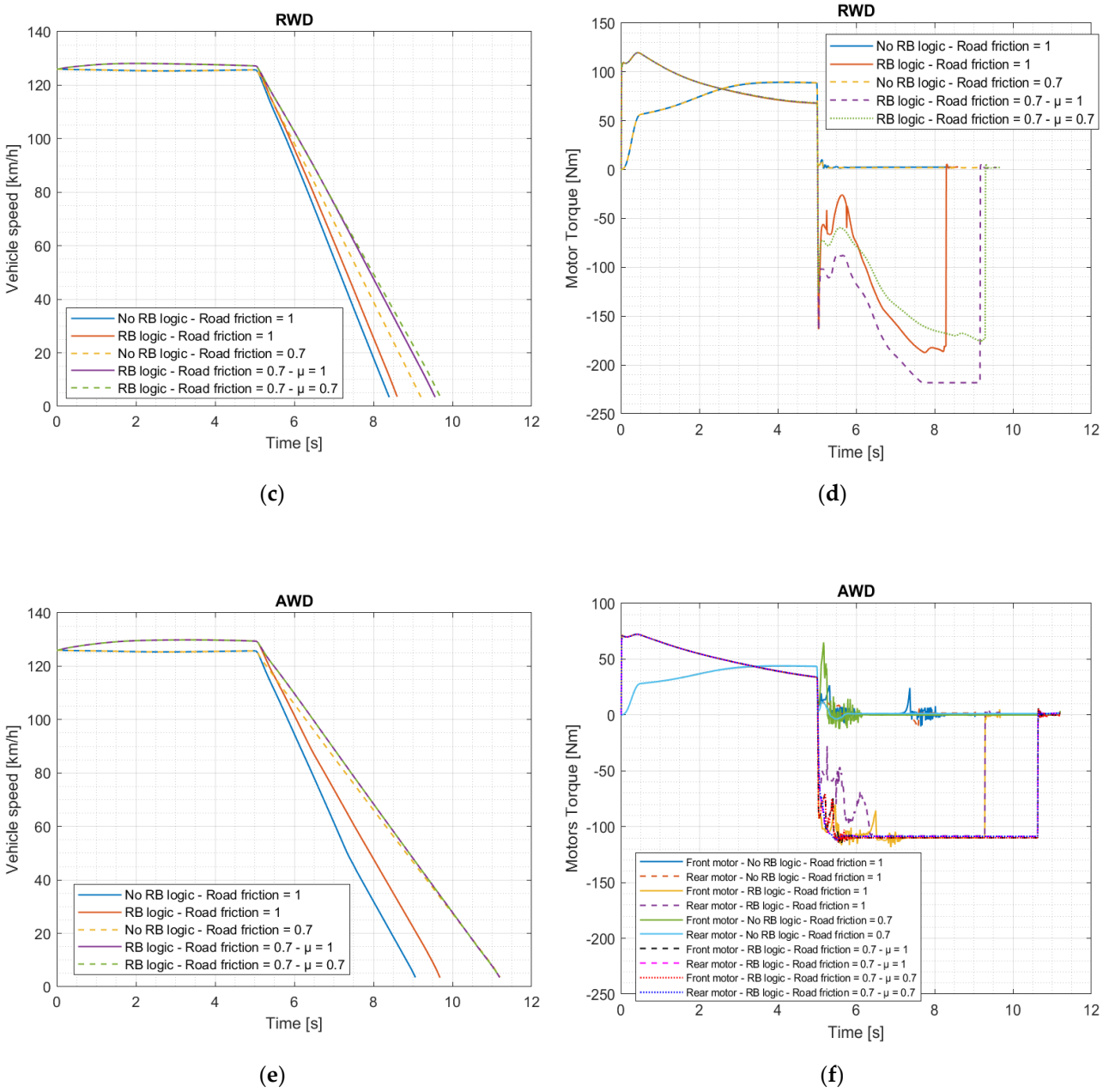

Figure 3.8. *Vehicle speeds and motor torques during the "braking in turn" tests. (**a**) Vehicle speed of FWD vehicles (with and without RB logic) on surfaces with road friction coefficients equal to 1 and 0.7; (**b**) motor torque of FWD vehicles (with and without RB logic) on surfaces with road friction coefficients equal to 1 and 0.7; (**c**) vehicle speed of RWD vehicles (with and without RB logic) on surfaces with road friction coefficients equal to 1 and 0.7; (**d**) motor torque of RWD vehicles (with and without RB logic) on surfaces with road friction coefficients equal to 1 and 0.7; (**e**) vehicle speed of AWD vehicles (with and without RB logic) on surfaces with road friction coefficients equal to 1 and 0.7; (**f**) motor torques of AWD vehicles (with and without RB logic) on surfaces with road friction coefficients equal to 1 and 0.7.*

Figure 3.8 shows the vehicle speeds and motor torques of FWD, RWD, and AWD vehicles for all the "braking in turn" tests performed.

As shown by Figure 3.8, panels (**a**), (**c**), and (**e**), the RB logic leads to a slight deterioration of the braking performance in the "braking in turn" test for the FWD vehicle on the surface with a coefficient of friction equal to 0.7, for the RWD vehicle on both surfaces, and for the AWD vehicle on the surface with a friction coefficient equal to 1. In the remaining cases, the RB logic does not lead to substantial differences in the behaviour of the vehicle when braking in cornering compared to the case of a vehicle without regenerative braking.

Even in these tests, the contribution of the variation of the RB logic μ model coefficient does not lead to substantial variations in the behaviour of the cars.

The RB logic object of this chapter allows for an intensive intervention of the electric motors in generator mode, as can be seen from panels (**b**), (**d**), and (**f**) of Figure 3.8.

Figure 3.9 shows the trajectory of the centre of gravity of the vehicles during the tests. In particular, the coordinates of the centre of gravity of the vehicle are reported along two orthogonal axes, where the initial position of the vehicle at the start of the test corresponds to zero coordinates at the origin of the orthogonal coordinate system.

Figure 3.10 shows the angular speed of each wheel for all the FWD vehicles in the "braking in turn" tests (with road friction coefficients equal to 1 and 0.7): the vehicle without RB logic, the vehicle with RB logic with a μ model coefficient equal to 1, and the vehicle with RB logic with a μ model coefficient equal to 0.7.

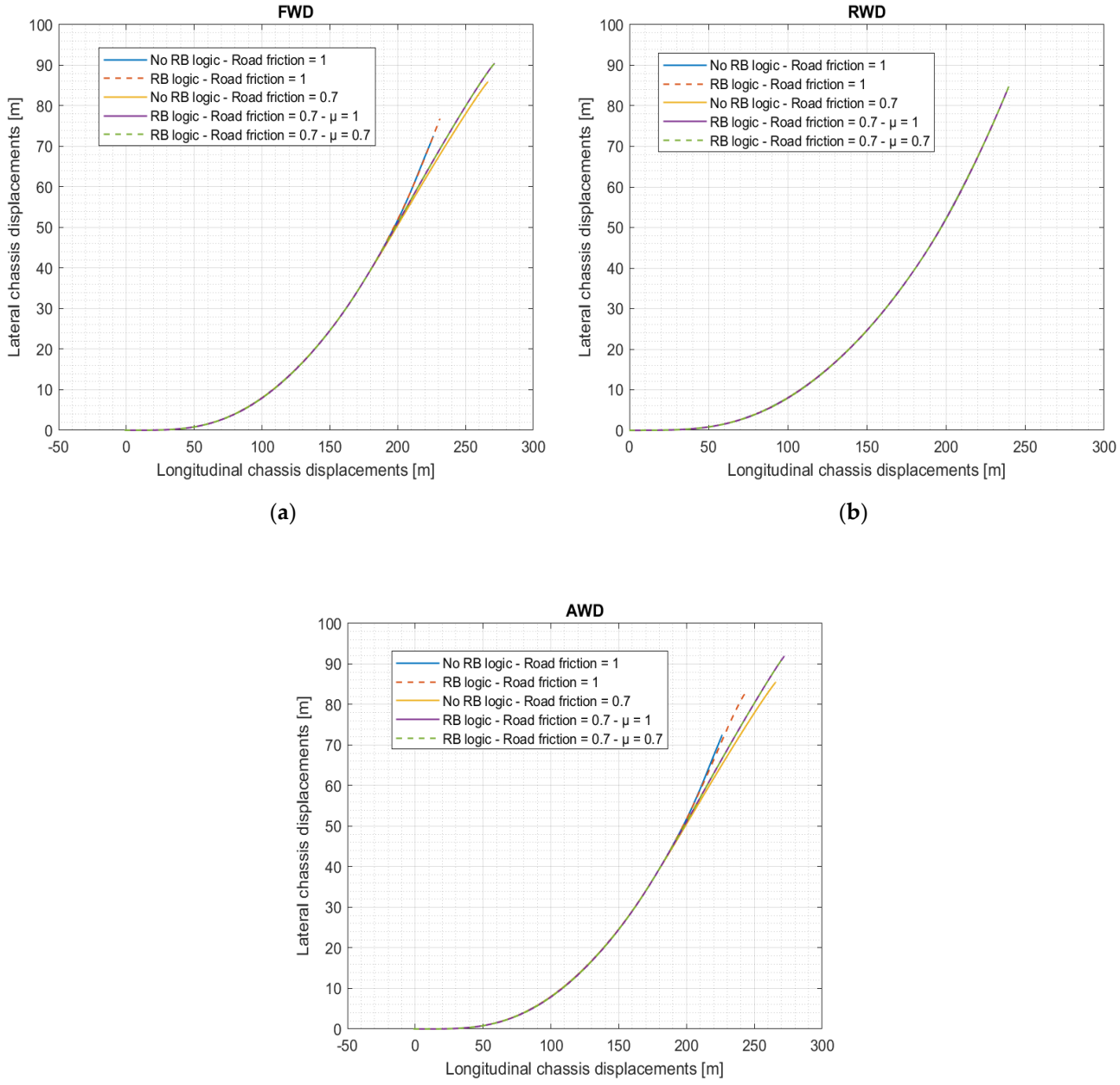

Figure 3.9. *Lateral chassis displacements as a function of longitudinal chassis displacements during "braking in turn" tests. In particular: (**a**) tests with the FWD vehicle; (**b**) tests with the RWD vehicle; (**c**) tests with the AWD vehicle.*

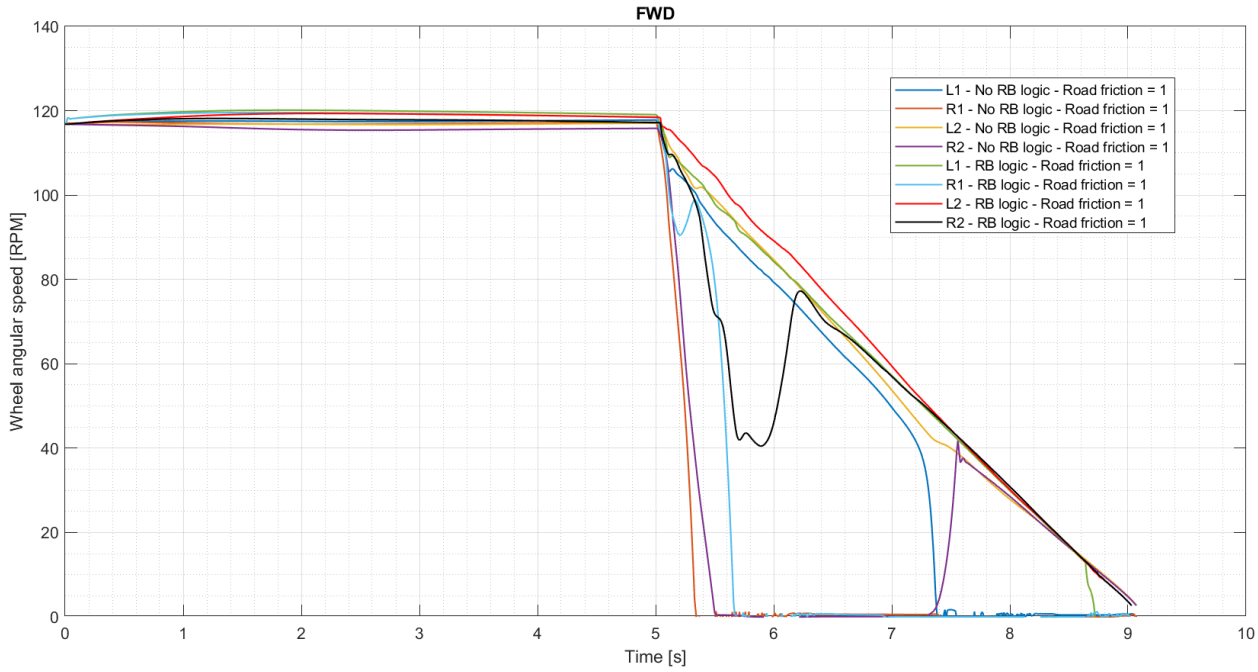

(**a**)

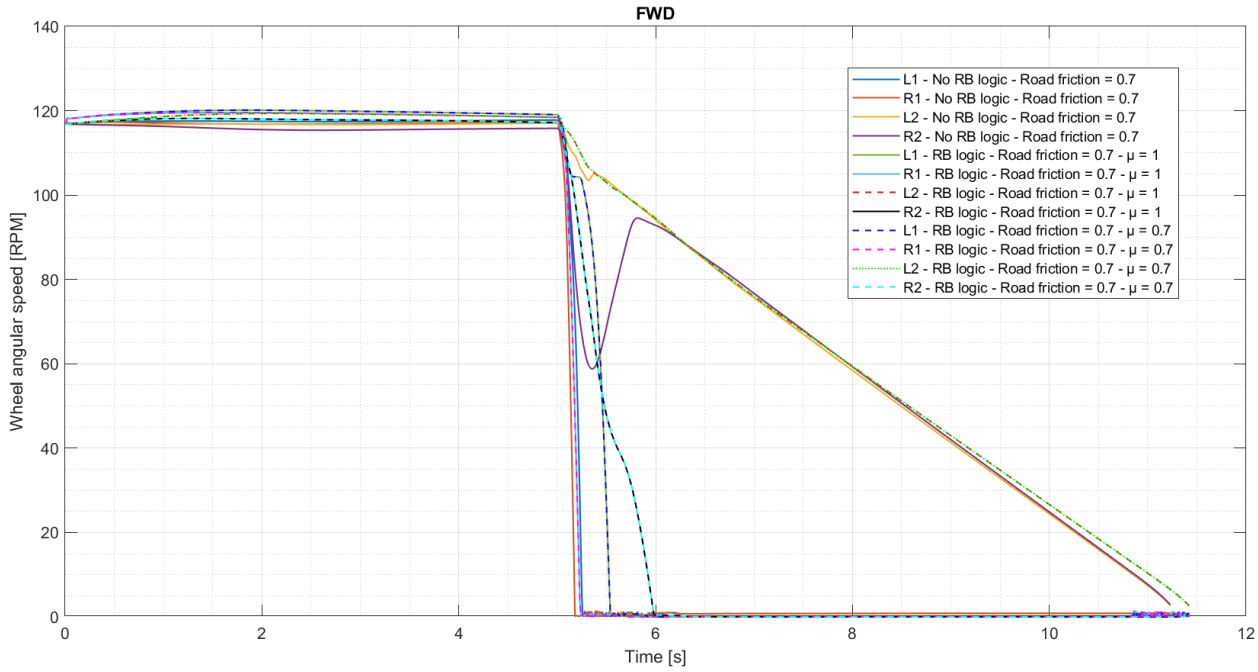

(**b**)

Figure 3.10. *Angular speed of each wheel of the FWD vehicles (with and without RB logic) during "braking in turn" tests, where L1 is the front left (outer) wheel, R1 the front right (inner) wheel, L2 the rear left (outer) wheel, and R2 the rear right (inner) wheel. In particular: (**a**) tests on a road surface with a friction coefficient equal to 1; (**b**) tests on a road surface with a friction coefficient equal to 0.7.*

As can be seen from the graphs in Figure 3.10, in the tests with a road friction coefficient equal to 1, the vehicle without RB logic first locks the front

inner (right) wheel; then the rear inner (right) wheel; and then, finally, the front outer (left) wheel. The rear outer (left) wheel is not locked during the test. The vehicle equipped with RB logic, on the other hand, locks only the front wheels (the front inner wheel first and the front outer only toward the end of the test). For this test, the regenerative braking logic can, therefore, lead to benefits in terms of vehicle stability.

In the tests with a road friction coefficient equal to 0.7, the vehicle without RB logic locks the front wheels and not the rear wheels, while the vehicle equipped with RB logic has the same behaviour with μ model parameters equal to both 1 and 0.7, and it locks the front wheels first and the then the rear inner (right) wheel. On the low road surface friction, the RB logic, therefore, resulted in locking the rear wheel inside the curve as a detrimental effect, and it delayed the locking of the front outer (left) wheel with respect to the front inner (right) one as compared to the case of the vehicle without regenerative braking.

Figure 3.11 shows the angular speed of each wheel for all the RWD vehicles in the "braking in turn" tests.

As can be seen from the graphs in Figure 3.11, in the RWD tests, there is never a complete locking of any wheel, for any vehicle.

Figure 12 instead shows the angular speed of each wheel for all the AWD vehicles in the "braking in turn" tests.

As can be seen from Figure 3.12, in the tests with a road friction coefficient equal to 1, the vehicle without RB logic first locks the front inner (right) wheel; then the rear inner (right) wheel; and then, finally, the front outer (left) wheel. The rear outer (left) wheel is not locked during the test. The vehicle equipped with RB logic, on the other hand, locks only the front wheels (the front inner wheel first and the front outer wheel afterward). For this test, the regenerative braking logic, therefore, led to benefits in terms of AWD vehicle stability, as with the front-wheel drive vehicle.

In the tests with a road friction coefficient equal to 0.7, the vehicle without RB logic locks the front wheels and not the rear wheels, as does the vehicle equipped with RB logic, which has the same behaviour with μ model parameters equal to both 1 and 0.7.

Therefore, on the low road friction surface, the RB logic for this vehicle does not lead to substantial changes in the behaviour of the vehicle itself.

Finally, for "braking in turn" tests it is also interesting to show the yaw angle of the vehicles during the test (Figure 3.13).

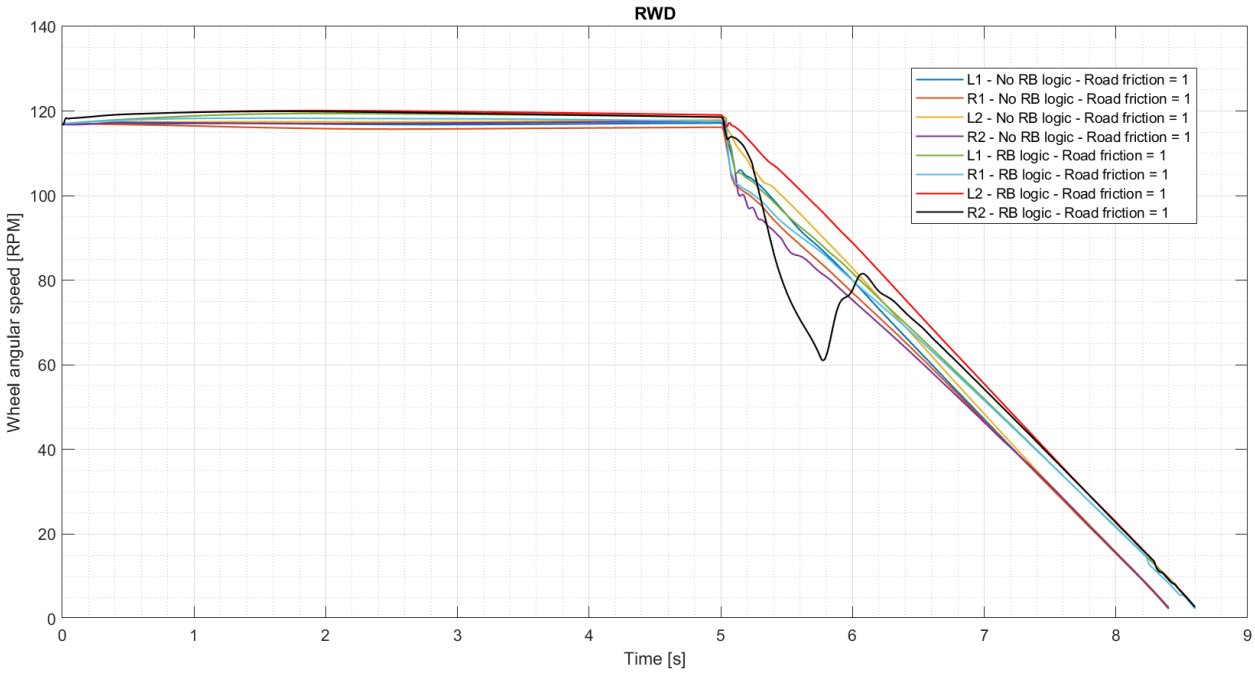

(**a**)

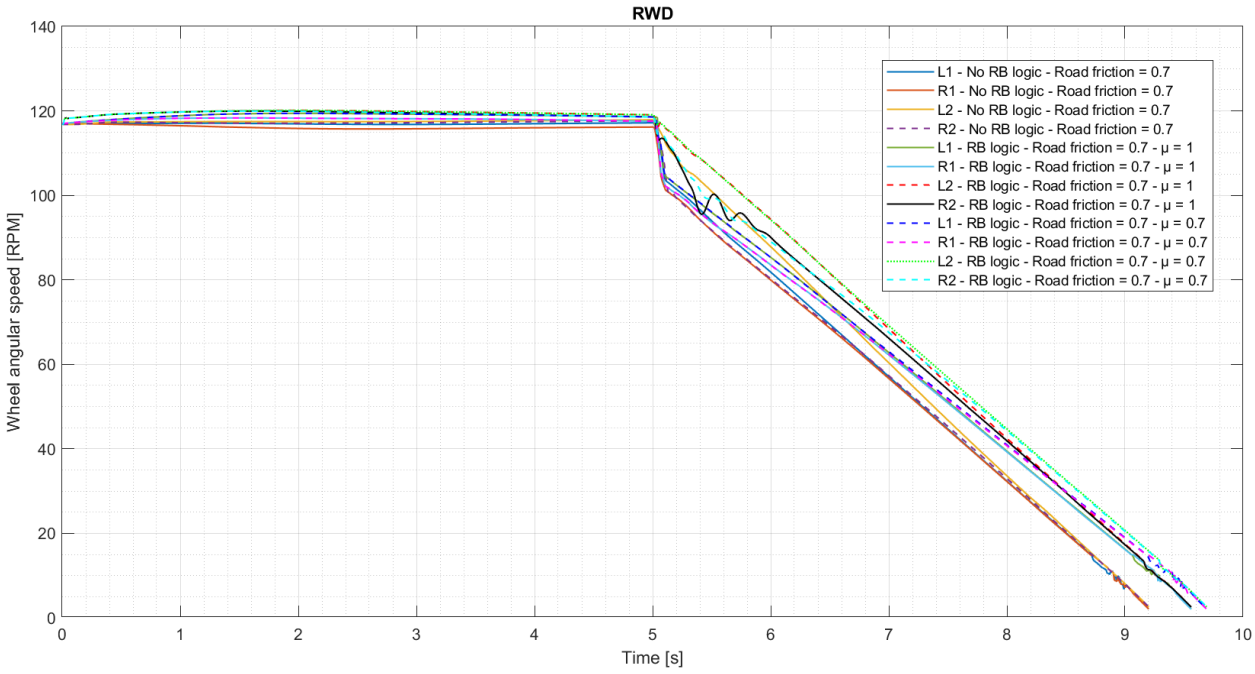

(**b**)

Figure 3.11. *Angular speed of each wheel of the RWD vehicles (with and without RB logic) during the "braking in turn" tests, where L1 is the front left (outer) wheel, R1 the front right (inner) wheel, L2 the rear left (outer) wheel, and R2 the rear right (inner) wheel. In particular: (**a**) tests on a road surface with a friction coefficient equal to 1; (**b**) tests on a road surface with a friction coefficient equal to 0.7.*

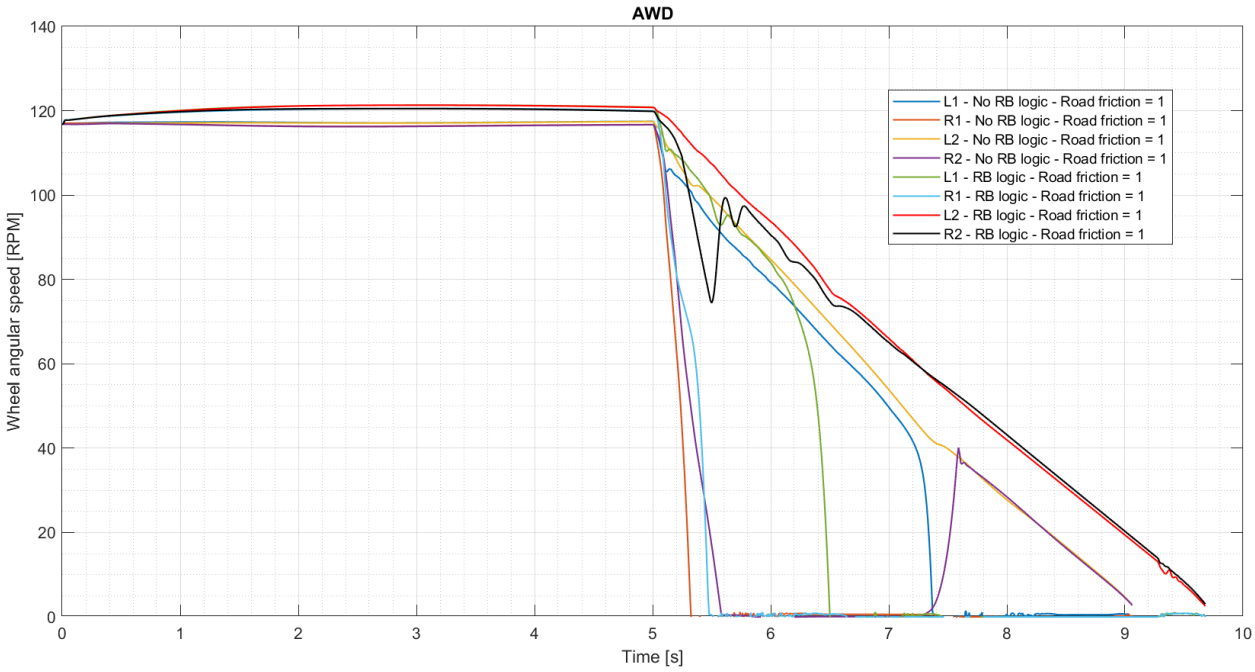

(**a**)

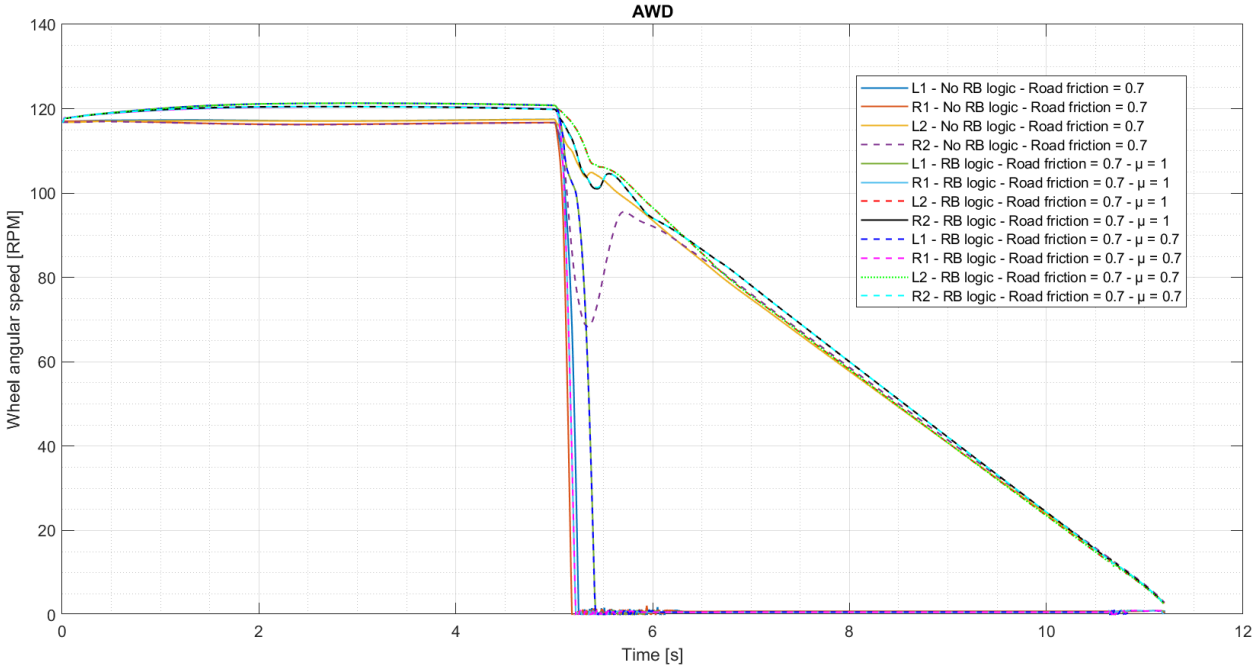

(**b**)

Figure 3.12. *Angular speed of each wheel of the AWD vehicles (with and without RB logic) during the "braking in turn" tests, where L1 is the front left (outer) wheel, R1 the front right (inner) wheel, L2 the rear left (outer) wheel, and R2 the rear right (inner) wheel. In particular: (**a**) tests on a road surface with a friction coefficient equal to 1; (**b**) tests on a road surface with a friction coefficient equal to 0.7.*

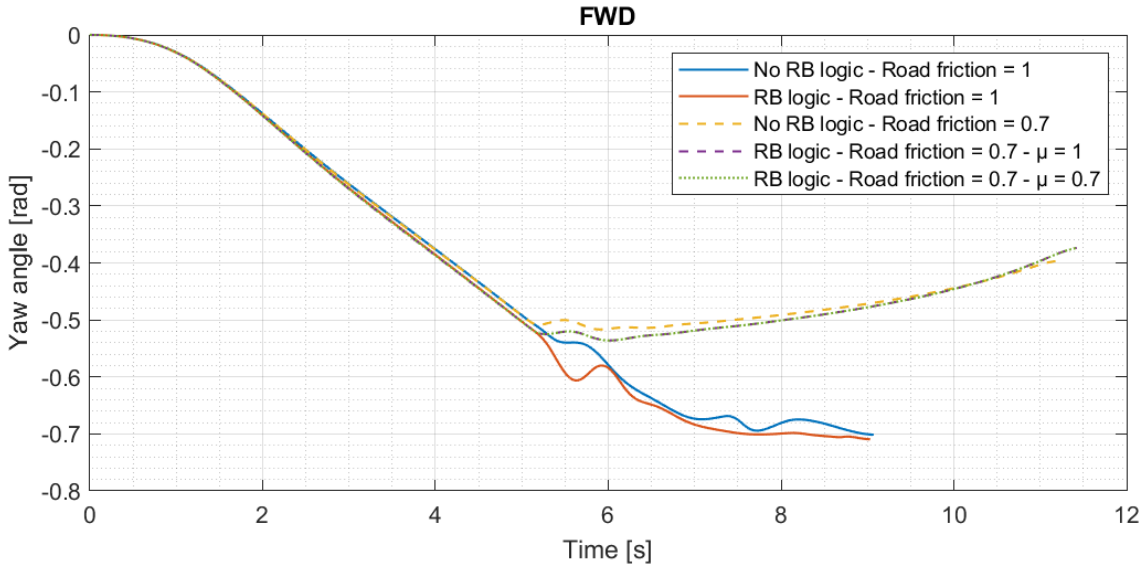
FWD
No RB logic - Road friction = 1
RB logic - Road friction = 1
No RB logic - Road friction = 0.7
RB logic - Road friction = 0.7 - μ = 1
RB logic - Road friction = 0.7 - μ = 0.7
Yaw angle [rad]
Time [s]
0
-0.1
-0.2
-0.3
-0.4
-0.5
-0.6
-0.7
-0.8
0
2
4
6
8
10
12

(**a**)

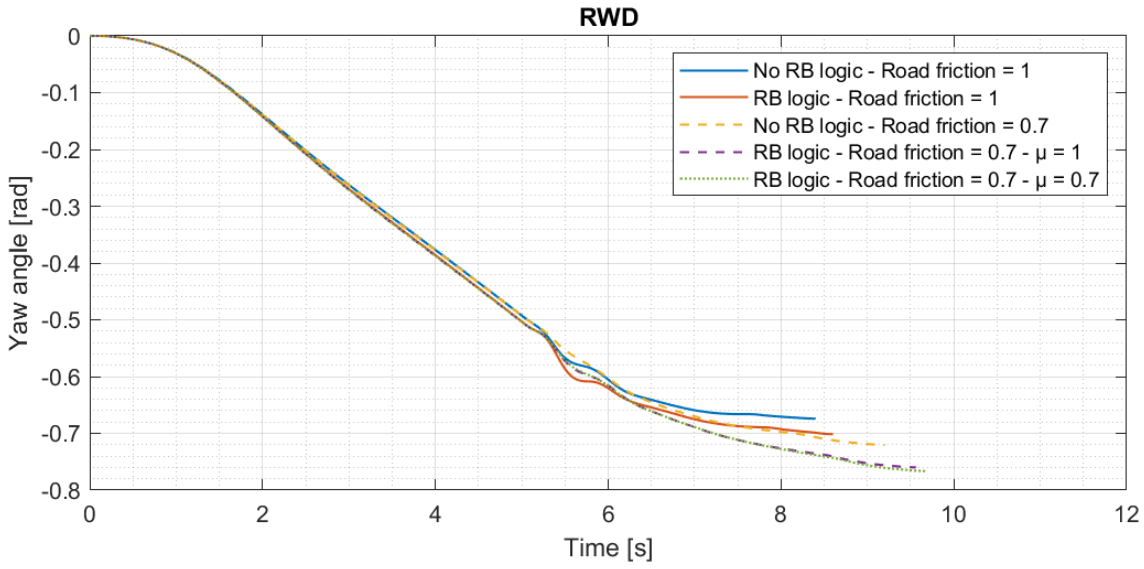
RWD
No RB logic - Road friction = 1
RB logic - Road friction = 1
No RB logic - Road friction = 0.7
RB logic - Road friction = 0.7 - μ = 1
RB logic - Road friction = 0.7 - μ = 0.7
Yaw angle [rad]
Time [s]
0
-0.1
-0.2
-0.3
-0.4
-0.5
-0.6
-0.7
-0.8
0
2
4
6
8
10
12

(**b**)

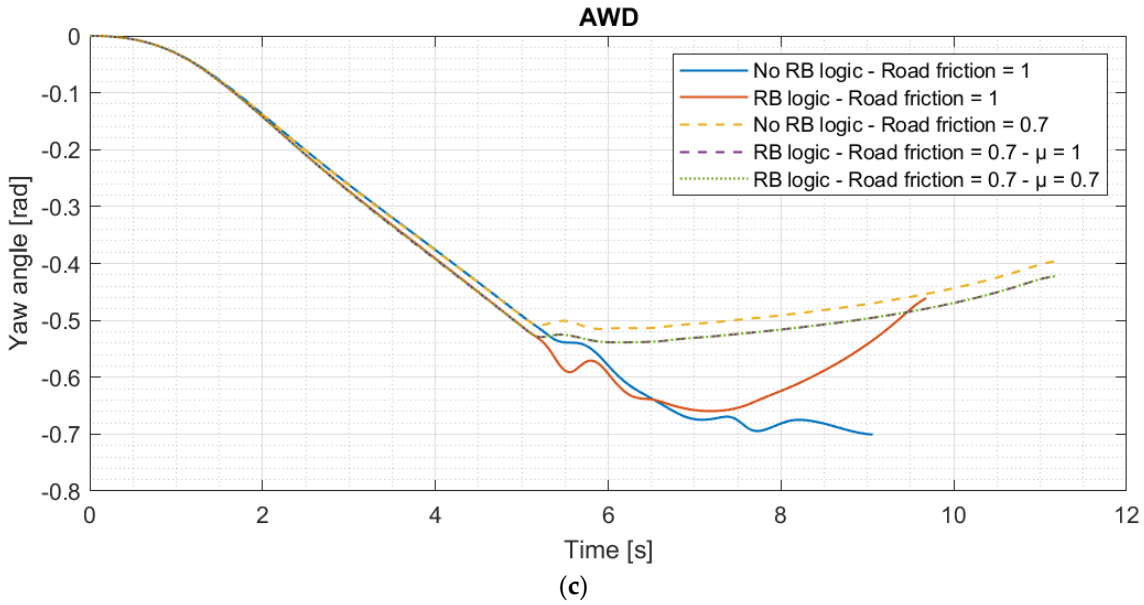

(c)

Figure 3.13. *Chassis yaw angle in function to the time elapsed since the start of the "braking in turn" tests. In particular: (**a**) tests with the FWD vehicle; (**b**) tests with the RWD vehicle; (**c**) tests with the AWD vehicle.*

As can be seen from Figure 3.13, panels (a) and (b), the FWD and RWD vehicles, during the test, have a yaw angle with a similar trend as regards vehicle without regenerative braking logic and vehicle equipped with RB logic, both on road surfaces with a high friction coefficient (1) and low coefficient of friction (0.7). The same applies to the tests with a coefficient of friction equal to 0.7 for the AWD vehicle (Figure 3.13, panel (c)). For the AWD vehicle, on the other hand, a worsening given by the RB logic can be observed for the case with unit friction coefficient (Figure 3.13, panel (c)), where the yaw angle, after about 7 seconds, begins to decrease in module for the vehicle equipped with RB logic, while it has a tendentially increasing behaviour in module for the whole test for the same vehicle without regenerative braking logic.

3.3.4 Energy Consumption and Recovery Estimation

This section uses the test model described in paper [10] to estimate the energy savings associated with the adoption of the regenerative braking logic (RB logic, [13]), covered by this chapter of thesis, in the three vehicles (FWD, RWD, and AWD). In particular, the RB logic is integrated into the TEST model [10], and through the graphic user interface of the model, it is possible to activate this logic or keep it deactivated and simulate the braking phase as described in paper [10], which is considered a classic, traditional, or standard regenerative braking logic,

the simplest adopted on the market. The integration of the RB logic [13] into the TEST model [10] will be detailed in Section 3.5.

The energy consumption of the three vehicles (FWD, RWD, and AWD) equipped with RB logic, without brake recovery, and equipped with a classic and simple regenerative braking logic, commonly adopted on electric vehicles on the market, which will be explained later, has been estimated on the basis of two different standard driving cycles (WLTC and US06), keeping in mind that energy consumption is strongly influenced by the driving cycle considered [24]. Vehicles without regenerative recovery and vehicles equipped with classic logic are used to estimate the energy savings guaranteed by the RB logic.

3.3.4.1 Vehicle Models

The vehicles subject to simulations using the TEST model [10] are the same (FWD, RWD, and AWD) as those previously analysed through the tests with VI-CarRealTime, i.e., those described in Section "3.3.1 Reference Vehicles" with characteristics shown in tables from Table 3.1 to Table 3.4. The AWD vehicle features a 50% distribution of the drive torque between front and rear in acceleration and, in the case of regenerative recovery with classic logic, in braking as well.

As already mentioned, three simulations are carried out for each vehicle type, one with RB logic, one without braking energy recovery, and one with a classic regenerative braking logic according to [10].

In the case of classic regenerative braking, maximum torque is considered for regenerative braking, which has a trend that increases linearly as a function of the time elapsed from the beginning of braking and then reaches a predefined maximum value (absolute value only). This is the approach typically adopted in electric vehicles on the market. This approach is also the one adopted in the waste collection vehicle in the prototype state used for the validation of the TEST model in paper [10] and in the Section 2.4.1 of this thesis. The values of the maximum regenerative braking trend (Figure 3.14), i.e., the slope (22.5 Nm/s) of the increasing linear section and the constant plateau value (50 Nm), are also taken from the waste collection vehicle considered in paper [10] (see Section 2.4.1 of this Ph.D. thesis). These values are used for the simulations of the FWD and RWD vehicles, while for the AWD vehicle, such values are equally split between the two motor units (11.25 Nm/s and 25 Nm) so that the total contribution of the maximum regenerative braking is the same as the other vehicles.

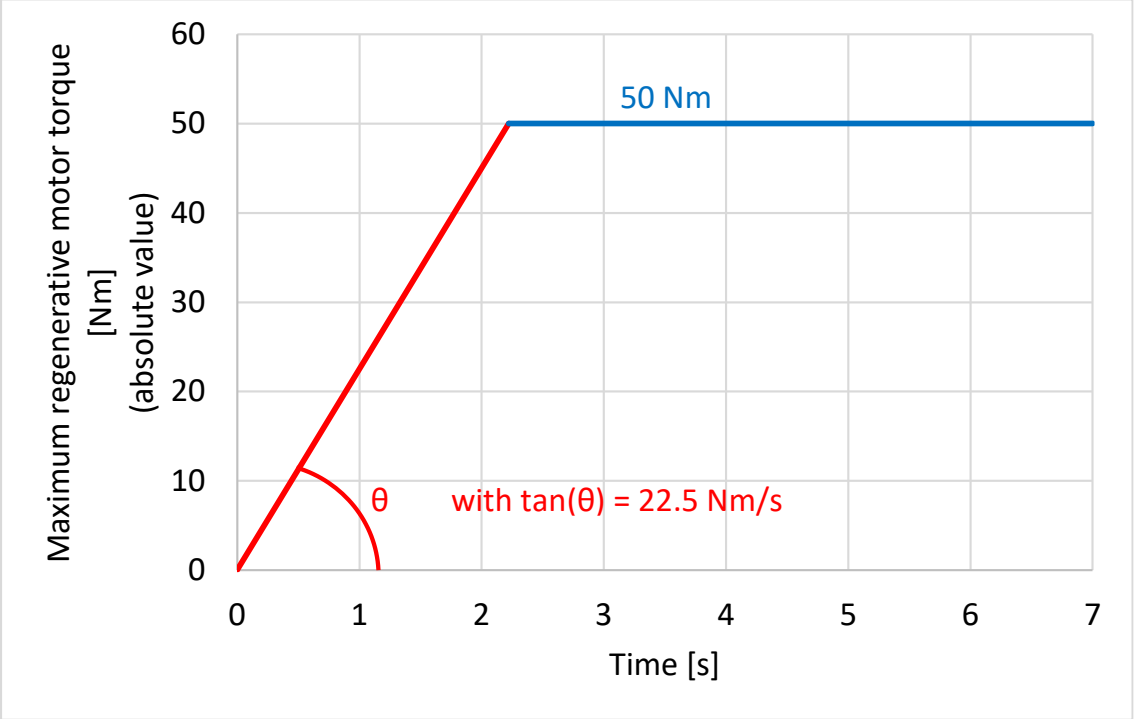

***Figure 3.14**. Maximum regenerative motor torque trend for the classic regenerative braking logic for the FWD and RWD vehicles.*

For both regenerative braking logics, a minimum speed of 15 km/h is set for the activation of the logic itself. Below this speed, there is no energy recovery during braking.

The simulations were carried out starting with a battery SOC equal to 70% so as to exploit the central range of SOC in such a way that only limitations due to the maximum current and maximum power (in absolute value, positive and negative, in input and output from the battery pack) come into play within this range, therefore avoiding the more stringent limitations related to the extremes of the SOC range.

3.3.4.2 WLTP Procedure

First, consumption and energy recovery are estimated on the regulated cycle known as WLTC (Worldwide Harmonized Light-Duty Vehicles Test Cycle), as described in the WLTP procedure (Worldwide Harmonized Light-Duty Vehicles Test Procedure) [38].

The standard in [38] differentiates various classes for the WLTC depending on the power/weight ratio. The vehicles examined have a maximum power of 87 kW and a weight of 1548.4 kg with a power/weight ratio of approximately 56.2 W/kg; therefore, they fall within class 3. Furthermore, the

maximum speed of these vehicles is higher than 120 km/h; therefore, they fall into subclass 3b. The class 3b WLTC is composed of the phases "Low$_3$", "Medium$_{3\text{-}2}$", "High$_{3\text{-}2}$", and "Extra High$_3$", as defined by [38].

The tests with the TEST model [10] were then carried out on the class 3b WLTC cycle, which has a duration of 1800 s on a distance of about 23.3 km.

Figure 3.15 reports some results of the simulations carried out for the FWD vehicles.

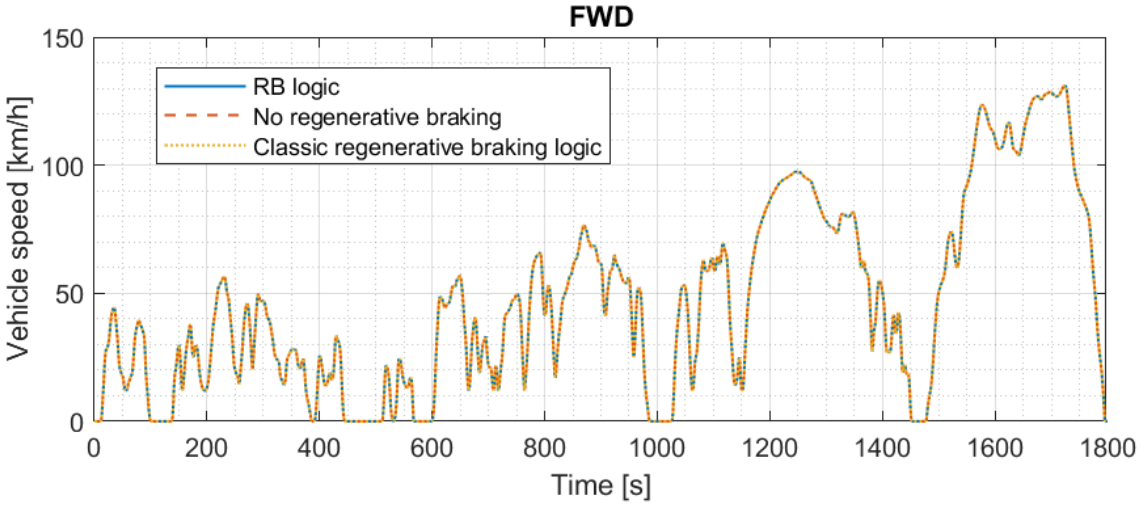

(**a**)

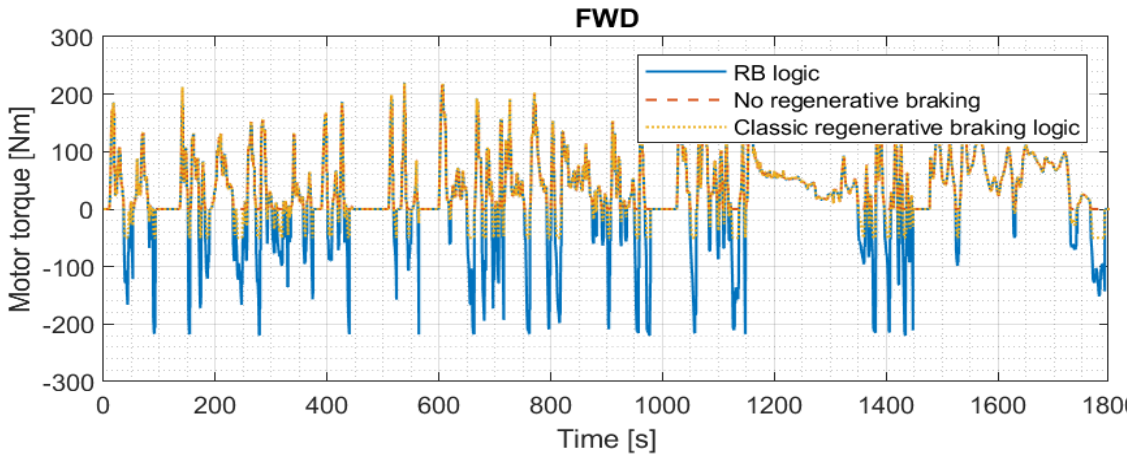

(**b**)

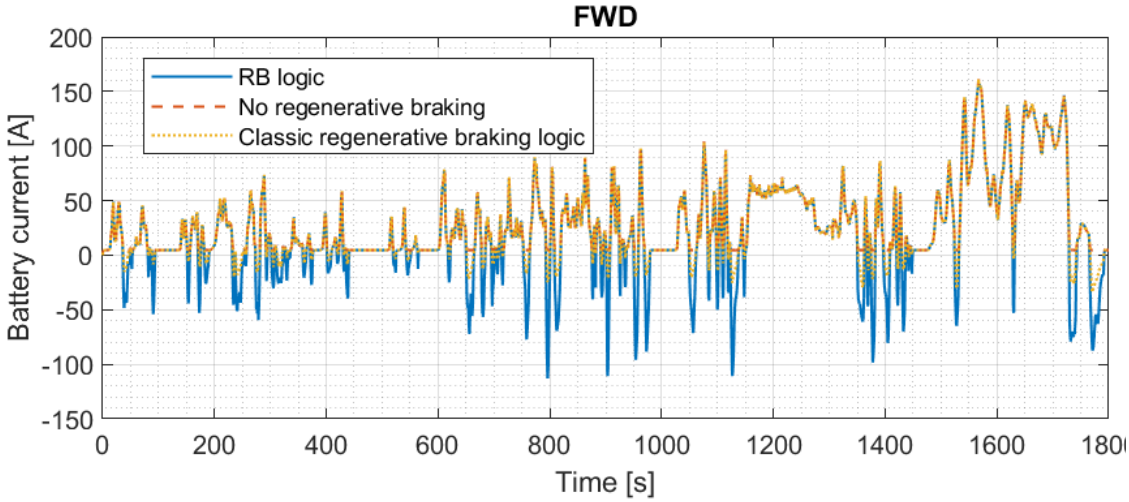

(**c**)

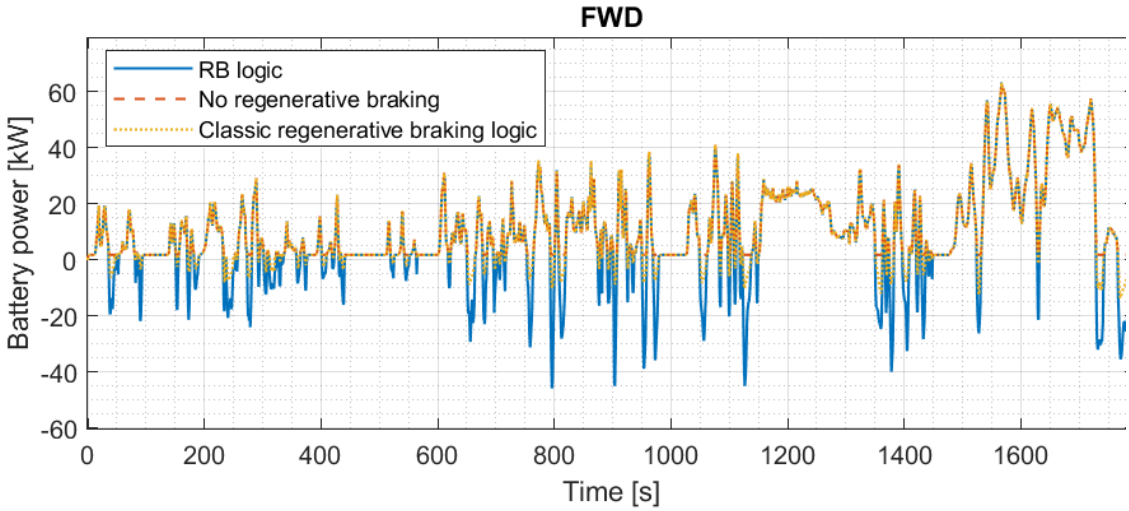

(**d**)

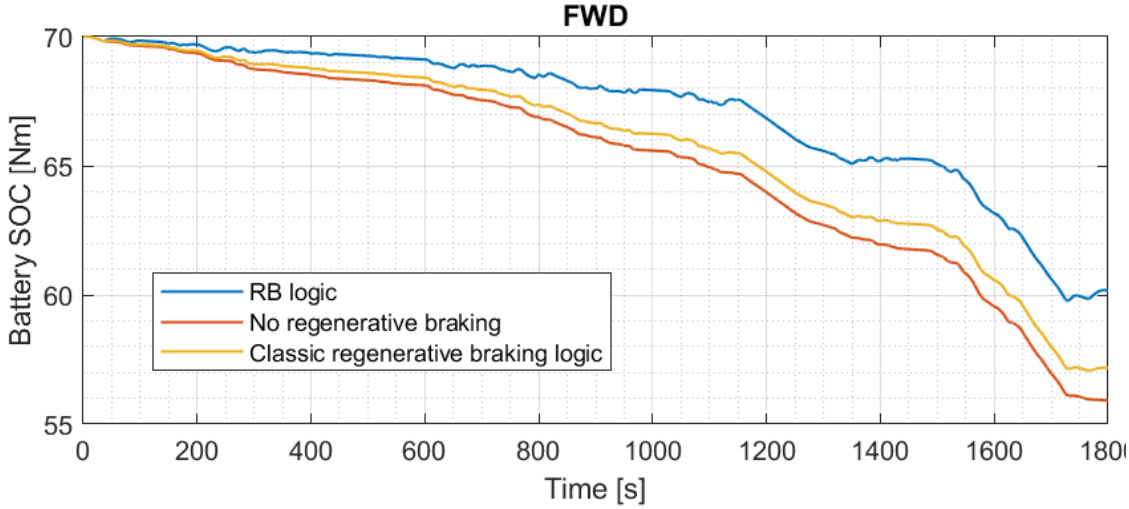

(**e**)

Figure 3.15. *Results of FWD vehicle simulations on the class 3b WLTC. (**a**) Vehicle speed; (**b**) motor torque; (**c**) battery current; (**d**) output (positive) and input (negative) power to the battery pack; (**e**) battery SOC.*

In panels (**a**), (**b**) and (**d**) of Figure 3.15, it can be seen how the regenerative braking of the RB logic is decidedly more intensive than that of the vehicle equipped with classic logic. This results in a higher SOC at the end of the driving cycle, as can be seen in panel (**e**) of Figure 3.15.

FWD vehicles, as well as RWD and AWD vehicles, manage to faithfully follow the class 3b WLTC. Graph (**a**) of Figure 3.15 is, therefore, basically the same for all vehicle types.

Figure 3.16 reports some results of the simulations carried out for the RWD vehicles.

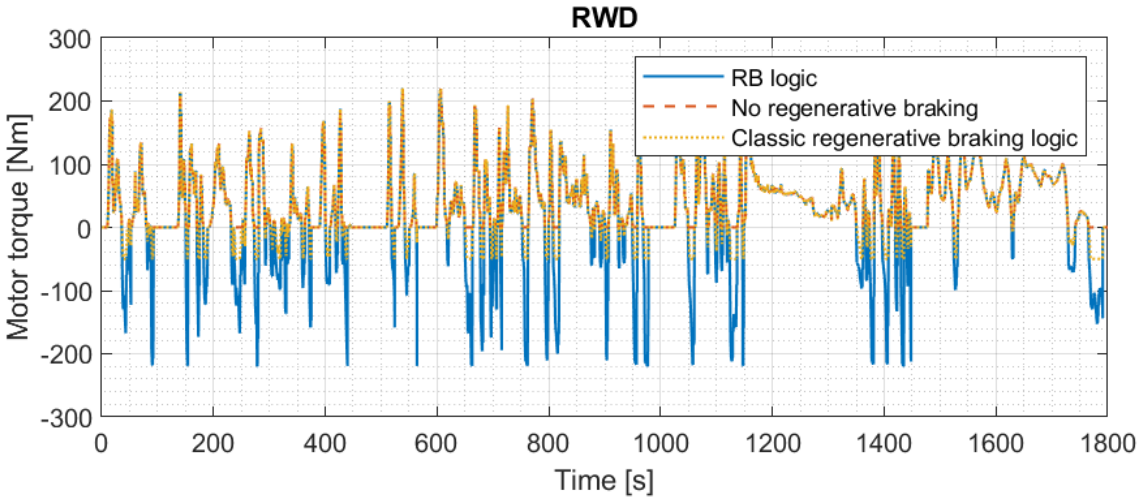

(**a**)

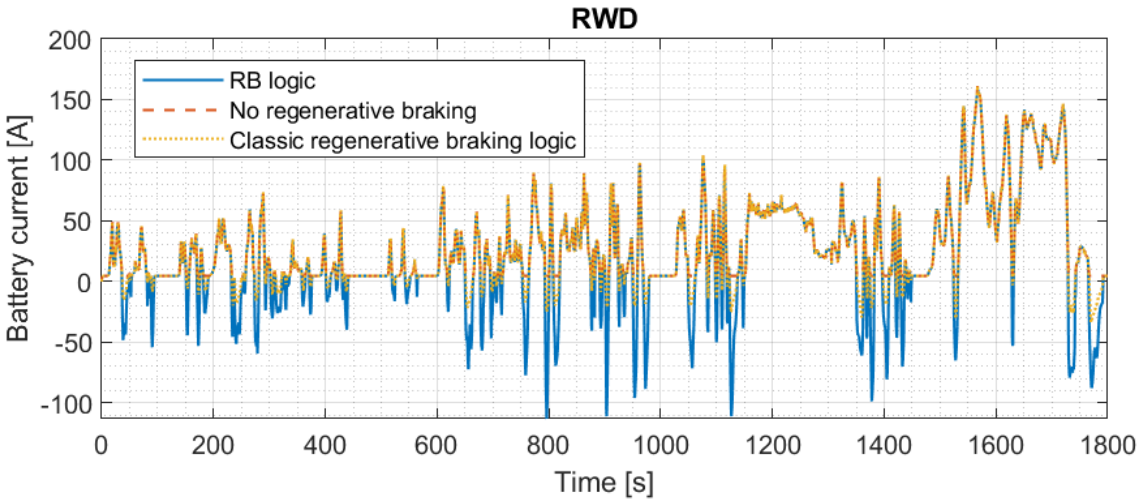

(**b**)

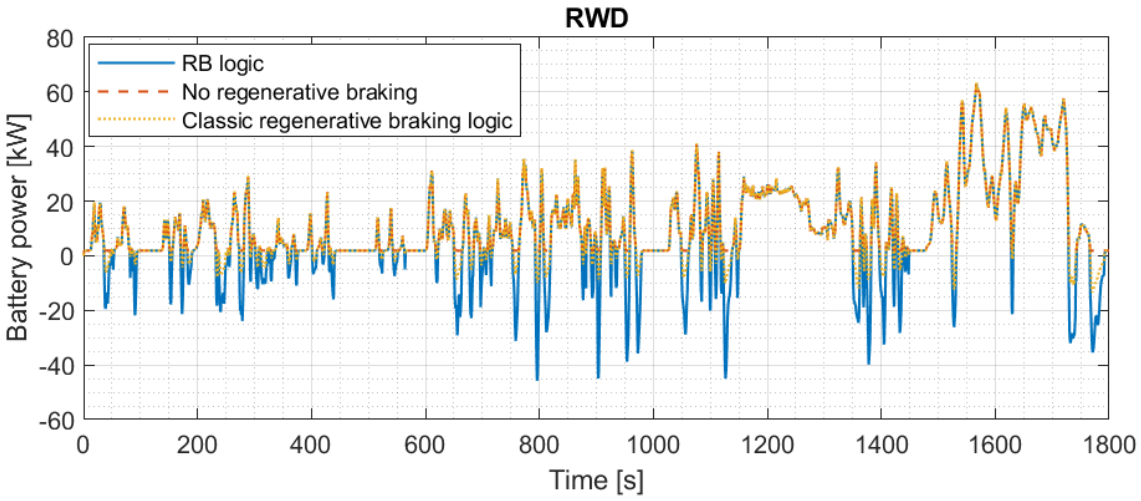

(**c**)

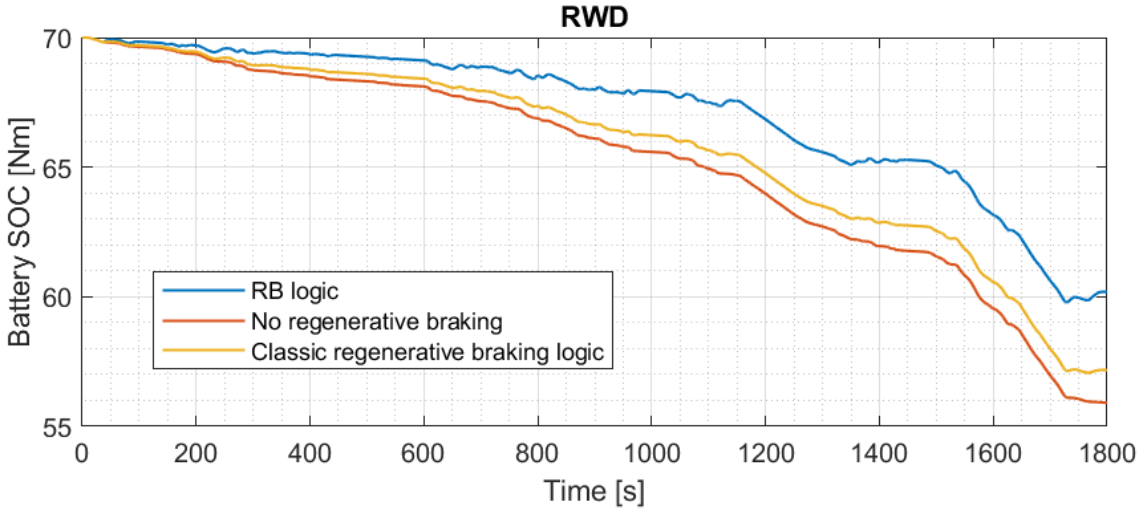

(**d**)

Figure 3.16. *Results of the RWD vehicle simulations on the class 3b WLTC. (**a**) Motor torque; (**b**) battery current; (**c**) output (positive) and input (negative) power to the battery pack; (**d**) battery SOC.*

Panels (**a**), (**b**) and (**c**) of Figure 3.16 show how the regenerative braking of the RB logic is decidedly more efficient for the RWD vehicle as well. This again improves the average SOC during the driving cycle, as shown in panel (d) of Figure 3.16.

Figure 3.17 reports some results of the simulations carried out for the AWD vehicles.

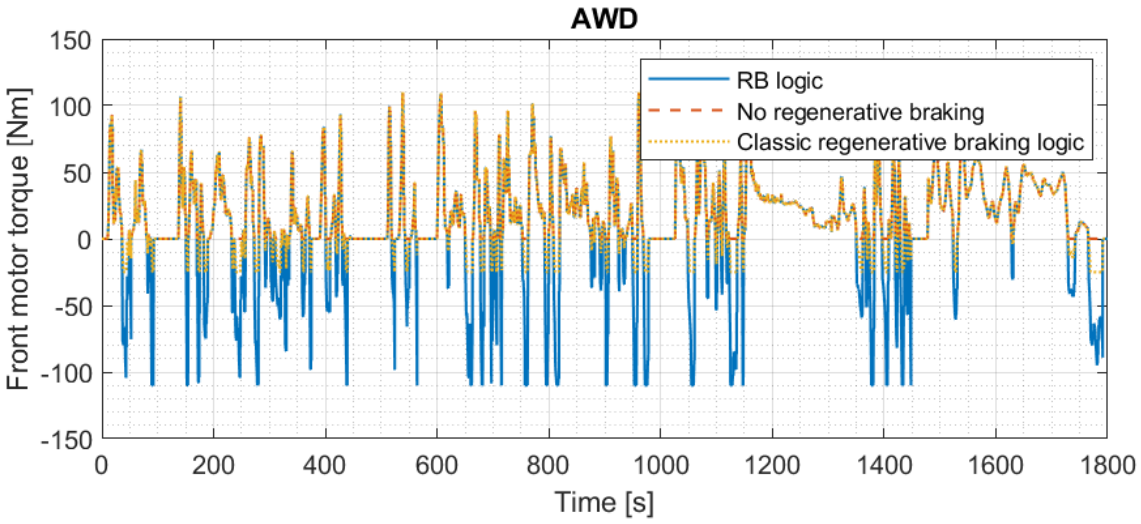
AWD
RB logic
No regenerative braking
Classic regenerative braking logic
Front motor torque [Nm]
Time [s]

(**a**)

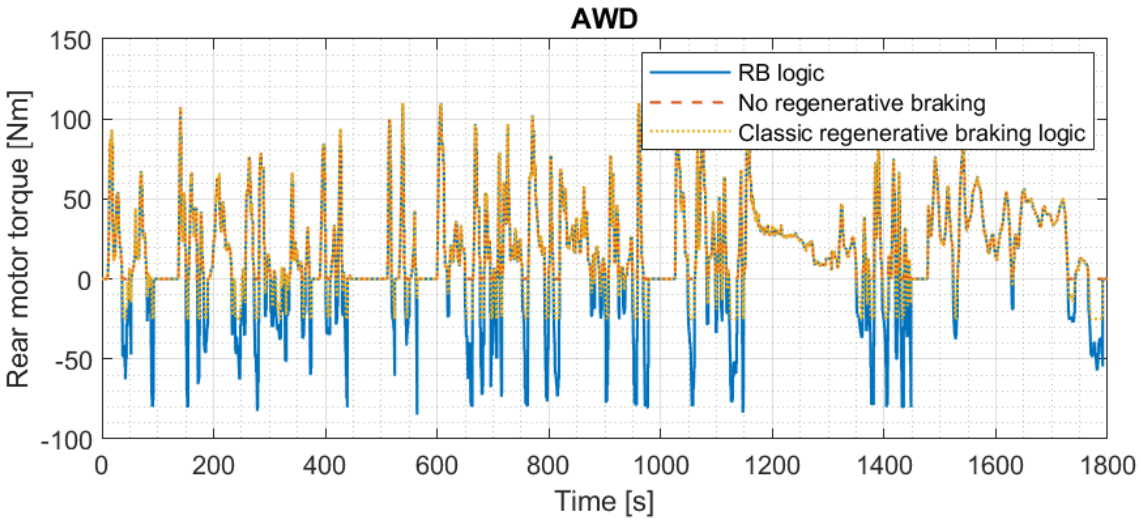
AWD
RB logic
No regenerative braking
Classic regenerative braking logic
Rear motor torque [Nm]
Time [s]

(**b**)

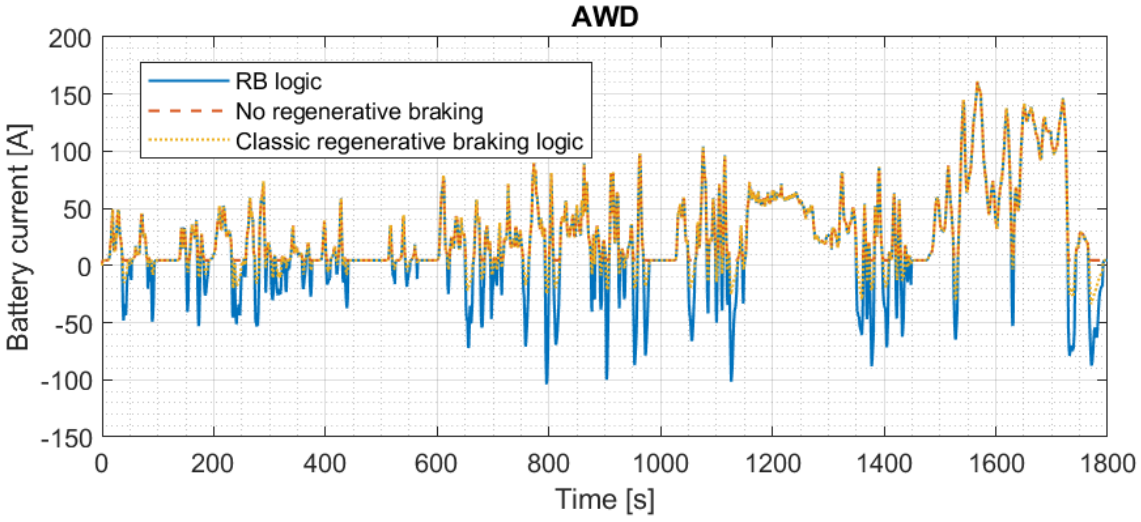
AWD
RB logic
No regenerative braking
Classic regenerative braking logic
Battery current [A]
Time [s]

(**c**)

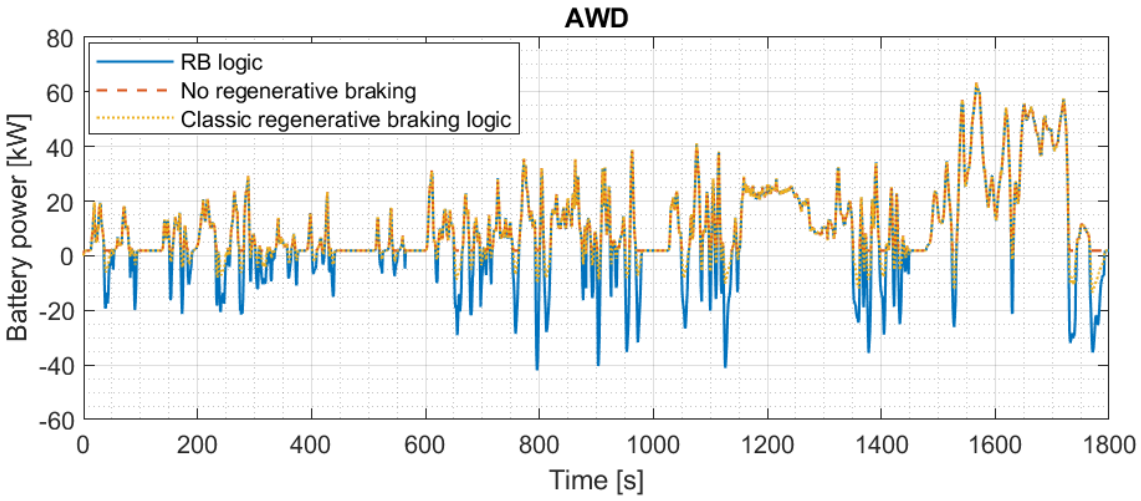

(**d**)

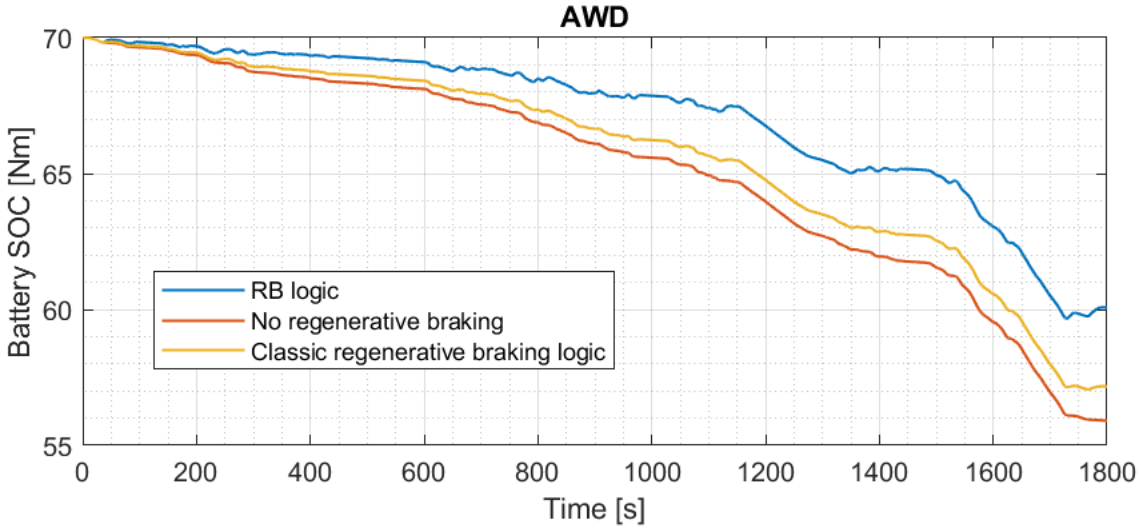

(**e**)

Figure 3.17. *Results of simulations with AWD vehicles on the class 3b WLTC. In particular: (a) front motor torque; (b) rear motor torque; (c) battery current; (d) output (positive) and input (negative) power to the battery pack; (e) battery SOC.*

The same considerations made for FWD and RWD vehicles can also be made for the simulations of AWD vehicles, i.e., those from panels from (**a**) to (**d**) of Figure 3.17; it can be seen how the regenerative braking of the RB logic is an improvement over the traditional logic. This results in a lower decrease in SOC during the driving cycle, as can be seen in graph (e) of Figure 3.17.

Table 3.8 reports energy consumption and SOC on the class 3b WLTP cycle, for the FWD, RWD, and AWD vehicles, equipped with RB logic, classic regenerative braking logic, and without braking recovery. The final SOC of the

simulation on the single cycle is also reported, remembering that the initial SOC was set to equal 70%. The specific energy consumption is also reported on the basis of the distance travelled by the vehicles during the simulation.

Table 3.8. *Consumption in the class 3b WLTC.*

Type of Vehicle	Regenerative Braking Logic	Final SOC (%)	SOC Consumption (%)	Energy Consumption (kWh)	Specific Energy Consumption (kWh/(100 km))
FWD	RB logic	60.18	9.82	4.12	17.73
	No brake recovery	55.91	14.09	5.92	25.43
	Classic logic	57.17	12.83	5.39	23.16
RWD	RB logic	60.19	9.81	4.12	17.72
	No brake recovery	55.91	14.09	5.92	25.43
	Classic logic	57.17	12.83	5.39	23.16
AWD	RB logic	60.07	9.93	4.17	17.92
	No brake recovery	55.91	14.09	5.92	25.44
	Classic logic	57.17	12.83	5.39	23.17

3.3.4.3 US06 Cycle

Consumption and energy recovery are also estimated on the SFTP-US06-regulated cycle, described in the EPA Supplemental Federal Test Procedure (SFTP). We also chose to carry out simulations on the US06 cycle to obtain results on a cycle with more intense acceleration and deceleration levels than the relatively mild ones of the WLTP. The simulations were performed again by means of the TEST model [10].

The US06 cycle has a duration of 600 s, and the vehicle travels about 12.9 km on this cycle.

Figures from Figure 3.18 to Figure 3.20 graphically report some results of the simulations carried out for the FWD, RWD, and AWD vehicles on the US06 cycle.

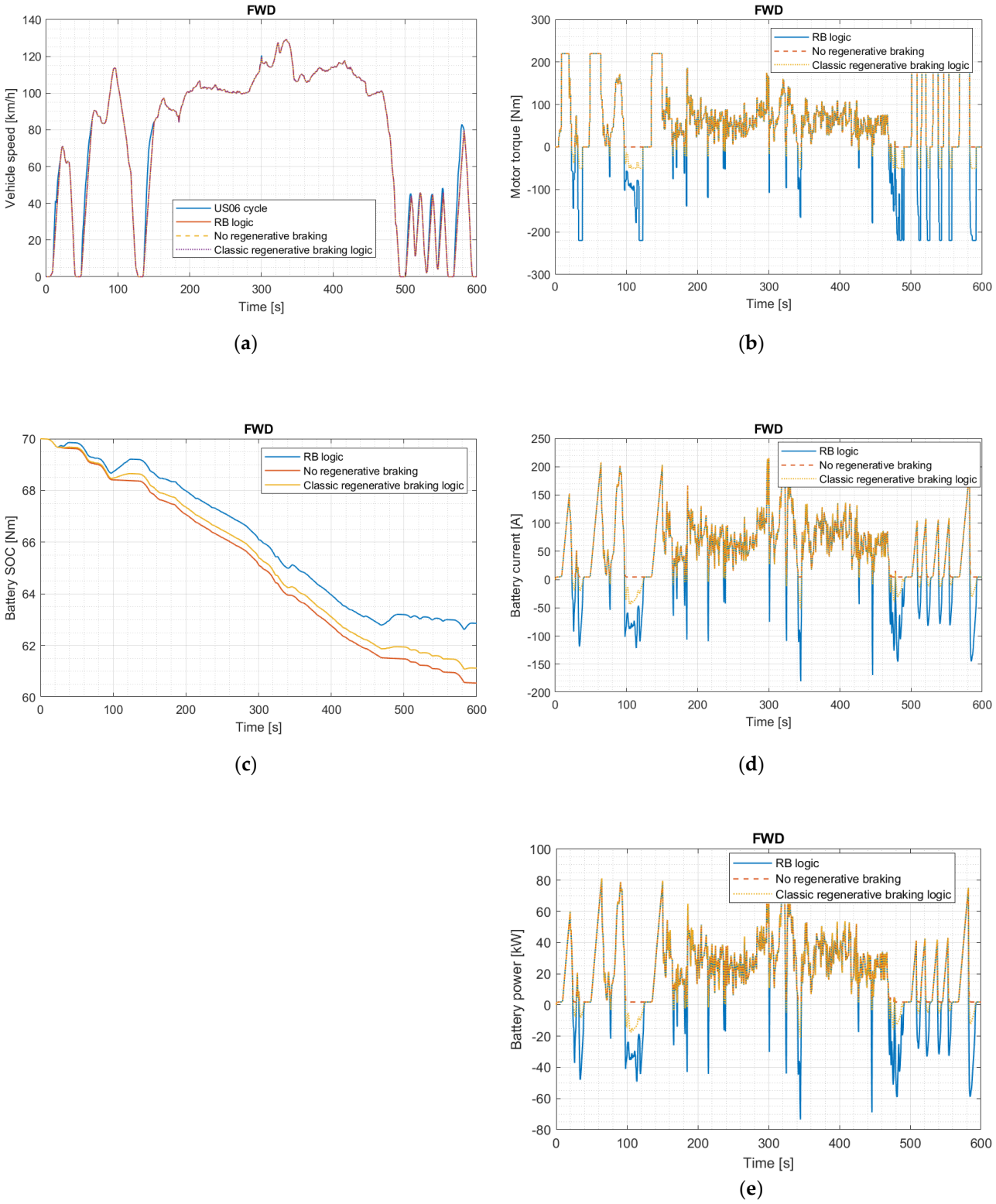

Figure 3.18. *Results of simulations with FWD vehicles on the US06 cycle. In particular: (**a**) vehicle speed; (**b**) motor torque; (**c**) battery SOC; (**d**) battery current; (**e**) output (positive) and input (negative) power to the battery pack.*

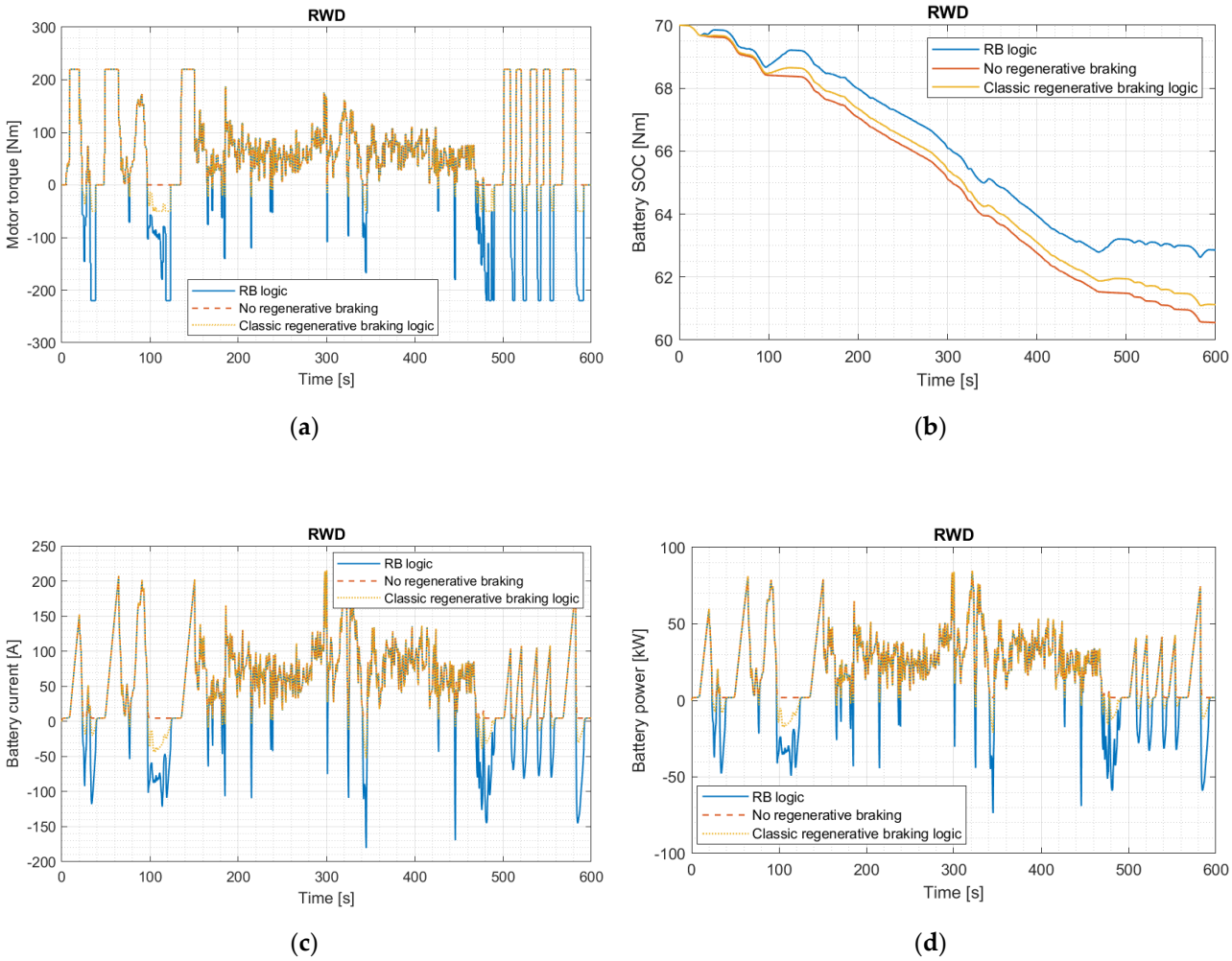

Figure 3.19. *Results of simulations with RWD vehicles on the US06 cycle. In particular: (**a**) motor torque; (**b**) output (positive) and input (negative) power to the battery pack; (**c**) battery current; (**d**) battery SOC.*

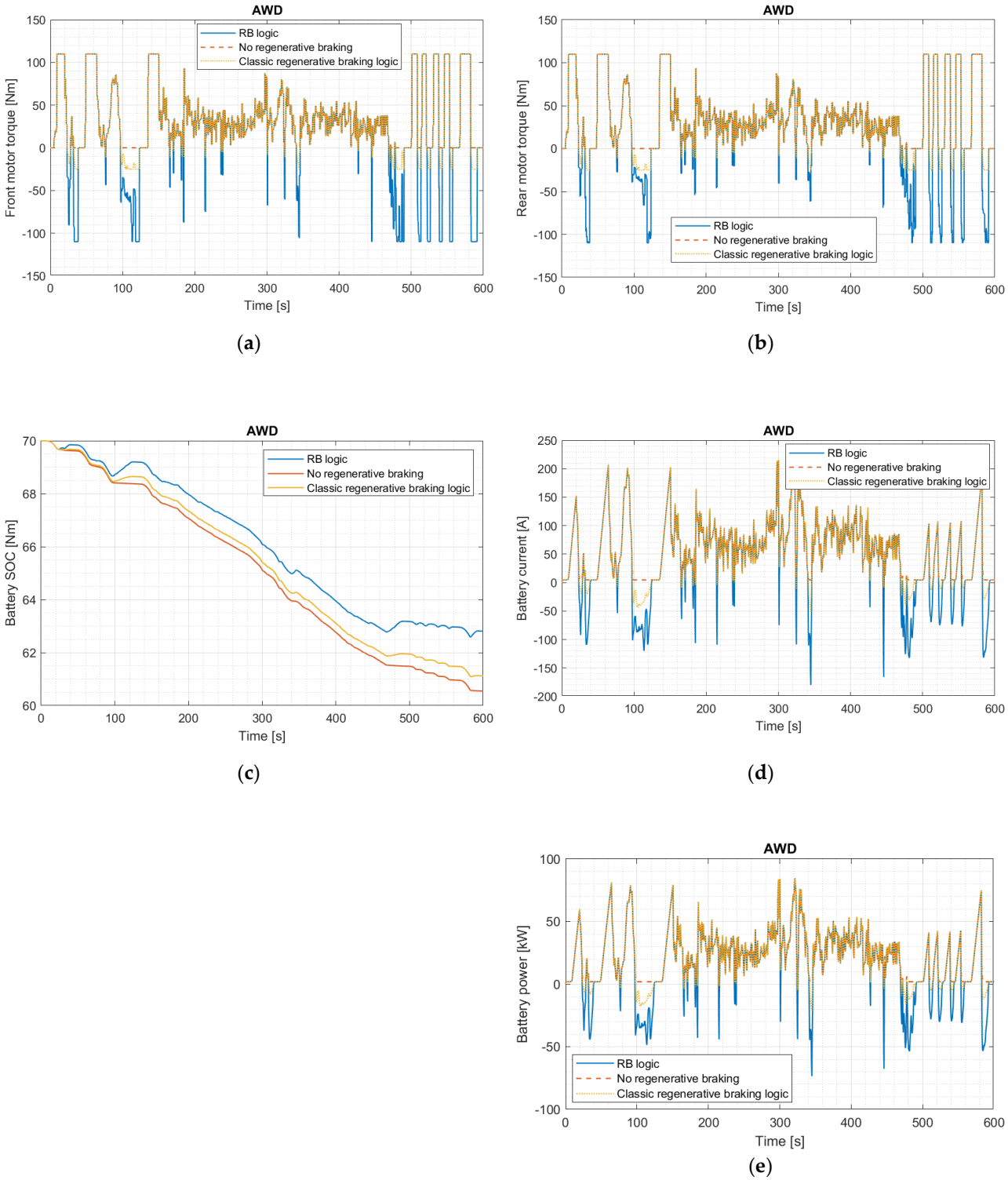

Figure 3.20. *Results of simulations with AWD vehicles on the US06 cycle. In particular: (**a**) front motor torque; (**b**) rear motor torque; (**c**) battery SOC; (**d**) battery current; (**e**) output (positive) and input (negative) power to the battery pack.*

As shown in section (**a**) of Figure 3.18, the FWD vehicle (both with the two regenerative braking logics and without any) is unable to follow the target profile defined by cycle US06; the vehicle speed deviates from the target in some acceleration phases. The same situation was found for all RWD and AWD vehicles, whose speed profiles are the same as the FWD vehicle, i.e., section (**a**) of Figure 3.18. As a matter of fact, the vehicles in question lack the torque and performance to faithfully follow the US06 standard cycle, which is particularly demanding with regard to acceleration phases.

Again, on the US06 cycle, braking energy recovery is generally higher for vehicles equipped with the RB logic presented in this thesis, and this is true for all vehicles considered (FWD, RWD, and AWD). This can be easily seen in graph (**b**), (**d**) and (**e**) of Figure 3.18; (**a**), (**c**) and (**d**) of Figure 3.19; and (a), (b), (d) and (e) of Figure 3.20.

Table 3.9 reports the energy consumption and SOC on the US06 cycle, again for all three vehicles featuring RB logic, traditional braking logic, and without braking recovery. The final SOC of the simulation on the single cycle is also reported, remembering that the initial SOC was set to equal 70%. The specific energy consumption is also reported.

Table 3.9. *Consumption on the US06 cycle.*

Type of Vehicle	Regenerative Braking Logic	Final SOC (%)	SOC Consumption (%)	Energy Consumption (kWh)	Specific Energy Consumption (kWh/(100 km))
FWD	RB logic	62.86	7.14	3.00	23.67
	No brake recovery	60.55	9.45	3.97	31.33
	Classic logic	61.12	8.88	3.73	29.42
RWD	RB logic	62.86	7.14	3.00	23.68
	No brake recovery	60.55	9.45	3.97	31.32
	Classic logic	61.12	8.88	3.73	29.43
AWD	RB logic	62.81	7.19	3.02	23.84
	No brake recovery	60.55	9.45	3.97	31.34
	Classic logic	61.12	8.88	3.73	29.44

3.4 DISCUSSION AND FUTURE DEVELOPMENTS

In this chapter, a regenerative braking logic aimed at the optimization of energy recovery during braking is presented to be adopted on electric vehicles with FWD, RWD, or AWD (equipped with a motor for each axle) transmission layouts.

Section 3.3.2 shows the operation of the RB logic and, in particular, how regenerative torque and pressures in the front and rear brake systems intervene during the braking phase in a normal braking manoeuvre.

In Section 3.3.3, a panic braking manoeuvre is used to verify that the RB logic does not lead to a loss of vehicle stability. A comparison is made with similar vehicles without any regenerative braking logic. Section 3.3.3.1 presents straightline panic braking and shows how deceleration performance is not made worse when compared to a reference vehicle without regenerative recovery. Section 3.3.3.2, on the other hand, shows the correct operation of the RB logic even during a phase of intense braking when cornering.

Section 3.3.4 demonstrates the energy savings that can be obtained thanks to the use of the RB logic, either on the WLTC or on the more demanding US06 cycle. For both cycles and for all vehicle types (FWD, RWD, and AWD), a comparison is also made with the consumption obtained by implementing a standard type of regenerative logic.

The RB logic in the FWD vehicle made it possible to save 7.70 kWh (savings of 30.3%) of battery on the class 3b WLTC and 7.66 kWh (savings of 24.4%) on the US06 cycle compared to the same vehicle without regenerative recovery. Comparing the RB logic with a classic logic commonly adopted on the market, a saving of 5.43 kWh (savings of 23.4%) on the WLTC and 5.75 kWh (savings of 19.5%) on the US06 cycle was found instead.

The RB logic in the RWD vehicle made it possible to save 7.71 kWh (savings of 30.3%) of battery on the class 3b WLTC and 7.65 kWh (savings of 24.4%) on the US06 cycle compared to the same vehicle without regenerative recovery. Comparing the RB logic with a classic logic commonly adopted on the market, a saving of 5.45 kWh (savings of 23.5%) on the WLTC cycle and 5.75 kWh (savings of 19.5%) on the US06 cycle was found instead.

Finally, the RB logic in the AWD vehicle made it possible to save 7.52 kWh (savings of 29.5%) of battery on the class 3b WLTC and 7.50 kWh (savings of 23.9%) on the US06 cycle compared to the same vehicle without regenerative recovery. Comparing the RB logic with a classic logic commonly adopted on the

market, a saving of 5.25 kWh (savings of 22.6%) on the WLTC cycle and 5.59 kWh (savings of 19.0%) on the US06 cycle was found instead.

The RB logic performs better in terms of energy savings on the relatively mild WLTC compared to the US06.

The different tests reported in this thesis were all carried out with a constant tire–road friction model coefficient (μ); in particular, in the base case, μ is equal to 1. By setting μ to be constant in the model, however, it is possible to optimize the operation of the RB logic for a certain friction coefficient and then act on the two safety limits (SC_F and SC_R) to avoid locking the drive wheels in other cases (with different coefficients of adhesion) due to regenerative braking alone, even before the braking system has intervened.

For the correct operation of the RB logic, it is necessary to correctly set all the vehicle parameters within the model and, if necessary, to use the unknown parameters as calibration values. It is also necessary to tune the braking system of the vehicle correctly for a correct distribution between the maximum pressures in the front and rear braking system in particular in order to guarantee correct braking even in the event of 100% brake demand.

Another interesting opportunity is the adoption of an ABS strategy specifically tuned for the RB logic, where control of the regenerative torques offered by the electric motors is also taken into account when necessary. In this way, it is possible to optimize the logic for a given condition, for example, in different road friction conditions.

The RB logic also lends itself to further optimization in cases where a real-time estimate of the road friction coefficient is available. Review paper [55] reports various techniques for this purpose, as well as the role and practicality of this coefficient in the vehicle system.

Paper [56] reports another review on the topic. Various estimation methods are also classified based on:

- Offboard sensors (laser profilometer, camera, intelligent tire with accelerometer, ultrasonic transmitter, receiver, etc.);
- Onboard sensors and vehicle dynamics model (lateral, longitudinal, and coupled dynamics model);
- Data-driven (neural networks and so on).

The RB logic model has a modular structure, so it lends itself to modifications and improvements. Here are some aspects concerning possible future developments of the RB logic:

- Integration of the logic with a model for the estimation of the tire–road friction coefficient, as stated above;
- Improvement of the tire simulation model—in particular, the tire–road interaction, for example, by implementing a fully nonlinear Pacejka Magic Equation;
- Integration of a specific ABS strategy also acting on the braking torques of the electric motors; see [45] for an example.

3.5 INTEGRATION OF THE RB LOGIC IN THE TEST MODEL

The regenerative braking (RB) logic [13] has been integrated into the TEST [10] model in order to create a new version of the latter also suitable for fuel consumption estimation and simulation of vehicles equipped with this RB logic. In particular, the RB logic has been inserted as a Simulink "submodel" in the main board of the TEST model and the inputs and outputs of the logic have been linked, directly or with appropriate calculations, to the variables of the model. In addition, it was necessary to make some changes and additions to the TEST model.

The "submodel" of the RB logic is performed in the TEST model only if the logic is active (the RB logic can be activated through the appropriate panel of the graphic user interface, see Section 3.5.1) and only for $F_{ref\_wheels} < 0$, i.e. if a braking force is required from the wheels.

The battery voltage (V) is calculated in the TEST model described in Section 2 and used as an input variable in the RB logic. The absolute value of the acceleration (a), calculated in the TEST model, is used as input j for the RB logic, remembering that the "submodel" of the RB logic will provide results only in case of $F_{ref\_wheels} < 0$ and therefore for negative acceleration (deceleration) of the vehicle. The variables v, ω_{motF}, ω_{motR} are also calculated in the TEST model and their calculation value, relative to the instant of iteration preceding the one considered, is used as an input variable in the RB logic. For the ω_{wheelF} input of the RB logic, the speed v_{prev} is used, calculated in the TEST model, divided by the front wheel radius R_{wheelF}. Similar situation with regard to the ω_{wheelR} input, which is associated with the v_{prev} variable divided by R_{wheelR}. The input a_y of the RB logic is extrapolated thanks to a Lookup Table containing information regarding the lateral acceleration as a function of time, defined by the user of the model as an input quantity. The input $Crnt_{MAX}$ of the RB logic is instead set equal

to the absolute value of I_{chrg_limit} if this charge limit is defined in current, equal to the absolute value of P_{chrg_limit} divided by the voltage V, if the charge limit is defined in the form of power. Finally, as regards the definition of the $BrakeDemand$ input of the RB logic, a preliminary calculation is required within the TEST model, as described below.

In particular, $BrakeDemand$ is calculated in the TEST model as the inverse of the ratio between F_{ref_wheels} and F_{brake_maxRB}, all limited between the values of 0 and 1. Where F_{brake_maxRB} is the maximum braking force that the traditional hydraulic brake system of the vehicle equipped with RB logic can unload to the ground and it is calculated in the TEST model using the following equation (3.41).

$$F_{brake\_maxRB} = 2 \cdot \frac{Pres_{MAXbrakeF} \cdot A_{pistonF} \cdot \mu_{padF} \cdot R_{discF}}{R_{wheelF}} + 2 \cdot \frac{Pres_{MAXbrakeR} \cdot A_{pistonR} \cdot \mu_{padR} \cdot R_{discR}}{R_{wheelR}} \tag{3.41}$$

The T_{motF} and T_{motR} outputs of the "submodel" of the RB logic are used as input values for the "Power Required" block (see Section 2.2.2.1) of the TEST model, in case of active RB logic and in $F_{ref\_wheels} < 0$ condition. Under these conditions, T_{req_F} is replaced with T_{motF} in equation (2.18) and T_{req_R} is replaced with T_{motR} in equation (2.19).

On the other hand, the $Pres_{brakeF}$ and $Pres_{brakeR}$ outputs of the RB logic are used as inputs for the "Vehicle Acceleration" block (see Section 2.2.3) of the TEST model.

In the version of the TEST model described in Section 2, the total braking force given by traditional hydraulic brakes (F_{brake}) is obtained as the minimum between the force required by the hydraulic braking system (F_{brake_req}) and the maximum force that can be developed by this system (F_{brake_max}). In the new version of the TEST model described in this section, born from the integration of the TEST model of Section 2 with the RB logic object of this chapter, F_{brake} is set null for $F_{ref\_wheels} \geq 0$, vice versa it is calculated again as in the block "Traditional Brakes" described in Section 2.2.3 if the RB logic is inactive (it is not present on the simulated vehicle), otherwise, with active logic (vehicle equipped with RB logic), it is calculated through equation (3.42) in an additional module, called "Traditional Brakes with RB Logic", inserted in the model inside the "Vehicle Acceleration" block. Furthermore, in this new version, the "Traditional Brakes" block of the version of the TEST model described in Section 2 is renamed "Traditional Brakes without RB Logic", to distinguish it from the "Traditional Brakes with RB Logic" block.

$$F_{brake} = 2 \cdot \frac{Pres_{brakeF} \cdot A_{pistonF} \cdot \mu_{padF} \cdot R_{discF}}{R_{wheelF}} + \\ +2 \cdot \frac{Pres_{brakeR} \cdot A_{pistonR} \cdot \mu_{padR} \cdot R_{discR}}{R_{wheelR}} \tag{3.42}$$

Finally, also the binary variable $Limit_{trad\_brak}$, mentioned in Section 2.2.3, has been updated in the model in such a way as to take into account the possibility of the presence on the vehicle of the RB logic. However, it will still be defined equal to 1 in case of limitation by the traditional system occurred, that is, if the traditional hydraulic system is not able to meet the requests necessary to satisfy the braking request by the driver (remembering that part of braking will be guaranteed by the electric motor/s), equal to 0 vice versa.

3.5.1 Graphic User Interface Integration

In the graphic user interface of the TEST model described in Section 2.3, two new Tabs have been added for the definition of the inputs and of all those quantities necessary for the operation of the RB logic, quantities that are not already defined through the other interface panels (see Section 2.3).

Thanks to the panel of Figure 3.21 it is possible to activate (On) or deactivate (Off) the RB logic. In the event of inactive logic, the vehicle will be equipped with regenerative braking logics defined through the appropriate parameters in the interface panels relating to the electric motors (Figure 2.17 and Figure 2.18).

Through the "Regenerative Braking Logic" panel (Figure 3.21) it is possible to define the following parameters: the wheelbase of the vehicle (L), the distance between the center of gravity and the front axle (L_a), the height of the centre of gravity (h_g), the maximum pressure that can be generated inside the front brake hydraulic system ($Pres_{MAXbrakeF}$), the maximum pressure that can be generated inside the rear brake hydraulic system ($Pres_{MAXbrakeR}$), the road friction coefficient μ used as a constant parameter within the RB logic, the two safety factors SC_F and SC_R and finally the minimum speed necessary for the intervention of the regenerative braking.

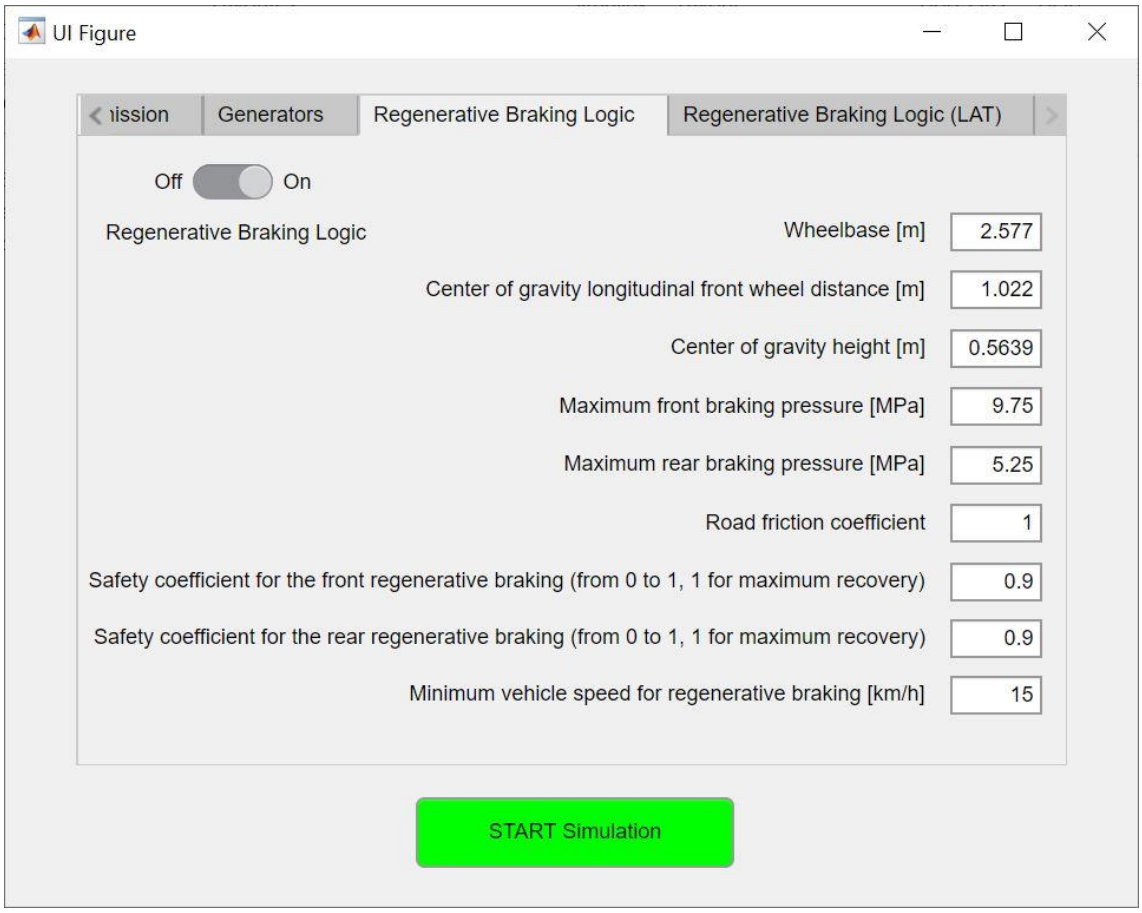

Figure 3.21. *"Regenerative Braking Logic" panel of the Graphic User Interface of the TEST model. In particular, this panel allows you to enter the inputs regarding the "RB logic" parameters.*

Through the "Regenerative Braking Logic (LAT)" panel (Figure 3.22), it is possible to define all those parameters necessary for the correct operation of the RB logic in the event of lateral acceleration. The latter can in fact be provided as an input variable thanks to the "Define lateral acceleration of the vehicle" button in Figure 3.22, which allows you to define the lateral acceleration values as a function of the time elapsed from the start of the simulation.

Through the panel of Figure 3.22, it is therefore possible to define the following parameters: the height of the front roll centre (h_{CRf}), the height of the rear roll centre (h_{CRr}), the stiffness of the front anti-roll bar (k_{ARBf}), the stiffness of the rear anti-roll bar (k_{ARBr}), the stiffness of the front suspension springs ($k_{springF}$), the stiffness of the rear suspension springs ($k_{springR}$), the front unsprung mass of a single wheel assembly (m_{nsF}), the mass rear unsprung mass of a single wheel assembly (m_{nsR}), the front suspended mass of the vehicle (m_{sF}),

the rear suspended mass (m_{sR}) and, finally, the front ($track_F$) and rear ($track_R$) track of the vehicle.

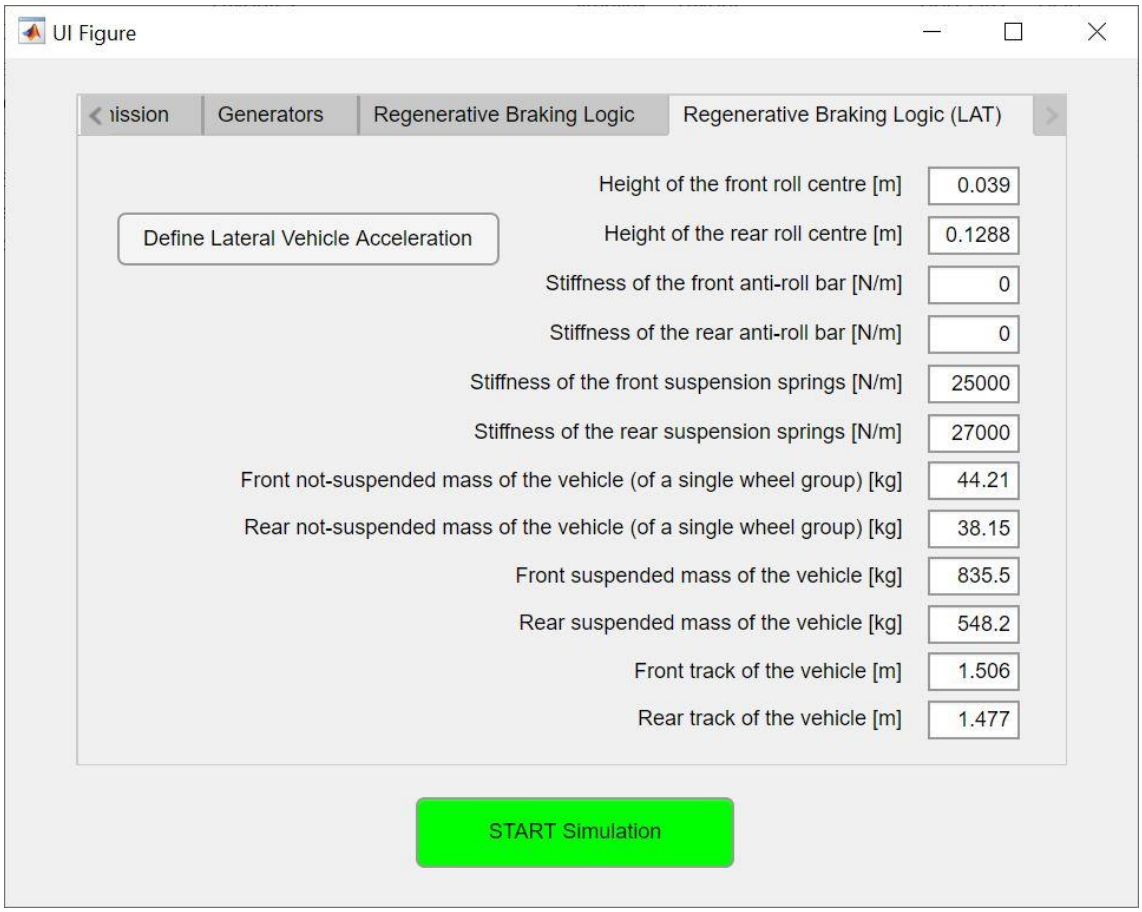

Figure 3.22. *"Regenerative Braking Logic (LAT)" panel of the Graphic User Interface of the TEST model. In particular, this panel allows you to enter the inputs regarding the "RB logic" parameters, necessary for the correct operation of the logic in the event of lateral acceleration of the vehicle.*

3.6 COMPACT SIMULATOR

A very important tool for this work was the compact simulator available at the University of Brescia, in particular available to "Automotive Engineering and Design Group" of DIMI Department (Figure 3.23).

The simulator helped a lot in the code development phase of the regenerative braking logic (Figure 3.24). In fact, thanks to co-simulations between the VI-CarRealTime software, the simulator and the RB model, it was possible to qualitatively test the logic and find various bugs and errors in the development phase. It was also possible to test the perception of the driver driving a vehicle

equipped with RB logic, in order to verify that this does not lead, for example, to abrupt changes in the amount of braking following small variations in the pressure that the driver applies to the brake pedal.

Figure 3.23. *Driver's station of the compact driving simulator available at the University of Brescia.*

Once any errors and inaccuracies in the logic have been resolved, through various tests on the compact simulator during the development of the logic itself, it was possible to ascertain how the behaviour of the vehicle with RB logic is perceived unchanged compared to the case of the same vehicle without this logic.

In particular, total braking (hydraulic plus regenerative braking) has been set in the logic with a linearly variation as a function of the brake pressure. The logic, starting from this initial information, calculates the braking torque of the electric motor (or motors) and the pressures in the hydraulic systems of the traditional front and rear brakes, in order to integrate the braking, to bring it back to the value defined initially, directly related to the input that the driver provides on the brake pedal.

Figure 3.24. *PC station of the compact driving simulator: for data analysis during tests, for setting the simulation environment and for saving test data.*

During operation, the proportion of regenerative motor torque unloaded to the ground and ground force given by the hydraulic braking system varies according to the operating conditions and the amount of braking request. Through the simulator, it was possible to ascertain that the result perceived by the driver is linear braking as a function of the pressure input on the brake pedal. This aided in the development of the logic, providing confirmation that the logic being implemented was working correctly.

By appropriately defining the graphs of the "SIMulation Workbench Control Center" tool, it is possible to monitor the trend of the different quantities during driving simulations. In Figure 3.24, the screen on the left shows the graphics window of this software.

As already mentioned, in the current state of work on the RB logic, well-structured tests with the driving simulator have not yet been carried out. The tests carried out were mainly of a qualitative nature. One of the next steps will be the use of the compact simulator for the realization of a well-structured and meaningful set of tests to show the behaviour of the RB logic.

Below, by way of example, are the screenshots of some graphics during tests carried out with the FWD vehicle of Section 3.3.1, during a panic braking, during a really mild braking and during an intermediate braking between the two (from Figure 3.25 to Figure 3.31).

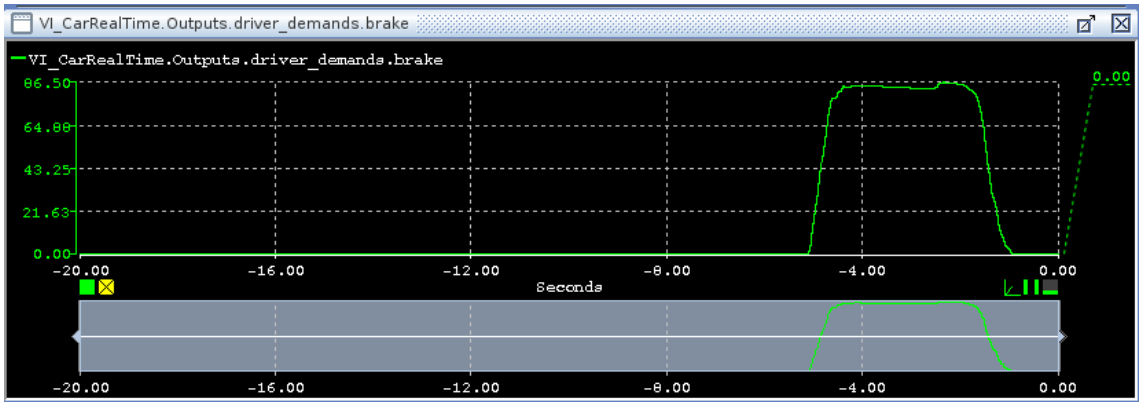

(**a**)

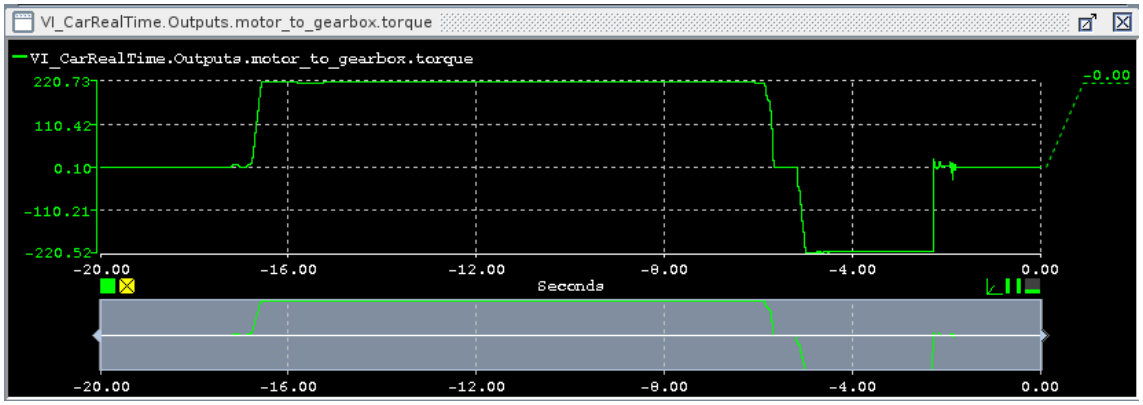

(**b**)

Figure 3.25. *"SIMulation Workbench Control Center". Graphs related to a panic braking test on the compact simulator. In particular, in function of the time (in seconds): (**a**) brake demand (in percentage); (**b**) motor torque (in Nm).*

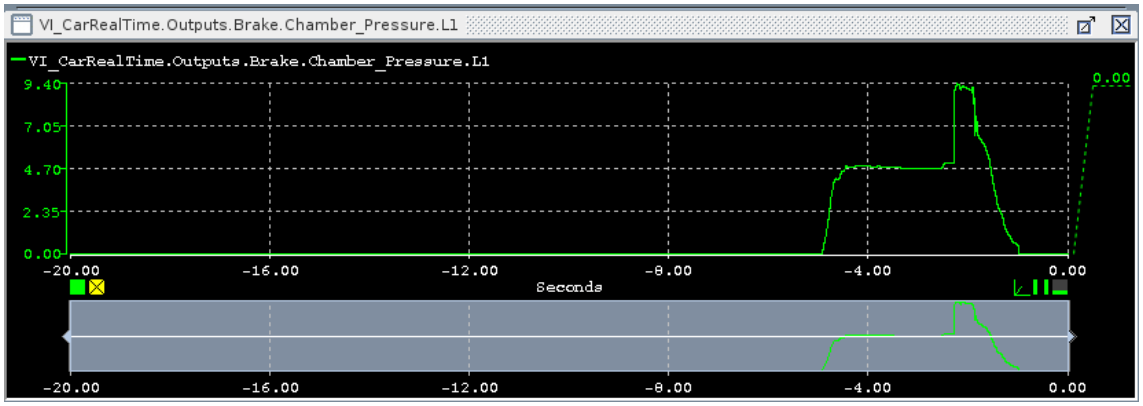

(**a**)

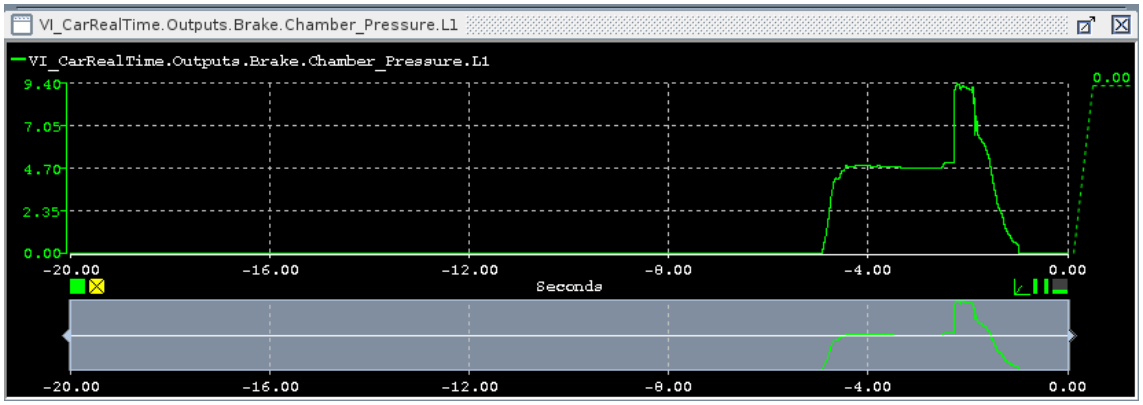

(**b**)

Figure 3.26. *"SIMulation Workbench Control Center". Graphs related to a panic braking test on the compact simulator. In particular, in function of the time (in seconds): (**a**) pressure of the left front brake chamber (in Mpa); (**b**) pressure of the left rear brake chamber (in MPa).*

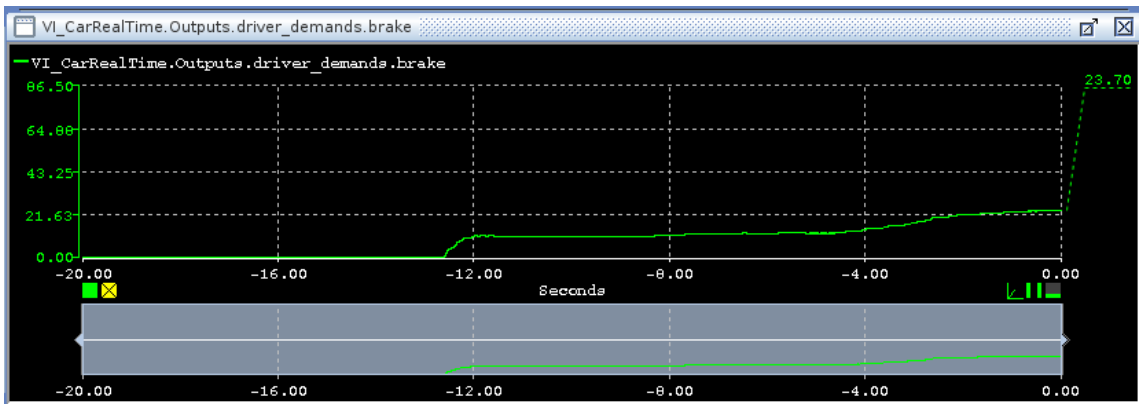

(**a**)

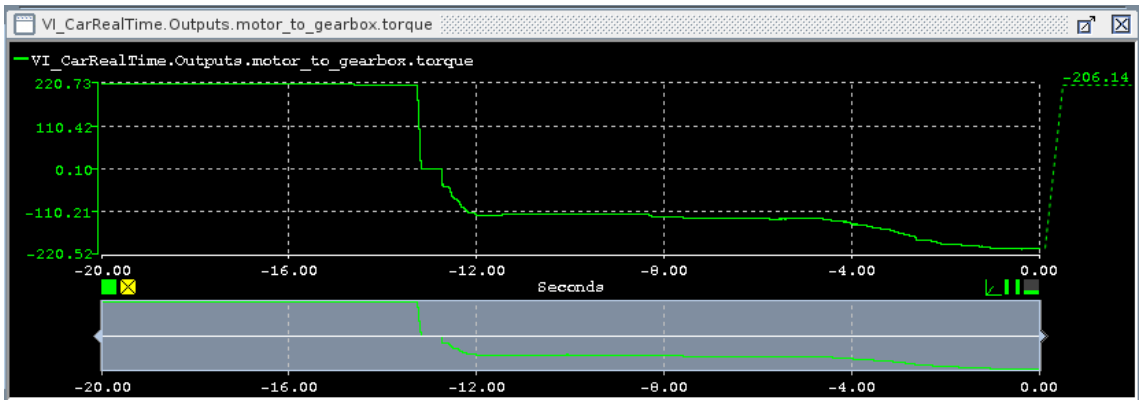

(**b**)

Figure 3.27. *"SIMulation Workbench Control Center". Graphs related to a really mild braking test on the compact simulator. In particular, in function of the time (in seconds): (**a**) brake demand (in percentage); (**b**) motor torque (in Nm).*

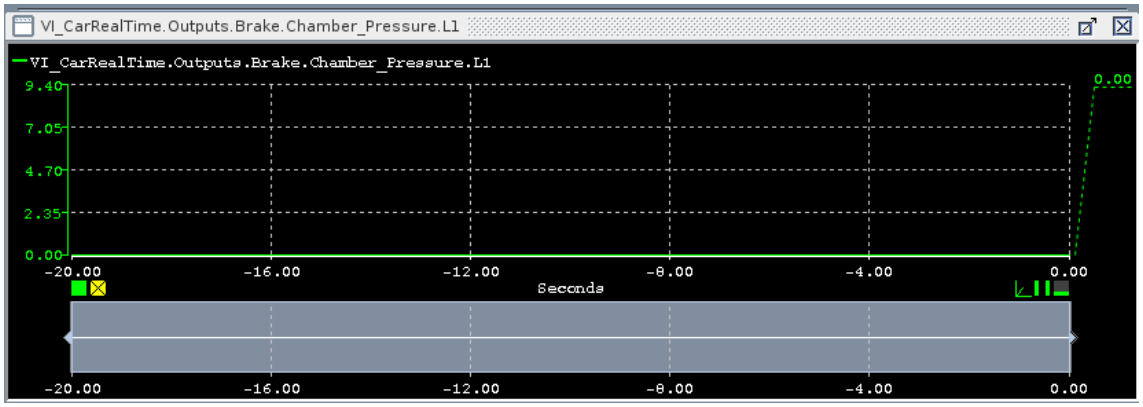

(**a**)

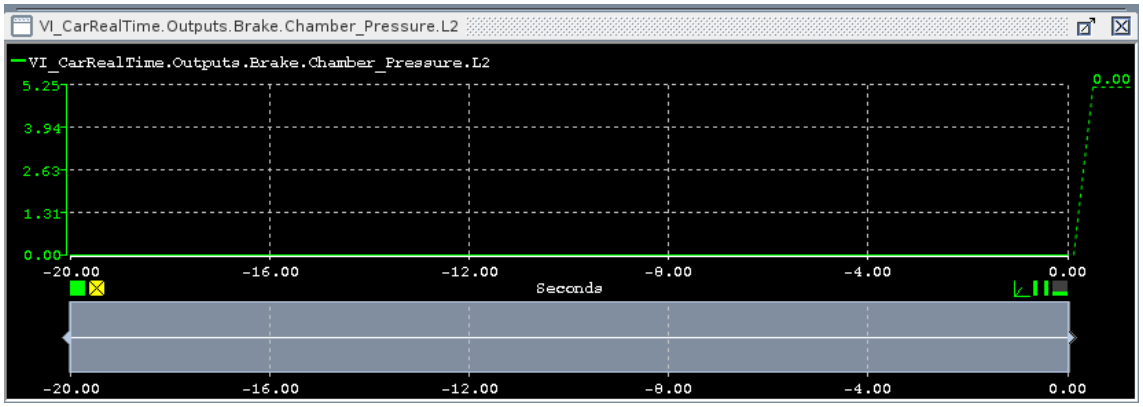

(**b**)

Figure 3.28. *"SIMulation Workbench Control Center". Graphs related to a really mild braking test on the compact simulator. In particular, in function of the time (in seconds): (**a**) pressure of the left front brake chamber (in Mpa); (**b**) pressure of the left rear brake chamber (in MPa).*

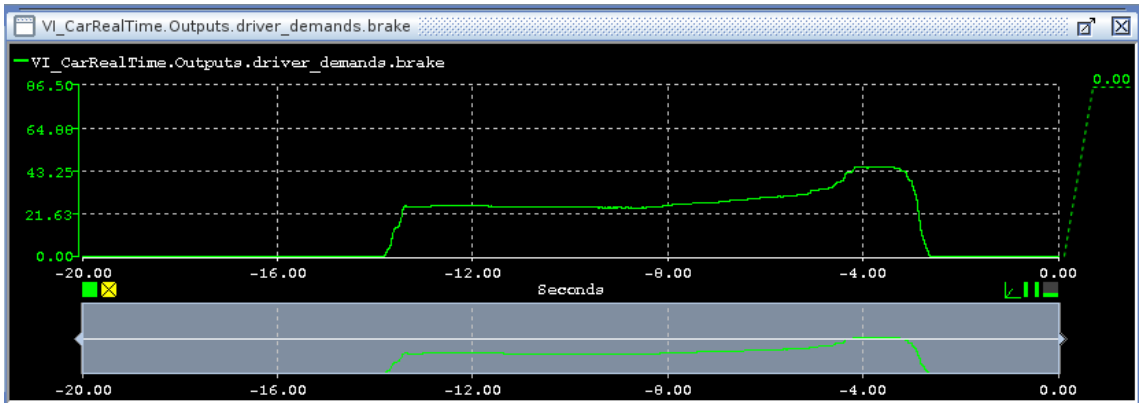

(**a**)

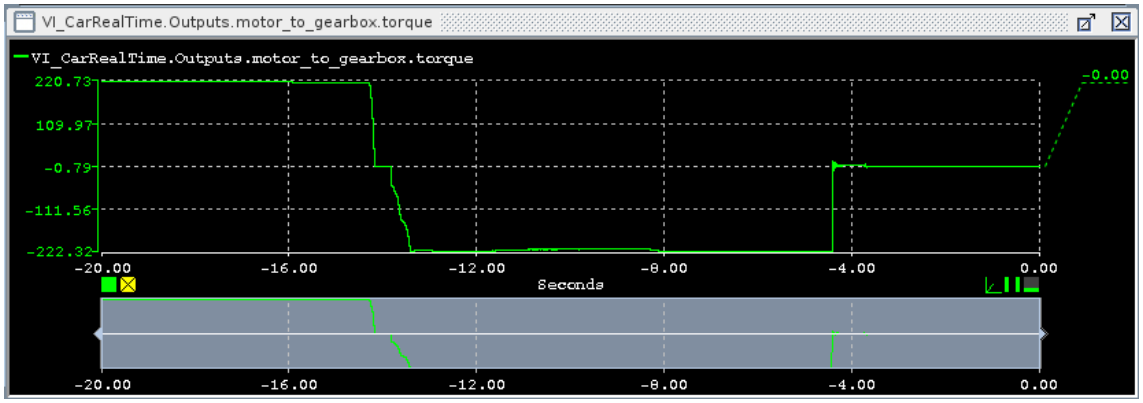

(**b**)

Figure 3.29. *"SIMulation Workbench Control Center". Graphs related to a medium braking test on the compact simulator. In particular, in function of the time (in seconds): (**a**) brake demand (in percentage); (**b**) motor torque (in Nm).*

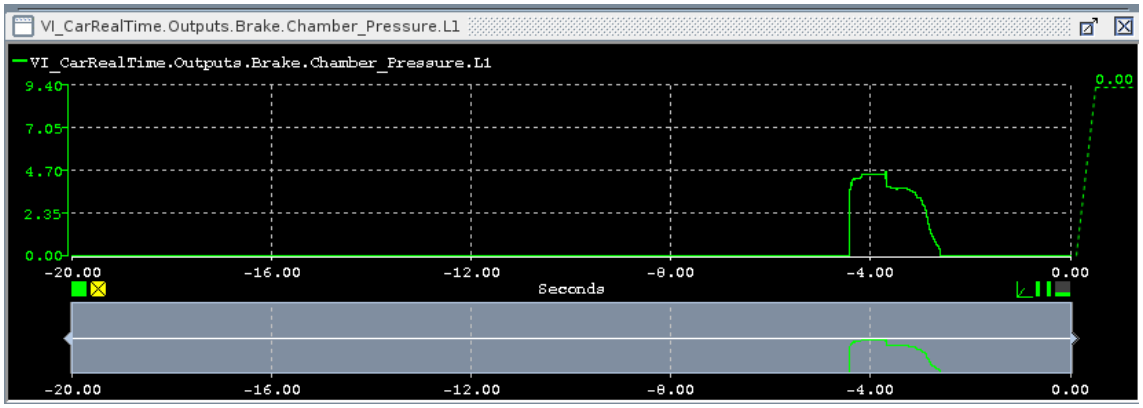

(**a**)

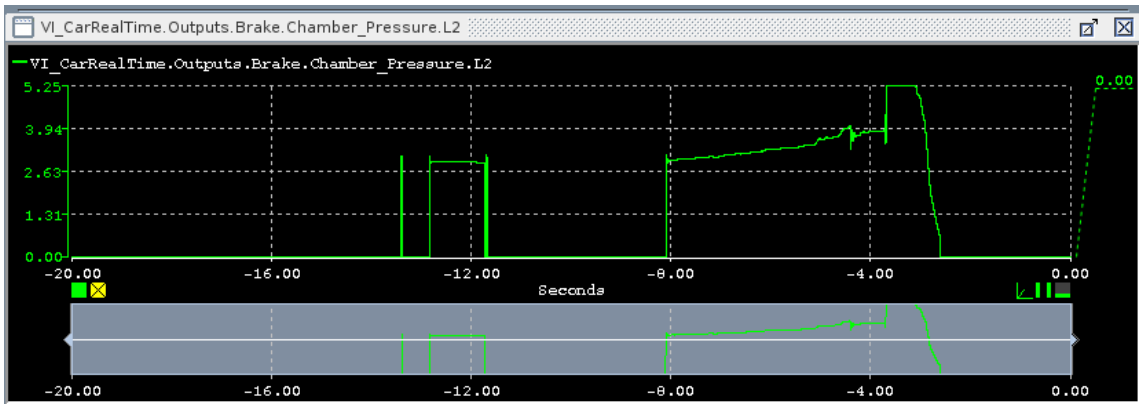

(**b**)

Figure 3.30. *"SIMulation Workbench Control Center". Graphs related to a medium braking test on the compact simulator. In particular, in function of the time (in seconds): (**a**) pressure of the left front brake chamber (in Mpa); (**b**) pressure of the left rear brake chamber (in MPa).*

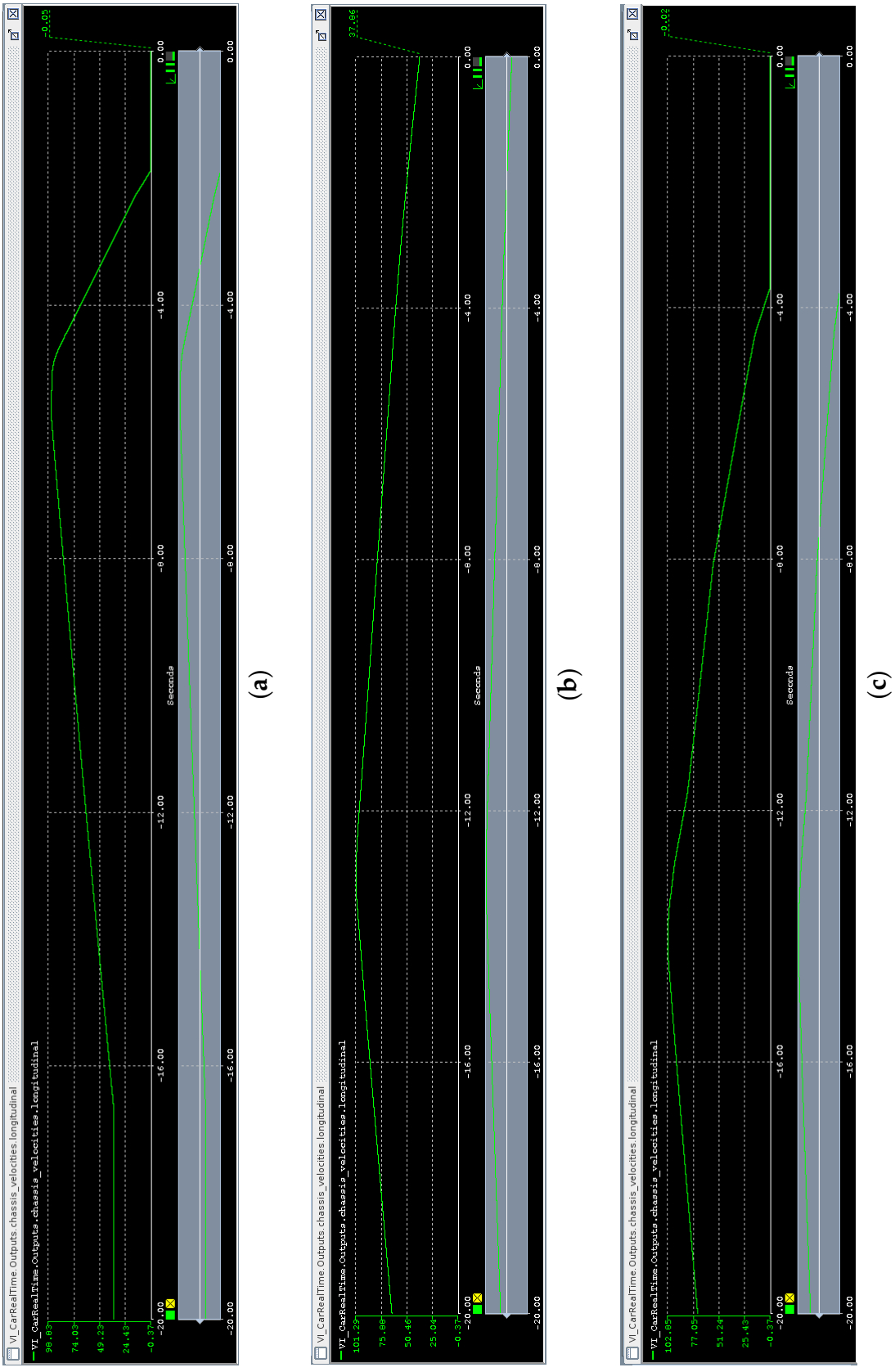

Figure 3.31. *"SIMulation Workbench Control Center". Vehicle speed (in km/h) in functions of the time (in seconds). In particular, tests on the compact simulator, related to: (**a**) a panic braking test; (**b**) a really mild braking test; (**c**) a medium braking test.*

The images from Figure 3.32 to Figure 3.34 show the graphical results obtained by performing different braking tests on the compact driving simulator, with the front-wheel drive vehicle equipped with RB logic, vehicle presented in Section 3.3.1. From all three figures it is possible to observe the zeroing of the motor torque below 15 km/h, the limit set for regenerative braking.

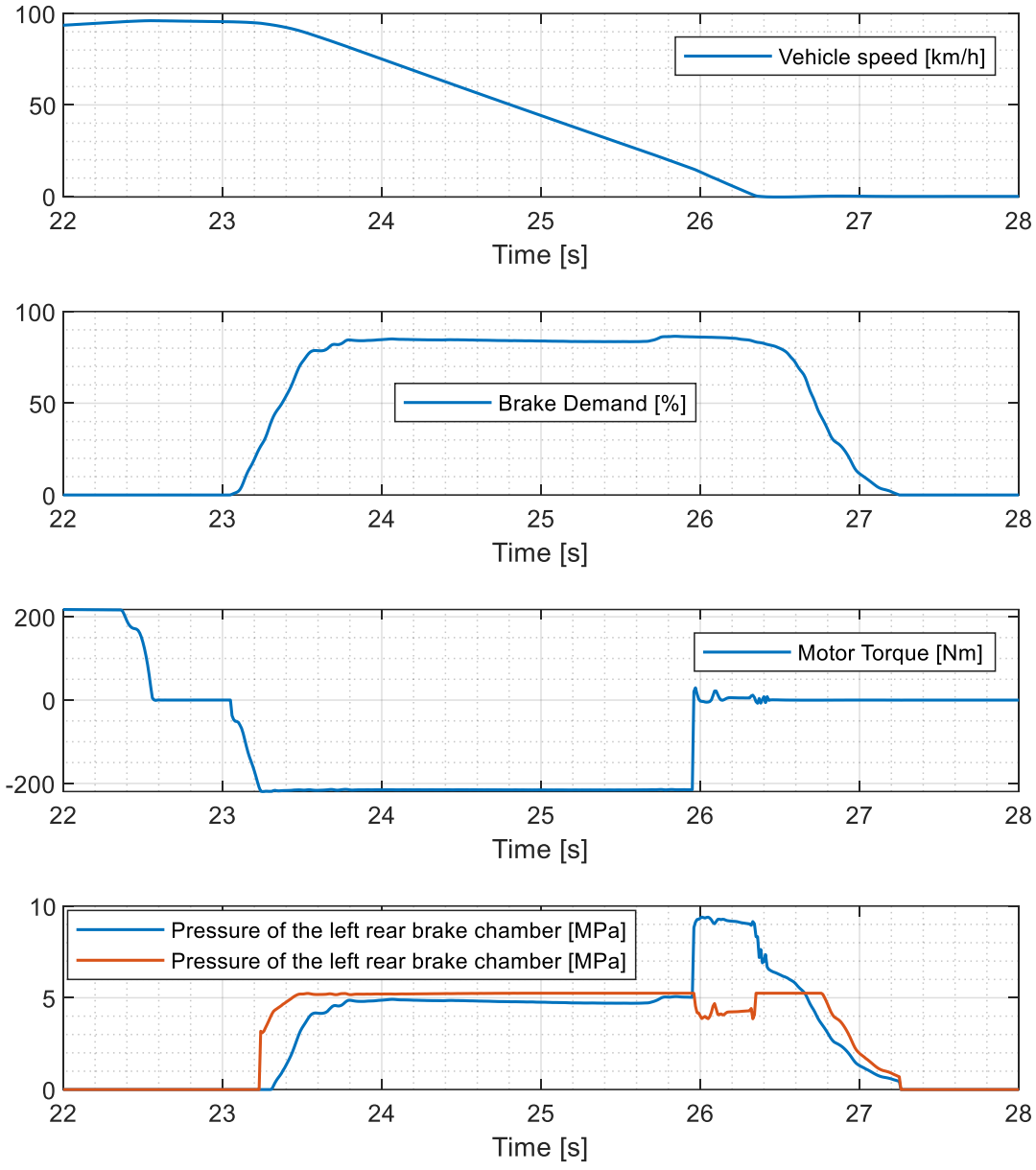

Figure 3.32. *Graphic results of the panic braking test on the compact driving simulator. FWD vehicle with RB logic.*

From the results of panic braking (Figure 3.32), it can be seen that pressure is generated in both hydraulic brake systems (front and rear) in a timely manner as a result of the driver pressing the brake pedal. Likewise, the maximum regenerative torque of the motor is reached in a short time.

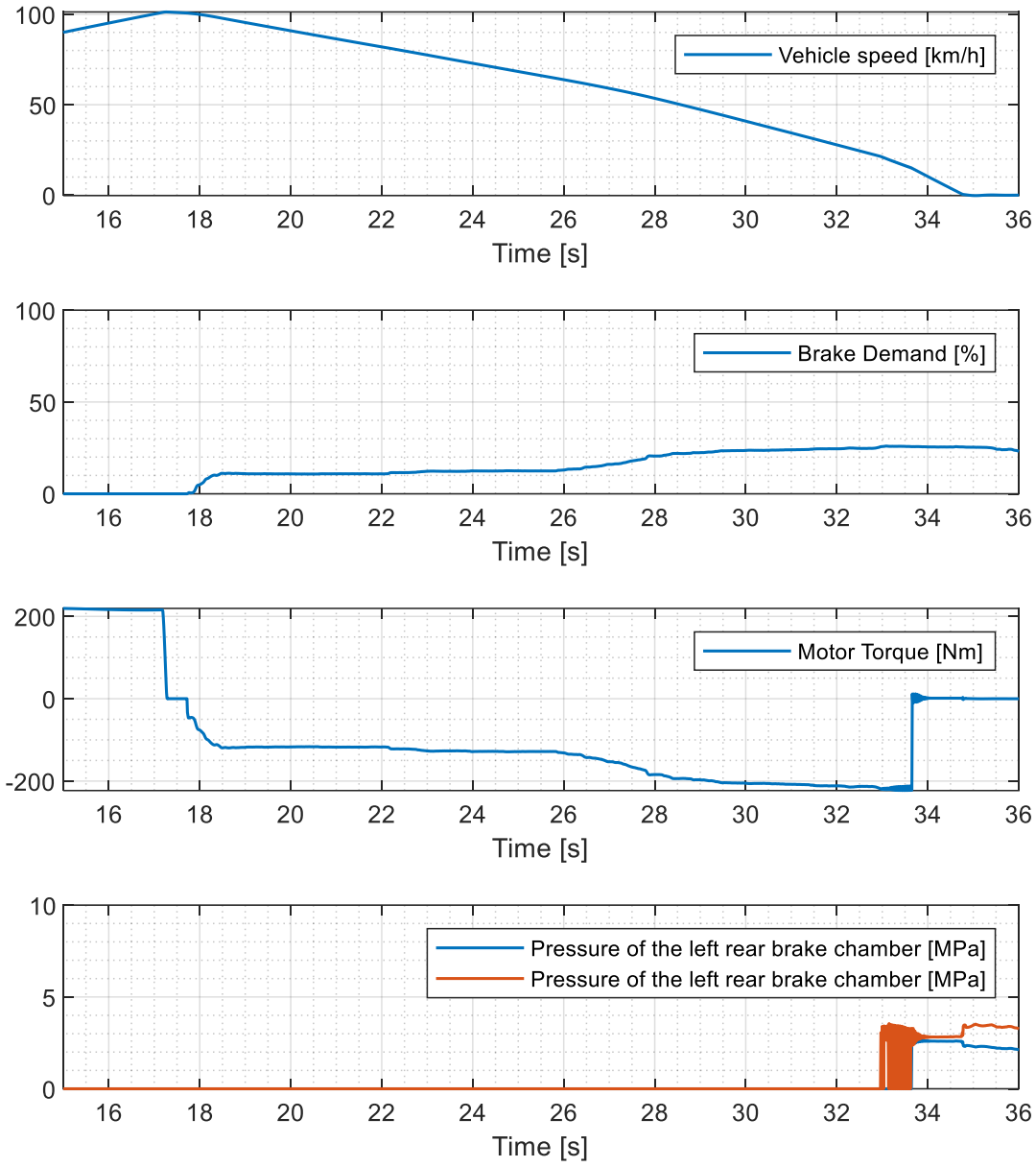

Figure 3.33. *Graphic results of the really mild braking test on the compact driving simulator. FWD vehicle with RB logic.*

From the results of very mild braking (Figure 3.33), it can be seen how the electric motor alone, thanks to regenerative braking, can guarantee the required braking amount. The traditional hydraulic braking system only intervenes approximately in conjunction with the limit of 15 km/h. Finally, thanks to the intermediate braking test (Figure 3.34), it is possible to notice how the hydraulic system intervenes to integrate the regenerative braking of the electric motor, in such a way as to respect the brake demand.

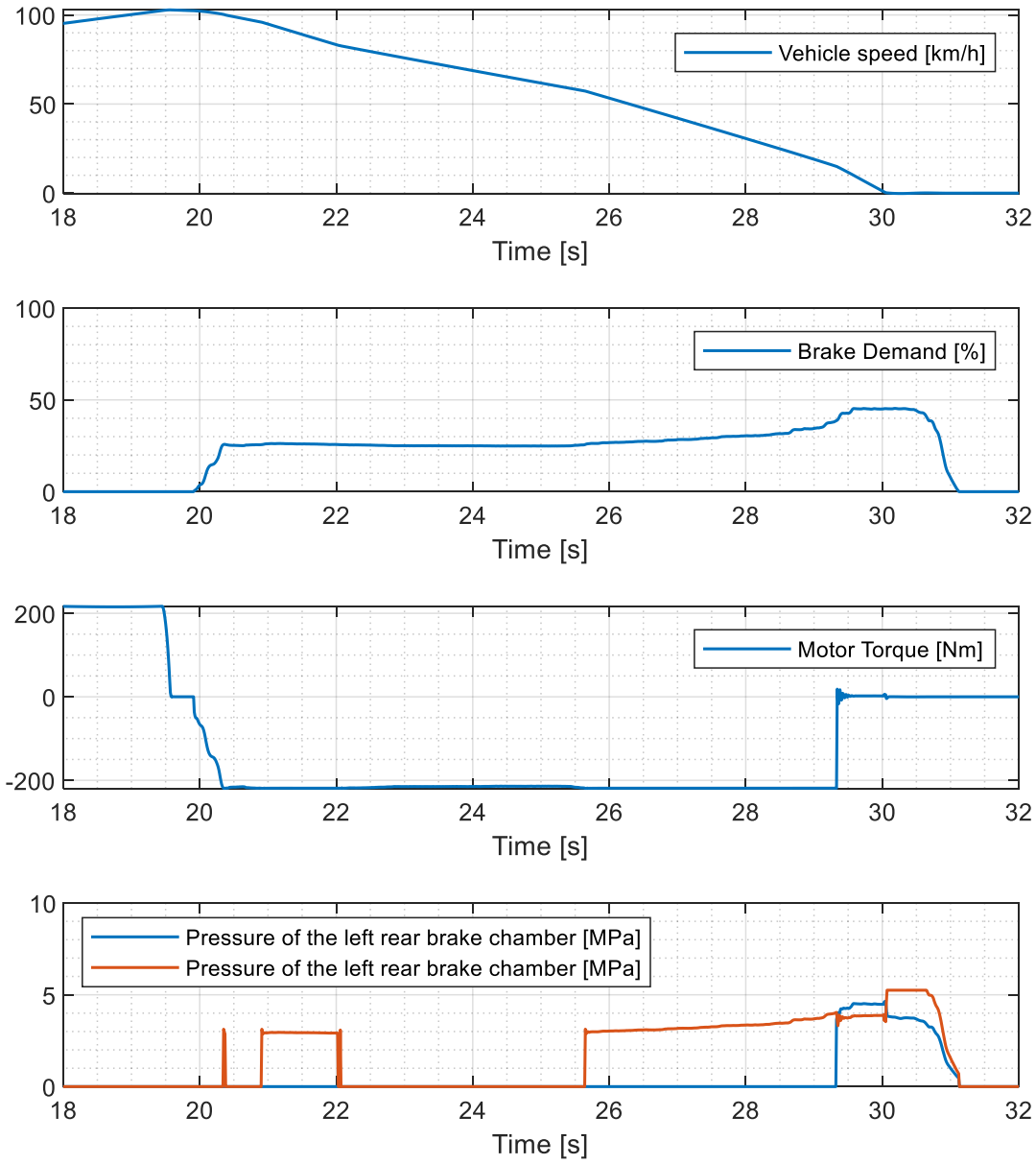

Figure 3.34. *Graphic results of the medium level braking test on the compact driving simulator. FWD vehicle with RB logic.*

Finally, a next step, for this work on the regenerative braking logic, will be to implement the TEST logic inside a MoTeC control unit (Figure 3.35) and to test everything in co-simulation with the compact driving simulator (Figure 3.36).

Figure 3.35. *MoTeC M150 control unit, available to "Automotive Engineering and Design Group" of the University of Brescia (DIMI Department).*

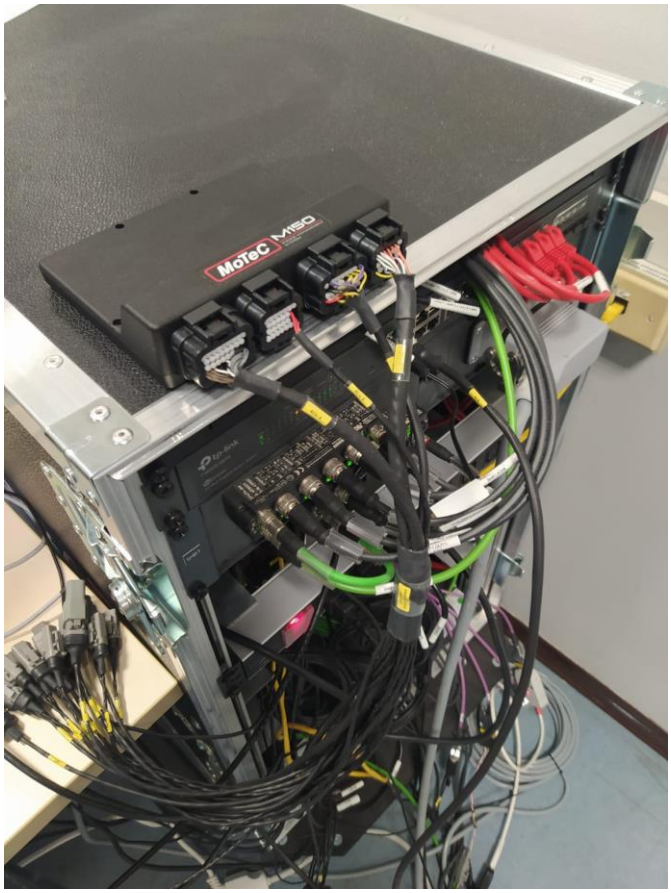

Figure 3.36. *MoTeC M150 control unit connected to the computer of the compact driving simulator of the University of Brescia.*

3.7 FINAL CONSIDERATIONS

This chapter presents a regenerative braking logic aimed at maximizing energy recovery when braking without compromising the stability of the vehicle. Such RB logic was tested on the vehicle dynamics models of FWD, RWD, and AWD compact cars. Furthermore, the RB logic has been integrated into the TEST model [10] (see Chapter 2), obtaining a more complete version.

In summary, the RB model ensures that the regenerative torque of the electric motor(s) is exploited to the maximum while also preventing the locking of drive wheels at the same time, and subsequently, if necessary, integrating motor braking with the action of the traditional brake system.

For FWD and RWD vehicles, the integration between regenerative and traditional braking also aids the optimal braking distribution and the maximization of regenerative braking at the same time.

In the case of an AWD vehicle, the logic aims to pursue, instant by instant, the optimal motor braking distribution on the basis of the longitudinal acceleration and related load transfer effects.

For the FWD and RWD compact cars, the RB logic makes it possible to save around 30% in terms of energy consumption on the class 3b WLTP cycle compared to a vehicle without regenerative recovery and about 23.5% compared to a vehicle equipped with a classic regenerative braking logic, commonly adopted on vehicles on the market according to [10]. On the US06 cycle, on the other hand, it made it possible to save 24.4% and 19.5%, respectively. Similar, promising results have been achieved with the AWD car.

The next work on the RB logic will concern tests to be carried out on the compact driving simulator and the implementation of the logic inside a control unit, which will then be connected to the simulator.

Finally, it is pointed out that the paper [13] relating to the work presented in this chapter has been cited in the scientific article [57] (published on "MDPI – Applied Sciences"), therefore a first interest in the scientific world has already been found.

4 MODELLING OF A HYBRID FUEL CELL POWERTRAIN WITH POWER SPLIT LOGIC FOR ONBOARD ENERGY MANAGEMENT (PEMFC MODEL)

This work presented in this chapter aims to develop a mathematical model for the simulation of a Fuel Cell (FC) hybrid powertrain. This study was carried out in collaboration with a master's thesis [58] and was presented in the scientific article [20].

The work starts from modelling a single cell to obtain information on the entire FC stack's characteristic curve (current and power). The model obtained was integrated into the TEST simulation tool presented in the literature and in the Section 2 of this thesis, that, as already mentioned, simulates the longitudinal dynamics of APU (Auxiliary Power Unit) hybrid electric vehicles and fully electric vehicles. Therefore, the integrated model allows the simulation of hybrid vehicles equipped with FC and a battery pack that acts as a peak power source. The tool simulates the mechanical and electrical behaviour of the vehicle, introducing an investigation of the power flows relating to the FC and batteries. In this regard, an appropriate power split logic has been implemented, allowing the correct management of the power distribution between the FC (delivered power) and the battery pack (both input and output power). The importance of analysing FC vehicles' behaviour arises from the recent necessity to find alternative propulsion systems, overcoming the range problems associated with full electric vehicles. The innovation lies in the versatility and modularity of the model, which is open to modifications and features a low computational burden, making it suitable for testing new solutions by performing first design and sizing calculations.

This chapter is organized as follows.

- In Section 4.1 the operating principles of a hydrogen fuel cell are briefly explained.
- In Section 4.2 a summary overview of the application of hydrogen FC technology in the automotive field is carried out, and a typical architecture, adopted on vehicles, for a proton exchange membrane fuel cell is described.
- In Section 4.3 a literature review is carried out.
- Section 4.4 describes the model for the FC stack [59,60] and the integration of the FC hybrid system in a longitudinal dynamic simulation tool, the "TEST" model described in paper [10] and in

Chapter 2 of this thesis, which is a model with the same functionality as the one described in article [22].

- Section 4.5 presents the validation of the FC model and the data adopted for a generic simulation.
- Section 4.6 illustrates the simulation outline, the model's output graphs, and a brief analysis of the results, recalling that the aim of the work is to present software useful for the simulation of FCHEV, not a study of a particular hybrid vehicle equipped with FC.
- Section 4.7 describes a fuel cell compressor model.
- Section 4.8 provides discussions about the proposed FC model and some future developments.
- Section 4.9 gives some concluding remarks and some final considerations.

4.1 Operating Principle of a Hydrogen Fuel Cell

A fuel cell is a galvanic cell in which the chemical energy of a fuel is converted into electrical energy through an electrochemical process. The fuel and oxidizing agents are hydrogen and oxygen, while the reaction products are water, electricity, and heat. The chemical reaction in a fuel cell is similar to that in a battery, but, in contrast to a chemical battery, reactants are not stored in the cell. On top of that, energy is produced as long as the fuel supply is maintained, without the need for a charge.

The following steps summarize the operating principle of a hydrogen fuel cell (FC):

1. The FC is fed with hydrogen coming from a tank and air from the external environment containing the oxygen necessary for the chemical reactions;
2. Within the FC, chemical reactions take place, which lead to the consumption of hydrogen and oxygen for the production of electricity;
3. Following the chemical reactions that take place inside the FC, electricity, heat and water are produced by the fuel cell itself. Electricity is the desired product; heat and water are released into the environment, and the heat can possibly be used in a heating system (both for stationary use and for heating the passenger compartment of the vehicle).

4.2 USE OF HYDROGEN FUEL CELLS ON BOARD THE VEHICLE

The different types of FC are distinguished mainly by the type of electrolyte used, and, among the various types, PEM (polymer electrolyte membrane) fuel cells are preferred for use in road vehicles [61,62] due to their low operating temperature, high power density, long cell life, and ability to respond quickly to variable power needs. Furthermore, compared to an internal combustion engine, they have greater efficiency at partial load, which corresponds to the normal use conditions in a propulsion system. These cells require the membrane to be kept humid in order to operate properly, that is, to conduct ions. Therefore, they need water management, which is one critical issue of this system. Some fuel cell stacks use an external humidifier to supply water by the electrodes.

In a fuel cell system, the reactants are stored externally from the cell. Typically, the hydrogen is contained in the gaseous state inside a high-pressure tank, while oxygen is not stored but is obtained from the air outside the vehicle [63]. This is why an FC requires some auxiliary systems to feed the cell. They include a compressor, a water pump, a fuel supply pump, and an electrical control unit, all powered by the FC itself. Among these auxiliaries, the compressor is the most demanding in terms of energy. When the FC works at low power, the auxiliaries use up a large share of the FC output power, and the system efficiency is low. FCs are usually coupled with a PPS (peak power source) such as a battery or a supercapacitor [64] under a hybrid layout to overcome the problem stated above. Furthermore, the adoption of a PPS, a battery pack, for example, also makes it possible to recover energy during braking, thus increasing the overall efficiency of the propulsion system.

A fuel cell has an optimal operation range, usually within the middle of its possible current range: the FC can therefore exploit its optimum operating point to work at high efficiency, providing traction to the electric motor and using the surplus power to recharge the batteries whenever required. The power demand in fuel-cell hybrid vehicles (FCHEVs) alternates between the FC and the battery, thus requiring a reliable energy management system (EMS), which controls the power flow between FC and battery according to the operation mode or power demand of the vehicle [65,66]. Several physics-based, dynamic models of FC have been developed [67,68].

4.2.1 Architecture of a Fuel Cell Propulsion System

The Fuel Cell system, in order to provide the power required by the vehicle in operating conditions, must necessarily be integrated with other components. In fact, it requires:

- A system that feeds the anode with hydrogen;
- An air suction and treatment system for the cathode;
- A humidifier, to ensure the correct humidity of the membrane, of particular importance for PEM fuel cells;
- A cooling system to keep the cell in its optimal temperature regime.

Figure 4.1 shows a schematic representation of a proton exchange fuel cell (PEMFC).

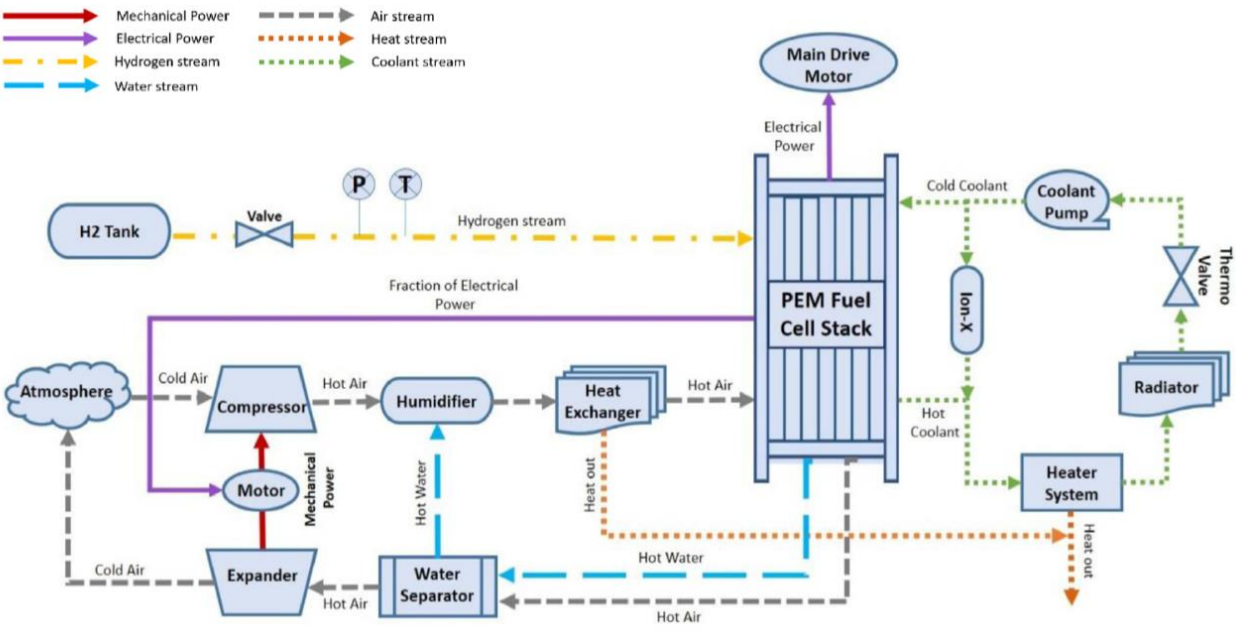

Figure 4.1. *Schematic representation of a complete system of a PEMFC* [69].

In the fuel supply circuit, to store hydrogen at the high pressures required (around 70 MPa), it is essential to equip the system with a tank. In particular, there are three main forms of hydrogen storage on vehicles [70]:

- the most used one, represented in Figure 4.1, involves the compression of hydrogen at high pressure and at environmental temperature;

- storage of hydrogen in liquid form through the use of cryogenic temperatures;
- storage of hydrogen in solid form through materials capable of combining with hydrogen to form metal alloys, such as metal hydrides.

As far as the storage of hydrogen under pressure is concerned, high pressurization is an obligatory choice due to energy factors, as can be seen from Figure 4.2, which shows the energy contained in a litre of hydrogen as a function of pressure and the equivalent litres of gasoline that guarantee the same amount of energy. In particular, the energy available in a litre of hydrogen is a low, less than 2 kW, even at a pressure of 700 bar, whose petrol equivalent is less than 0.2 litres.

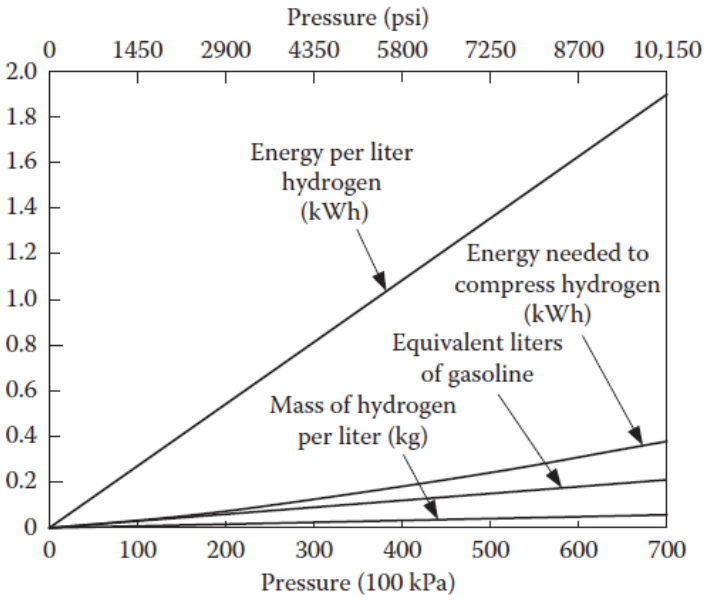

Figure 4.2. *Energy contained in a litre of hydrogen and equivalent litres of petrol, depending on the storage pressure* [62].

Furthermore, in the graph of Figure 4.2, the energy required to compress hydrogen is also shown, it represents about 20% of the total energy of hydrogen. The losses due to the air compression process, on the other hand, cover about 25% of this energy.

From Figure 4.1, it can be seen that a safety valve is installed downstream of the tank. This valve is connected to the pressure and temperature sensors, receives their signals and uses them to manage the hydrogen flow, guaranteeing the optimal predefined level of pressurization [69]. The hydrogen then flows towards the anode of the FC, an area maintained at high pressure and high

temperature to promote diffusivity through the proton exchange membrane of the PEM.

In the layout shown in Figure 4.1 there is a two-stage turbocharger, but in other configurations there may be only one centrifugal compressor driven by an electric motor. The two-stage turbocharger (or simply the single compressor) draws air from the atmosphere and sends it to the humidifier, necessary to maintain the optimal level of humidity of the membrane to ensure its maximum efficiency and durability. After being humidified, the air enters the cathode side of the FC. The pressure at which the air is in the cathode is greater than the atmospheric one because a higher pressure favours the development of the reaction and decreases the voltage losses due to the concentration of the reactants.

When the gaseous hydrogen comes into contact with the PEM (Proton Exchange Membrane), it dissociates into an ionic form. The membrane allows only the passage of hydrogen cations, while the electrons are forced to pass through an external circuit, to go towards the cathode. The incoming oxygen reacts with hydrogen cations and with free electrons to form water molecules, this is the result of an exothermic reaction.

The excess humid air that comes out of the FC and the water produced by the reaction are conveyed to the water separator, which by separating the air from the water is able to supply the air flow needed by the expander to produce a fraction of the work required by the compressor. The water collected at the separator instead feeds the humidifier, which is necessary to bring the air entering the fuel cell to the optimal hygrometric level.

The refrigerant fluid circuit is also present, an essential part of the FC system as it is able to maintain a correct operating temperature. In fact, the heat generated by the stack, in the absence of a circuit for thermal management, could excessively raise the temperature and damage the membrane of the fuel cells [69]. The refrigerant circuit is equipped with a radiator to lower the temperature of the refrigerant itself, kept in circulation by the action of a pump that guarantees the maintenance of the optimal flow rate in the circuit. In fact, a too high flow rate can damage the microchannels of the FC, while a too low flow rate may not dissipate enough heat.

In the end, an ion exchanger has also been incorporated into the system of Figure 4.1. The ion exchanger task is to remove excess ions from the refrigerant flowing into the stack. These excess ions are in fact the main cause of microchannel erosion.

As can be seen from Figure 4.1, the auxiliaries of the FC are powered by the FC itself, therefore, these auxiliaries will affect the efficiency of the system and the portion of energy generated by the fuel cell stack that can power the propulsion system. Figure 4.3 [62] shows the efficiency of the entire FC system, this efficiency differs from that shown in Figure 4.4 [62], which instead reports the efficiency of the single cell, without considering the contribution of the auxiliaries of the system.

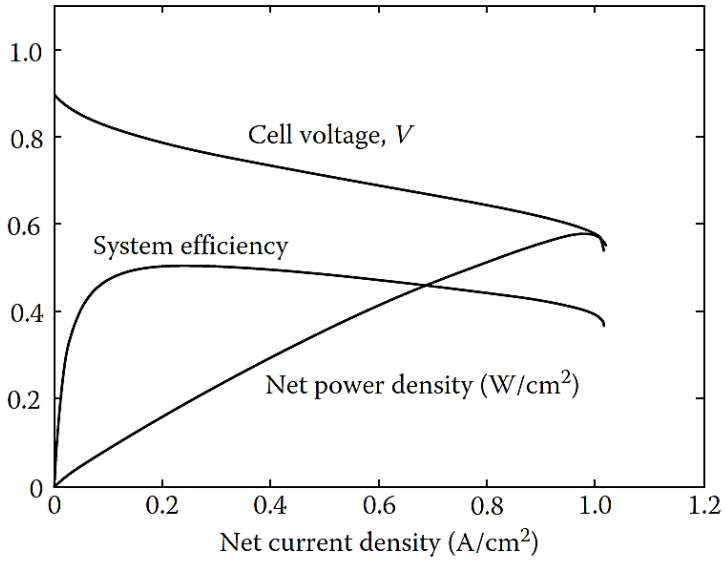

Figure 4.3. *FC system efficiency, single cell voltage and net power density as a function of the net cell current density for a Fuel Cell system* [62].

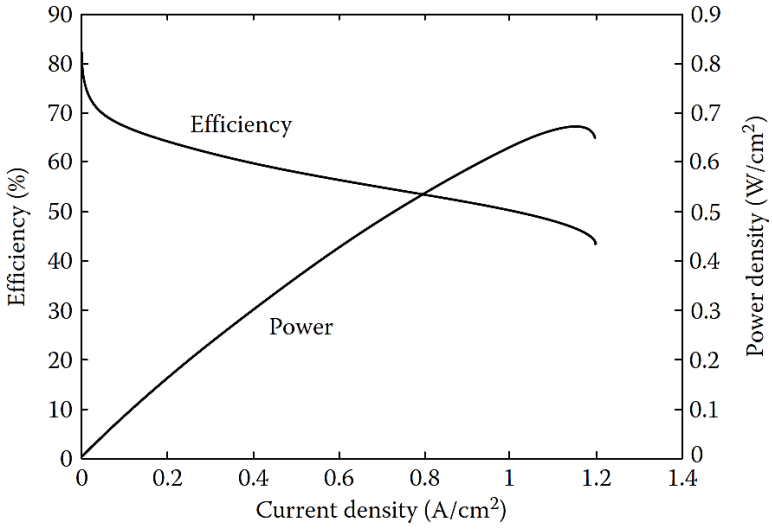

Figure 4.4. *Efficiency and output power from the single cell of the stack as a function of the current density for a hydrogen fuel cell* [62].

Figure 4.3 it can be seen that for low currents, where the cell works at high efficiency, most of its energy produced is used to power the auxiliaries, drastically reducing the efficiency of the system [62]. At high currents, on the other hand, both the voltage losses and the high-power consumption of the compressor intervene. The optimal use region of the Fuel Cell is therefore that within its average current range.

4.3 LITERATURE REVIEW

In this chapter, a model of FC and battery-based hybrid powertrain is developed as an integration of a longitudinal vehicle dynamics model. A simple EMS (Energy Management System) logic and an approximation of the FC auxiliary systems to obtain a versatile simulation tool while keeping calculation time under control are usually required for first step design and powertrain sizing. The tool is suitable for first-level design analysis, i.e., selecting the size of the various powertrain components (electric motor units, fuel cell, battery pack, etc.) and estimating fuel consumption and overall efficiency.

Some of the authors' previous work was inspirational for the model. For example, a power split logic module aimed at tuning the energy management strategy in an FC hybrid system similarly to [23], while the EMS logic applied to a longitudinal vehicle dynamics model was presented in [10] and in the Section 2 of this thesis. Such a model can be considered consolidated and validated as it has been widely used in the past few years (my Ph.D. years) by our research group (Automotive Engineering Group of the Mechanical and Industrial Engineering Department of the University of Brescia); see [22] as well, for instance.

Among the related literature, article [71] describes a hybrid vehicle model powered by FC and battery pack and created in MATLAB/Simulink. This model was created ad hoc for a vehicle, in particular, the Daewoo Tico, unlike the tool proposed in this chapter, which can be set for the simulation of various vehicles, from small cars to commercial vehicles to heavy vehicles, by appropriately setting the vehicle data and the various variables of the model through the graphical user interface of the tool itself.

Article [72] also describes a model suitable for simulating an FCHEV. This study focuses more on optimizing the energy management strategy, neglecting vehicle modelling, which is rather simplified. Some aspects are, in fact, overlooked, such as the efficiency of the transmission and the inertia of various components (wheels, rotating parts of the transmission, etc.). The same is true for the study presented in [73]. The tool described in the present chapter, created

with the integration of an FC model and an energy management logic [10], accurately considers the different components of the vehicle driveline, considering the related efficiencies and inertias.

Again, the study presented in [74] describes a power management strategy based on a fuel cell, battery and supercapacitor. The fuel economy analysis starts with the load power data resulting from a driving cycle. At the same time, the model focuses only on the FC, battery and supercapacitor components without simulating the entire vehicle, unlike the work proposed in this thesis, which was built from an existing vehicle model (TEST model [10], see Section 2) allowing for the simulation of the entire powertrain, including the driveline, FC, battery pack and power management strategy.

4.4 FC MODEL AND INTEGRATION IN THE TEST MODEL

A model was developed to study the behaviour of an FC-based hybrid powertrain system. In particular, a model simulating a PEMFC (proton exchange membrane fuel cell) was created. This model was then integrated into a powertrain model, in particular in the TEST model (see paper [10] and Section 2 of this thesis), to be used as the propulsion system in a specific simulation tool for EV vehicles through appropriate logic. The PEMFC model is written in MATLAB/Simulink. It consists of a main submodule that simulates the FC stack, integrated into the TEST model with two other submodules: one that simulates power generation by the fuel cell and the second for the power distribution control system.

4.4.1 PEMFC Stack Model

The output voltage from a fuel cell is not constant: it is linked to various operating parameters of the cell itself, such as the current delivered, the temperature of the cell, and the pressure of the reagents. For this reason, the mathematical model computes the link between voltage and current in the cell (polarization curve), as well as the open-circuit voltage and voltage drops as a function of the operating parameters of the cell. The fuel cell stack is composed of several cells in series, so the purpose is to find the output voltage of a single, elementary cell to easily calculate the total voltage of the entire FC pack as the sum of all the voltages of the individual cells, that are supposed to be equal to each other.

The net output voltage of a cell (V_{cell}) can be calculated as the difference between the open-circuit voltage and the losses in the cell when the current is drowned, as in equation (4.1).

$$V_{cell} = V_r - \nu_{act} - \nu_{ohm} - \nu_{conc} \tag{4.1}$$

where V_r is the open-circuit cell voltage, while ν_{act}, ν_{ohm}, and $\nu_{conc}$are the voltage drop due to the activation, ohmic, and concentrations loss, respectively. The reversible open-circuit voltage or Nernst voltage is given by the energy released from the chemical reaction inside the cell and is mathematically calculated applying the Nernst equation [59,75]. The standard Nernst voltage is evaluated using the thermodynamic values of the standard state, as shown in [62]. If the temperature is different from the standard one (298.15 K), the open circuit voltage can be calculated by modifying the equation as shown in (4.2).

$$V_r = 1.229 - 0.85 \cdot 10^{-3}\left(T_{fc} - 298.15\right) + 4.3 \cdot 10^{-5}\, T_{fc} \left[\ln\left(p_{H_2}\right) + \frac{1}{2}\ln\left(p_{O_2}\right)\right] \tag{4.2}$$

where the Nernst voltage (V_r) is expressed in Volts. The value 1.229 is the reference potential expressed in Volts, T_{fc} is the temperature (expressed in Kelvin) of the Fuel Cell, and p_{H_2} and p_{O_2}, expressed in atm, are the partial pressure at the anode and at the cathode, respectively. The definition of the three voltage drops depends on different cell operating conditions, such as the temperature, the humidity of the membrane, and the current required.

The activation loss (ν_{act}) results from the chemical reaction occurring in the two electrodes: the break of chemical bonds, the transfer of electrons, and the creation of new bonds. The relation between the activation loss, expressed in Volts, and the output current (I_{fc}) is described in (4.3), where a series of parametric coefficients (ξ_1, ξ_2, ξ_3, ξ_4) is used to explain the Tafel equations [59].

$$\nu_{act} = -\left[\xi_1 + \xi_2 T_{fc} + \xi_3 T_{fc} \ln\left(p_{O_2} 1.97 \cdot 10^{-7} e^{\frac{498}{T_{fc}}}\right) + \xi_4 T_{fc} \ln\left(I_{fc}\right)\right] \tag{4.3}$$

where the output current is expressed in Ampere, and the temperature is expressed in Kelvin.

The Ohmic loss (ν_{ohm}) is related to the internal resistance of the cell due to the resistance of the electric circuit of the cell (R_C) and the resistance in the membrane during the transfer of protons (R_M). The second one is dominant, and it is related to the geometrical parameters of the cell, as shown in (4.4).

$$\nu_{ohm} = I_{fc} \cdot R_{ohm} = I_{fc} \cdot (R_C + R_M) = I_{fc} \cdot \left(Rc + \frac{\rho_M \cdot l_M}{A}\right) \tag{4.4}$$

where ν_{ohm} is expressed in Volts, R_{ohm} is the total resistance of the cell (in Ohm), while ρ_M is the membrane resistivity ($\Omega \cdot$ cm), l_M is the membrane thickness (cm), and A is the active cell area (cm^2). Usually, R_C, l_M, and A are constant values

reported in the dataset of the cell, while resistivity is correlated with the operative parameter of the cell (I_{fc} and T_{fc}), and it can be expressed as follows in equation (4.5).

$$\rho_M = \frac{181.6 \cdot \left[1 + 0.03 \cdot (I_{fc}/A) + 0.062 \cdot (I_{fc}/A)^{2.5} \cdot (303)^2\right]}{\left[\lambda - 0.634 - 3 \cdot (I_{fc}/A)\right] \cdot e^{4.18\left((T_{fc}-303)/A\right)}} \tag{4.5}$$

The parameter λ defines the humidity of the membrane, and it could be considered a constant and expressed in the dataset of the cell.

Lastly, the concentration loss (v_{conc}) is a loss of potential due to the inability of the cell to replace the reactants instantaneously in the electrodes, so it is related to the mass transfer. In (4.6), v_{conc} is expressed in Volts, and it is a function of the fraction between the actual current density ($J = I_{fc}/A$) and the maximum current density of the cell (J_{max}), both expressed in A/cm^2.

$$v_{conc} = -\beta \, ln\left(1 - \frac{J}{J_{max}}\right) \tag{4.6}$$

where β is a parametric coefficient expressed in Volts.

The net output voltage range produced from the single cell is usually between 0 and 1 Volts (typically 0.7 V).

In this model, pressures at the electrodes are assumed constant, and variation of temperature during the cell cycle is considered negligible, so the temperature is also constant. To obtain the polarization curve, the current required is set as a value that linearly grows between the minimum and maximum values. The model calculates the output voltage of the single cell, and this value is multiplied by the number of cells to obtain the output voltage and the polarization curve of the FC stack.

4.4.2 Integration of FC Powertrain into TEST Model

Through the above model, it is possible to define the characteristic curve of the FC stack. These data are then transferred to the TEST model [10], where they are used to define the dataset of the FC-based powertrain system. As previously mentioned, the TEST model simulates electric vehicles, so it was necessary to integrate new modules able to simulate the behaviour of the FC into the original model. However, all the original features of the model are maintained. Thus, it is still possible to simulate full electric vehicles and APU (Auxiliary Power Unit) hybrid electric vehicles. The user can set the presence or absence of the FC through a graphical user interface, and if the FC is not present on the vehicle, the model will follow the same calculation steps described in

Section 2 of this thesis. The schematic illustration of the operations performed in the TEST model is reported in Figure 4.5, with a focus on the new module added in this study, represented by the blocks in dashed lines. The purpose is also to maintain the characteristics of the TEST model: reliability, calculation speed, and flexibility. The first step is the introduction of a module that manages the power split between FC and PPS.

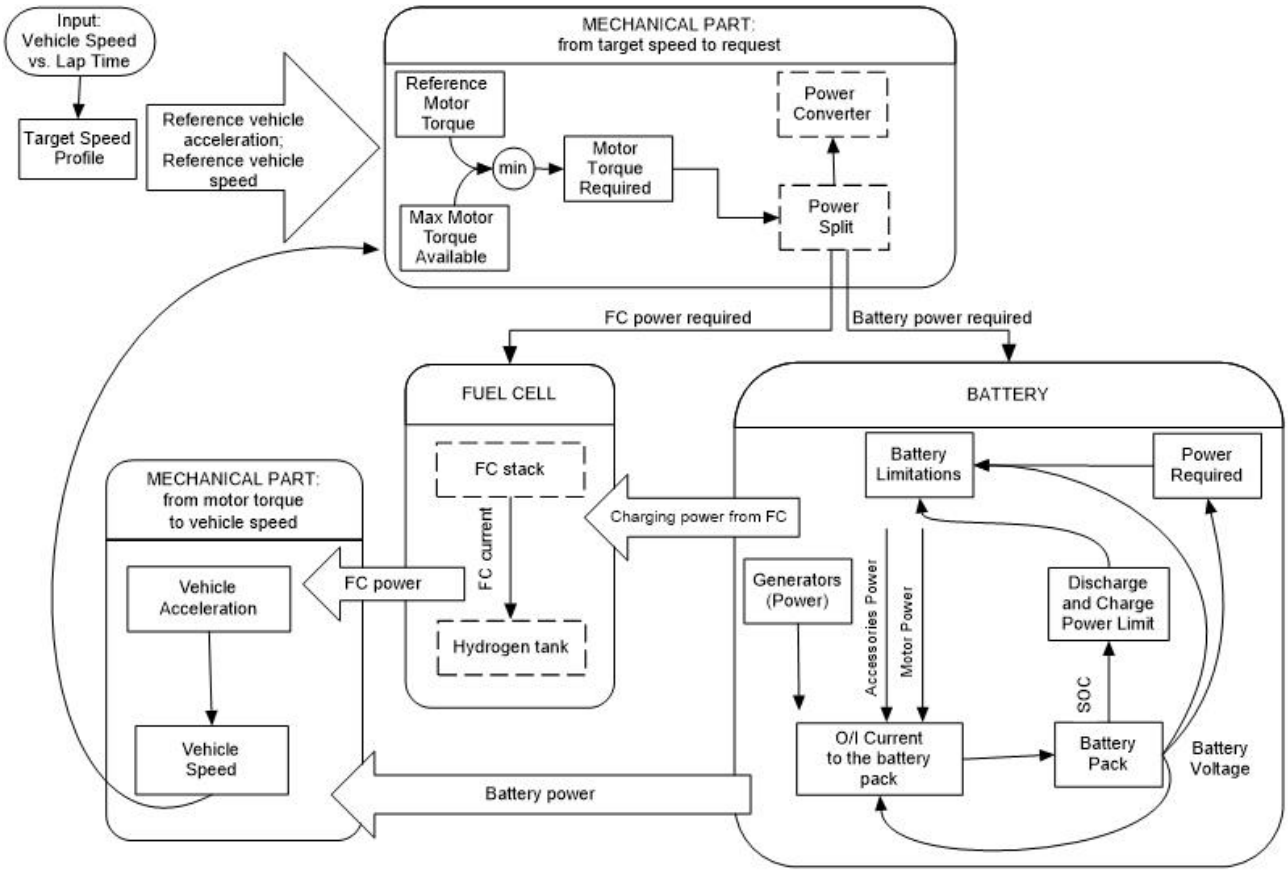

Figure 4.5. *Conceptual scheme of the TEST model* [10]. *The new modules introduced for the simulation of the FC hybrid powertrain are reported in dashed lines. The arrows indicate the computational flow (not the energy flow): a backward-facing approach is adopted as in* [10,21]. *In the field of vehicle dynamics simulations, a backward-facing approach consists, in fact, of a calculation flow that goes from the target speed profile or, in any case, from the variables (forces, torques, speeds, etc.) associated with the wheels, all the way back to the variables related to the motors and to the system supplying the energy (battery pack and FC). Following the backward-facing approach, the power that the FC is requested to generate is calculated starting from the required motor torque; therefore, once the operating point of the FC has been calculated, it is possible to calculate the hydrogen consumption and the flow from the hydrogen tank.*

4.4.2.1 Power Split Module

Because of the low efficiency of the FC stack at low and high power, due to the high consumption of energy of the auxiliaries, the FC is usually introduced in hybrid vehicles with a series architecture. The power flows between the peak power source (PPS) and FC are controlled by the power management system of the vehicle. According to the power or torque inputs received from the accelerator, the brake pedal, or other operating signals, the vehicle controller splits the energy flow between the fuel cell system and the PPS. The control strategy should ensure that the fuel cell system operating point is within its optimal operating region, which is typically in the middle power range [76]. Furthermore, the PPS's energy level is always maintained within its optimal region. The possible operating modes of the drivetrain are the following.

1. *Hybrid traction mode*: if the power required by the electric motor is greater than the maximum power of the FC (P_{FCmax}), the fuel cell system operates at its rated power.
2. *FC alone traction mode*: if the power required is between the minimum (P_{FCmin}) and maximum (P_{FCmax}) power of the FC, the traction is guaranteed only by the latter. The battery pack can be recharged by the FC if necessary.
3. *PPS alone traction mode*: if the power required is smaller than the pre-set minimum power (P_{FCmin}) of the fuel cell system, the fuel cell system can be turned off, or it can charge the batteries if needed.
4. *Charging mode*: if the power required is smaller than the maximum power of the fuel cell system and the PPS needs charging, FC charges the batteries. This operating mode can be active both in the case of "*FC alone traction mode*" and in the case of "*PPS alone traction mode*".

A power split module input is the traction power required by the electric motor/s (P_{tot_req}), computed in the power required module as the sum of the front and rear motor power, obtained by means of equations (2.18) and (2.19) reported in Chapter 2. A second input of the module is the battery pack's state of charge (SOC), referred to as the previous instant of the iteration. The power split block includes a series of "if" checks that first verify if the tested vehicle has the Fuel Cell and, in the case of the FC hybrid powertrain, define the operating modes. In this case, using the logic described before, the module calculates the power required from the battery (P_{batt_req}) and the power required from the FC (P_{FC}). In the case of charging mode, it is also necessary to define the fraction of FC power that is used to charge the PPS ($P_{gen\_FC\_th}$).

In the case of "*hybrid traction mode*", the power required from the batteries is calculated as in equation (4.7), and $P_{gen\_FC\_th}$ is set equal to zero.

$$P_{batt\_req} = P_{tot} - P_{FCmax} \tag{4.7}$$

where P_{tot} is the sum of the traction power request (P_{tot_req}) and the power of the auxiliary systems.

The "*PPS alone traction mode*" is divided into two cases, according to the battery SOC. If the SOC is less than a set limit value (SOC_{max}), the FC works at idle and charges the batteries ($P_{gen\_FC\_th}$ is equal to P_{FCmin}). Vice versa, the FC is turned off ($P_{gen\_FC\_th}$ is equal to zero). In both two cases, the battery pack alone guarantees traction (P_{batt_req} is set equal to P_{tot}).

The "*FC alone traction mode*" is also divided into two cases, according to the battery SOC. If the SOC is less than a set limit value (SOC_{min}), which must be less then SOC_{max}, the FC operates at its maximum power, ensuring vehicle traction and supplying the excess power to the batteries. In this case, $P_{gen\_FC\_th}$ is calculated as the difference between P_{FCmax} and P_{tot}. On the other hand, the FC delivers exactly the power required to ensure traction without recharging the batteries ($P_{gen\_FC\_th}$ is set equal to zero). In both cases P_{batt_req} is set equal to zero.

Finally, the power of the FC is calculated as in equation (4.8).

$$P_{FC} = P_{tot} + P_{gen\_FC\_th} - P_{batt\_req} \tag{4.8}$$

Lastly, a binary output signal is generated to define which system between the battery pack and FC is the main energy source in an instant.

4.4.2.2 Power Converter Module

The power converter block, shown in Figure 4.5, defines the power bus voltage of the hybrid FC and PPS system as a function of the binary value calculated in the power split module. If the FC is off, the bus voltage is imposed equal to the battery voltage, obtained in output from the data sheet battery block of the Simulink Library Browser [10]. Otherwise, the bus voltage is set equal to FC voltage, calculated as the ratio of PFC and the FC current. The latter is estimated thanks to the lookup table containing the information regarding the characteristic curve of the FC (power vs. current) obtained from the PEMFC stack model (see Section 4.4.1).

4.4.2.3 Adjustment to the Electrical Part

As shown in Figure 4.5, the battery power required (P_{batt_req}) is sent to the battery limitation module, which verifies if the input and output power limits to the battery pack are respected and defines the effective power of the battery.

Within this block, the inequalities (2.24) and (2.25) reported in Section 2.2.2, that compute the case of battery discharge or charge, are replaced with inequalities (4.9) and (4.10), which are introduced in the inequalities of the power generated by the fuel cell ($P_{gen\_FC\_th}$), calculated in the previous section.

Discharge of battery pack:

$$P_{batt\_req} + P_{acc} - P_{gen\_th} - P_{gen\_FC\_th} \geq 0 \tag{4.9}$$

Charge of battery pack:

$$P_{batt\_req} + P_{acc} - P_{gen\_th} - P_{gen\_FC\_th} < 0 \tag{4.10}$$

P_{acc} is the total power consumed by the vehicle auxiliaries, and P_{gen_th} is the power supplied by generators, imposed to zero in the case of the FC hybrid powertrain.

The power generated by the fuel cell and sent to the battery pack is also introduced into the equation to calculate the power available from the battery. In case of discharge, the available power ($P_{available}$), which can be taken from the battery pack, is defined in equations (2.26) and (2.27) in the Section 2.2.2.1 of the Chapter 2. These equations are rewritten with equations (4.11) and (4.12).

If the discharge limit of the battery pack is supplied as a limit current (positive, $I_{dischrg\_limit}$):

$$P_{available} = (V \cdot I_{dischrg\_limit}) - P_{buffer} - P_{battI2R} + P_{gen\_th} + P_{gen\_FC} \tag{4.11}$$

If the discharge limit of the battery pack is supplied as a limit power (positive, $P_{dischrg\_limit}$):

$$P_{available} = P_{dischrg\_limit} - P_{buffer} - P_{battI2R} + P_{gen\_th} + P_{gen\_FC} \tag{4.12}$$

V is the battery voltage, P_{buffer} is a constant power that defines a tolerance, and $P_{battI2R}$ is the power dissipated by the Joule effect. In this case, the input power supplied by the fuel cell does not have to be limited, so usually, there is no limitation on FC power, and the FC power that is given to the battery charge (P_{gen_FC}) is equal to $P_{gen\_FC\_th}$. In case of a discharge of the battery pack, if there are no limitations, the total power that the motors absorb (P_{mot_tot}) is calculated using equation (4.13).

$$P_{mot\_tot} = P_{batt\_req} + P_{FC} - P_{gen\_FC} \tag{4.13}$$

In case of limitations due to the battery state, if the available power of the batteries is sufficient to power the auxiliaries, part of this power will be delivered to them, and the remaining part will be used to power the motors in addition to

the power that the FC sends to the motors. The last modification relating to this case, in the presence of FC, is to use the bus voltage to calculate the motor torques. In equations (2.28) and (2.30) presented in Section 2.2.2.1, the voltage V of the battery pack is replaced by the bus voltage.

Whenever the battery charge is active, the following inequality is checked to verify if the battery pack can absorb all the input power: equation (4.14) replaces the inequality (2.35) reported in Chapter 2.

$$P_{absorbable} + P_{gen\_th} + P_{gen\_FC\_th} - P_{tot\_req} \leq 0 \tag{4.14}$$

where $P_{absorbable}$ is the maximum power that the battery pack can absorb at that instant. It is therefore observed that the addition of the power generated by the fuel cell, in this case, is more limiting. Where there are limitations in the charging phase, the original model turns off (or partializes) the generators. In this case, where the generators are replaced by the FC, this FC is turned off. This is managed through switches that recognize the presence of the fuel cell through a parameter, which is set equal to one if the fuel cell is not present; otherwise, it is equal to zero. Even in the case of charging, if there is a limitation of the motors, in the presence of FC, the motor torque computation is based on the bus voltage instead of the battery pack voltage.

In equations (2.38) and (2.40), the voltage V of the battery pack is replaced by the bus voltage. In the output of the battery limitation block, the effective FC charging power absorbed by the batteries (P_{gen_FC}) is also added with respect to the model described in Chapter 2 and in paper [10]. The effective FC charging power value is equal to $P_{gen\_FC\_th}$ in case there are no limitations, and it is sent to the fuel cell block.

4.4.2.4 Fuel Cell Module

Once the power required from the fuel cell has been calculated, it is possible to define its operative working point. This operation is carried out within the fuel cell block. In this module, the hydrogen consumption is also calculated, which is useful to define the autonomy range of the vehicle. Inputs to this block are the FC power required (P_{FC}), the theoretical charging power ($P_{gen\_FC\_th}$), and the effective power absorbed by the battery pack (P_{gen_FC}). The first operation in this module is to verify the operative condition of the FC: if the power required is zero, the FC is off, and the FC voltage and current are set to zero. If the power is higher than zero, the effective FC output power (P_{FC_eff}) is calculated, considering the effective charging power sent to the battery, using equation (4.15).

$$P_{FC\_eff} = P_{FC} - P_{gen\_FC\_th} - P_{gen\_FC} \tag{4.15}$$

From the effective power, it is possible to know the operative voltage (V_{fc}) and current (I_{fc}) of the cell through the array obtained by the module's FC stack. The output current is then used to calculate the consumption of hydrogen mass flow ($\dot{m}_{H_2}$), expressed in g/s, using equation (4.16).

$$\dot{m}_{H_2} = W_{H_2}(nI_{fc}/2F) \tag{4.16}$$

Where W_{H_2} is the molar mass of hydrogen (2.016 kg/mol), n is the number of FC cells, and F is the Faraday number. By subtracting the integration of $\dot{m}_{H_2}$ over time from the mass of hydrogen present in the tank at the start of the simulation, the quantity of hydrogen in the tank during the cycle is estimated.

4.4.3 PEMFC Graphic User Interface

In the graphic interface of the TEST model described in Section 2.3, a Tab has been added for the definition and for the control of the quantities necessary for the operation of the portion of the model relating to the PEMFC logic (see Figure 4.6).

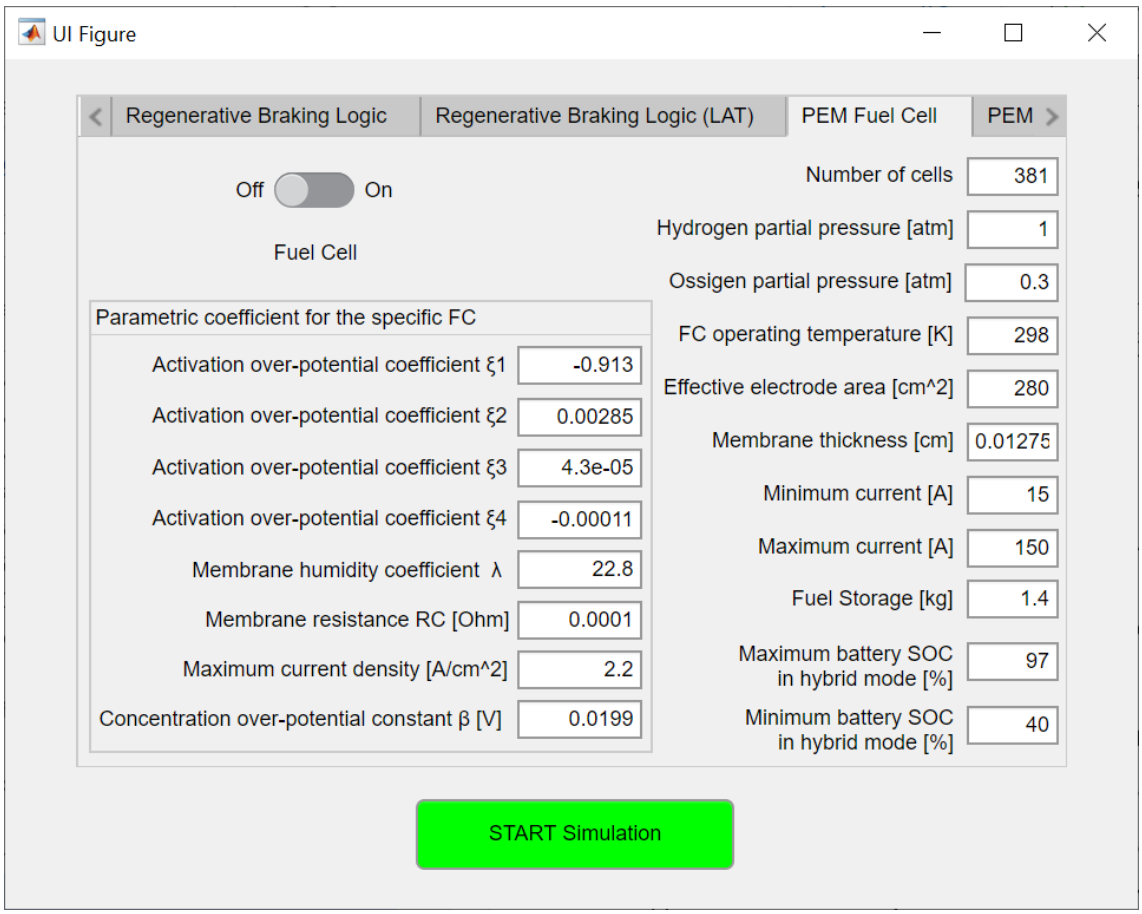

Figure 4.6. *"PEM Fuel Cell" panel of the Graphic User Interface of the TEST model. In particular, this panel allows you to enter the inputs regarding the PEMFC logic.*

In particular, thanks to the panel shown in Figure 4.6 it is possible to define the following parametric coefficients of the proton exchange membrane fuel cell model: the four parametric coefficients (ξ_1, ξ_2, ξ_3 and ξ_4), the humidity coefficient of the membrane (λ), the membrane resistance (R_C), the maximum allowable current density (J_{max}) and, finally, the constant of the concentration over-potential (β).

Again thanks to the Tab shown in Figure 4.6, it is also possible to set the values of the following quantities: the number of cells (n) of the fuel cell stack, the partial pressure of hydrogen at the anode of the fuel cell (p_{H_2}) , the partial pressure of oxygen at the cathode (p_{O_2}), the operating temperature of the cell (T_{fc}), the effective area of the electrodes (A), the thickness of the cell membrane (l_M), the minimum and maximum current admissible (or desired) output from the fuel cell stack, the maximum quantity of hydrogen that can be stored in the relative tank and, finally, the two values, minimum (SOC_{min}) and maximum (SOC_{max}), of SOC of the battery pack used for the EMS logic of the hybrid vehicle equipped with fuel cell.

4.5 VALIDATION AND SIMULATION

4.5.1 Validation of the FC Stack Model

The model of the FC stack was validated using the information collected in [60] on the PEMFC stack model BCS 500W (American Company BCS Technologies, North Sydney, Australia). For the validation of the PEMFC model, reference was made to paper [60] as it describes the same FC in a very exhaustive way, and it is complete with all the necessary data, reported here in Table 4.1.

Table 4.1. *Specifications of the studied BCS-500W PEMFC stack from the dataset* [60].

Parameter	Value	Unit
Number of cells	32	-
Effective electrode area	64	cm^2
Membrane thickness	0.0178	cm
Maximum density of the cell	0.469	A/cm^2
Hydrogen partial pressure	1	atm
Oxygen partial pressure	0.209	atm
FC operating temperature	333	K

Table 4.2 reports the optimized parameters extracted in the study; these values are obtained with the MAEO optimization algorithm (Table 4 of [60]). The range of output current required was set between 0.5 A and 30 A.

Table 4.2. *Parameters of BCS-500W PEMFC stack obtained by optimization algorithms* [60].

Parameter	Value	Unit
ξ_1	−0.856	–
ξ_1	2.73×10^{-3}	–
ξ_1	6.63×10^{-5}	–
ξ_1	1.928×10^{-4}	–
λ	1.004×10^{-4}	–
β	20.7	V
R_C	0.016	Ω

The model outputs are compared with the experimental values measured from the cell, obtained from the graphs of FIGURE 7 of study [60]. The results are displayed in Figure 4.7 and reveal a good estimation of PEMFC output power and a little overestimation of output voltage.

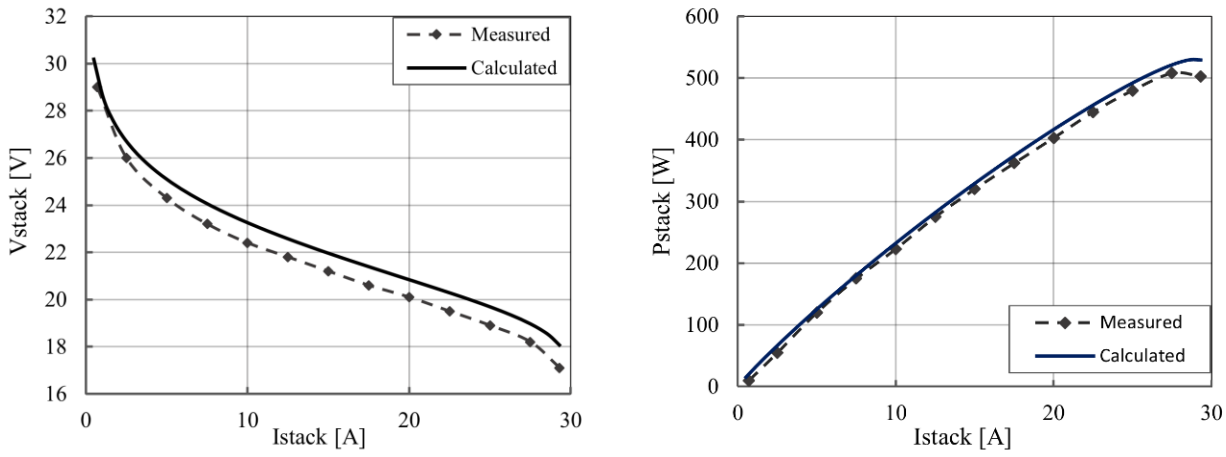

(**a**) (**b**)

Figure 4.7. *FC model results ("Calculated") compared with effective values ("Measured")* [60] *for the BCS-500W PEMFC stack; (**a**) polarization curve; (**b**) power vs. current curve.*

4.5.2 Simulation Data

This section presents a simulation carried out with the model described above. The simulation parameters are presented first, related to the specific vehicle and the FC adopted in particular. The vehicle and fuel cell under consideration were chosen mainly due to data availability. In any case, what is important to show here is not the numerical results and the input parameters chosen for the simulation but the type of results that can be obtained from the model, i.e., the quantities that are obtained and the trend of quantities shown in

the graphs of the following section, useful, in particular, to understand the power split logic and therefore the interaction between FC and PPS.

The model was tested on a low-power vehicle, particularly a prototype of a full-electric waste collection vehicle, which was converted to a hybrid hydrogen vehicle. The data of this vehicle are taken from [10] (data reported in Section 2.4.1 of this thesis), where it is used for the validation of the original tool (original TEST model) and are collected in Table 2.1. For this test, a study for the sizing of the batteries was not initially performed; therefore, the original batteries [10] (described in Section 2.4.1.3 of this thesis) were maintained as a peak power source, a fuel cell was added as the primary power device, and a high-pressure hydrogen tank has also been added. The weight of the vehicle does not change from the original case. This is due to the assumption that the increase in weight caused by the addition of the FC is balanced with a reduction of the maximum load of the waste collected.

The FC Ballard Mark 700, produced by Ballard Power Systems, Burnaby, Canada, (used in the model Ford P2000) is chosen for this vehicle. The data of this cell are collected in [68] and reported in Table 4.3 in the section "Specifications of the Studied PEMFC Stacks". From this case study, the polarization curve of the single cell was also taken to calculate the corrective parameters described in Section 4.4.1, which are obtained experimentally starting from the allowable range values of PEMFC parameters described in Table 1 of paper [60]. The results are reported in Table 4.3, section "Optimized Parameters".

Table 4.3. *Parameters of the PEMFC Ballard Mark 700* [68].

Specifications of the Studied PEMFC Stacks		
Parameter	**Value**	**Unit**
Number of cells	381	-
Effective electrode area	280	cm^2
Membrane thickness	0.01275	cm
Maximum current density	2.2	A/cm^2
Hydrogen partial pressure	1	atm
Oxygen partial pressure	0.3	atm
FC operating temperature	298	K
Optimized Parameters		
Adjustable parameter ξ_1	−0.913	-
Adjustable parameter ξ_2	0.00285	-
Adjustable parameter ξ_3	4.3×10^{-5}	-
Adjustable parameter ξ_4	1.1×10^{-4}	-
Water content in the membrane λ	22.88	-
Coefficient for concentration loss β	0.0199	V
Resistance of a single cell R_C	0.001	Ω

The design of the FC was chosen according to the maximum power (40 kW) of the traction motor during a typical driving cycle of the vehicle in an urban environment. The peak power of this FC is 50 kW; thus, the current working range for the fuel cell is limited to a lower range, from 15A to 150A, which corresponds to a minimum power of 5 kW and a maximum of 40.8 kW, so as not to overestimate the work of the FC during the cycle. These are, however, only general, base-level considerations. For a thorough powertrain design of the vehicle under consideration, real-world data of FC, PPS, and hydrogen tanks would be required. The capacity and pressure of the hydrogen tank were set equal to the data available for the Ford P2000: the tank features a capacity of 1.4 kg of hydrogen at the pressure of 24.8 MPa [63]. These values were chosen in agreement with the FC in the exam [68]. Passenger cars in Europe, however, can store hydrogen up to a maximum pressure of 700 bar. It is, therefore, possible to consider an increased storage pressure with the consequent effects on the maximum flow rate from the tank. The latter is an input to the model and can be modified through a graphical user interface.

In the end, the power management system parameters were set; the SOC limit values adopted in the logic were defined: SOC_{min} was set equal to 40%, and the SOC_{max} was set to 90%. These values were chosen to preserve the FC's correct operating working conditions and avoid numerous FC shutdowns during braking. They could be modified for a different type of vehicle, battery pack and driving cycle. For the simulation, the initial SOC of the battery pack was chosen to be equal to 92% to analyse different FC working modes.

4.6 SIMULATION RESULTS

The target speed profile simulated in this work is a WLTC for Class 1 vehicles [38,77], shown in Figure 4.8. The vehicle studied in this work is aimed at waste collection, so it's typical driving cycle features many stop-and-go cycles and short travelling distances at low speed through an urban route. Its typical mission profile is similar to this type of driving cycle [24].

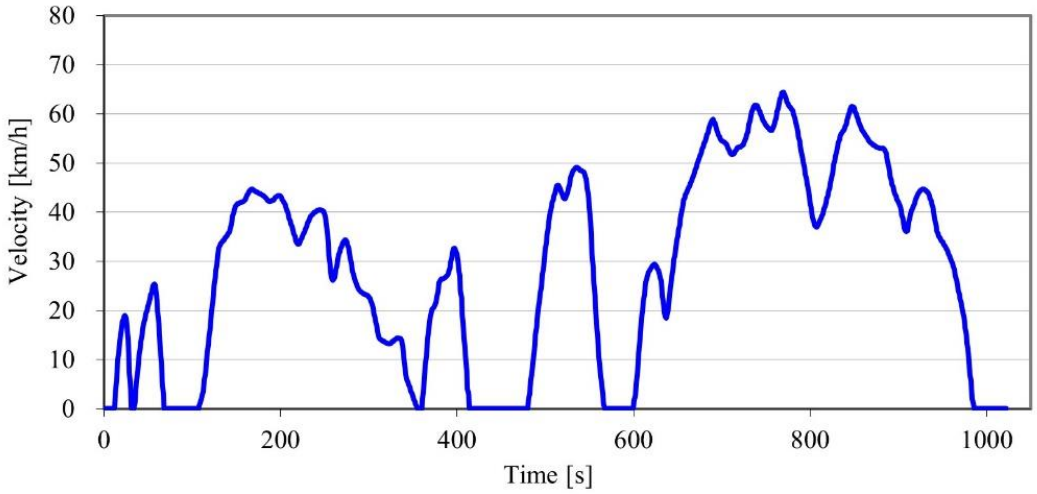

Figure 4.8. *WLTC Class 1 speed profile* [38,77].

In addition to the charts featured by the original model [10] described in Chapter 2, showing trends associated with the vehicle's mechanical and electrical systems, a chart with the FC operating parameters is added to the output graphs, as shown in Figure 4.9. This chart reports the electric parameters of the FC (power, current, voltage), the bus domain settings (a binary parameter equal to 1 if the PPS is the primary power source, equal to 0 if the FC is the primary power source), the input voltage to the electric motor, and the mass of hydrogen in the fuel tank.

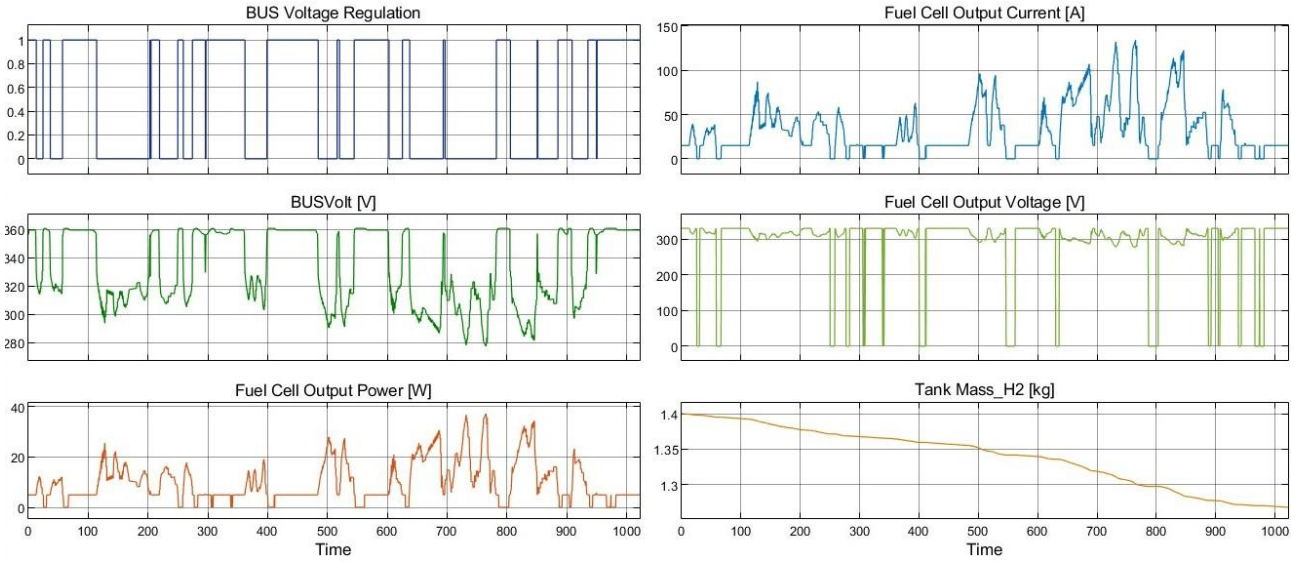

Figure 4.9. *Overview of the model results. In abscissa, the time is expressed in seconds. (**Top left**): the "Bus Voltage Regulation" that is the binary parameter equal to 1 if the FC is off or at idle (when the PPS is the primary power source), or equal to 0 if the FC is on and it is the primary power source of the propulsion system. (**Middle left**): "BUSVolt", the input voltage to the electric motor. (**Bottom left**): fuel cell power. (**Top right**): fuel cell current. (**Middle right**): fuel cell voltage. (**Bottom right**): mass of hydrogen in the tank.*

The first result that is analysed is the behaviour of the EMS, illustrated by the binary output of the power split module represented in Figure 4.10.

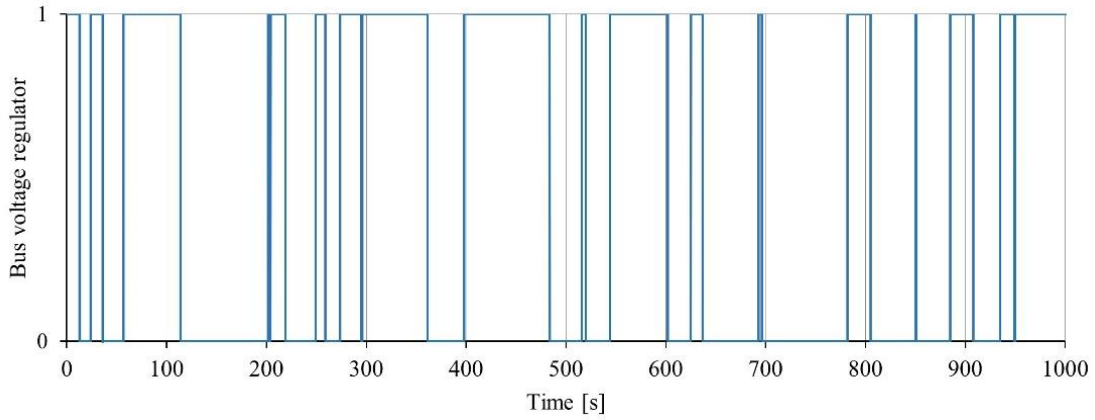

Figure 4.10. *The binary output of the power split module for the control of the power flux. The binary value is equal to 1 if the FC is off or at idle (the battery pack is the primary power source) and 0 if the FC is active and it is the primary power source.*

Due to the several stop-and-go cycles and frequent decelerations, the output of Figure 4.10 is a square signal, and both the power sources come into play during the cycle. In the design and dimensioning phase, this situation of frequent on/off of the FC should be avoided. In Figure 4.11, it is possible to see the output power of the FC during the simulation: the FC works at idle or is inactive whenever the battery is the primary power source, in other words, when the BUS voltage regulator is equal to one.

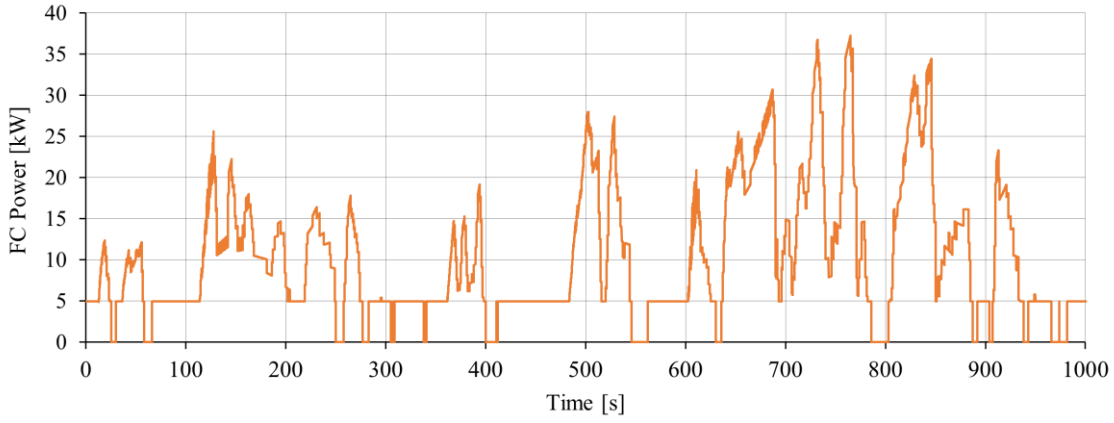

Figure 4.11. *Output power of the fuel cell stack.*

Figure 4.11 also shows that sometimes the FC is switched off because of limitations due to the maximum power absorbable to the battery. In fact, in some time intervals with low power demand, the FC cannot work at idle by recharging the batteries with the surplus power as the latter exceeds the maximum charging power accepted by the battery pack (for example, because the latter is already at a high state of charge). In Figure 4.12, the intervention of the FC limitation due to the battery is shown. In these short intervals, the vehicle is braking, and the charging power in input to the battery is too high, so the EMS suspends the FC charging mode to preserve the PPS.

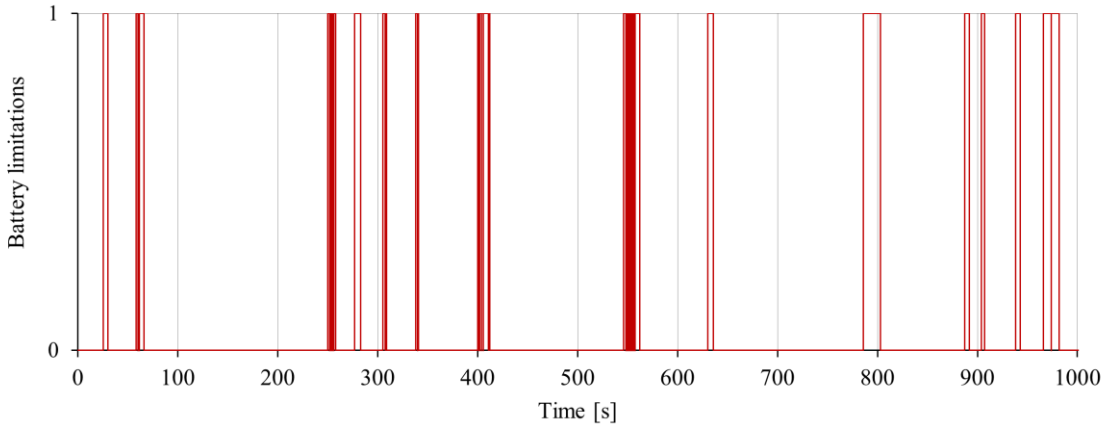

Figure 4.12. *The battery limitation binary parameters. The binary value of "Battery limitations" is equal to 1 if any battery limitations occur; it is equal to 0 if vice versa. "Battery limitations" means that the battery pack cannot be recharged with the power that the EMS logic would provide by the FC. Therefore, the system is limited, and the EMS logic causes the FC to stop power flow towards the PPS.*

During the cycle, many limitations occur, and this is due to the logic implemented in the hybrid system, but in particular, it is due to the parameters of the simulation (PPS size, FC). The system should therefore be correctly sized to avoid this. The last parameter of the FC system is the mass of hydrogen in the tank, shown in Figure 4.13, which is useful for estimating the vehicle's range. During this simulation, the vehicle consumed approximately 0.13 kg of hydrogen. The system will therefore also be sized in such a way as to minimize hydrogen consumption, thus making the system more efficient and increasing the range of the vehicle, or vice versa, reducing the volume and weight of the tank within the same vehicle range. The suitable range will be selected based on the typical mission profile for the vehicle.

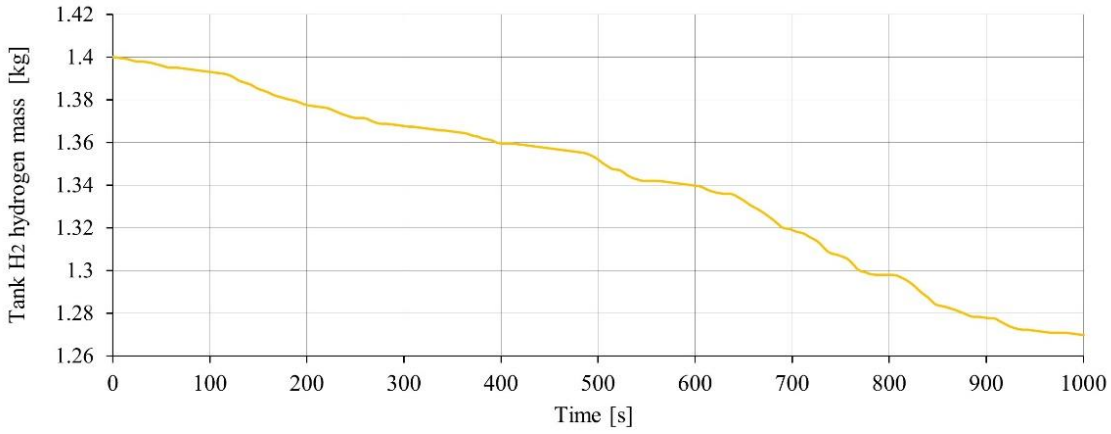

Figure 4.13. *Mass of hydrogen contained in the tank. Useful for monitoring the consumption of hydrogen and the vehicle's remaining range.*

Lastly, it is interesting to analyse the state of charge of the battery pack during the cycle, as illustrated in Figure 4.14. The logic improvement guarantees that the SOC decreases during the cycle staying in its optimal range. This situation is to be pursued during the design phase, taking into account the optimal range of the battery pack chosen for the project, which may vary according to the type of battery.

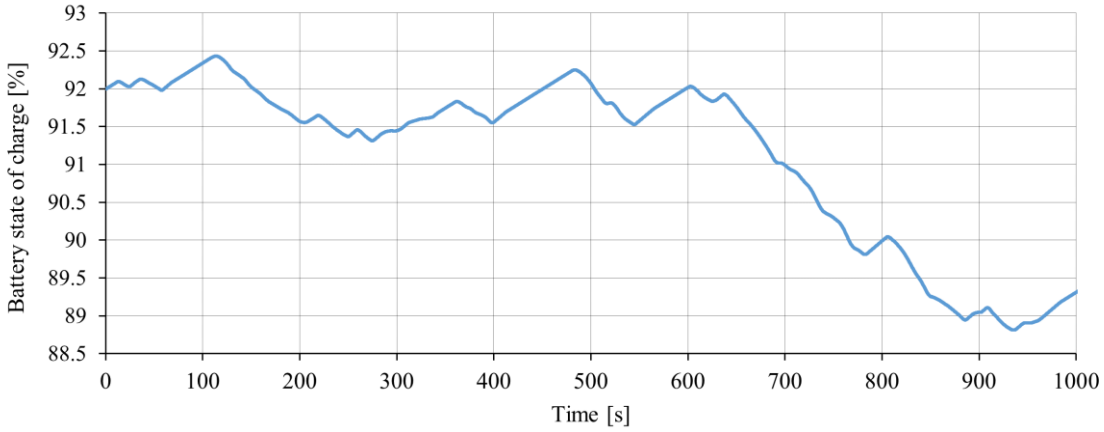

Figure 4.14. *Battery pack state of charge (SOC).*

4.7 FC COMPRESSOR MODEL

One of the FC auxiliaries responsible for a large part of the energy demand is the compressor, which is estimated to be able to absorb up to 80% of the power consumed by the total auxiliaries and given that it provides the supplement of

oxygen necessary for the reaction with hydrogen, it remains one of the key parts in the whole FC system. For this reason, it was chosen to integrate a compressor model within the TEST/PEMFC model [10,20,58], in order to analyse and size this component too through the simulations of the TEST model. This compressor modelling work was carried out in collaboration with a master's thesis work [78] and thanks to the contribution and analysis of the scientific article [69].

For the compressor modelling, two modules have been added to the version of the Simulink TEST model with integrated the possibility of simulating hybrid vehicles equipped with proton exchange fuel cell (PEMFC):

- the "Air request" subsystem, for the calculation of the required air flow, instant by instant, for each operating point during the simulation;
- and the "FC Compressor" subsystem, which contains the main compressor information, and which calculates the power required to supply the compressor itself.

In addition, the ability to enable or disable the logic described in this section has been implemented. If the compressor model is disabled, for the simulation in question, the calculations carried out in the "Power Split" block, described in Section 4.4.2.1, remain unchanged. In particular, the total power P_{tot} required by the vehicle system is equal to the sum of the power required for traction (P_{tot_req}) and the power required to power all the auxiliaries of the vehicle (including those relating to the fuel cell system). In this case, therefore, when the user sets the simulation data in the graphic user interface of the TEST model, he must also include the auxiliaries of the FC in the definition of the power of the vehicle accessories (P_{acc}, see Section 2.3 and Figure 2.14). If, on the other hand, the compressor logic is active, the P_{tot} power is calculated as in the following equation, (4.17):

$$P_{tot} = P_{tot\_req} + P_{acc} + P_{comp} \cdot \frac{100\%}{Perc_{comp/acc}} \tag{4.17}$$

where P_{comp} is the power required to supply the compressor and $Perc_{comp/acc}$ is the portion, expressed as a percentage, of the power consumed by the compressor with respect to the total power consumed by all the auxiliaries of the FC (including the compressor itself). This percentage, as already mentioned, is typically estimated at 80%.

The term $P_{comp} \cdot \frac{100\%}{Perc_{comp/acc}}$ therefore allows us to consider the power consumed by the compressor, calculated by means of the compressor model itself

and the remaining portion of power consumed by the other accessory components of the FC.

In the following sections, the two modules mentioned above will be described in detail: for the calculation of the air flow required by the compressor and the power required for its operation.

4.7.1 "Air request" Module

The "Air request" subsystem, built in Simulink, receives the hydrogen flow ($\dot{m}_{H_2}$) at the input from the "Fuel Cell" module and outputs the air flow requested to the compressor, calculated using the relation (4.18).

$$\dot{m}_{air} = \frac{\dot{m}_{O_2} \cdot W_{air}}{W_{O_2} \cdot \emptyset} \tag{4.18}$$

where $\dot{m}_{O_2}$ is the oxygen flow rate (expressed in kg/s), calculated through the equation (4.19), W_{air} is the molecular mass of ambient (humid) air, W_{O_2} is the molecular mass of oxygen and $\emptyset$ is the percentage of oxygen in the air mixture.

$$\dot{m}_{O_2} = \frac{\theta_{H_2/O_2} \cdot \dot{m}_{H_2} \cdot W_{O_2}}{W_{H_2}} \tag{4.19}$$

Where W_{H_2} is the molecular mass of hydrogen and θ_{H_2/O_2} is the stoichiometric ratio between hydrogen and oxygen.

4.7.2 "FC Compressor" Module

Finally, the "FC Compressor" module receives in input the requested air flow rate ($\dot{m}_{air}$) and the total power requested to the fuel cell (P_{FC_eff}) and calculates the power absorbed by the FC compressor (P_{comp}), through the relation (4.20).

$$P_{comp} = \frac{\frac{\dot{m}_{air}}{W_{air}} \cdot R \cdot T_{amb} \cdot \frac{k_{heat}}{k_{heat} - 1} \cdot \left(\frac{P_{out}}{P_{in}}\right)^{\left(k_{heat} - \frac{1}{k_{heat}}\right)} - 1}{\eta_{comp}} \tag{4.20}$$

where R is the universal gas constant $\left(8.31446 \frac{J}{mol \cdot K}\right)$, T_{amb} is the ambient temperature, k_{heat} is the specific heat ratio and η_{comp} is the efficiency of the whole compressor system (therefore of the compressor itself and of the electric motor necessary for its operation).

η_{comp} must be provided by the user as input data, depending on the power delivered by the fuel cell, and its value, relative to the operating point considered, during the simulation, is obtained using a Lookup Table Simulink (and P_{FC_eff}).

4.7.3 Graphic User Interface

The new version of the TEST model therefore includes the possibility of simulating hybrid vehicles equipped with proton exchange membrane fuel cell and also of activating the logic relating to the FC compressor. The graphic user interface of the TEST model has therefore been integrated, by adding an additional panel (see Figure 4.15), for setting all the input data necessary for the operation of the model portion relating to the compressor).

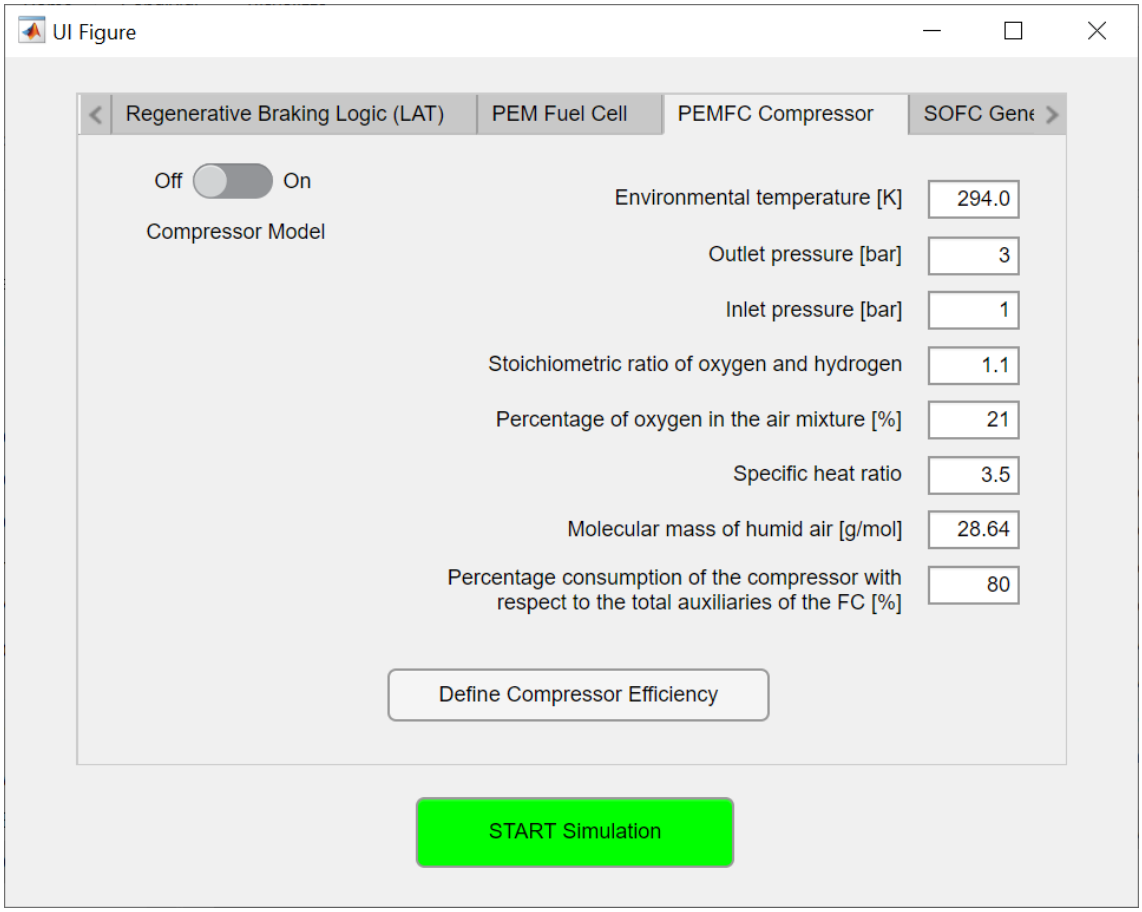

Figure 4.15. *"PEMFC Compressor" panel of the Graphic User Interface of the TEST model. In particular, this panel allows you to enter the inputs regarding the FC compressor logic.*

In particular, the Tab of Figure 4.15 allows you to set the value of the following input quantities: the ambient temperature (T_{amb}), the pressure at the outlet (P_{out}) and at the inlet (P_{in}) to the compressor, the value of the stoichiometric ratio between hydrogen and oxygen (θ_{H_2/O_2}), the percentage of oxygen in the intake air (Ø), the specific heat ratio (k_{heat}), the molecular mass of the humid air (W_{air}), the percentage of power consumed by the compressor compared to to the total power required by all the auxiliaries of the fuel cell ($Perc_{comp/acc}$) and, finally, the efficiency values of the compressor system (of the compressor itself and of its electric motor) as a function of the power of the FC.

In particular, this last table of values can be set by the user by pressing the "Define Compressor Efficiency" button shown in Figure 4.15.

Finally, the "On/Off" switch in the "PEMFC Compressor" panel (Figure 4.15) allows the user to decide whether ("On") or not ("Off") to activate the logic of the FC compressor.

4.8 DISCUSSION AND FUTURE DEVELOPMENTS

This chapter describes a tool suitable for carrying out analysis, sizing, base level design calculations, and energy or hydrogen consumption estimates for hybrid vehicles powered by fuel cells and a PPS, which in the current state of Simulink model is represented by a battery pack. As shown in the "Simulation Results" section (Section 4.6), the model outputs are the trend of various quantities, suitable for selecting the correct size of the hybrid powertrain and for testing the power split logic aimed at managing the interaction between FC and PPS. In particular, by monitoring the state of the FC and the nominal capacity of the battery pack.

The FC powertrain system described in this chapter is developed to integrate the TEST model described in Chapter 2 with a hydrogen power source while preserving its main attributes: high calculation speed, robustness, and flexibility. The necessity of conserving a light model structure and reasonably short calculation times resulted in the introduction of several approximations. The main approximation is the initial omission of the compressor consumption (subsequently integrated into the model) in the computation of the FC auxiliary power required. This results in an overestimation of the FC system efficiency. For this reason, a simple compressor model was subsequently integrated into the model, which allows a smaller approximation, but maintaining a high degree of computational speed of the entire tool.

Flexibility and the modular structure are maintained. For these reasons, the model is open to simple modification from the user; on top of that, it can switch between different powertrain architectures. Thanks to this modularity, for example, in the future, it will be possible to add a supercapacitor model as PPS in the case of FCHEV simulation.

A further future step could involve the introduction of a dynamic and/or thermal FC stack model, considering possible variations in partial pressure and/or temperature inside the FC during the simulation cycle.

Finally, the sizing of the FC and battery pack for the waste collection vehicle object of this chapter could be reported in a future study.

In summary, the high flexibility of the model makes it very easy to introduce changes and future developments to this simulation tool, as done in this study, starting from the original model described in Chapter 2 and in paper [10].

4.9 FINAL SUMMARY CONSIDERATIONS

This study describes a MATLAB and Simulink model of a PEMFC system integrated into a vehicle's EV dynamic powertrain system. The first step of the process is creating a model for the single FC chemical reaction, evaluating the net output voltage of the FC stack. Subsequently, it is necessary to develop a correct control strategy to governate the power flux into the hybrid system, in which the FC should operate within its optimal range while the battery pack acts as a peak power source. The option of battery recharging from the power grid is not currently provided in the model. The main goals of the control logic here are preventing several shutdown cycles of the FC and avoiding battery charging above the maximum SOC.

The model is suitable for analysing the behaviour of different powertrain layouts (EVs, APU hybrid electric vehicles and, particularly, FC/PPS hybrid vehicles). It can therefore be used as a tool for estimating the design parameters at the design and prototyping stage, sizing the system components, defining the power flow control strategy, and estimating energy and hydrogen consumption.

In summary, starting from a tool for the simulation of fully electric and hybrid APU vehicles (TEST model described in Chapter 2 and in the paper [10]), a new tool was created for the analysis and study of hybrid vehicles equipped with FC and battery pack with peak power source function. The modularity of the model means that with appropriate modifications and integrations, it is possible to simulate and study other configurations; for example, hybrid vehicles with FC and supercapacitors as PPS, or vehicles in which the FC acts only as a generator for recharging the battery pack as the only source for tractive power. It is also possible to integrate models of other types of fuel cells or FCs powered using different fuels such as methane or biomethane. Thanks again to the modularity, it is also possible to make the tool more precise by adding models suitable for the simulation of components that have been approximated or neglected, as was done for the fuel cell compressor.

5 MODEL OF AN HYBRID ELECTRIC VEHICLE EQUIPPED WITH A SOFC POWERED BY BIOMETHANE (OR METHANE)

With regard to FC it is good to know that there is no single technology and that each application finds the most suitable one; those currently on the market are the following: alkaline cells, direct methanol cells, phosphoric acid cells, sulphuric acid cells, proton-exchange membrane cells, molten carbonate cells, solid oxide cells and solid polymer cells [62,79] (Figure 5.1).

Types	Electrolyte	Operating T (C)	Fuel
Alkaline (AFC)	Potassium hydroxide (KOH)	50–200	Pure hydrogen, or hydrazine
Direct methanol (DMFC)	Polymer	60–200	Liquid methanol
Phosphoric acid (PAFC)	Phosphoric acid	160–210	Hydrogen from hydrocarbons and alcohol
Sulphuric acid (SAFC)	Sulphuric acid	80–90	Alcohol or impure hydrogen
Proton-exchange membrane (PEMFC)	Polymer, proton exchange membrane	50–80	Less pure hydrogen from hydrocarbons or methanol
Molten carbonate (MCFC)	Molten salt such as nitrate, sulphate, carbonates...	630–650	Hydrogen, carbon monoxide, natural gas, propane, marine diesel
Solid oxide (SOFC)	Stabilised zirconia and doped perovskite	600–1000	Natural gas or propane
Solid polymer (SPFC)	Solid sulphonated polystyrene	90	Hydrogen

Figure 5.1. *Technical characteristics of the different types of fuel cells* [79].

Fuel cells are electrochemical devices capable of carrying out a direct conversion from chemical energy to electrical energy in the form of direct current between two electrodes maintained at a constant potential difference [80]. One of the main advantages of their use is the possibility of carrying out the energy conversion while maintaining high efficiencies, avoiding the irreversibility of combustion typical of thermodynamic cycles (Figure 5.2).

Among the types of fuel cells shown in Figure 5.1, the solid oxide fuel cells (SOFCs) are those that can also be powered by biomethane (or simply by methane). From Figure 5.2 it can also be seen how SOFC systems have higher efficiencies than other systems (diesel-powered systems, gas engine systems, steam systems, etc.) and how SOFCs are the most efficient fuel cells among those

shown in the graph: PAFC (Phosphoric Acid Fuel Cell) and PEFC (Polymer Electrolyte Fuel Cell).

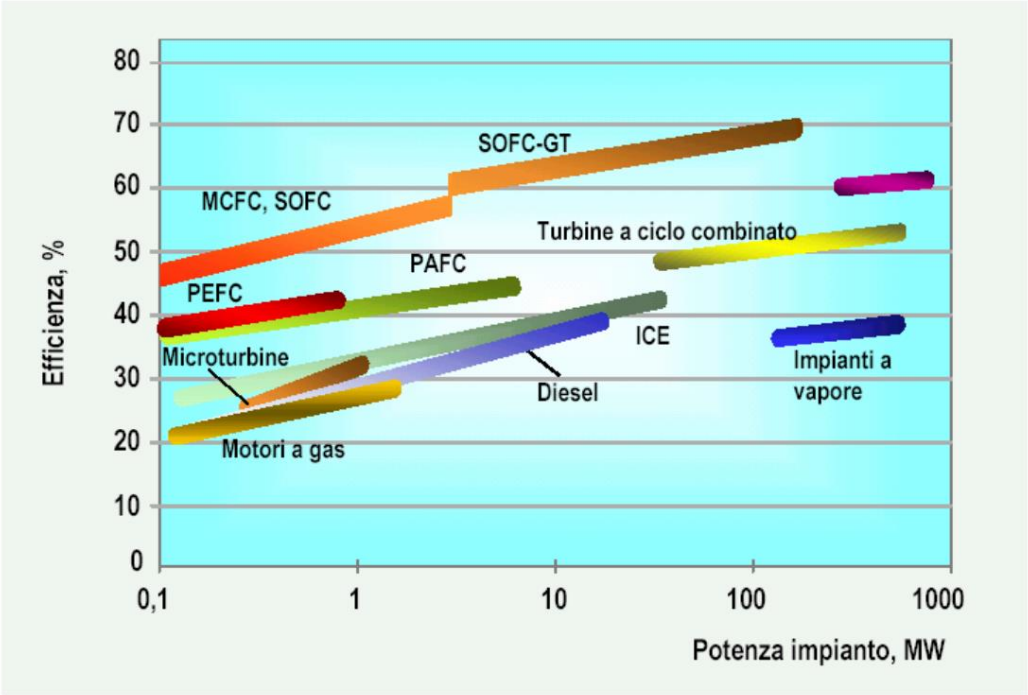

Figure 5.2. *Efficiency-power diagram of the main energy conversion technologies* [79]. *In particular, the Italian term "Turbine a ciclo combinato" means "combined cycle turbine", "Motori a gas" means "gas enigines", "Microturbine" means "microturbines" and "Impianti a vapore" means "steam systems". "Efficienza" means "efficiency" and "Potenza impianto" means "system or plant power".*

The peculiar characteristic of solid oxide fuel cell systems (SOFCs) is precisely that of being able to be fuelled with fuels other than hydrogen, such as natural gas, biogas, methane, bioethanol, etc., remembering that natural gas is composed of approximately 90% methane. The SOFC system is also suitable for being fed with synthesis gas obtained from the reforming of high molecular weight hydrocarbons, including diesel.

Most natural gas-fired power plants currently in operation have efficiencies around 30%. The conversion of natural gas into solid oxide fuel cells (SOFCs) promises an increase in system-wide conversion efficiencies of more than 60%, doubling the current efficiencies of traditional systems and significantly reducing CO_2 emissions by a factor of 2 [81]. It is therefore possible to exploit SOFC technology also on vehicles to improve their efficiency, compared to traditional internal combustion vehicles fuelled by methane.

This chapter will therefore propose a vehicle model equipped with a solid oxide fuel cell that could represent a future application of SOFC technology on board electric vehicles to exploit the high efficiency of the system, combined with the possibility of powering these vehicles with biomethane, which is theoretically considered to have zero CO_2 impact. In fact, the carbon dioxide that is released into the atmosphere by the fuel cell as a waste product, from a life cycle perspective, is already considered amortized by the entire production process of the biomethane itself. The impact given by this CO_2 is in fact inevitable, even in the event of failure to produce biomethane and, consequently, of its failure to use.

The bibliographic part of this chapter (Section 5.1 and 5.2) was created in collaboration with a master's degree thesis work [78]. The realization of the vehicle model equipped with SOFC represents, instead, the fulcrum of the part of the "Biomass Hub" project that is presented in this thesis.

This chapter is organized as follows.

- In Section 5.1 the structure and operating principles of SOC systems are explained.
- In Section 5.2 the theory concerning the modelling of solid oxide cells is presented.
- Section 5.3 describes the model of the hybrid electric vehicle equipped with a SOFC stack.
- Section 5.4 gives some concluding remarks and some final considerations.

5.1 STRUCTURE AND OPERATING PRINCIPLES OF THE SOFCS

Solid Oxide Fuel Cell (SOFC) is a fuel cell technology in which oxygen ions are transferred through a solid electrolyte material (an oxide), at a high temperature, to react with hydrogen on the anode. Generally, the solid electrolyte consists of a high temperature ceramic membrane, which stands in conditions of use around 1000–1200 °C [62]. These materials have low conductivity at ambient temperature and, for this reason, heating to such extreme temperatures is required to reach values comparable to those of liquid solutions, i.e. of the order of 0.1 $(S \cdot cm)^{-1}$ (where S is the symbol of the Siemens unit of measurement, and Siemens multiplied by meter is the SI unit of measurement of electrical conductivity, also known as specific conductance). The basic mechanism of a SOFC does not differ too much from what happens for other FCs, such as for

example for the PEMFC, with the exception of the operating temperatures, which are at higher values, and of the constituent materials of the FC itself.

SOFCs are characterized by two porous electrodes separated by a dense electrolytic layer, generally made of YSZ (Yttria-Stabilized Zirconia).

Oxygen is supplied to the cathode, where it is reduced to ion O^{2-}, which migrates through the electrolyte, to reach the anode and participate in the oxidation reaction of the hydrogen obtained from reforming process or from a mixture containing directly H_2, from the reaction H_2O, and CO_2 in the case, for example, of methane fuelling, will be obtained (Figure 5.3). In particular, starting from the hydrogen obtained from the reforming of methane (or biomethane), the formation of carbon dioxide is inevitable.

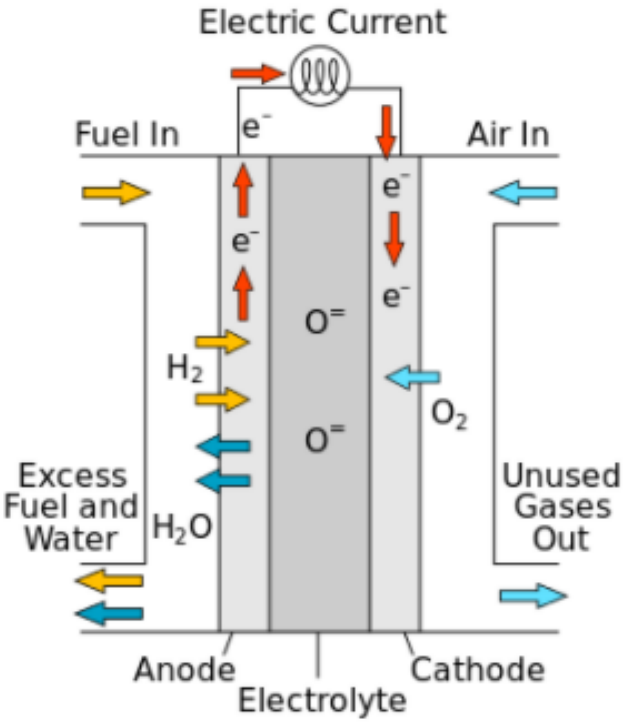

Figure 5.3. *Operation diagram of a solid oxide fuel cell* [79,82].

The cells never operate as single units, but they are connected in series to obtain an output power suitable for different uses and, for this reason, a bipolar separator, called "interconnector", must be considered as a constituent part of the system. The interconnector must consist of a layer of suitably dense material to separate the fuel stream from that of the oxidizing gas, as shown in Figure 5.4, for a stack of planar geometry cells.

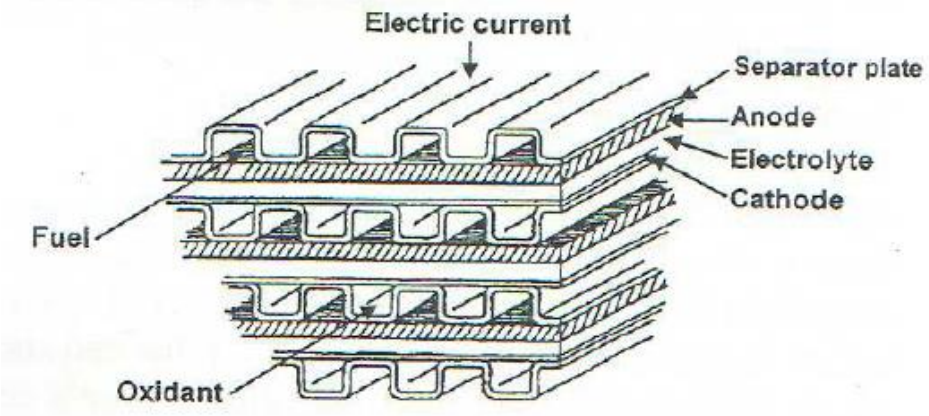

Figure 5.4. *Typical planar SOFC stack* [79].

From a geometric and dimensional point of view it is good to specify that there are different configurations of SOFC: tubular, "segmented in-series cell", monolithic and planar, even if currently only the tubular and planar configurations seem to offer the possibility of greater development. In the tubular geometry (Figure 5.5) the cell components are deposited in the form of thin layers on a tube-shaped cathode (which acts as a support element) prepared by extrusion, often formed by a sintered porous film based on lanthanum manganite addicted to strontium. The electrolyte, as anticipated, is formed by a layer of YSZ (electrochemically deposited by the vapor phase) and the anode is made up of a Ni/YSZ film.

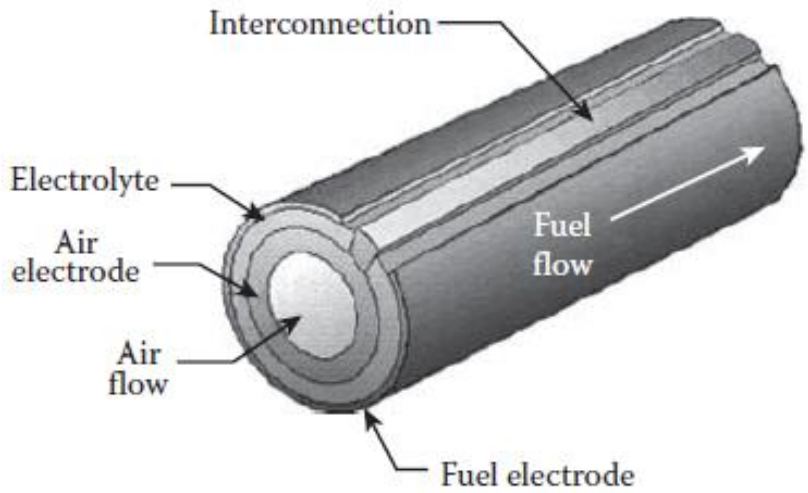

Figure 5.5. *Tubular geometry of the cell of a SOFC system* [62].

The main advantages of tubular technologies include easier sealing and reduced constraints on the ceramic. The disadvantages are mainly the lower efficiency and the lower power density, moreover the ceramic electrolyte and the electrodes are extremely fragile, which is very disadvantageous if you think about their application on vehicles, where vibrations are a frequent occurrence [62].

In the planar structure cell (Figure 5.6), on the other hand, the components are made in the form of thin and flat plates supported by the electrolyte or by an electrode. The YSZ-based dense electrolyte is prepared either by deposition on tape, by sintering of powders, or by chemical vapor deposition, while the electrodes are made by plate moulding or by thermal vaporization.

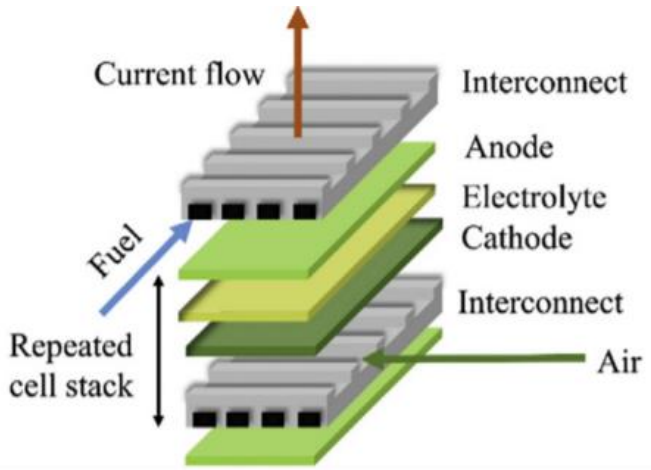

Figure 5.6. *Planar geometry of the cell of a SOFC system* [83].

The porosity of the components is one of the factors involved in contributing to good energy efficiency: the electrodes must have sufficient porosity for a good diffusion of the gases, while the electrolytic material between them must avoid contact with the latter, which otherwise would react without produce electric current.

As also happens for PEMFCs, the electrolyte used contributes to characterize the fuel cells, as it strongly affects the operating temperature of the cell, the type of ions, the direction of diffusion, the composition of the reacting gases and the nature of the construction materials. Furthermore, the type of electrolyte used, and consequently the type of ion transported, determines the electrode in which the water is formed, with a significant impact on the design of

the materials and on the structure of the system. In this regard, it is possible to list two types of conductors that allow further differentiation between the SOFCs:

- anionic conductor of O^{2-} ions;
- proton conductor of H^{+} ions.

The two types of electrolytes, due to the difference in the migrating ion, differ in which side of the cell the water is produced, a by-product resulting from the redox reactions that occur at the electrodes [79]. In fact, in anionic conduction cells, water forms on the surface where the fuel is fed, i.e., at the interface of the electrolyte with the anode, while in proton conduction cells it occurs at the interface with the cathode, where it has access the oxidizer (Figure 5.7).

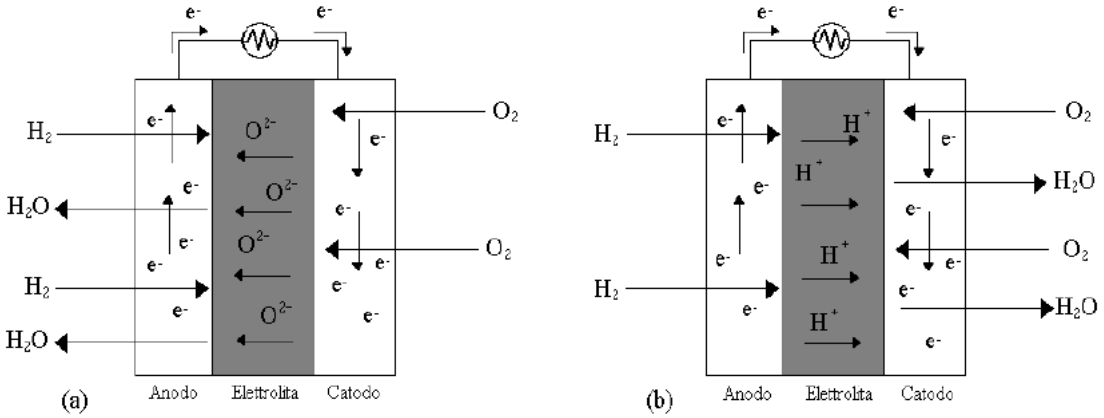

Figure 5.7. *Operation diagram of a fuel cell with (**a**) anion conduction electrolyte and (**b**) proton-conducting electrolyte* [79].

Considering the nature of the materials used, it should be specified that the use of an electrolyte consisting of a ceramic material based on zirconium oxide (ZrO_2), doped with 8-10% of yttrium oxide (Y_2O_3, YSZ) is often used for SOFC cells. The doping process, in the field of semiconductors, consists in the addition to the pure semiconductor of small percentages of atoms that are not part of the semiconductor itself, to modify the electronic properties of the material. In this case, in fact, following doping, some Y^{3+} ions replace the Zr^{4+} ion in the fluorite-like structure of the zirconium oxide, generating a certain number of vacant sites for oxygen through which the O^{2-} ions can move ensuring so does ionic transport [84].

To understand the reason for the increasingly widespread use of solid oxide fuel cell systems, we can list the numerous advantages, some of which have already been discussed, such as, for example, the use of non-precious metals and a stable solid electrolytic compound, which eliminates the problems of corrosion

and evaporation, thus reducing the management costs of the entire system. Moreover, the presence of all the components in the solid state allows the production of very thin layers or of FC with precise shapes, that make the system very compact, a result not reachable in the presence of a liquid electrolyte [85].

0_2 is the most common oxidant, as it is cheap and available in the air, while H_2 is currently the most used fuel due to its high reactivity and higher calorific value. It can be easily obtained from common fuels such as hydrocarbons, alcohols or coal directly in the SOFC system: with the use of ceramic materials, in fact, devices are obtained whose high operating temperature promotes the kinetics of the reactions, thus allowing to directly generate H_2 during the reaction within the cell itself (Figure 5.8), through a process that takes the name of "fuel reforming" (formula (5.1), for methane) and the oxidation of CO to CO_2 through the "water-gas shift" reaction (formula (5.2)); two reactions that when coupled allow the obtain H_2 and CO_2 (formula (5.3)).

$$CH_4 + H_2O \leftrightarrows CO + 3H_2 \tag{5.1}$$

$$CO + H_2O \leftrightarrows CO_2 + H_2 \tag{5.2}$$

$$CH_4 + 2H_2O \leftrightarrows CO_2 + 4H_2 \tag{5.3}$$

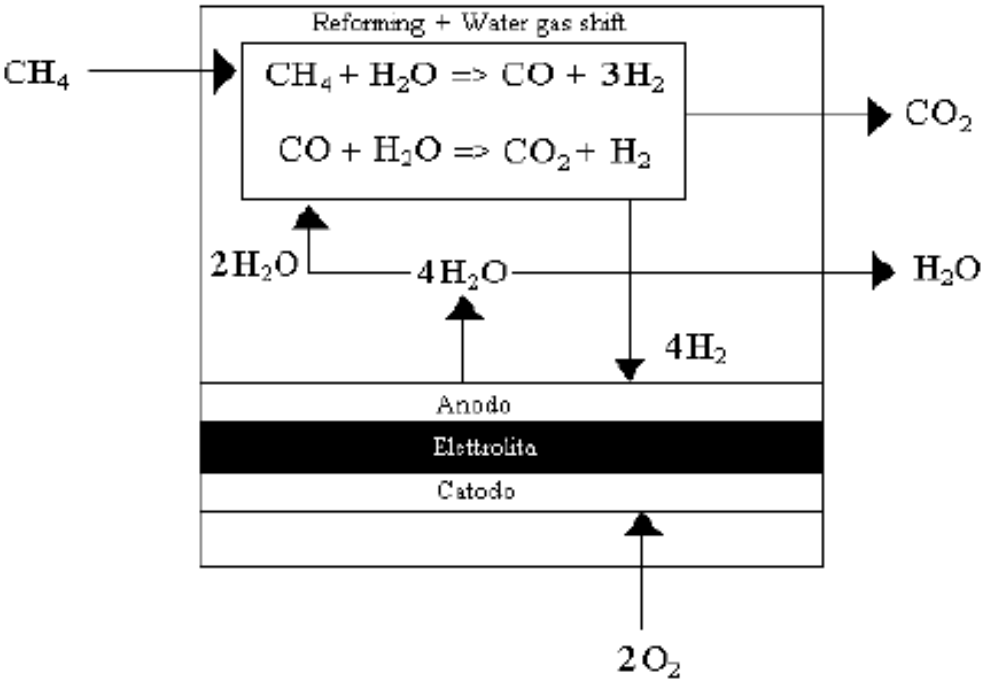

Figure 5.8. *Schematic representation of the fuel reforming inside a SOFC cell* [79].

Fuel reforming is a process aimed at transforming the primary fuel (for example, methane) into a mixture containing molecular hydrogen and other products (carbon dioxide, steam, carbon monoxide, methane, non-reformed fuel, etc.). Reforming is a process characterized by various reactions, including unwanted ones, which influence the purity of hydrogen, which also depends on process variables, such as: temperature, pressure, molar ratios between reactants, activity catalysts, and so on. It is therefore always essential to know the effects of these variables on the final composition of the reformed gas in the design phase of the cell and consequently the thermodynamic analysis of the process is important.

The reactions that occur at the anode of a methane-powered SOFC are shown below (5.4) (5.5) (5.6).

$$H_2 + O^{2-} \leftrightarrows H_2O + 2e^- \tag{5.4}$$

$$CO + O^{2-} \leftrightarrows CO_2 + 2e^- \tag{5.5}$$

$$CH_4 + 4O^{2-} \leftrightarrows 2H_2O + CO_2 + 8e^- \tag{5.6}$$

Below is the reaction that takes place at the cathode (5.7).

$$\frac{1}{2}O_2 + 2e^- \leftrightarrows O^{2-} \tag{5.7}$$

Finally, the overall reaction that takes place in the SOFC cell is shown below (5.8).

$$CH_4 + 2O_2 \leftrightarrows 2H_2O + CO_2 \tag{5.8}$$

Despite the advantages described above, the SOFC systems are however very sophisticated systems which are often accompanied by problems due to the high operating temperatures, such as the low compatibility of the components due to their different coefficients of thermal expansion. The latter aspect involves a careful selection of materials in the design phase and careful testing of the materials used. Furthermore, the elevated temperature influences the choice of support materials, as well as the geometry of the cell itself.

The wide variety of fuels that can be processed there, although a valuable feature of this technology, conceals problems on which research is constantly evolving. Here are some reflections in this regard, but for a more detailed study of the topic, please refer to the full reading of the article [86] cited among the references. The fact that, as already mentioned, the SOFCs can theoretically function, in addition to pure hydrogen, also with hydrocarbon fuels (therefore also with biomethane and methane, the main component of natural gas), makes

the use of pre-reformers superfluous, thus reducing the complexity, size and cost of the entire SOFC system.

However, the incompatibility of zirconia stabilized with Ni/yttrium (YSZ) cermet (ceramic metal, materials deriving from the union of a metallic material with a substance of a ceramic nature) with hydrocarbon fuels makes it difficult to exploit these benefits because nickel, catalysing the decomposition of hydrocarbon fuels, it leads to severe carbon deposition at the anode. The latter mainly generates three structures: amorphous, filamentous, and graphitic. Considering the high operating temperature of these fuel cells (600-1000 °C), graphitic carbon is the most favoured structure, although amorphous and filamentous carbon have also been observed. Amorphous carbon, in fact, preferentially forms up to 600 °C, but it can evolve into filamentary carbon and, eventually, be converted into graphitic forms at higher temperatures. However, all this represents a problem since it has been observed that the presence of graphite, formed by the carbon that has diffused through the anode, causes the disintegration of metallic Ni, to form a powder in a process known as "metal dusting" [86]. The presence of carbon fibres, at high temperature (>600 °C), is caused by the dissolution of the adsorbed carbon in the metal crystallite, its diffusion through the metal and its precipitation on the back of the metal particle. Filamentary carbon is easier to remove by electrochemical oxidation than graphitic carbon, because it can be combusted/oxidized at lower temperatures. However, carbon fibres can cover the active sites of Ni-YSZ and embed themselves in the anodic lattice, thus causing structural deformations and fragmentations that lead to greater degradation. The carbon accumulation on Ni causes complications, such as the blocking of the active sites on the anode, the loss of the nickel catalyst and the loss of structural integrity.

Despite the disadvantages described, the use of Ni-based anodes nevertheless remains attractive, not only for their excellent characteristics, including exceptional catalytic performance, high electronic conductivity and good chemical stability in relation to the electrolyte, but also for their relative ease of manufacture, mechanical strength and low cost [86]. With continuous research in this field, various strategies have been validated to improve performance and resistance to coke (material consisting of a series of components with a high content of carbon and that is deposited on the catalyst during the process, and which is oxidized in the regeneration phase). One possible approach, for example, involves the use of nickel-based anodes combined with materials with excellent catalytic activity and resistance to coke, such as ceria (or ceric oxide, CeO_2). In fact, mixed oxides have mixed ionic and electronic

conductivity in reducing atmospheres, excellent catalytic activity for the combustion of hydrocarbons and adequate resistance to carbon deposition. Furthermore, the addition or the coating of CeO_2 increases the oxidation activity of methane and reduces the deposition of carbon in the Ni/YSZ. However, the main weakness of ceria is its low thermal stability in conditions of preparation and also of operation in a SOFC, because its surface is strongly influenced by the calcination temperature (temperature of the heating process prolonged for the time it takes to eliminate all the volatile substances from a solid mixture or a single compound). As anticipated, these are just some of the problems on which research has the possibility investigate, to refine more and more the knowledge of new strategies and materials that make SOFC technology more and more reliable, resistant, and efficient.

5.2 SOLID OXIDE FUEL CELL (SOFC) MODELLING THEORY

The modelling of fuel cells represents a fundamental point for research and development work: it allows to study the performance of systems in different configurations, bypassing the long-time frames, high costs and risks that their actual implementation in the test phase would entail. With mathematical modelling, in fact, the physics of the system under study are reproduced through a set of equations whose numerical analysis returns all the precious information sought. Modelling is useful for experimenting with new design ideas and for analysing the hypothetical behaviour of the real system. Investing in this direction is therefore important, carefully taking care of the set of equations that describe the entire operation of the system, paying attention to incorrect simplifications that could lead to results that are too different from the real ones, aspect detectable with physical tests subsequently performed on the various prototypes in laboratory. Examples of studies carried out in this area are reported in articles [87–91], but these are not the only ones.

For the SOFC cell modelling, as also happens for other types of fuel cells, it is necessary to calculate the voltage of the cell itself, obtained by subtracting the different voltage drop components (activation voltage v_{act} , losses by concentration v_{conc} and ohmic losses v_{ohm}) from the Nernst voltage V_r (or open circuit voltage of the cell). The relationship (4.1), shown in Section 4.4.1, is therefore also valid for SOFC cells.

With reference to the Nernst voltage (V_r) it should be emphasized that, as analysed in detail in the article [92], it is subject to various inaccuracies found in the literature that involve the modelling of solid oxide fuel cells or proton

exchange membrane FC. It is claimed that the problem arises due to an incorrect intermediate step in the derivation of the cell output voltage.

In this section, the Nernst voltage V_r will be indicated with the symbology E_{Nernst}, consistent with what has been done in the scientific article [92] from which the information of interest reported below has been extrapolated.

The Nernst equation (5.9), considered a cornerstone of fuel cell thermodynamics, provides the expression of the reversible thermodynamic potential, also known as "equilibrium voltage" or "open circuit voltage" or "electromotive force" (EMF) of the fuel cell.

$$E_{Nernst} = E_0 + \frac{RT}{n_e F} \cdot ln\left(\frac{\prod_i a_{reactant_i}^{c_i}}{\prod_j a_{product_j}^{c_j}}\right) \tag{5.9}$$

where E_0 is the reference EMF (standard EMF); i and j are the species numbers of reactants and products respectively (how many reactants and how many products); $a_{reactant}$ represents the activity of the reagents and $a_{product}$ the activity of the products; c_i is the stoichiometric coefficient of the i-th species; c_j is the stoichiometric coefficient of the j-th species; R is the universal gas constant; F is Faraday's constant; n_e is the number of electrons transferred for each fuel molecule participating in the reaction; and T is the cell temperature. For a hydrogen and oxygen fuel cell (e.g., solid oxide fuel cell powered directly by hydrogen or proton exchange membrane fuel cell), hydrogen and oxygen are the reactants, while water (or water vapor) is the product.

The reference EMF depends on the temperature and is calculated using equation (5.10).

$$E_0 = E_0^0 + (T - T_0) \cdot \frac{\Delta s}{n_e F} \tag{5.10}$$

where E_0^0 is the standard EMF at the standard temperature (T_0) and Δs is the entropy variation.

The activity of an ideal gas is expressed in terms of pressure (or partial pressure). For the activities of hydrogen (a_{H_2}) and oxygen (a_{O_2}) the relationships (5.11) e (5.12) are valid respectively.

$$a_{H_2} = \frac{p_{H_2}}{p_0} \tag{5.11}$$

$$a_{O_2} = \frac{p_{O_2}}{p_0} \tag{5.12}$$

where p_{H_2} is the partial pressure of hydrogen, p_{O_2} the partial pressure of oxygen and p_0 is the standard pressure (equal to 1 atm).

At high temperatures, for example approaching 1000 °C (plausible operating value of a solid oxide FC), it can be assumed that steam behaves like an ideal gas and, therefore, the activity of water (a_{H_2O}) can be calculated via the equation (5.13).

$$a_{H_2O} = \frac{p_{H_2O}}{p_0} \tag{5.13}$$

where p_{H_2O} is the partial pressure of the water vapor.

Setting p_0 equal to 1 atm and noting that for a hydrogen fuel cell we have $n_e = 2$, we obtain the following writing of the Nernst equation (5.14).

$$E_{Nernst} = E_0 + \frac{RT}{2F} \cdot ln\left(\frac{p_{H_2} \cdot \sqrt{p_{O_2}}}{p_{H_2O}}\right) \tag{5.14}$$

If the fuel cell is operated below 100 °C, so that liquid water is produced (as in PEMFCs), the water activity can be considered unitary ($a_{H_2O} = 1$) and the Nernst equation can be rewritten as in equation (5.15).

$$E_{Nernst} = E_0 + \frac{RT}{2F} \cdot ln\left(p_{H_2} \cdot \sqrt{p_{O_2}}\right) \tag{5.15}$$

Drawing inspiration from the work presented in article [90], where a dynamic model of a SOFC plant is developed, many other studies have been carried out (for example those reported in articles [87,93–119]) but, in an attempt to build models based on the model of [90], the "original" has been modified, deriving and expressing the partial pressures of the reactants and products as functions of the cell current, then inserting these partial pressures into the Nernst equation.

For an in-depth analysis of these aspects, see article [92]. Instead, the following is the equation (5.16), which represents the inaccurate form of the Nernst equation [96,97,102,104–106,109,110].

$$E_{Nernst} = E_0 + \frac{RT}{2F}\left\{ln\left(\frac{K_{H_2O}}{K_{H_2}}\sqrt{\frac{K_r}{r_{HO}K_{O_2}}}\right) + \frac{1}{2}ln\left(I_{FC}\left(\frac{1}{u} - 1\right)^2\left(\frac{2}{u} - r_{HO}\right)\right)\right\} \tag{5.16}$$

where K_{H_2}, K_{O_2} and K_{H_2O} are the molar constants of hydrogen, oxygen and water respectively; $K_r = \frac{1}{4F}$; r_{HO} is the ratio between the inlet molar flow rates of hydrogen and oxygen; u is the fuel utilization ratio; I_{FC} is the load current of the cell.

Equatuion (5.16), or one of its many variants (implicit or explicit), has been the cornerstone of a whole line of fuel cell modeling research for about two decades. Not all models report it explicitly, but often express, directly or indirectly, the Nernst voltage as a function, among other variables, of the current. The problem with equation (5.16) is that it mixes equilibrium and non-equilibrium expressions. The Nernst voltage is in fact the reversible thermodynamic potential that is applied only to the equilibrium condition of the cell, which instead is lost when the current is drawn from it. In other words, the Nernst voltage is, by definition, the open circuit EMF and therefore cannot be expressed in terms of cell load current or current density. The questionability of the use of I_{FC} in equation (5.16) is also highlighted by the fact that imposing $I_{FC} = 0$ causes part of the equation to be mathematically indefinite. As explained in article [92], it is wrong to mix equilibrium conditions and non-equilibrium conditions, inserting the cell current (the load current) in the expression of the Nernst voltage. It can therefore be argued that expressing the Nernst voltage as a function of current remains a quick but imprecise trick, even if it facilitates modelling. If done, however, it is important not to forget that the scientific rigor of the equation is compromised for practical convenience.

What we have seen so far in relation to the Nernst equation refers to a SOFC directly powered by hydrogen. If, on the other hand, we consider a methane power supply, the writing of the Nernst equation is the following (5.17).

$$E_{Nernst} = E_0 + \frac{RT}{8F} \cdot ln\left(\frac{p_{CH_4} \cdot p_{O_2}^2}{p_{H_2O}^2 \cdot p_{CO_2}}\right) \tag{5.17}$$

where p_{CH_4} and p_{CO_2} are the partial pressure of methane and carbon dioxide, respectively.

When the stack begins to supply current to an external load, the FC system moves away from the state of equilibrium and the voltage drops of the equation (4.1), presented in Section 4.4.1 occur. Activation losses are associated with overcoming the reaction energy barriers at the electrode-electrolyte interfaces. On the other hand, ohmic losses are associated with electron and ion conduction processes that occur in the electrodes, electrolyte and interconnections, as well as due to contact resistances across each interface of the material. Finally, the losses by concentration are associated with the limitations of the diffusion processes of

the reactants and the products between the mass flow and the reaction in the sites.

Starting from the analysis of activation losses, as analysed in depth in the article [120], different calculation methods found in the literature were compared, highlighting some common errors. A hypothesis often made in the past was to overlook activation losses, especially for SOFC cells, generally for two main reasons:

- SOFCs operating around 1000 °C have a very fast chemical kinetics, which makes the activation losses significantly lower than the others;
- The ohmic losses, at these temperatures, are much greater in absolute value than the other losses and dominate the entire behavior of the cell at normal operating current densities.

These hypotheses may still be valid, especially if we are dealing with the tubular geometries of older design that operate at the high temperature of about 1000 °C, but if we refer to more modern systems, designed to work at decidedly lower temperatures, 800 °C or less, with planar geometries and much shorter conduction networks, the absolute value of the activation losses is closer to that of the other two types of losses, as shown in Figure 5.9. The approximation is therefore fine, as long as it is done in the right context.

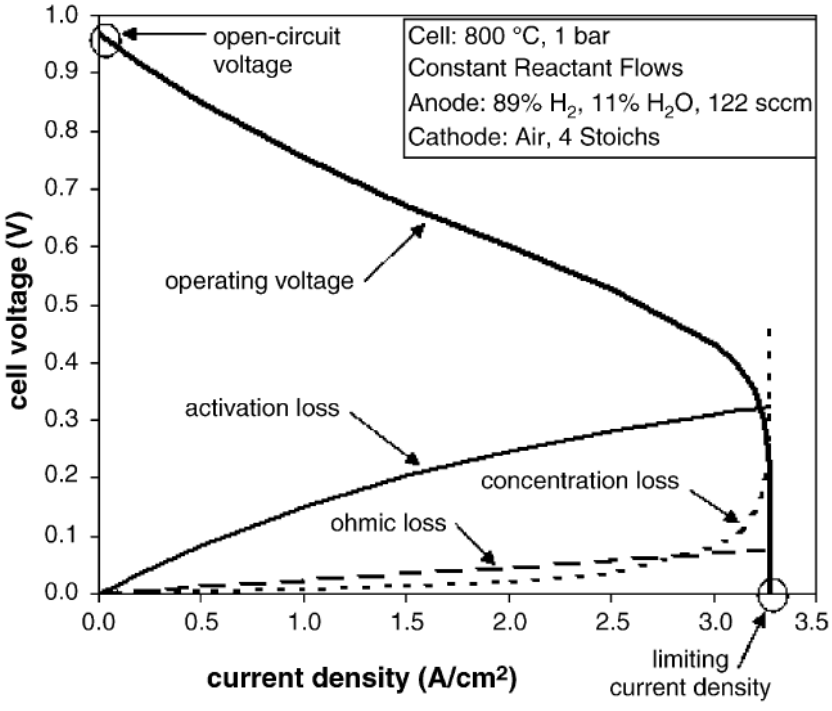

Figure 5.9. *Example of a characteristic curve of planar SOFCs for a single cell operating at 800 ◦C* [120,121].

Another mistake made in fuel cell modelling is related to the common and erroneous idea that the predominantly linear profile of many SOFC voltage-current curves is the result of the prevalence of ohmic losses. It is true that these are a linear function of the current density but, on the contrary, both the activation losses and the concentration losses are logarithmic functions, and it does not mean that their contribution is not significant to the overall voltage drop when the voltage-current curve is almost linear.

Activation losses tend to constantly increase in the operating range of SOFCs due to relatively large values of the equilibrium exchange current density (i_0). Conversely, low temperature fuel cells tend to have lower current densities and consequently the rapid increase in activation losses at low operating currents is followed by greater smoothing at higher currents. It is also evident in Figure 5.9 that the magnitude of the losses per concentration is relatively small over most of the operating range and therefore does not significantly affect the slope of the voltage-current curve until the limit current density i_L is reached, defined as the maximum possible current density in which reagents are consumed at the highest possible degree of replenishment [120].

The governing equation for activation losses at each electrode-electrolyte interface (two terms are considered for the equation, one for the anode and one for the cathode) is the Butler-Volmer equation (5.18).

$$i = i_0 \cdot \left(e^{\alpha_1 (F/RT) \Delta v_{act}} - e^{-\alpha_2 (F/RT) \Delta v_{act}}\right) \tag{5.18}$$

where i is the current density of the fuel cell.

The equilibrium exchange current density (i_0) is a function of materials, construction and temperature and is typically calculated using the Arrhenius relation (5.19).

$$i_0 = A_T \cdot e^{-E_{act}/RT} \tag{5.19}$$

where E_{act} represents the activation energy, the term A_T is generally a function of the cell temperature and the partial pressures of the reactants and products. The reduction and oxidation coefficients, α_1 and α_2 respectively, are governed by the electron transfer processes occurring at the electrode-electrolyte interface.

A simplification made in many SOFC models consists in assuming that each reaction that occurs is a single-step process, with the transfer of a single electron [120]. This translates into the following form of the Butler-Volmer equation (B-V) (5.20).

$$i = i_0 \cdot \left(e^{(1-\beta_V)(F/RT)\Delta v_{act}} - e^{-\beta_V(F/RT)\Delta v_{act}}\right) \tag{5.20}$$

where the symmetry factor β_V is defined as that fraction of the voltage loss by activation that affects the activation energy of the barrier and therefore the electrochemical transformation rate. For simplicity, this factor is set equal to 0.5 even if experimental evidence shows that it oscillates between 0.3 and 0.6.

Since the entire B-V equation would have to be implicitly solved for activation voltage losses, the literature is full of several explicit approximations. However, it is essential to understand what the applicability field of each of these equations is to minimize modeling inaccuracies.

When activation losses are high ($v_{act} > 200\ mV$), the first exponential term in the B-V equation is much larger than the second which therefore, if neglected, allows us to obtain the Tafel equation (5.21), valid when $i/i_0 > 4$.

$$\Delta v_{act} \cong \frac{RT}{\alpha_1 F} \cdot ln\left(\frac{i}{i_0}\right) \tag{5.21}$$

If the exponential terms of the one-step B-V equation with single electron transfer are expanded into a series of powers and the higher-order terms (non-linear) are neglected, the resulting equation is an approximation called the "linear current-voltage equation" (5.22), valid when $i/i_0 < 1$.

$$\Delta v_{act} \cong \frac{RT}{F} \cdot ln\left(\frac{i}{i_0}\right) \tag{5.22}$$

Another approximation of the B-V equation sees the latter rewritten using the hyperbolic sine function. By doing this, the equation (5.23) is obtained.

$$\Delta v_{act} \cong \frac{RT}{\alpha_1 F} \cdot sinh^{-1}\left(\frac{i}{2i_0}\right) \tag{5.23}$$

In article [120], where it is possible to further explore the topic, the applicability of each equation for the calculation of activation losses within a model was shown, validating everything through experimental data obtained from a planar cell SOFC.

The curves of Figure 5.10 show what has been obtained, namely that the results of the model, using the equation B-V and the approximation of the hyperbolic sine, are almost identical and align well with the experimental curves.

The results obtained using equations (5.21) and (5.22), on the other hand, differ significantly from the experimental ones, except in very limited current density ranges, which is why their field of applicability is more restricted.

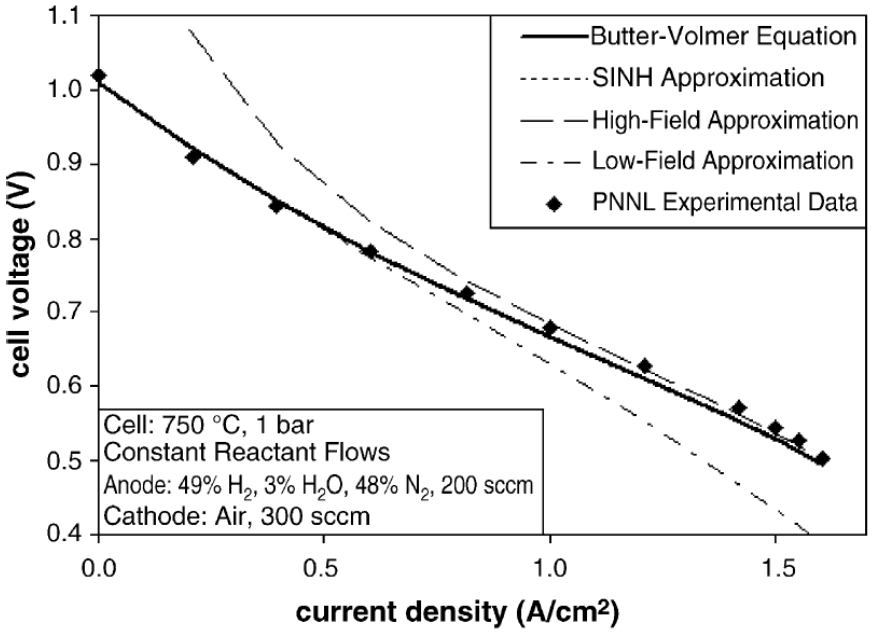

Figure 5.10. *Comparison of experimental voltage-current curves with model-based curves using the different approximate equations for activation losses* [120].

As for the potential drop associated with the concentration losses (v_{conc}), from the polarization curve of Figure 5.9 it can be seen that their presence is more evident when the current density of the fuel cell approaches the maximum values that can be developed and it is found also dependence on the flow. These concentration losses are due to the progressive reduction of the reactant concentration in the electrode region as fuel is consumed as the electrochemical reaction progresses. The reagents consumption at the respective electrodes, i.e., hydrogen at the anode and oxygen at the cathode, leads to a slight reduction in their concentrations. Due to this, there is a drop in the partial pressures of the gases present, which will result in a reduction in the voltage produced by the cell.

There are several ways to estimate the concentration losses, such as equations that exploit experimental coefficients, giving excellent results in the modelling phase, or more theoretical equations.

Article [89], for example, reports that in the realization of a transient dynamic model for a SOFC fuel cell system powered directly by methane.

Equation (5.24), entirely empirical, has aroused considerable interest due to the accuracy of the results.

$$v_{conc} = m_{conc} \cdot e^{n_{conc} \cdot i} \tag{5.24}$$

where i is the current density [A/cm^2], output from the cell, while m_{conc} and n_{conc} are constants obtained experimentally:
$m_{conc} = 3 \cdot 10^{-5}\ V;\ n_{conc} = 8 \cdot 10^{-3}\ \frac{cm^2}{mA}$.

A more "academic" equation with which the value of concentration losses can be estimated is equation (5.25), much more common in literature and traceable in scientific material, for example in articles [91,122].

$$v_{conc} = \frac{RT}{n_e F} \cdot \ln\left(1 - \frac{i}{i_L}\right) \tag{5.25}$$

The last term to be subtracted from the Nernst voltage to obtain the cell voltage is represented by the potential drop due to ohmic losses (v_{ohm}). These losses occur due to resistance to the flow of ions in the electrolyte and resistance to the flow of electrons through the electrode materials. This total resistance (r) depends on the cell temperature and can be calculated using the relation (5.26) [122].

$$r = \alpha_r \cdot e^{\beta_r\left(\frac{1}{T_0} - \frac{1}{T}\right)} \tag{5.26}$$

where T is the cell temperature, while α_r and β_r are constant coefficients. Here, once r has been obtained, it can be used to estimate ohmic losses using equation (5.27) [91,122].

$$v_{ohm} = r \cdot I_{FC} \tag{5.27}$$

where I_{FC} is the current (in Ampere) supplied by the fuel cell (by the single cell).

5.3 MODEL OF VEHICLE WITH SOFC ON BOARD

The goal of the work proposed in this section is to create a model of vehicle powered by biomethane (or methane), in which methane is not burned as in internal combustion engines, but which provides energy thanks to the chemical reactions carried out by means of a fuel cell stack.

As seen in the previous sections, the type of fuel cell that lends itself to being fuelled by methane is the solid oxide one. Some useful information relating to SOFCs is summarized below, to be taken into account during modelling, partly seen and explained in the previous sections and commented here to show how they interfaced with the creation of the biomethane fuel cell vehicle model.

- The SOFCs, thanks to the reforming process, accept different possible feeds: hydrogen, natural gas, biogas, methane, biomethane, bioethanol, diesel, etc. For this reason, this type of fuel cell was chosen for the vehicle model, so that the latter can be powered by biomethane (or methane).

- Undesirable characteristics of SOFCs are fragility and low vibration resistance. These limits impose difficulties in use in the automotive sector, the limit given by these characteristics must be exceeded for the actual construction of a vehicle based on the model proposed in this work.

- SOFCs are characterized by high operating temperatures (600÷1000 °C) and by different coefficients of thermal expansion. The fragility of SOFCs derives in part from this aspect. Therefore, accurate thermal management will be required on the vehicle subject of this study.

- Solid oxide FCs are characterized by slow transients (order of minutes). This makes them unsuitable for use on a vehicle as a primary energy source. Typically, vehicle missions are in fact characterized by rapid changes in power. For this reason, the vehicle model provides a configuration with purely electric traction, powered by a battery pack (which acts as a primary energy source), and an on-board SOFC stack that acts as a generator, recharging the battery pack, consuming biomethane (or methane).

- Finally, SOFCs are also characterized by long ignition times (order of hours). To overcome this problem, once the new vehicle has been put into operation and the FC has been switched on, it has been chosen to never switch off the SOFC. The methane-powered FC will then recharge the battery pack during the vehicle use phase and also when the vehicle is off, where there is a need to raise the state of charge of the batteries. By taking advantage of this charging method, the vehicle model has been designed without the possibility of recharging the battery pack by connecting it to the electricity grid. Once the battery pack has reached the desired SOC, the off vehicle will have to be connected to the stationary electrical network and the SOFC, which will always remain on, will recharge the electricity grid itself.

The following assumptions have been made for the vehicle model object of this work.

- Use of a solid oxide FC stack (SOFC).

- Biomethane (or methane) power supply, assuming to use a biomethane with a purity comparable to that of methane and therefore to be able to use the two power supplies (biomethane and methane) interchangeably.

- FC which acts as a constant power generator for recharging the battery pack.

- Fuel Cell always on, even when the vehicle is off. The vehicle, for safety reasons, must in any case be equipped with an emergency system that can turn off the SOFC in the event that any problems occur, including the exceeding of a certain maximum SOC threshold of the battery pack.

- It is considered a vehicle that works in a fleet, with a predefined mission, in particular a waste collection vehicle. In fact, a vehicle with a fixed mission lends itself to the configuration of the vehicle in question, that is, with the SOFC always on, being able to ensure an adequate state of charge of the battery pack, avoiding any

overcharging of the same, due precisely to the FC always on. This can be achieved thanks to a careful sizing of the vehicle system.

- During the inactivity phases, the vehicle must be connected to the electricity grid, in fact, once the battery pack has reached the desired SOC (State of Charge), the Fuel Cell will recharge the electricity grid itself. Alternatively, it will be possible to recharge other vehicles in the fleet (for example full electric vehicles) or a stationary energy storage system.

5.3.1 Vehicle

The vehicle used in the model is a vehicle that operates in fleet for waste collection, with a predefined mission, and is the same, with the same characteristics, used for the low-performance validation of the TEST model (see Section 2.4.1). The main information of the vehicle is shown in Table 2.1 in Section 2.4.1. In Figure 2.20 of Section 2.4.1.2 the torque curve of the vehicle's traction motor is graphed.

However, some changes have been made to the vehicle presented in Section 2.4.1, the first obviously relates to the fact that a SOFC system has been installed on the vehicle, system which acts as a generator by recharging the battery pack.

Another change concerns the total transmission ratio, set equal to 6.22, divided into a ratio of 3.11 for the motor reducer and equal to 2 for the rear differential (remembering that the vehicle is a rear-wheel drive). This is to allow the vehicle to reach a maximum speed that allows it to complete all the predefined missions that will be imposed on it during the use phase.

Figure 5.11 shows the motor power and the power needed to overcome the resistance due to the aerodynamic force (drag) and the rolling resistance given by the interaction between tires and the ground.

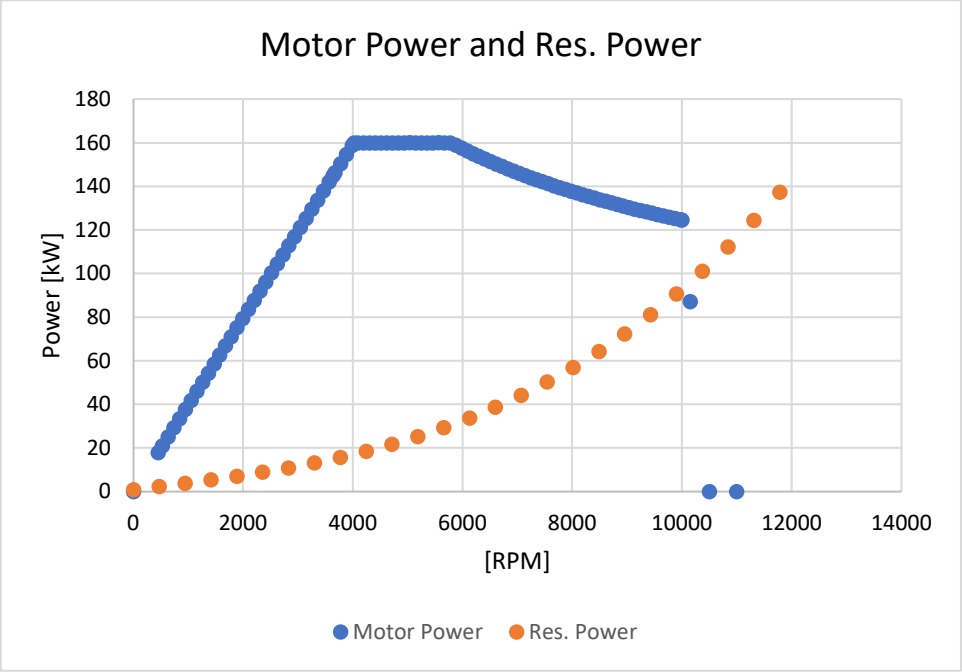

(**a**)

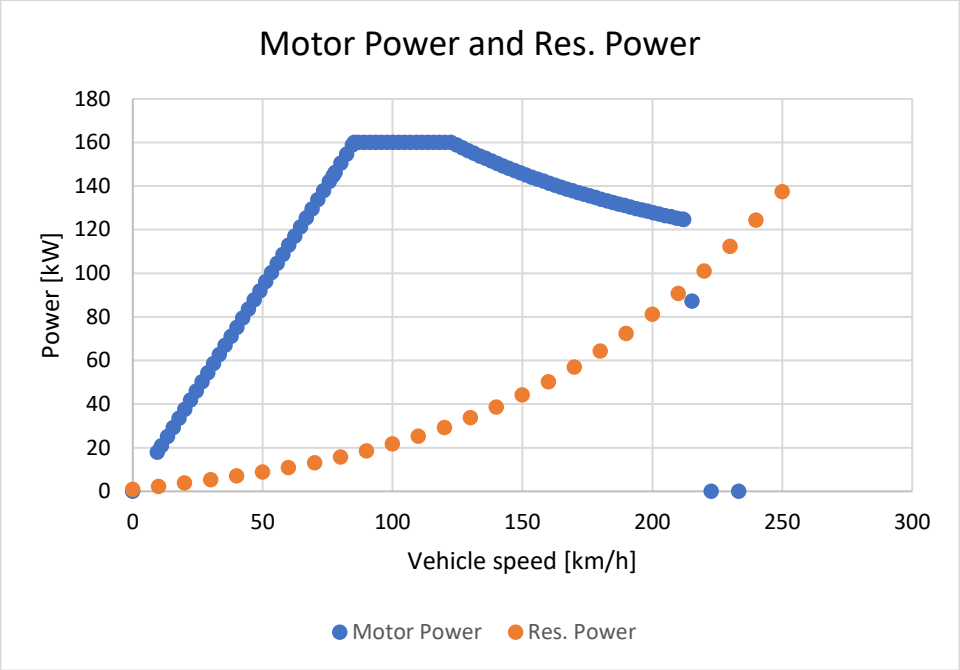

(**b**)

Figure 5.11. *Maximum deliverable power of the electric traction motor (in blue) and sum of the resisting powers due to aerodynamic force and rolling resistance (in orange), as a function of (**a**) the angular rotation speed of the electric motor (in RPM) and (**b**) the constant speed travelled by the vehicle. Assuming a total mass of the vehicle (including the transported load) equal to 3530 kg.*

Another aspect that differentiates the simulations of Section 2.4.1 from the vehicle model object of this work is the mass. The simulations in this section were carried out with variable mass of the vehicle, as a function of time during the mission. In particular, the variable mass is that associated with the load carried during the speed profiles of the mission.

First, an unladen mass of the vehicle (including battery pack, solid oxide fuel cell and tank with biomethane) equal to 1900 kg is considered. Furthermore, a constant driver mass equal to 80 kg and a variable mass relative to the load carried by the vehicle during the speed profiles of the missions are considered. This last aspect will be explored in the following section (Sezione 5.3.2).

Finally, a final change concerns the battery pack (object of sizing, together with the sizing of the fuel cell, for this work) and the size of the section of the electrical connection cables between the electric motor and the batteries.

It was chosen to consider a hypothetical configuration and type of battery pack that allows the delivery of a current (discharge current) equal to a maximum of 360 Amps, the object of the sizing is instead the capacity of the pack itself. Therefore, considering this limitation, the electric cables have been dimensioned in such a way as to allow the crossing of a maximum current of 360 A. For the dimensioning of the cables, a maximum current density of 3.5 A/mm^2 was also considered as regards the cable itself.

By dividing the maximum current of 360 A by the current density, a cable section of approximately 102.86 mm^2 was calculated, which corresponds to a cable diameter (circular section) of approximately 11.44 mm. To maintain safety, a conductor cable diameter of 12 mm has been set for the simulations and for the model. During the construction of the prototype, the commercial section immediately above 102.8 mm^2 should be chosen, which corresponds to 120 mm^2 (diameter of 12.36 mm). It would therefore have been more appropriate to adopt a diameter of 12.36 mm in the model, but having approximated to 12 mm does not involve substantial differences in the results obtained.

5.3.2 Speed Profiles of Vehicle Mission

The mission of the waste collection vehicle is known, in particular the information relating to the different daily speed profiles was acquired thanks to a MoTeC control unit and various sensors installed on board the original internal combustion engine vehicle powered by diesel. The goal is therefore to correctly size the hybrid electric/FC (powered by biomethane) waste collection vehicle so that it can perform the same mission as the original traditional diesel vehicle.

In particular, the acquisitions of interest concern the speed profile (vehicle speed as a function of the elapsed time) obtained by GPS detection, the electric current absorbed by the vehicle's electrical auxiliaries and the relative voltage (of the service battery with nominal voltage of 12 Volts), the flow rate and the hydraulic pressure necessary for the activation of the hydraulic auxiliaries (stabilizing feet, bin lift, waste compactor and tipping body) and, finally, it is necessary to know the vehicle weights at certain moments of the driving cycle, to estimate the mass of the transported load, moment by moment, during the mission.

The electrical power consumed by the vehicle's auxiliaries is calculated by multiplying the current by the voltage. The hydraulic power is instead obtained by multiplying the hydraulic flow by the pressure. Of the two powers absorbed by the vehicle auxiliaries, electric and hydraulic, the average over each driving cycle is considered as an input parameter for the simulation. In particular, the sum of the two average powers will be set as input, as the total power consumed by the vehicle accessories.

The missions are carried out in flat territory, in fact the altitude variation detected by the GPS is negligible. For the simulation the complete absence of ground gradient was therefore imposed.

Table 5.1 shows the main characteristics of each of the 10 vehicle mission speed profiles.

Table 5.1. *Main information of the driving cycles of the waste collection vehicle mission.*

Mission profile n°	Distance traveled [km]	Average speed [km/h]	Cycle time [h:min:s]	Maximum speed [km/h]	Average electrical power [W]	Average hydraulic power [W]	Total power of the auxiliaries [W]
1	34.707	8.8	3:56:31	86.4	540.9 *	215.6	756.5
2	39.361	8.3	4:42:59	55	442.6	174.6	617.2
3	43.570	9.0	4:51:34	62.5	671.6	73.3	744.9
4	13.780	13.6	10:07:08	108.7	531.2	131.5	662.7
5	81.789	16.1	5:04:55	105.5	561.5	241.0	802.5
6	50.003	9.0	5:32:58	75.1	566.9	247.2	814.1
7	72.137	12.4	5:47:39	83.3	597.3	202.6	799.9
8	60.671	14.7	4:07:42	85.7	540.9 *	303.6	844.5
9	89.048	16.1	5:31:43	106.6	498.7	267.7	766.4
10	85.977	19.5	4:24:27	92	457.6	255.3	712.9

* Electric power not available, estimated.

Of mission profiles number 1 and 8, the acquisitions relating to the current absorbed by the vehicle's electrical auxiliaries are not available, due to problems with the sensors during the acquisitions themselves. It was therefore not possible to calculate, instant by instant, the electrical power consumed and therefore not even the average over the cycle. For speed profiles 1 and 8, the average electrical power was therefore estimated to be equal to the average of the average electrical power value of the remaining cycles (from 2 to 7, plus 9 and 10).

The graphs related to the 10 daily speed profiles of the mission are shown below (from Figure 5.12 to Figure 5.21). In particular, the speed profile acquired by the MoTeC control unit via GPS signal is represented in blue, the manually "cleaned" speed profile in orange. The "cleaning" of the profiles was carried out by deleting the data relating to those acquisition points where the GPS signal has abruptly switched to speed values too high or too low, so as to consider these values unrealistic and associated with detection errors. Furthermore, the profile in orange, which is the one provided in input to the TEST model (see Section 2) represents the module of the speed profile, any lengths made in reverse (negative speed) by the vehicle are treated as lengths travelled in forward gear (positive speed), this to simplify the simulation in the TEST model, in which the possibility of traveling in reverse is not implemented. This simplification is irrelevant as regards the results obtained.

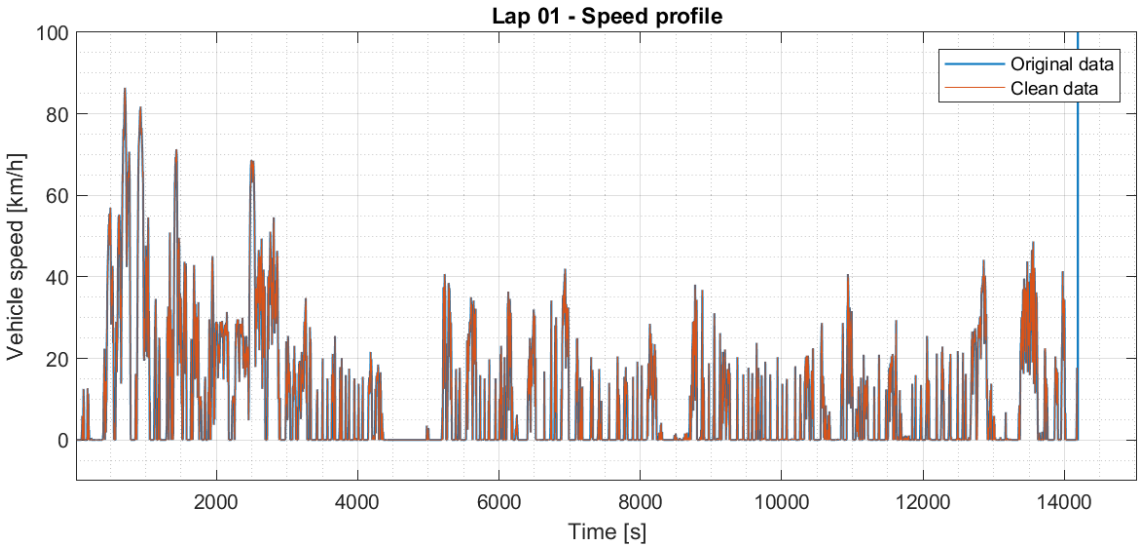

Figure 5.12. *Speed profile of cycle number 1 of the waste collection vehicle mission.*

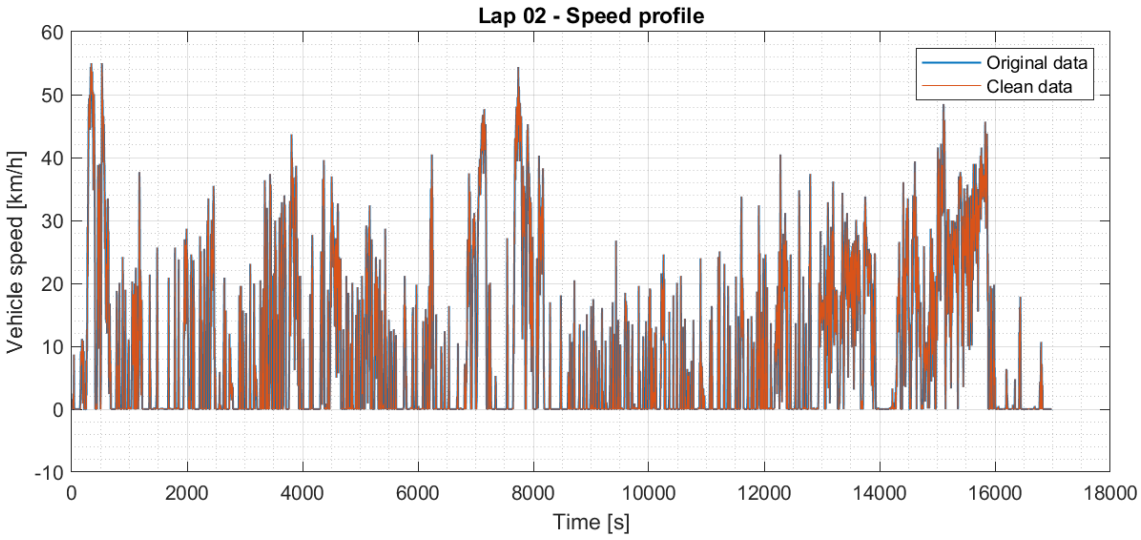

Figure 5.13. *Speed profile of cycle number 2 of the waste collection vehicle mission.*

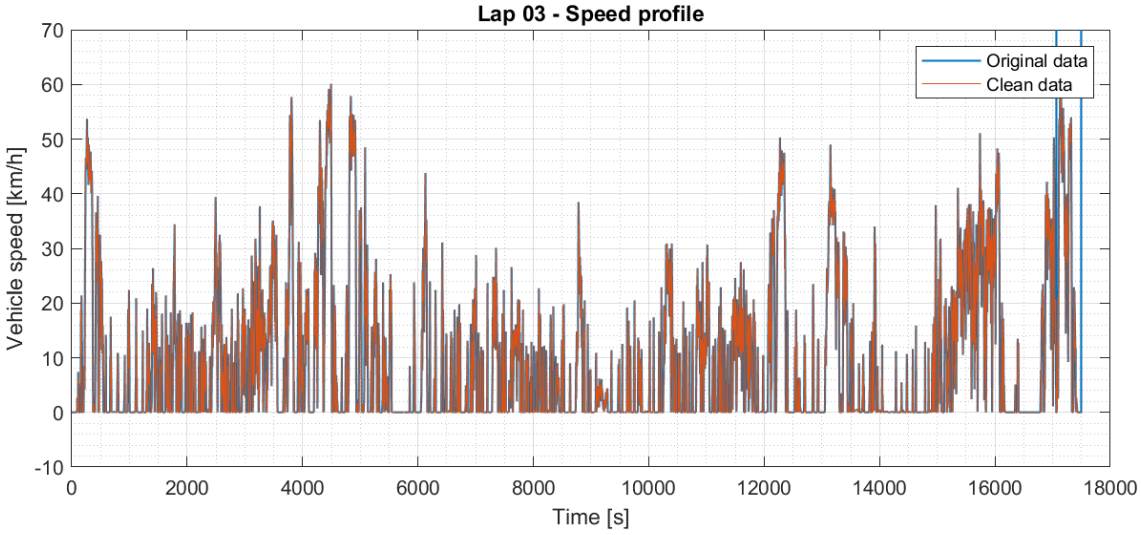

Figure 5.14. *Speed profile of cycle number 3 of the waste collection vehicle mission.*

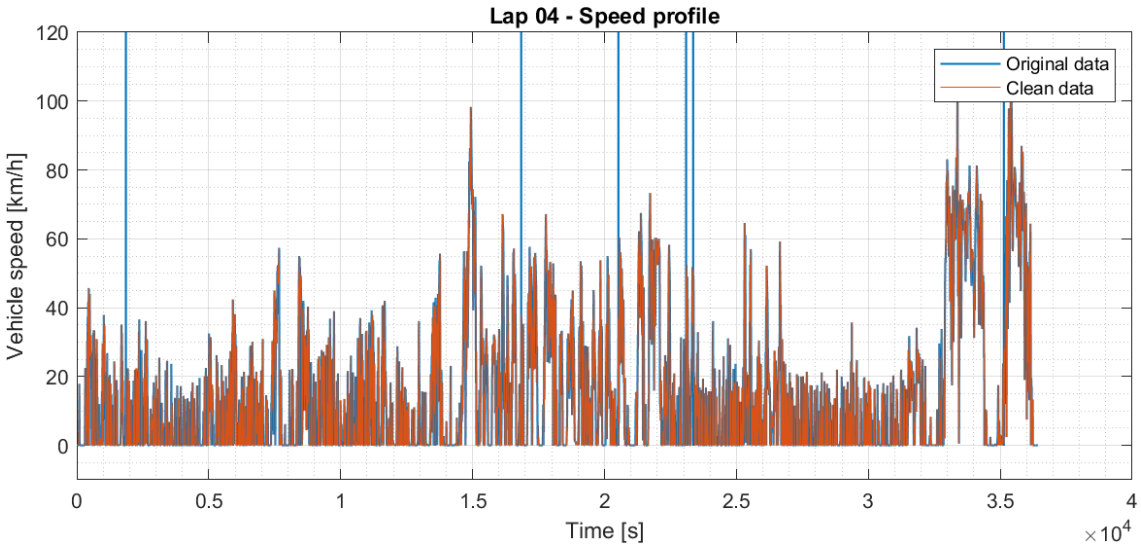

Figure 5.15. *Speed profile of cycle number 4 of the waste collection vehicle mission.*

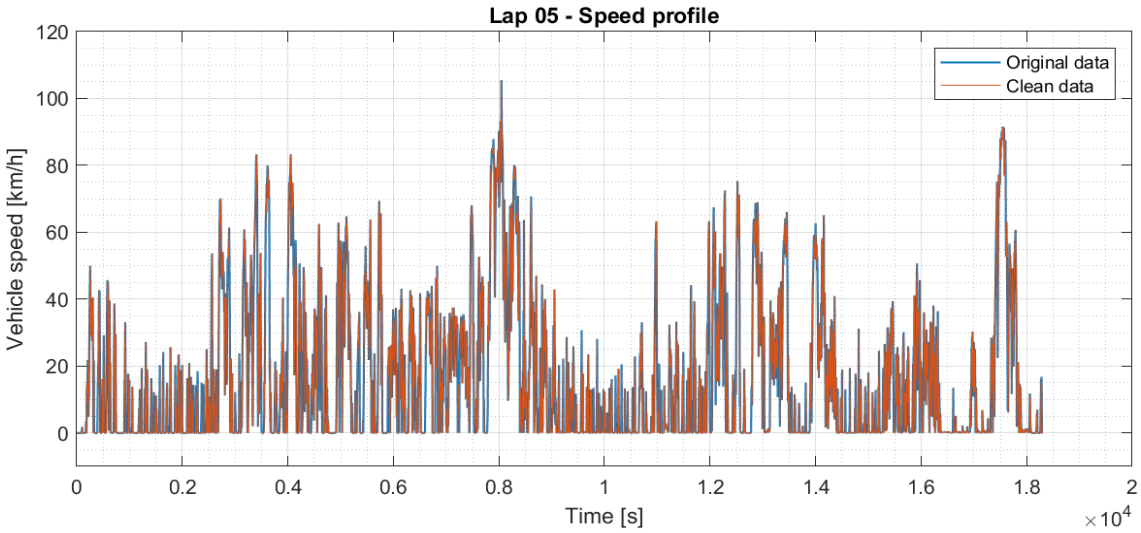

Figure 5.16. *Speed profile of cycle number 5 of the waste collection vehicle mission.*

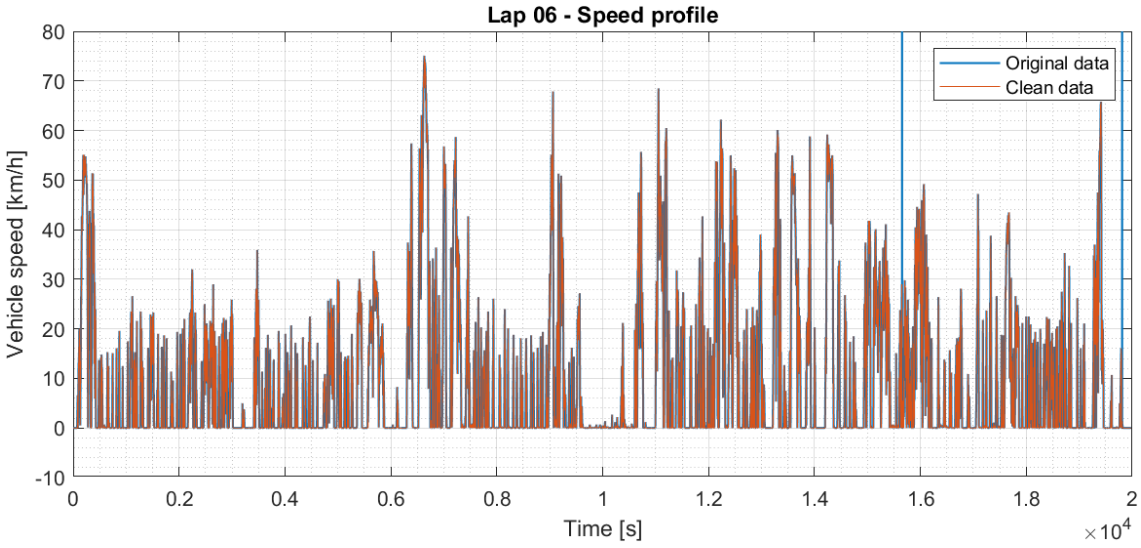

Figure 5.17. *Speed profile of cycle number 6 of the waste collection vehicle mission.*

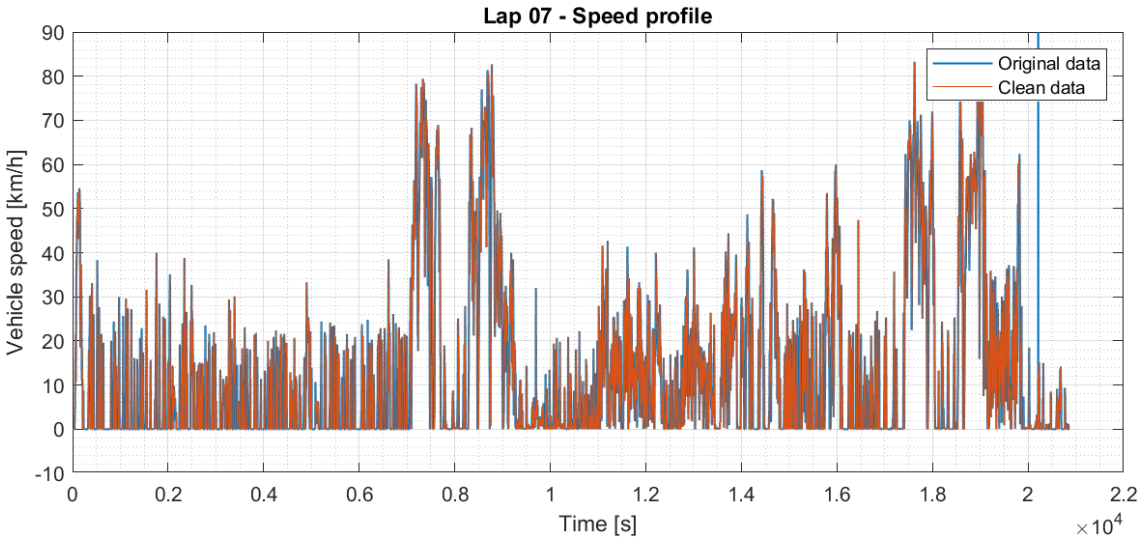

Figure 5.18. *Speed profile of cycle number 7 of the waste collection vehicle mission.*

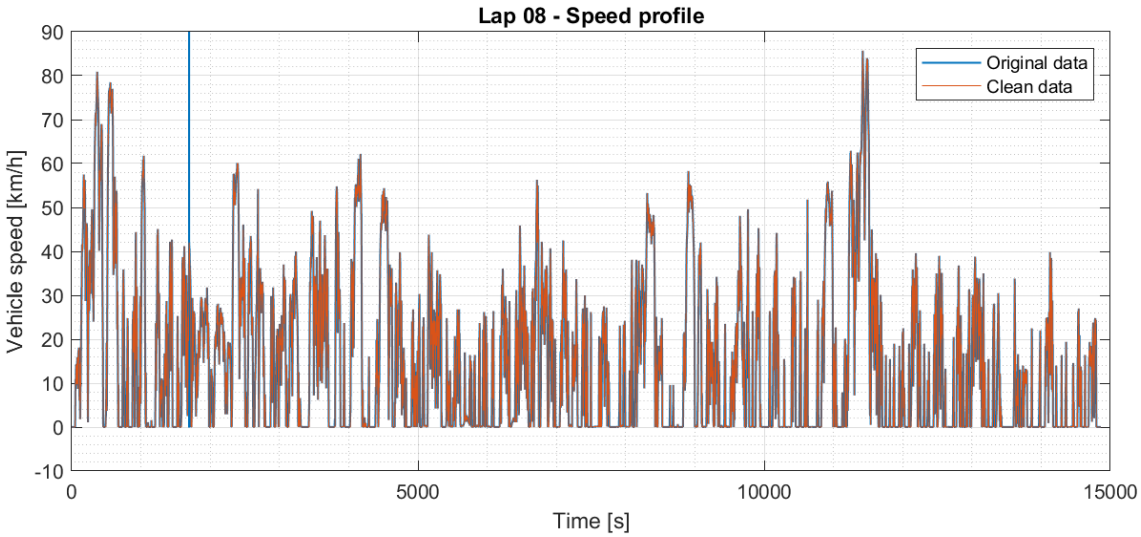

Figure 5.19. *Speed profile of cycle number 8 of the waste collection vehicle mission.*

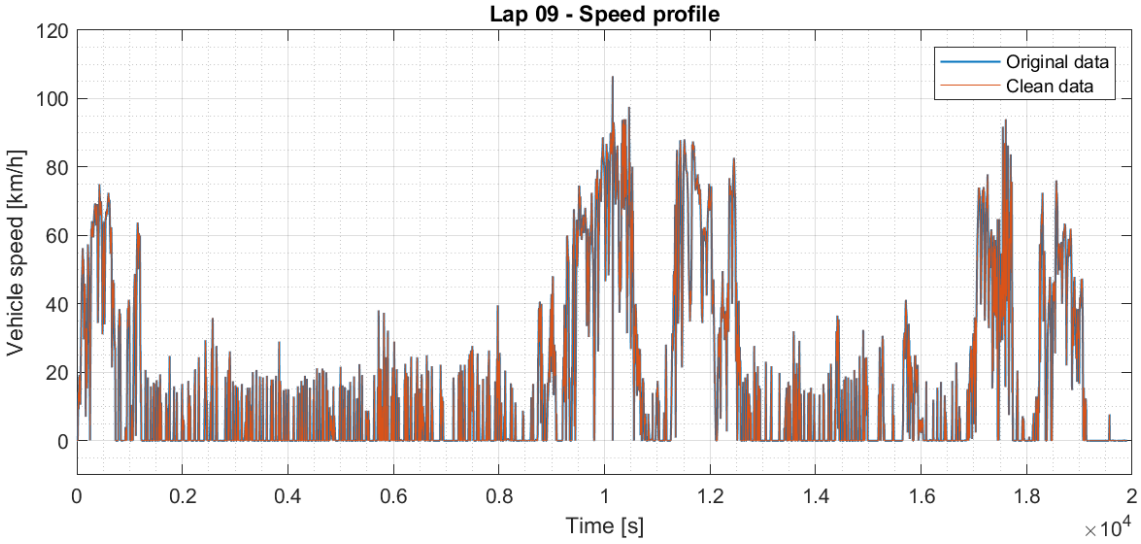

Figure 5.20. *Speed profile of cycle number 9 of the waste collection vehicle mission.*

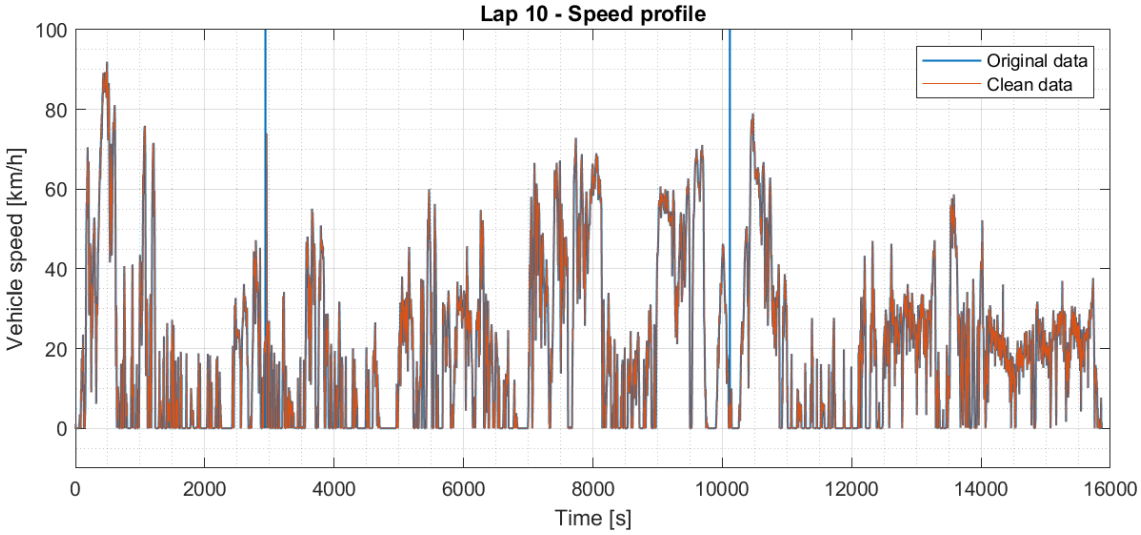

Figure 5.21. *Speed profile of cycle number 10 of the waste collection vehicle mission.*

For each mission speed profile, the number of discharging cycles of the transported waste and the total weight discharged were monitored (Table 5.2). Keeping in mind that discharging is not always carried out in a landfill, but is often carried out in intermediate areas, discharging into a heavy vehicle (typically a truck), the latter, once full, will then discharged at the landfill.

Table 5.2. *Number of waste discharges and total weight discharged, for each mission speed profile.*

Mission profile n°	Type of waste	Number of discharges	Total weight discharged [kg]	Average weight discharged at each unloading [kg]
1	GLASS	1	1550	1550
2	ORGANIC WASTE	2	3000	1500
3	GENERAL WASTE	1	560	560
4	GLASS	2	1120	560
	YARD WASTE	1	400	400
	GENERAL WASTE	1	600	600
5	PLASTIC	7	900	128.57
6	PAPER	7	1700	242.86
7	ORGANIC WASTE	2	2680	1340
8	YARD WASTE	3	1250	416.67
	ORGANIC WASTE	2	2980	1490
9	ORGANIC WASTE	2	2720	1360
10	PLASTIC	4	650	162.5

Not having sufficient information available to define the entity of the waste mass transported by the vehicle instant by instant, it was decided to divide each mission profile into as many temporally equal parts as the discharges carried out and to distribute the discharged weight equally for each discharge (or for each group of discharges of the same type of waste, as regards cycles 4 and 8). For each time interval between one discharging and the next, it has been assumed that the transported waste mass grows linearly from the zero value to the average discharging value (reported under the item "Average weight unloaded at each unloading [kg]" in Table 5.2 (Figure 5.22). A slightly different approach was used for profile 4: at time 14191 seconds the final discharging of the first group, consisting of two discharging, was carried out; it was therefore assumed to carry out the first discharging exactly halfway through the time elapsed before the second discharging (at 7095.5 s); the remaining time interval of the profile was equally divided among the other discharges; the approach adopted for the mass of the transported waste mass, on the other hand, remains

unchanged compared to that adopted for the other cycles. Figure 5.22 shows the trend of the waste mass during the missions.

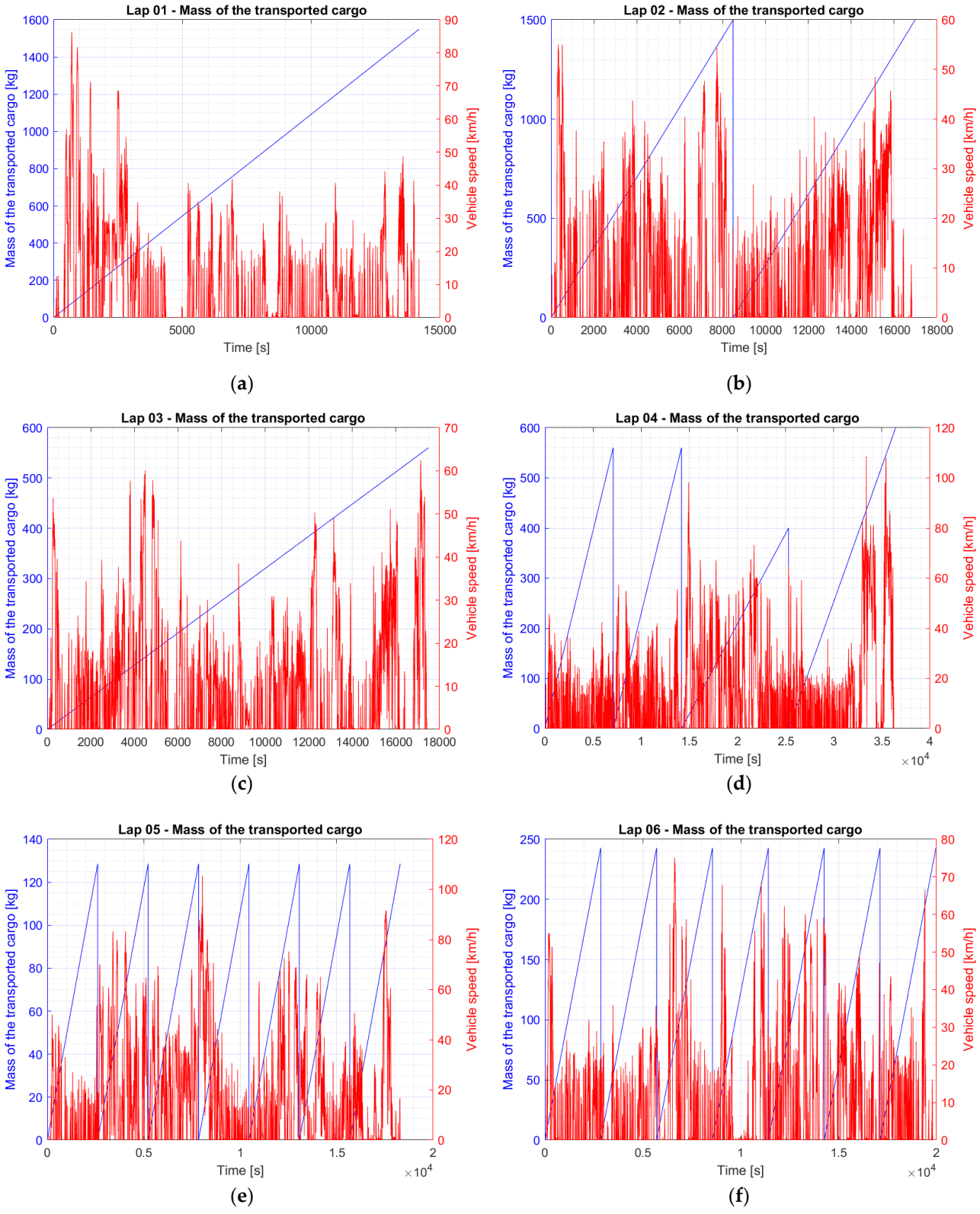

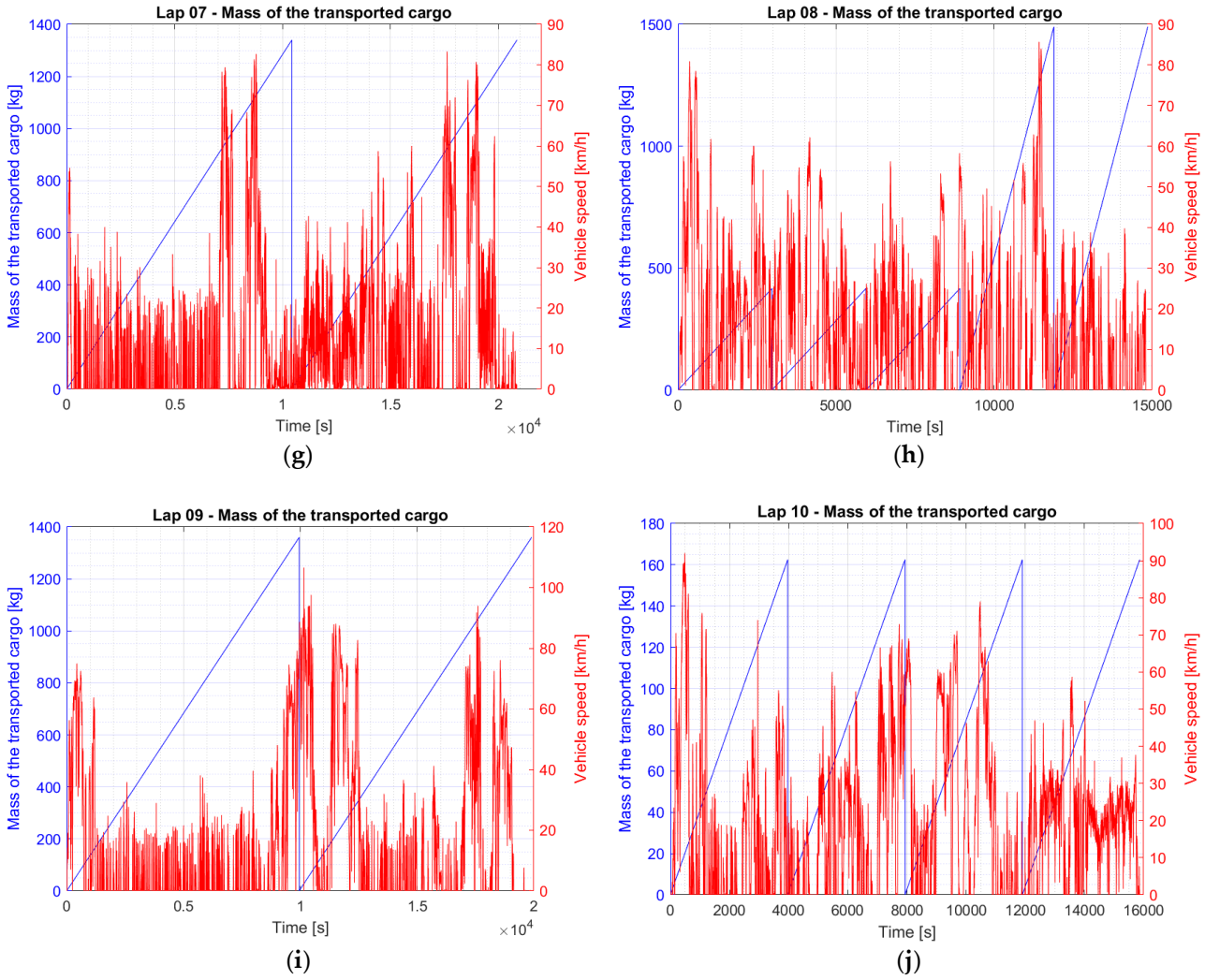

***Figure* 5.22.** *Carried load (waste mass) and speed profile of the mission: (**a**) profile 1; (**b**) profile 2; (**c**) profile 3; (**d**) profile 4; (**e**) profile 5; (**f**) profile 6; (**g**) profile 7; (**h**) profile 8; (**i**) profile 9; (**j**) profile 10.*

5.3.3 Simulation Model

For the simulations of the vehicle and its missions, the TEST model described in Section 2 was used, in particular the latest version of the model was used, the one containing the integration of the hydrogen FC and its compressor, described in Section 4. The use of the version with PEMFC or of the version described in Section 2 is irrelevant, in fact, during the simulations shown in this chapter, the PEMFC was disabled by means of the appropriate switch (shown in Figure 4.6) of the graphic user interface of the TEST model.

A further integration was also made to this latest version of the TEST model, which allows it to also simulate vehicles equipped with a solid oxide fuel cell (SOFC), which acts as a generator by recharging the battery pack.

In particular, a Simulink subsystem, called "SOFC peak power source", has been added to the Simulink TEST model. This subsystem outputs the power (P_{SOFC_th}) that the SOFC system can supply at the input to the battery pack. In the first version of the TEST model, presented in paper [10], there was already a generator, or more generators, that can be activated to recharge the batteries. The power that the generator, or generators, can supply as input to the battery pack, as explained in Section 2, is defined with the variable P_{gen_th}, which is then supplied as input to the "Battery Limitations" module shown in Figure 2.5. If the SOFC is present on the vehicle (activated by means of an appropriate switch presented later, Figure 5.23), the output power from the "SOFC peak power source" subsystem (P_{SOFC_th}) is assigned to the variable P_{gen_th}, through a Simulink "Switch", which allows you to switch between the power of the generator(s) and the power deriving from the SOFC, depending on the presence of the first or the second. The rest of the calculation flow of the TEST model remains unchanged from previous versions.

For this study, the SOFC is seen as a sort of "black box", only the constant power supplied by the FC (P_{SOFC}) and an efficiency relating to the DC/DC converter ($\eta_{DC/DC}$) are considered. DC/DC converter is in fact essential to carry the SOFC output voltage at the correct voltage for recharging the battery pack. The calculation carried out within the "SOFC peak power source" module is therefore reduced to the equation (5.28) alone.

$$P_{SOFC\_th} = P_{SOFC} \cdot \eta_{DC/DC} \tag{5.28}$$

Finally, in the graphic user interface of the TEST model, a tab has been added, relating to the definition of the variables P_{SOFC} and $\eta_{DC/DC}$, in which there is also a switch that allows you to activate ("On") or deactivate ("Off") the solid oxide fuel cell (Figure 5.23).

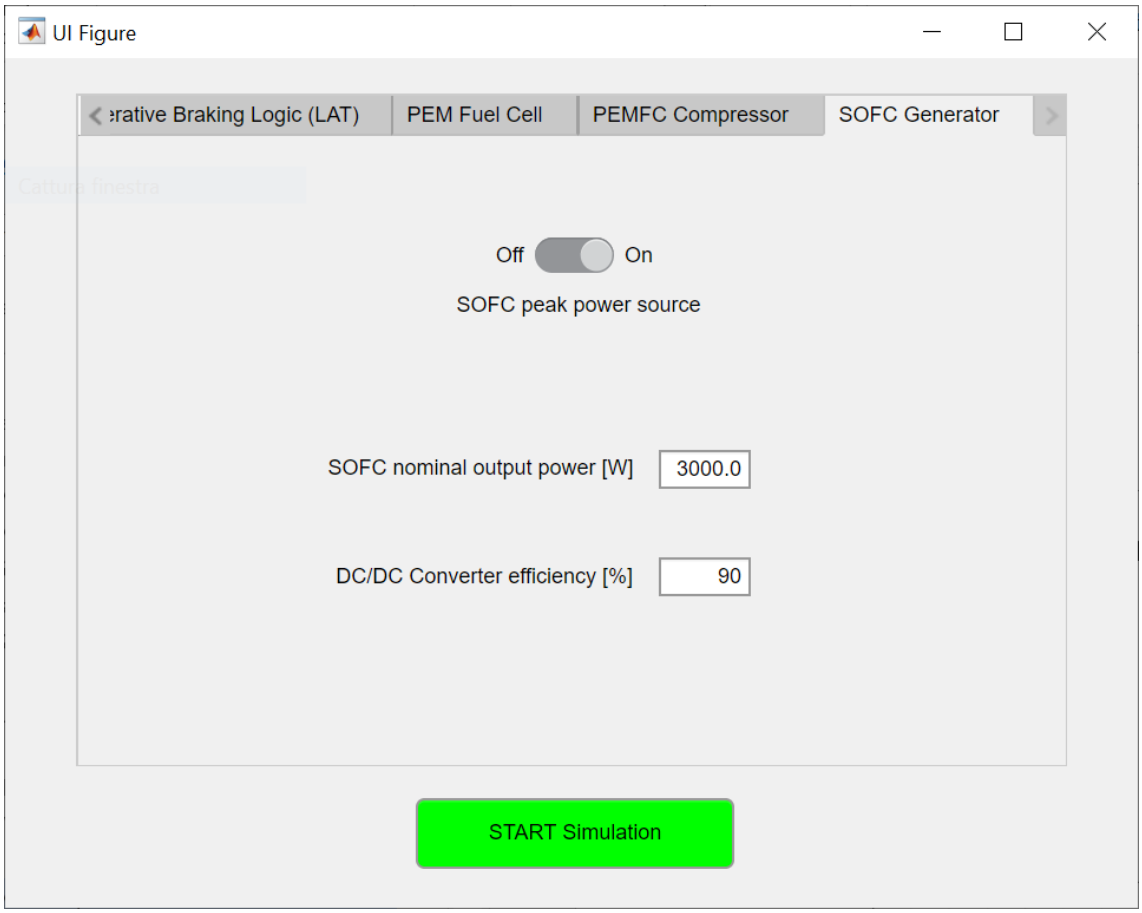

Figure 5.23. *"SOFC Generator" panel of the Graphic User Interface of the TEST model. In particular, this panel allows you to enter the inputs regarding the SOFC system.*

5.3.3.1 Simulation Input Data

For simplicity, most of the input data used for the simulation will be shown through the graphical user interface panels of the TEST model, whose settable parameters have been accurately described out in Section 2.3.

As for the main simulation data (to be set via the "Simulation" panel presented in Figure 2.10):

- The relative "clean" speed profile, presented in Section 5.3.2, is used for each cycle;
- Each profile is filtered using the parameter $k = 30$, remembering that the latter corresponds to the number of elements with which the moving average is calculated based on the speed function;
- The battery pack temperature is set constant, and equal to 23 °C, for each mission profile;
- The elevation profile is defined constant and null for each speed profile;

- For all simulations, a "Sample Time" (t_s) equal to 0.05 seconds was adopted, which corresponds to the sampling interval of the GPS signal for each speed profile;
- The initial state of charge of the battery pack, for each speed profile, is subject to sizing.

The vehicle being simulated is the waste collection vehicle presented in Section 2.4.1, albeit with some minor modifications and with the addition of the SOFC system on board (see Section 5.3.1), and, as seen in Section 2.4.1, this vehicle does not require any calibration as regards the mechanical part of the TEST model. The coefficients to be set in the "Calibration" panel (Figure 2.12) are therefore all set to null value, except for c_0 to which the unit value is assigned; in this way no calibration is carried out.

Here are some environmental parameters and other parameters common to all simulations (for all mission profiles), defined through the "Environmental and other" panel (Figure 2.13) of the graphic interface.

- Air density: $\rho = 1.225\ kg/m^3$
- Gravity acceleration: $g = 9.81\ m/s^2$
- Electrical resistivity of conductor cables (copper):
  $\rho_{Cu} = 1.225\ \frac{\Omega \cdot mm^2}{m}$
- Driver's weight (and no passengers): $m_{driver} = 80\ kg$
- Mass of fuel transported: $m_{fuel} = 0$
  (the weight of the transported biomethane is already included in the weight of the SOFC system and already considered in the empty mass of the vehicle).

The mass of the transported load (the waste mass), defined as a function of the time elapsed from the start of the simulation, depending on the mission profile analysed, is set as defined in Section 5.3.2.

Using the tab shown in Figure 5.24 the inputs relating to the vehicle and the wheels are set, the values shown in the figure are those adopted for the simulations of all the mission profiles. The only exception is represented by the value of the total power consumed by the vehicle's auxiliaries, which relates only to speed profile number 7.

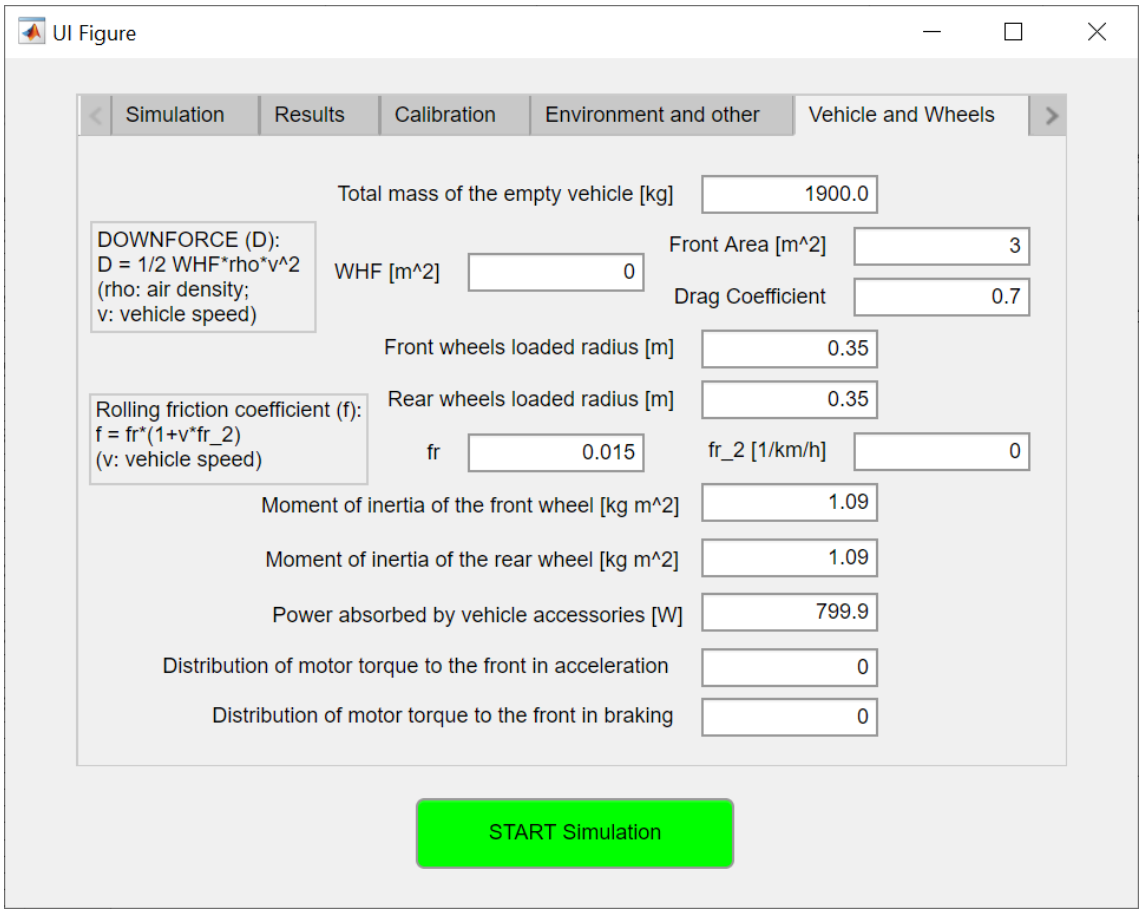

Figure 5.24. *"Vehicle and Wheels" panel of the Graphic User Interface. In particular, the panel in the figure shows the values adopted for the simulations of the waste collection vehicle equipped with SOFC, relating to the vehicle in general and to the wheels. The only exception is represented by the value of the total power consumed by the vehicle's auxiliaries, which relates only to speed profile number 7.*

The values of the total power consumed by the vehicle auxiliaries (P_{acc}), for each driving cycle, are those indicated under the item "Total power of the auxiliaries [W]" in Table 5.1.

Figure 5.25 shows the values of all the parameters relating to the vehicle's hydraulic braking system, adopted for all simulations.

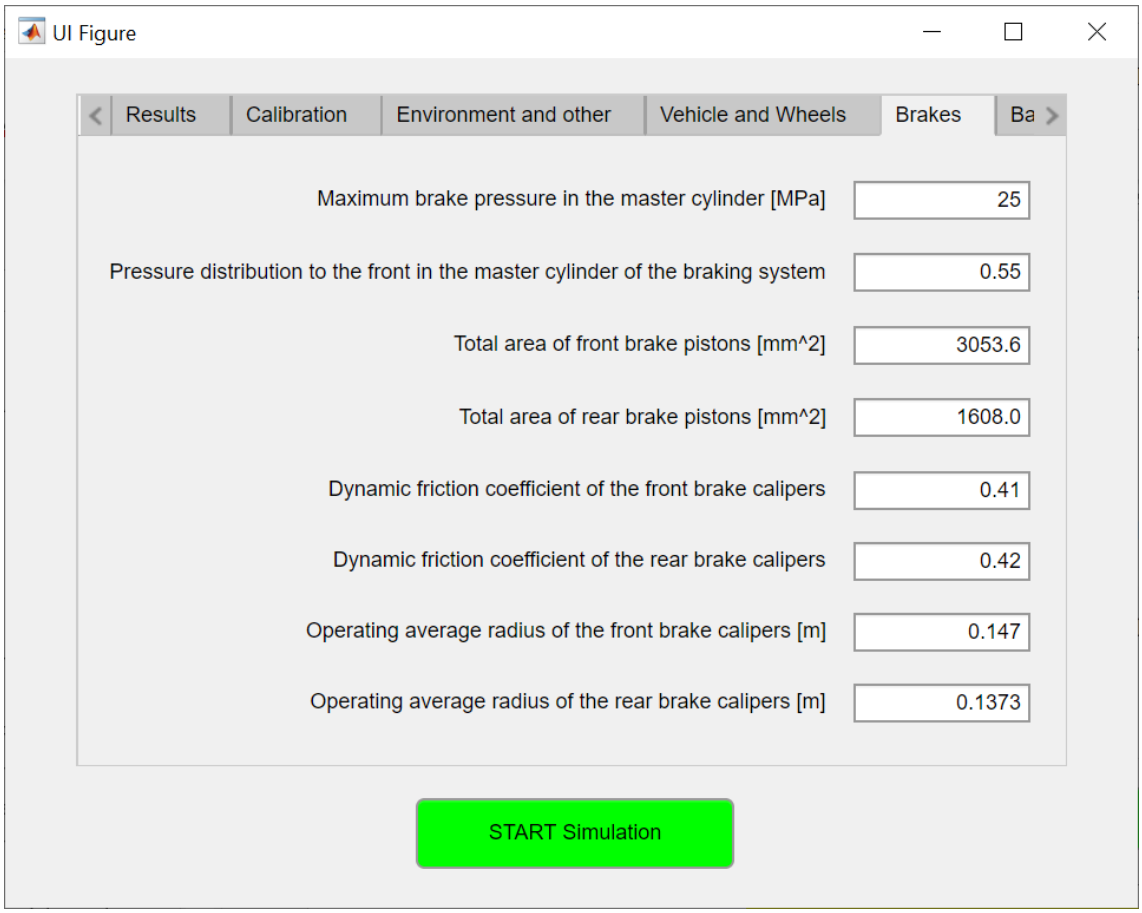

Figure 5.25. *"Brakes" panel of the Graphic User Interface. In particular, the panel in the figure shows the values adopted for the simulations of the waste collection vehicle equipped with SOFC, relating to the hydraulic braking system.*

As regards the battery pack, a configuration was chosen that avoids the occurrence of limitations to the performance of the vehicle on the driving cycles of the mission, limitations due to the maximum current that can be supplied by the pack itself. The capacity of the battery pack has been dimensioned and this aspect will be better seen in the next section (Section 5.3.4).

The following performances have been set for the inverter that connects the battery pack and the motor.

- Inverter efficiency in the discharge phase of the battery pack: $\eta_{inv\_disch} = 0.88$
- Inverter efficiency in the charge phase of the battery pack: $\eta_{inv\_ch} = 0.8$

It can be noted that, as it should be, the discharge efficiency is lower than that in charge.

The vehicle is rear-wheel drive, so in the interface of the TEST model the front electric motor has been set to "Off" using the relative switch (Figure 2.17).

Figure 5.26 shows the various parameters set for the simulations, inherent in the electric traction motor (which acts on the rear axle).

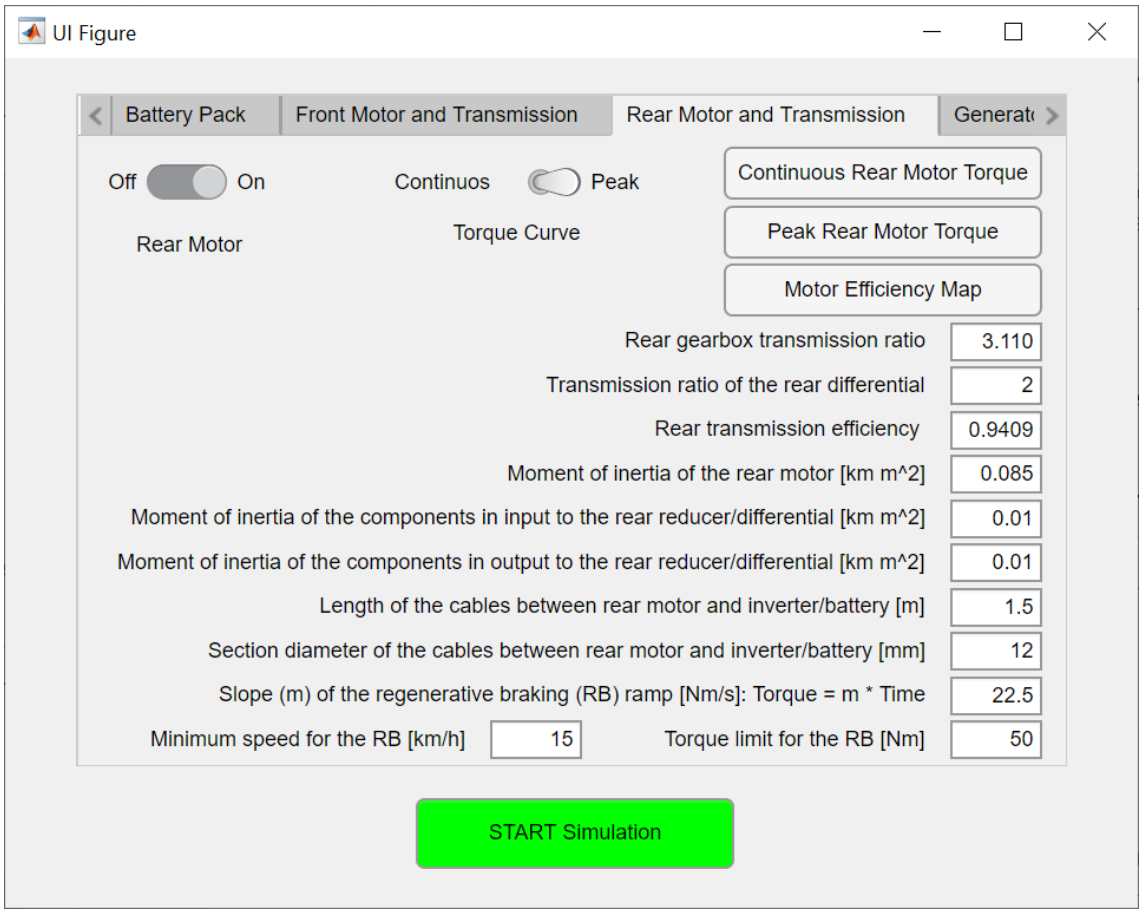

Figure 5.26. *"Rear Motor and Transmission" panel of the Graphic User Interface. In particular, the panel in the figure shows the values adopted for the simulations of the waste collection vehicle equipped with SOFC, relating to the electric motor.*

The motor torque curve of the vehicle being simulated is the peak one represented in Figure 2.20 in Section 2.4.1.2.

For the electric motor, the efficiency map has also been defined, known for the motor itself, in which the efficiency varies according to RPM and motor torque around the value of about 90%.

On board the vehicle, the only power generator is represented by the SOFC, there are no other generators, for example a turbine generator, so in the

"Generators" panel (Figure 2.19) a number of generators (N_{gen}) equal to zero has been set.

It has been chosen to consider a vehicle model as generic as possible, for this reason, the "RB logic" exposed in Chapter 3 has not been adopted on the vehicle itself. In the "Regenerative Braking Logic" panel (Figure 3.21), this logic has therefore been deactivated by setting its switch to "Off".

The vehicle also has no hybrid electric/PEMFC configuration, therefore, the hydrogen fuel cell has also been deactivated by means of the relative switch, present in the "PEM Fuel Cell" panel (Figure 4.6).

Obviously, however, the switch of the panel relating to the SOFC generator (Figure 5.23) is set to "On" to activate the solid oxide fuel cell system which acts as a generator. The efficiency of the DC/DC converter that connects SOFC and battery pack is estimated to be 90%, in accordance with what is reported in the literature [123,124]. The power supplied by the FC will instead be subject to sizing.

5.3.4 Sizing of SOFC and Battery Pack

By carrying out various simulations on the 10 speed profiles of the mission, with different capacities of the battery pack and with different constant powers supplied by the SOFC, it was found that, with the same capacity of the batteries and the same power of the SOFC, cycle 9 was associated with a greater consumption of SOC.

It was therefore found that profile 9 is the most expensive in energy terms, followed by cycle 4, which is the most time-consuming, with about 10 hours of cycle time (see Table 5.1).

It was therefore chosen to size the SOFC and the battery pack on cycle 4, the longest in terms of time, so that it can be carried out without stopping.

The sizing aims to obtain the following conditions:

- The system must be sized on the cycle of about 10 hours (profile 4), in such a way as to be able to carry out this cycle during the day without any stopping;
- The battery pack should be sized as small as possible (at the lowest possible capacity);
- The SOFC must be sized as small as possible (lowest possible power delivered);

- During the mission profiles the battery pack must never reach a SOC of 100% (or get too close to it), to avoid having to implement the emergency condition of switching off the fuel cell;
- The battery pack must never drop below a minimum SOC (defined as 20%) that can lead to the lack of energy necessary to complete the mission profile;
- The sizing on cycle 4 is carried out in such a way as to exploit as much SOC field as possible, to ensure that the capacity of the battery pack and the power supplied by the SOFC can be minimized;
- For the most energy-consuming profile (profile 9) a recharging stop is set at about mid-cycle, in fact, by dimensioning as defined in the previous point (on cycle 4), it is impossible to complete profile 9 without stopping.

By carrying out different simulations for profile 4, at different capacities of the battery pack and with different powers supplied by the SOFC, the best compromise was found for SOFC and battery pack size:

- Battery pack capacity of 30 Ah;
- Constant power supplied by the SOFC equal to 3 kW.

These values, for mission profile 4, allow to exploit a SOC range between a maximum of 95.6% and a minimum of 20.6%, starting the profile with an initial SOC equal to 90% and ending it with a residual SOC equal to 21.3%.

The vehicle, with the values of 3 kW of SOFC power and 30 Ah of battery pack capacity, is unable to completely complete profile 9, the most demanding in terms of energy, without stopping. The cycle has therefore been divided approximately in half (with respect to time), to plan an intermediate stop with the vehicle off in which the battery pack is recharged by the SOFC, which, remember, remains always on for the entire life of the vehicle.

For the subdivision of profile 9 into two phases, the GPS profile was overlying on the Google Earth map and an area of the profile at zero speed was found that would be convenient for making a stop. After 10862 seconds elapsed from the start of the cycle, the vehicle is stationary and located in a square, which can therefore be used to make a stop for charging.

The mission profile 9 is then divided into two partial phases, as shown in Figure 5.27, in profile 9.a and profile 9.b.

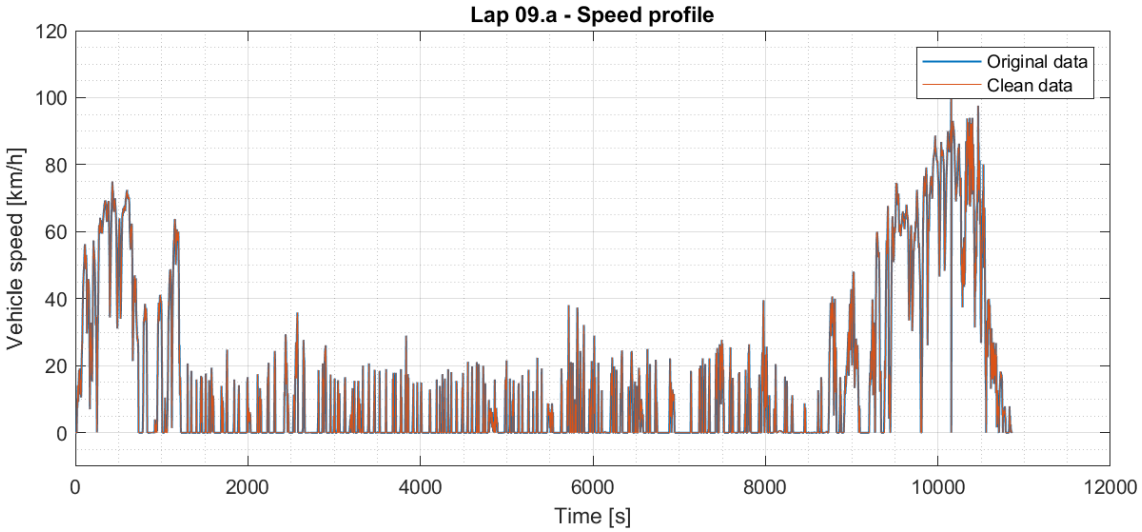

(**a**)

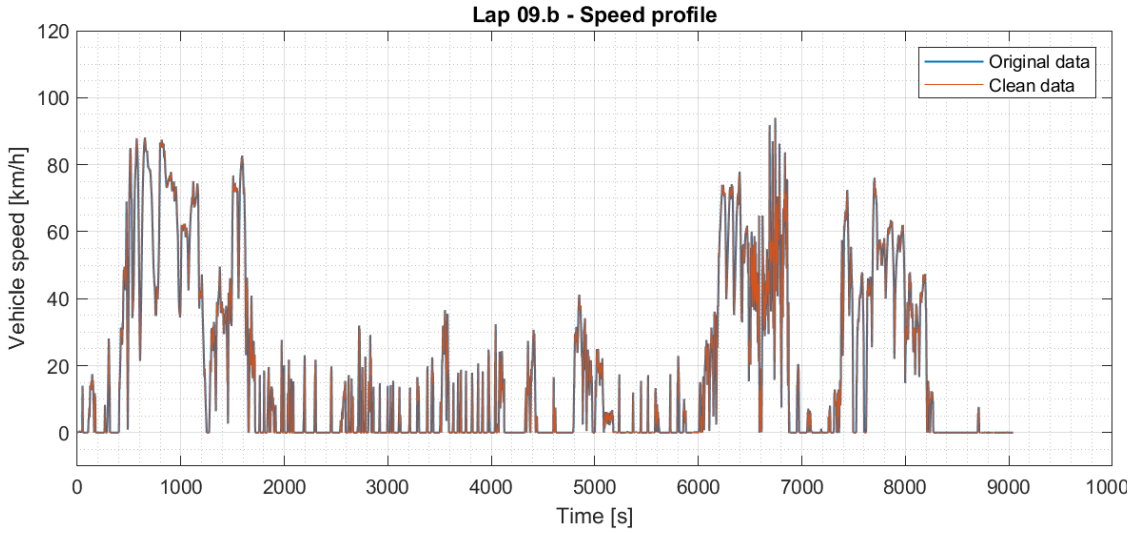

(**b**)

Figure 5.27. *Speed profile of cycle number 9 of the waste collection vehicle mission, divided into two phases: (**a**) first phase from 0 to 10862 seconds (profile 9.a); (**b**) second phase from 10862 seconds (referred to profile 9) to the end of the cycle (profile 9.b).*

Again, by overlapping the GPS profile with Google Earth, it was noted the presence of a waste discharge point at 9150 seconds elapsed from the start of the cycle. Subsequently, the vehicle moves unloaded for a certain time, without making any collections, to change the collection area. According to these hypotheses, the estimated and approximate trend of the mass of the transported

waste load was constructed as a function of the simulation time, as reported in Figure 5.28.

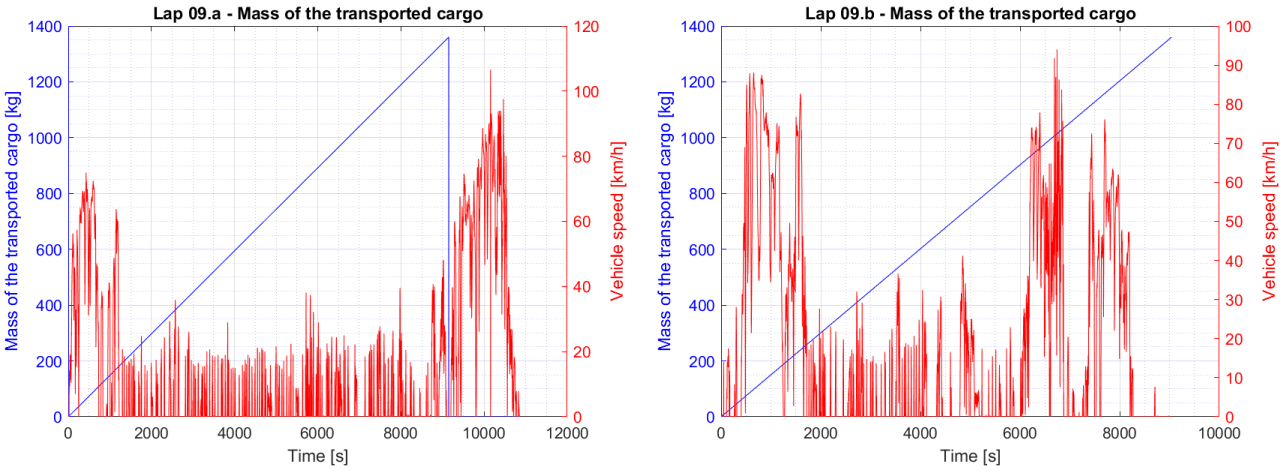

(**a**) (**b**)

Figure 5.28. *Carried waste load and speed profile of the mission: (**a**) first phase of cycle 9 (profile 9.a); (**b**) second phase of cycle 9 (profile 9.b).*

Finally, for the simulations of both cycles, profile 9.a and profile 9.b, the total power consumed by all vehicle auxiliaries was considered the average calculated on the entire mission profile number 9 (shown in Table 5.1).

From the simulations it emerged that a charging stop of an hour and a half is sufficient, between profile 9.a and 9.b, to allow the conclusion of the second phase of profile 9 without incurring a too low state of charge.

5.3.5 Results

Table 5.3 summarizes the main results obtained for the vehicle model with SOFC generator, that supplies constant power equal to 3 kW, and with a 30 Ah capacity battery pack.

Table 5.3. *Main results of the driving cycles of the mission of the waste collection vehicle equipped with SOFC. In particular, the item "SOC range [%]" refers to the portion of SOC used during the journey of the mission profile, it is therefore calculated as the difference between the maximum SOC and the minimum SOC reached during the cycle in exam.*

Mission profile n°	Initial SOC [%]	Final SOC [%]	Maximum SOC [%]	Minimum SOC [%]	SOC range [%]	Cycle time [h:min:s]	Charging time [h:min:s]
1	60 *	45.7	61.0	44.8	16.1	3:56:31	1:02:45
2	55 *	47.6	56.4	45.1	11.3	4:42:59	0:32:25
3	50 *	47.1	54.9	46.6	8.2	4:51:34	0:12:44
4	90 *	21.3	95.6	20.6	74.9	10:07:08	5:02:09
5	90 *	30.4	91.7	29.5	62.2	5:04:55	4:22:07
6	55 *	44.8	58.6	43.5	15.1	5:32:58	0:44:50
7	90 *	28.3	92.3	26.4	66.0	5:47:39	4:31:14
8	75 *	32.4	75.1	32.2	42.9	4:07:42	3:07:13
9.a	90 *	54.4	90.1	54.1	36.0	3:01:02	1:30:00 *
9.b	74.8	26.3	75.5	24.4	51.1	2:30:41	4:39:57
10	80 *	32.9	80.2	32.7	47.6	4:24:27	3:27:05

* Quantity subject to sizing.

The mission profiles from number 1 to 10 are daily cycles, to be carried out over two weeks (each cycle only once every two weeks), the two-week mission is then repeated continuously throughout the year, without weeks of stop. Each cycle must be carried out starting with an initial SOC equal to the value reported under the heading "Initial SOC [%]" of Table 5.3. Therefore the residual SOC (final SOC) of the cycle preceding the one considered must be reported on the initial value of the new daily cycle to be carried out on the following working day. Considering that the final SOC of each cycle is lower than its initial SOC, the sum of all the charging phases between one cycle and the next corresponds to the sum of all the charging phases necessary to bring the final SOC of a cycle back to the initial SOC of the cycle itself. This aspect greatly simplifies the problem, in fact, to obtain the total recharge time between the various mission profiles, it is sufficient to associate the value reported under the item "Charging time [h:min:s]" in Table 5.3 to each cycle. This value corresponds precisely to the time needed to recharge the battery pack from the final SOC of the profile to the initial SOC of the profile itself, with the vehicle off (and SOFC always on) add all these values together (time obtained through simulations). However, pay attention to the fact that the recharge time associated with profile 9.a corresponds to the partial recharge time of an hour and a half sized in order to then be able to complete cycle 9.b. The recharge time associated with profile 9.b is instead the

time required to recharge the battery pack from the final SOC of cycle 9.b to the initial SOC of profile 9, then to the initial SOC of profile 9.a.

Therefore, by adding all the charging times associated with each cycle, an overall charging time of 29 hours, 12 minutes, and 29 seconds is obtained every two weeks of vehicle operation. The total cycle time is instead given by the sum of all the values reported under the item "Cycle time [h: min: s]" of Table 5.3 and corresponds to a total of 54 hours, 7 minutes, and 34 seconds in which the vehicle is operational, again within two weeks.

The total time, every two weeks, in which the SOFC operates to supply energy for the mission profiles corresponds to the sum of the total time spent on the cycles and the total recharge time. It therefore corresponds to 83 hours, 20 minutes, and 3 seconds.

Considering that two weeks have a total of 336 hours, subtracting from these the time in which the SOFC operates to provide energy for the mission, in the remaining 252 hours, 39 minutes and 57 seconds the SOFC will supply power to the electrical grid, the vehicle, at least for these approximately 253 hours it will therefore have to be connected to the stationary electricity grid or, alternatively, to other infrastructure with similar functionality (infrastructure for charging other vehicles in the fleet, for example full electric vehicles; charging infrastructure for a stationary energy storage system; etc.).

5.4 FINAL CONSIDERATIONS

Thanks to the analysis of the literature and the study on the operation of solid oxide fuel cells, it was possible to lay the foundations and initial hypotheses for the construction of a hybrid electric/SOFC vehicle model.

The solution that has been found is that of a purely electric traction vehicle, with an electric motor powered by a battery pack, which is in turn recharged by a SOFC system, that acts as a constant power charging generator. This vehicle layout is therefore suitable for use for vehicles operating in a fleet, with a predefined mission.

The components of the system, in particular the battery pack and the SOFC, must be suitably sized in such a way as to guarantee the functionality of the vehicle and allow meeting the requirements of the mission.

In the work presented in this chapter, a waste collection vehicle was considered, which operates in fleet on predefined daily waste collection missions. Based on the mission data, it was possible to size the vehicle and establish the

pre-set conditions to which the various mission profiles will have to undergo during operation (in particular the initial SOC of the profile of each daily mission).

Therefore, starting from the creation of a model for a particular vehicle (the waste collection vehicle), it was possible to show the methodology to be adopted for the sizing and construction of a model of a generic SOFC vehicle that operates in fleet. The work done is therefore repeatable and can also be adapted to other types of vehicles, paying attention to the fact that there is a need for a predefined and fixed mission over a certain period (for example the two weeks of the waste collection vehicle).

Finally, thanks to the notions learned on the theory of SOFC modelling, it is possible, in the future, once the constant power of the SOFC in the hybrid vehicle system has been dimensioned, to choose the most appropriate SOFC configuration that guarantees the supply of the chosen constant power, to model a solid oxide single cell of the stack and, through a sensitivity analysis on the various parameters that influence the characteristic curve of the FC itself, investigate a possible optimization of the single cell.

6 THE ENVIRONMENTAL PERFORMANCE OF TRACTION BATTERIES FOR ELECTRIC VEHICLES FROM A LIFE CYCLE PERSPECTIVE

This chapter provides a deepening relating to the impacts associated with the life cycle of traction batteries for electric vehicles, carried out through a review of the available literature. As anticipated, this is in order to better understand the usefulness of an energy optimization on board the vehicle, which allows to reduce consumption in the use phase and to allow the sizing of a reduced battery pack in the design phase, which therefore allows to save resources in the production phase of the pack itself.

The work described in this chapter was also presented in paper [1] published in the journal "Environmental and Climate Technologies" and was created in collaboration with the activity of a master's degree thesis [125].

The aim of this review work is the analysis of the results obtained from the scientific literature concerning all the phases that make up the life cycle of traction batteries for electric vehicles, in order to evaluate the associated environmental impact. In this regard, some scientific articles dealing with LCA (Life Cycle Assessment) studies concerning electric vehicles, with particular reference to batteries, will be examined. The revision of these articles will provide a general framework for the production, use and recycling phases of traction batteries. In particular, different parameters that influence the outcome of the LCA studies will be shown, parameters on which we can then act to improve the environmental impacts of the transition from internal combustion vehicles to electric mobility. These parameters are represented by the chemistry of the battery considered, aspect at the centre of the discussion, by the specific energy and efficiency of the battery pack, by the durability of the latter, but also by other aspects, such as the energy mix considered (both for the production phase, for the use phase and for recharging) and the functional unit chosen for the study, which determines a different approach, related to the analysis of a specific problem or aspect rather than another. Finally, the usefulness of the recycling practice and the related problems will be shown. In fact, the recycling must be perfected according to the battery chemistry in question to obtain benefits and better reduce environmental loads.

This chapter is organized as follows.

- Section 6.1 presents a contextualization of the review work performed.
- Section 6.2 describes the methodology adopted for the selection of articles of interest for review.
- Section 6.3 reports the results of the literature review, divided according to the different phases of the traction battery life cycle: extraction and production phases, use phase and, recycling phase.
- Finally, Section 6.4 gives some concluding remarks and some final considerations.

6.1 CONTEXTUALIZATION

Environmental problems and the depletion of fossil resources have led to consider the use of renewable energies. To exploit this type of energy, accumulation systems are required that store the energy and make it available when necessary; for vehicles traction, to date, batteries are among the best candidates for this purpose [126].

This work mainly focuses on the contribution of the various battery chemistry types with regard to the environmental impact. The battery pack, in fact, is the component that has the greatest impact on the environment as regards the transition from internal combustion vehicles to electrified vehicles.

Thanks to the analysis of the articles in the literature, information relating to the life cycle associated mainly with traction batteries for electric vehicles was collected and reorganized.

Although lead-acid batteries are still adopted on some electric road vehicles [22] the most widespread technology for the moment is (and will be, at least in the short term) the lithium-ion batteries (LIBs) [126]. These, in fact, compared to other commonly used batteries (lead-acid, nickel cadmium, metal hydrides) have a higher energy density and higher power density, a long-life cycle, a strong environmental adaptability and a low level of self-discharge.

Types of commercial lithium-ion batteries are lithium-cobalt oxide ($LiCoO_2$; LCO), lithium-iron-phosphate ($LiFePO_4$; LFP), lithium-manganese oxide ($LiMn_2O_4$; LMO), lithium-nickel-cobalt-manganese oxide ($LiNi_xCo_yMn_zO_2$; NMC or NCM, the two symbols are interchangeable), lithium-nickel-cobalt-aluminium oxide ($LiNi_xCo_yAl_zO_2$; NCA) and lithium-titanium oxide ($Li_4Ti_5O_{12}$; LTO), which has lithium titanate as an anode.

All these batteries could be used in electric vehicles because they are able to provide the necessary performance in automotive applications and, based on their characteristics, different results are obtained: LMOs have a high specific power; NCAs and NMCs are the cheapest, thermally stable, and highest specific energy lithium-ion batteries; LFPs have a fairly flat open circuit voltage curve, but have low capacity and a high self-discharge rate; LTOs, on the other hand, have a long duration and fast recharge, but a low specific energy and a higher cost [127].

It is also important to remember that, for automotive applications, the battery pack is no longer deemed usable when it has an effective capacity approximately 80% less than its nominal capacity [128].

The interest in electric vehicles arises mainly from the fact that their motor does not emit atmospheric pollutants directly into the environment during the use phase. On the other hand, however, some emissions are necessarily produced during the production phase of the electric powertrain and during the vehicle use phase, due to the production of the electricity required to recharge the batteries. Therefore, it is necessary to investigate whether this effect goes to counterbalance the benefits that can be obtained during the use phase of the electric vehicle or even to aggravate the general result [129].

This work analyses the different stages that make up the battery life cycle: extraction and production, use and, finally, recycling. In this way, we will try to highlight, for each phase of the life cycle, the factors that act as a brake in the change towards electric mobility and the improvements that can help in this step, in order to actually obtain an overall benefit, presenting in short also the new emerging technologies born to achieve this goal.

It is not only the climate change aspect that will be addressed, although it is the issue most often discussed in such studies and especially most prevalent in common thinking, since a change in impact in terms of climate change may be accompanied by a change in environmental impact in other impact categories. For this reason, studies on the subject have been chosen in such a way as to achieve wide viewing angle, whereas many of the possible impact categories.

Today's research focuses on storage systems suitable for electric mobility, being the low battery range that most hinders the affirmation of electric vehicles on the market. The motivation that drives us to reconsider electric vehicles relates to the increasingly growing concerns about the environment, especially inherent to the phenomenon of global warming. The greenhouse gas most responsible for global warming is carbon dioxide. The source of carbon dioxide emissions is

connected to the transport sector for an amount equal to 32%, estimated in the period from 1980 to 1999 [130]. This percentage is however destined to increase in the event that they are not implemented measures that mitigate the amount of emissions released into the environment, since the transport sector is on the rise, particularly due to the growing number of developing countries, including Asia Pacific which represents a large share of the world population.

An EU-imposed target would therefore be to reduce transport-related emissions by 60% of 1990 levels by 2030 [131]. Furthermore, it is interesting to mention the law of 16 January 2019 (formal adoption on 3 April 2019) [3,4], as the European Parliament voted for the further reduction of carbon dioxide (CO_2) emissions for the newly registered vehicles. In particular, cars and light commercial vehicles (vans) registered from 2025 will have to emit 15% less CO_2 and by 2030 cars will have to emit 37.5% less CO_2, while light commercial vehicles will have to emit 31% less. These regulations were approved during the plenary session on 27 March 2019 and on 18 April of the same year the proposal was also launched to cut CO_2 emissions from new trucks by 30% compared to 2019 levels, by 2030 [132]. Furthermore, the most recent regulation 2021/1119/EU [5], in force since 29 July 2021, mandates a reduction in greenhouse gas emissions by 55% compared to 1990 levels by 2030. This law also provides for a series of actions that must lead to climate neutrality by 2050.

The problem associated with internal combustion vehicles is not only that of global warming, but it is also connected with the emissions of other pollutants associated with the combustion process while driving, such as unburned products and NOx. Furthermore, the problem is also associated with the non-infinite availability of fossil fuels [130,133] and noise pollution.

In fact, in most European countries, it is estimated that over 50% of the population is constantly exposed to noise exceeding 55 dB intensity, levels which, according to the World Health Organization, can cause serious harm to human health. The World Health Organization has recommended to stay below certain noise levels, which were within the targets set for 2020 but have not been achieved [134]. On the other hand, noise pollution is expected to increase due to the increasing mobility of people, this problem is partly resolvable thanks to electric mobility, but not entirely since an important source of noise comes from tires.

6.2 METHODOLOGY ADOPTED FOR THE REVIEW

The literature analysis was focused on articles that deal with studies conducted using the LCA (Life Cycle Assessment) methodology. LCA is often used in the automotive field in order to assess benefits and drawbacks of a specific technology, as in [135]. In this case various studies concerning traction batteries for electric vehicles were considered and compared.

The main objective of this literature review is to provide an overview of the batteries used for traction of electric vehicles, with the ultimate aim of identifying which are the most demanding phases from an environmental point of view and how these can be addressed in order to limit their impact.

6.2.1 Life Cycle Assessment (LCA)

The Life cycle assessment or LCA is an internationally standardized methodology for assessing environmental impacts associated with all the stages of the life cycle of a commercial product, process, or service. According to ISO 14040, the LCA structure consists of four main steps (Figure 6.1) [136,137], listed below.

1. Goal and Scope Definition: this is the preliminary phase of the study, in which the purposes, the functional unit, the boundaries of the system studied, the reference scenario, the assumptions and limits are defined.

2. Life Cycle Inventory (LCI): it is the phase dedicated to the analysis of energy and material flows (inputs and outputs) associated with the life cycle of the process or activity in question.

3. Life Cycle Impact Assessment (LCIA): it is the study of the environmental impact that the transport and use of resources cause in the various production processes analysed in the Inventory.

4. Life Cycle Interpretation: is the final part of the study, which aims to propose the necessary changes in processes and production activities. They must be evaluated iteratively through the LCA itself and possibly in parallel with studies of sensitivity and propagation of uncertainty.

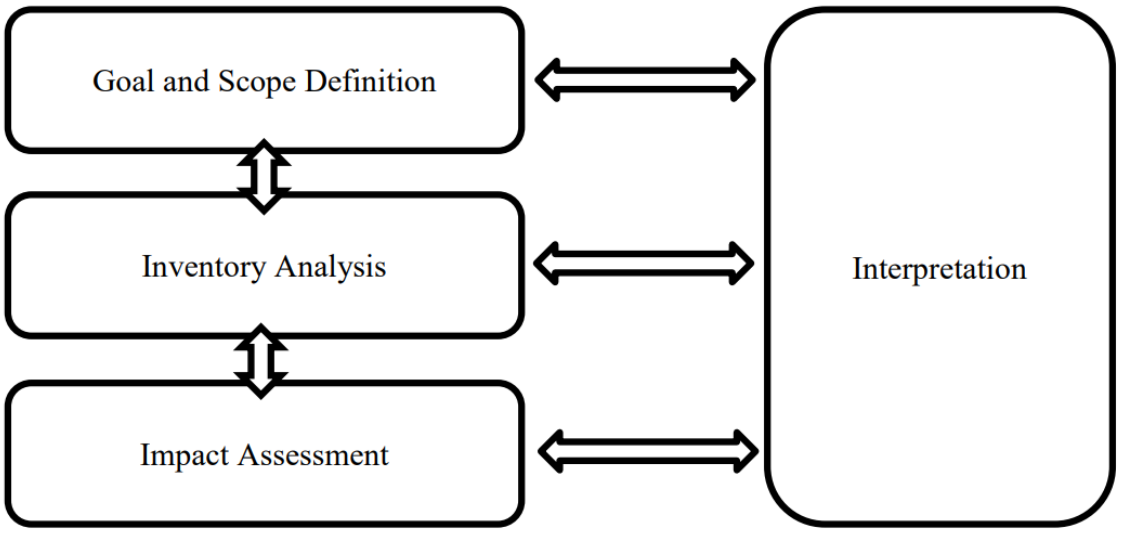

Figure 6.1. *Life Cycle Assessment (LCA) framework defined by ISO 14040.*

6.2.2 Search Engine

The search for significant articles in the literature was carried out mainly through the "Scopus" search engine and, secondarily, through "ResearchGate" and "ScienceDirect".

6.2.3 Selection of Articles

The research of the articles began with the aim of understanding how traction batteries for electric vehicles were addressed in the literature in LCA studies and which variables could influence the results. In this way, the different phases of the life cycle and the various thematic were researched in a targeted way when the need to expand some aspects emerged. Each topic was then explored by searching for specific keywords in the title and abstract of the articles, using the search engines mentioned in the previous section.

The research was further enriched through articles cited in the bibliography of some authors (of initially selected articles). The work was then completed by taking into consideration the results and comments of other studies (reported in the references in the form of bibliography and sitography) in order to have a picture as complete as possible of the topic dealt with.

The approach used for the choice of articles is atypical. The keywords used in search engines have not been fixed a priori but they have been modified according to the topics that you wanted to deepen. Furthermore, the research was further enriched through articles cited in the bibliography of some authors. The method adopted however led to good results, in fact it provided roughly the same articles as a study of the literature treated in parallel always by the

"Automotive Engineering and Design" research group of the University of Brescia, a study based on predetermined keywords.

The research then led to the analysis of 18 articles, which are the focus of the literature review of this article. It was considered that these articles were sufficient to describe the main issues related to electric vehicles, in particular as regards the environmental impacts of the different phases of the battery life cycle.

Article [138] deals with a specific chemistry, namely nickel-cobalt-manganese oxide (NCM), which is one of the most used due to its high specific density. This article offers an overview of the issues related to the production phase, especially the preparation phase of the cell materials, and the benefits associated with the recycling practice.

The article [139] analyses various types of recycling processes and different battery chemistries. Articles [140–142] deal with innovative technologies for the batteries production, in particular article [142] deals with the Sodium-ion Battery (SIB). The article [143] instead compares different production technologies. Articles [144] and [145] address the issue of resource depletion. Articles [146] and [147] deal with the issue of recycling. Article [148] instead presents the second life of batteries in applications other than those for which these batteries were produced (for traction). Articles [149] and [150] have been considered thanks to the bibliographic citations of some authors analysed. In particular, these articles deal with the aspect concerning the energy mix used for the production phase and, furthermore, article [150] also considers the mix for the use phase. Article [151] describes the different energy mix expected up to 2050. In article [133] a comparison is made between an internal combustion engine vehicle and an electric car for the Lithuanian case. The analysis of this study revealed a contrasting result compared to a similar study conducted in Italy and presented in the article [152]. [153] is a very comprehensive article concerning the operation mode. Finally, article [154] deals with LFP (lithium-iron-phosphate) chemistry, mentioned in several articles and indicated as an alternative to NCM.

6.3 LITERARY REVIEW

In the next sections the selected articles will be analysed. In particular, the different impact categories considered will be statistically characterized and the information contained in the articles will then be used to represent a general picture of the life cycle of traction batteries for electric vehicles, considering all the main phases of the cycle (cradle-to-grave approach): extraction and production, use and finally recycling.

6.3.1 Impact Categories

Most of the studies considered deal with the impact category relating to climate change (94.4%). The impact category relating to resource depletion also appears in several articles, in about 83.3%, and this reflects the growing concern related to the exploitation of fossil fuels for the ICEV and minerals for the electric ones. 66.7% of the studies considered risks related to human health as an impact category. The impact categories relating to the ecosystem range from 50% to 55%, due to the concern to safeguard both biotic and abiotic factors. The other impact categories are, on the other hand, less considered in scientific studies in the literature. Figure 6.2 shows a bar graph showing the incidence of the impact categories considered in the 18 selected articles.

Many LCA studies report only the impact categories for which reliable and comprehensive data exist. In fact, the dynamics of the effects induced by certain substances are not yet particularly known and moreover, often lead to different impact phenomena, giving rise to cascade effects that are difficult to evaluate [155].

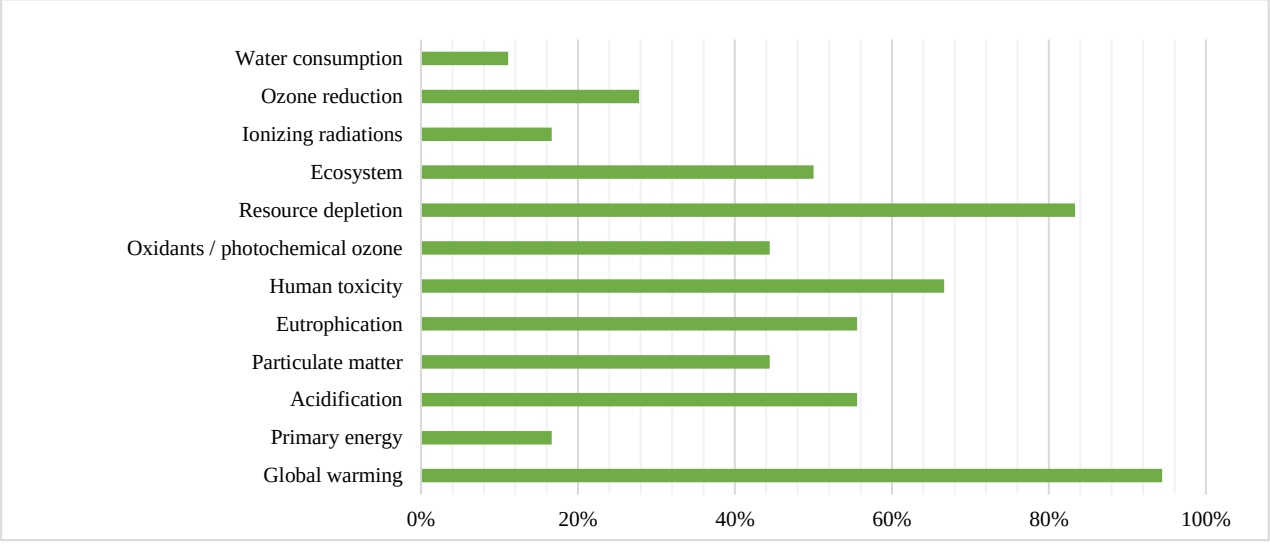

Figure 6.2. *Graphical representation of the percentage of incidence of the impact categories considered by the studies analysed in this review work.*

6.3.2 Extraction and Production Phases

The article [152] shows the comparison between an internal combustion vehicle and an electric vehicle, both based on the virtual model of the reference car of the ALLIANCE project [156], namely the SuperLightCar. The article [133] compares the Fiat TIPO ICEV powered by two different fuels, diesel and petrol, and the Nissan Leaf ACENTA electric vehicle, all vehicles of the year 2008.

In the results obtained from the two studies there is agreement in affirming the presence of a greater share of impact in the categories relating to human toxicity and the exhaustion of resources, in particular of metals, for the electric vehicle compared to the thermal one.

The results obtained in relation to human toxicity are also confirmed in other more recent studies conducted by other authors and they are mainly related to the production phase [133,152]. Human toxicity is mainly related to the processing of chemical substances and metals, necessary for the manufacture of batteries and electric motors, and to the mining activities necessary for the extraction of raw materials, which are used in the production phases of batteries [145,152]. Furthermore, the metal supply chain, in addition to determining exhaustion of the metals themselves, is the main cause of particulate emissions [145,152]. The creation of atmospheric particulate is also linked to the energy required for production if it is mainly based on the use of solid sources [145]. The contribution of the energy mix used is therefore important. For these reasons, the battery is the key element in determining the spread of electric vehicles.

In particular, it is the materials used for the production of batteries and their processing that cause a preponderant impact on human toxicity, on the exhaustion of metals, but also on other impact categories. Everything is therefore influenced by the chemistry of the battery in question, i.e., by the type of materials used and by their processing technology.

From the study of the article [138] it would seem that the greatest contribution to the environmental impact is mainly attributable to the preliminary phase of preparation and processing of the materials necessary for the manufacture of the cells' components, compared to the production phase of the battery pack (Figure 6.3).

The graph shown in Figure 6.3 was constructed considering the values reported in Fig. 3 and in Table 2 of [138]. In particular, the phases relating to the preparation of the cell materials (reported under the item "Material") and to the production of the cell itself (item "Production") are considered and these phases

were compared according to the percentage impact on the sum of the two phases themselves [125,157].

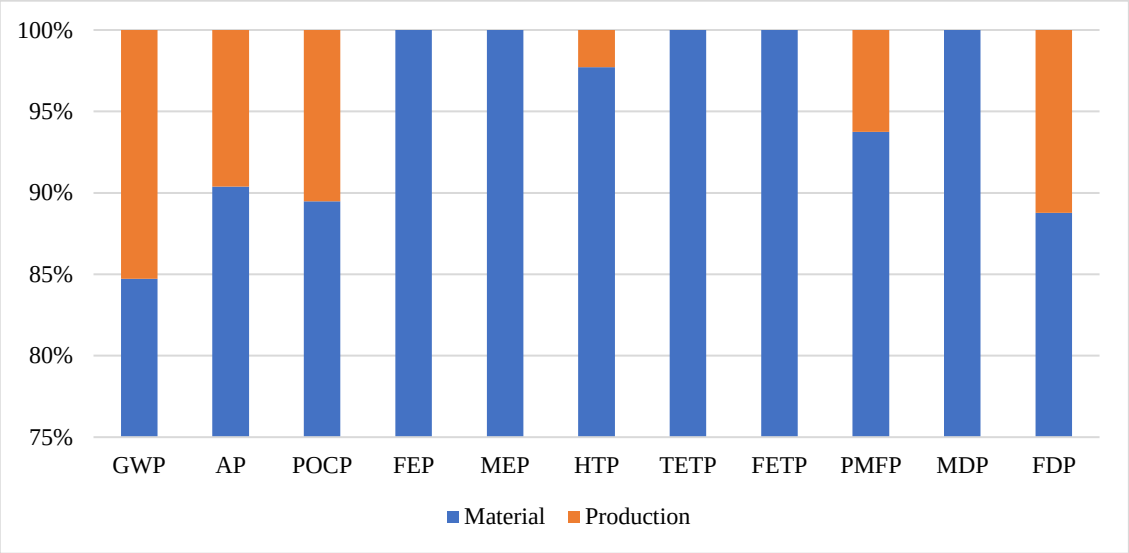

Figure 6.3. *Results obtained from the analysis of the life cycle of the 1 kWh of the NCM battery, in the impact categories according to the V1.11/World ReCiPe H method* [125,138,157].

Chemicals that include cobalt in the cathode structure determine a greater share of metal depletion, since it is defined as a critical element [139] and worsens its position if adequate measures are not applied to reduce its use [158]. The criticality of cobalt is confirmed by all five methodologies used for the assessment of environmental impacts in the study [144].

What was said for cobalt, it can also be said for nickel, which has a greater impact on resource depletion for NCM and NCA chemicals than LFP and SIB in the study [139] and the same is true for NiMH compared to LFP and NCM in the study [154]. Nickel is also indicated as critical in the study [144] for all five methodologies used and, in the form of nickel sulphate, it is considered to be, in the study [149], the second material to cause metal depletion for the cathode.

Copper is also defined as a critical element and its presence in the anodic collector involves a high consumption of resources and this is stated in several studies (for example in the studies [139,144,149]). Despite this, according to the study [158], the copper supply chain would not cause problems in the diffusion of low-carbon technologies (electric vehicles, photovoltaic and wind sector) until the period considered, i.e., 2030.

According to articles [140] and [149], manganese is a heavy metal that would cause significant resource depletion for the cathode of the NCM battery. In the study [145], manganese is the main reason for the difference in impact in

the metal depletion category between LMO and LFP batteries, LFP being manganese-free. Despite this, according to the study [158], a significant increase in manganese demand is not expected by 2030. The different importance attributed to manganese could be explained by the study [144], which states that the ReCiPe method of assessing environmental impacts, used by studies [140,145,149], is not adequate to evaluate the effective availability of resources, since it is based on the additional economic effort required by future generations to extract a resource that is abundant today, which will reduce its concentration as a result of today's exploitation. The same problem would also be present for the EcoIndicator99 method, which uses the same approach, but considering the additional energy instead of the additional cost. As for manganese, these methods lead to conflicting results also for aluminium [144]. Therefore, the results indicating a criticality for manganese and aluminium seem to be questionable.

The article [144] highlights the need to also take into account other essential materials for the electric powertrain, not used directly in the battery, used for example for the BMS and, in general, for battery electronics.

Essential materials for the production of lithium-ion batteries are lithium itself and graphite. An increase in the demand for lithium and graphite is expected [158], in particular by 2898% and 524% respectively by 2030 compared to today, in order to convert the entire current mobility into electric [159]. However, there is no certainty in stating whether lithium is indeed a critical element, as there are uncertainties about the extent of its reserves worldwide [158]. Furthermore, methodologies such as ReCiPe and EcoIndicator99 do not include the evaluation of this element in the resource depletion and therefore the criticality associated with its supply is underestimated [144,149,154].

Article [149] deals with an LCA analysis relating to the production of the NCM battery. The results of this LCA study show that the main responsible for most of the scores achieved on the various impact categories considered by the study are the manufacture of the cells, the realization of the negative current collector in copper, followed by the production of the positive cathode paste. These three production chains together are claimed to make up 56–87 % of the total battery impact.

Studies [139] and [154] state that, regardless of the chemistry of batteries, the energy requirements needed for production are a major cause of global warming. There is a conflict between the results obtained from studies [139,149,154] and those obtained from study [138], in which the production phase, which includes the manufacturing of the cells, generates almost

completely negligible environmental impacts compared to the materials preparation phase. The difference probably derives from the database used, the study [149] uses the data of Ecoinvent 3.1, while the [154] of Ecoinvent 2.2, determining a quantity of greenhouse gases emitted respectively six times higher for the entire production phase and two times higher for the cells fabrication, compared to those calculated by the study [138].

However, it is possible to find a common result among those obtained by the various authors: most of the greenhouse gas emissions produced during production phase (understood separately from the material preparation process) is attributable to the manufacturing phase of the cells. In particular, according to the study [149], the energy required constitutes 51% of the total impact caused in the category of global warming, relative to the production phase.

Therefore, the energy mix used during the manufacturing of the cells strongly influences the emissions produced during this phase. The influence of the energy mix in the cell manufacturing phase is addressed in articles [145] and [149], through a sensitivity analysis. Acting on the energy mix allows to reduce a part of the impact caused during the production phase, while another strategy is to use more eco-sustainable materials.

A fundamental aspect in the production phase is the specific energy of the battery, since the higher it is, the more the battery will be able to provide the vehicle with the required driving range with less weight and less consumption of materials [139,144] and less energy for its construction and use [139]. Research is in fact engaged in the development of new technologies for the construction of batteries that have greater density and energy efficiency and that avoid in their chemistry the presence of critical materials such as nickel, cobalt, manganese, copper and, secondarily, aluminium. The common NCA and NCM batteries offer high energy density, but they contain scarce metals such as nickel and cobalt and therefore, according to the study [139], the LFP battery would turn out to be a more eco-sustainable alternative from this point of view, in fact, being composed of iron phosphate, it does not require critical materials. Despite this, the LFP battery is not satisfactory from an energy point of view, since it is associated with a higher share of the energy for the cells manufacturing compared to the NMC and NCA batteries, bringing carbon dioxide emissions to an overall higher level [16]. However, this aspect can be solved by adopting less expensive production processes suitable for the chemistry of the battery in question and by preferring renewable sources to fossil ones.

The study [154] shows how the LFP battery brings a lower environmental impact than the NMC in all thirteen impact categories considered. This result was

obtained using a functional unit based on the energy supplied by the battery, therefore the longer life expectancy of the LFP compared to the NMC is considered, allowing to reduce environmental loads effectively. On the opposite, the functional units expressed in terms of specific energy and mass imply a lower relative variability between the two types of batteries.

The study [143] reports a migration from the use of the LCO battery to the LMO, in order to decrease the concentration of cobalt. However, the LMO battery is more invasive in the resource depletion and human toxicity than LFP [145], despite being more profitable than the latter for a share of 12% in the climate change.

Three different innovative technologies regarding battery chemistry will be briefly presented below.

Among the most promising battery technologies for next-generation electric vehicles is the lithium-sulphur (Li-S) battery. In the study [141], this new technology is compared with the traditional NCM battery, and it is stated that the lithium-sulphur battery is more sustainable. In particular, thanks to a reduction in environmental impacts for a share ranging from 9% to 90% for twelve impact categories out of thirteen, while the thinning of the ozone layer would suffer an increase of approximately 71%, compared to the NCM.

Another accumulator under research and development is the sodium-ion battery (SIB). The results obtained from the comparison between SIB and traditional LIBs show a positive attenuation of human toxicity and freshwater eutrophication thanks to the use of SIBs.

The lithium-air or lithium-oxygen (Li-O_2) battery is also at the focus of attention in the development of new technologies that are sustainable for the environment. The study [140] shows how Li-O_2 brings a greater environmental impact in the categories relating to human toxicity, terrestrial ecotoxicity and thinning of the ozone layer compared to the NCM battery. On the opposite, Li-O_2 appears to be positive in the other eight impact categories considered, especially in eutrophication, acidification, and toxicity of fresh and marine water. Li-O_2 would be the best, among the three new technologies just presented, in terms of ecological footprint (consumption of ecological resources), carbon footprint (CO_2 equivalent emissions related to greenhouse gas emissions problems) and water footprint (consumption and pollution of water by human activities) [143].

In conclusion, it can be said that the battery production phase is very expensive, both as regards the necessary metals and for the cell manufacturing

phase. The chemistry of the cells plays a fundamental role, in particular it is necessary to consider any critical materials and the possible need for particular manufacturing processes, with consequent different electrical consumptions. It is therefore important to consider an adequate energy mix, preferring the use of renewable sources. The search for innovative and more energy efficient processes is also important. It is important to create batteries with more eco-sustainable chemicals, also optimizing the production processes, adapting them to the type of chemistry treated. Furthermore, these innovative batteries must meet the requirements of high specific energy and high energy density, in order to reduce the amount of materials necessary for the construction of the batteries themselves and the energy required for their production, while maintaining the range required for the vehicle.

6.3.3 Use Phase

Even for LCA studies relating to the use phase of the vehicle or battery pack, the initial data and hypotheses are very important.

Between the studies of articles [133] and [152], relating to the comparison between thermal and electric vehicle, a different result in climate change can be noted. In the study [152], the diesel-powered vehicle (ICEV) turns out to be much more polluting than the electric one (BEV), while in [133] the exact opposite happens. The quantitative results, relating to the entire life cycle, expressed in Co_2-eq [g/km], are shown in Figure 6.4.

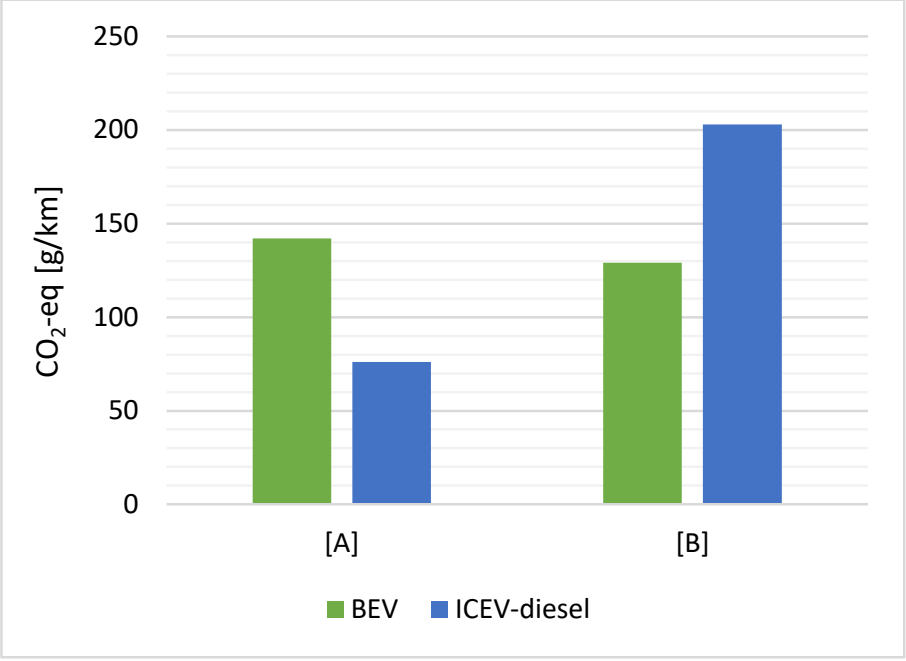

Figure 6.4. *LCA results relating to the impact of greenhouse gas emissions for the entire life cycle of vehicles, for:* ***[A]*** *study* [133] *in the year 2015;* ***[B]*** *study* [152] *in the year 2017.*

For both studies, emissions are calculated over a distance of 150 000 km and the use phase is the predominant source of greenhouse gas emissions. The reason for the difference in the results obtained lies in the fact that the diesel-powered vehicle of the case [152] has a much higher consumption than that of the study [133], while for electric vehicles the opposite occurs. Furthermore, the energy mix with which the batteries of the two electric vehicles under consideration are charged also entails a substantial difference in emissions; in fact, the amount of equivalent carbon dioxide emitted during the production of electricity is greater for the Lithuanian mix than for the average European mix.

The importance of a certain energy mix for an LCA study can be considerable, both for the production phase and for the use phase. The environmental loads associated with the energy mix used, in addition to depending on the type of sources that are used, also vary according to the time slots in which the batteries are recharged, in particular, the night one (00:00–7:00) tends to involve environmental charges lower than the daytime one (9:00–17:00) [153].

In the study [152] a break-even analysis is carried out, considering the kilometres travelled and three different energy mixes: the average European, the Norwegian one (mainly composed of renewable energies) and the Polish one (consisting almost exclusively of fossil fuels). The study showed that the energy mix of the use phase is irrelevant in modifying the environmental loads for the categories relating to human toxicity and metal depletion, in fact these two categories depend almost exclusively on the production phase.

Chemistry, in addition to influencing the impacts introduced by production, is in some cases one of the reasons for the greater dependence of some impact categories on the use phase rather than on the production phase. For example, acidification is more dependent on production for the NCM battery, for both studies [140] and [141], while the two innovative chemists treated, Li-O_2 and Li-S, respectively, have a large contribution given by the use phase. Furthermore, the chemistry implies a different efficiency of the batteries and their different life expectancy [153].

Another important aspect is associated with life expectancy, the kilometres travelled by the car (without replacing the battery pack), as reported in the study [152]. The greater the distance that the electric vehicle is able to travel, the greater the possibility of reducing the environmental loads introduced by production, also recovering the initial advantage of the ICEV.

The goal is therefore to have batteries with a high number of charge-discharge cycles [149]. In particular, the duration of a battery depends on its aging (increase in internal resistance and in the rate of self-discharge and reduction in capacity) and on various variables related to the use phase (intensity of current, operating and maintenance temperature, charging mode). The function of the BMS (Battery Management System) is therefore important.

It is well known that the driving cycle has a relevant impact on overall energy consumption and emissions [24]. The study [153] investigates the different outcome in terms of environmental impact associated with three different driving profiles for an LMO battery, namely aggressive (213.4 Wh/km), normal (182.8 Wh/km) and ECO (167.1 Wh/km). The latter would be able to generate a reduction in environmental impacts that is between 42% and 50% per km depending on the impact category considered (abiotic depletion, acidification, eutrophication and global warming), since the battery is discharged with a lower current and, therefore, the resulting losses and energy consumption are lower.

The study [149] shows how a higher efficiency level of the battery, and in general of the powertrain, is fundamental in determining a greater number of total kilometres travelled by the electric vehicle, with the same number of battery cycles; similarly, greater efficiency allows you to travel the same number of kilometres with fewer cycles.

In addition to the losses associated with the efficiency of the battery, there are those related to the transport of the battery itself (of its weight, in particular of the additional weight necessary to compensate for the low efficiency, to obtain the same vehicle range). This aspect is addressed by the study [150], which investigates the losses related to the weight of the battery and those associated with its internal efficiency. The latter, for an internal efficiency of 90%, are always higher than those attributable to the transport of the battery. Furthermore, it is possible to further reduce losses attributable to the weight of the battery thanks to regenerative braking [144][13] (see Section 3). However, the weight of the battery is not negligible; in fact, according to the calculations of the study [144], an increase in the weight-energy ratio from 15% to 50% determines an increase in the energy lost due to the three times higher weight of the battery, considering the mid-western European energy mix.

A reduction in volume is also important; in fact, in addition to implying a lower consumption of material in the production phase [160], it also involves a possible saving due to the missing fraction of vehicle destined to transport the additional volume of the battery.

Therefore, the research for ever lighter and more compact batteries must be accompanied by the need for greater efficiency (both of the battery and of the powertrain [149]) in order to obtain a reduced environmental impact, thanks to the reduction of all losses attributable to the battery.

In conclusion, to reduce the environmental loads of the use phase, it is important to use an energy mix mainly composed of renewable sources, preferring night-time charging cycles. Furthermore, the chemistry of the cells must ensure a highly efficient and large capacity battery. The duration of the use phase must also be adequate; in this regard it is important that the vehicle control unit manages control systems aimed at reducing consumption and extending the useful life of the battery pack. Finally, it is important to search for materials that make it possible to create ever lighter and more compact batteries.

6.3.4 Recycling Phase

Recycling is a useful methodology for recovering materials from exhaust batteries, materials that would otherwise have to be mined to produce new accumulators, resulting in the introduction of additional environmental loads.

Most of these materials are precious metals, such as nickel, lithium, cobalt and manganese, others are organic and plastic materials, which can produce large quantities of pollutants in the production and extraction phases [138,149]; some are highly toxic and dangerous if not disposed of properly, such as PVDF binder, as it releases hydrofluoric acid when burned, or flammable mixtures used in the electrolyte formation, such as those composed of ethylene carbonate and dimethyl carbonate [142]. For these reasons, appropriate end-of-life treatment practices are needed.

The study [146] shows that, for lithium-ion batteries, the Eco-indicator points deriving from the weighting process of the results obtained in the categories of damage related to human health, ecosystem quality and resource depletion, beyond under 200 cycles of battery charge/discharge, decrease as the recycling percentage increases and, markedly, when the latter reaches at least 40–50%.

A simple disposal does not allow to obtain the benefits that would derive instead from a correct recycling practice, as demonstrated by the study [147]. According to the latter, recycling would lead to a reduction in ecological points by a share of 23%.

Recycling practices also require energy and material input to the system itself, with the consequent introduction of environmental loads which are,

however, generally low compared with those that compete in the production and use phases [133,139–141,152].

There are different technologies used for recycling, the more classic ones involve methods of chemical extraction of metals, and they are pyrometallurgical and hydrometallurgical treatments [161]. The first uses high temperatures to obtain the constituent elements of the cathode, allowing the recovery of aluminium, copper, cobalt, nickel, manganese, and titanium; while the second uses an acid or alkaline solution through which salts of lithium, cobalt, nickel, manganese, magnesium, and titanium are obtained [139,148].

The pyrometallurgical treatment, if compared with the hydrometallurgical one, offers significantly lower advantages, above all due to the greater consumption of electricity required for the treatment [138], since it is carried out at a high temperature, and the loss of lithium in the waste [139]. According to the study [148], pyrometallurgical treatment appears to be the methodology to which the least environmental benefits are attributed for LMO, NCM and NCA batteries with regard to climate change, as affirmed in the study [139] for NCA, NCM, SIB and LFP batteries; in particular, the latter sees an increase with respect to the environmental impacts generated in production. Also with regard to the depletion of abiotic resources, pyrometallurgical process is the one that brings the least benefits, with the exception of the sodium ion battery, which with this treatment obtains greater advantages compared to the hydrometallurgical one.

However, hydrometallurgical recycling requires a large amount of water (water requirement problem). Nonetheless, hydrometallurgical process implies lower environmental loads than pyrometallurgic one, which is connected to higher emissions of atmospheric pollutants and greenhouse gases, due to the production and combustion of carbon coke during the process; this combustion is responsible for the releases of sulphur dioxide, with consequent damage to human health if they are not treated properly (using a washing system based on calcareous sulphur) [152].

In general, a pyrometallurgical or hydrometallurgical treatment does not allow the LFP and SIB batteries to considerably reduce the environmental impacts generated during the production phase, as is the case for NCM and NCA batteries. This depends on the materials recovered. The evolution towards innovative chemicals, which allow a reduction in the percentages of heavy and critical metals, must therefore be accompanied by a continuous research for suitable recycling processes.

The study [138] shows that, for the NCM battery, the hydrometallurgical treatment brings significant advantages in all impact categories considered. In particular, the best results are associated with the impact categories relating to the production of photochemical oxidants and human toxicity, with a reduction of 105.2% and 139.8% respectively, thanks to the large amount of recovered aluminium, which is the most responsible for the impacts caused in these two categories.

The study [145] analyses the hydrometallurgical treatment for LMO and LFP batteries, which is the standard one for these batteries. In this case, the hydrometallurgical treatment allows greater savings in electricity consumption, compared to the pyrometallurgical one [162].

The effectiveness of recycling treatments largely depends on the chemistry of the battery in question, therefore, for innovative chemicals, treatments designed specifically are required.

An innovative method is direct recycling, which is a non-destructive technique that allows the recovery of the cathode and electrolyte. It therefore allows the direct reuse of the material after preliminary light processing, if necessary [148,161]. In fact, the recovered materials are not always used in the production of batteries for the automotive sector. Many studies report the benefits associated with the second use of batteries in other areas.

The study [148] certifies the effectiveness of cascade use, i.e., the efficient use of resources using residues and recycled materials, for the analysed NCM, NCA and LMO batteries. In particular, the application in stationary energy storage systems would allow the reduction of environmental loads related to the life cycle of the batteries used during their first life in the automotive sector.

The study [148] states that direct cathode recycling is associated with lower environmental loads than those of hydrometallurgical and pyrometallurgical treatments, also with regard to global warming [148,163]. Furthermore, it would be able to guarantee a lower amount of waste from the recycling process [162] and it would be able to offer a high contribution in effectively reducing the impact generated in production phase of the batteries with low-cost chemicals such as LFP [139].

In general, the greatest benefit obtainable from recycling is the reduction of the metals used for the production of new batteries [139,145] and the lowering of the emissions related to the extraction and processing of the metals themselves. However, the greenhouse gas emissions released during the cell manufacturing

cannot be significantly reduced by recycling due to the high energy consumption required for this phase.

An important aspect is the efficiency of recycling, which determines the effectiveness or otherwise of the treatment and the quality of the recycled product.

We must also pay attention to the economic aspect, the recovery of metals of low monetary value through recycling could introduce greater economic burdens than environmental benefits.

Further attention should be paid to transport, which is necessary to bring exhausted batteries to recovery centres; in this phase, the generation of significant environmental loads must be avoided [162].

In conclusion, recycling treatments need to be refined according to the chemistry in question, so that they are also suitable for innovative chemicals.

6.4 DISCUSSION AND FINAL CONSIDERATIONS

Thanks to this literature review it was possible to show how different aspects and parameters influence the results of LCA studies applied to electric vehicles and, in particular, to their battery pack.

The absence of unified and/or accessible data regarding battery design [149] and manufacturing processes can lead to significant differences between LCA inventories and, therefore, between the results obtained.

The functional unit adopted, defining the study approach, also leads to different results. For example, analysing batteries with a functional unit based on their mass does not allow to fully consider the efficiency during the use phase [154] and the specific energy level [159]. The latter is the reason why NCM and NCA batteries have significantly lower environmental performance than LFPs when the functional unit is expressed in terms of mass, while when this is based on energy, the opposite result is obtained [159].

From the studies analysed, the battery production phase was often dominant in the life cycle. This is mainly related to the materials used and to the manufacturing of the cells, especially the energy required for this process. In this regard it is necessary to pay particular attention to the type of battery in question; in fact, a different chemistry involves different processes, materials and quantities of energy.

Having ascertained metals such as nickel, cobalt, manganese, copper and, secondarily, aluminium are particularly critical, some from the point of view of

toxicity, others from that of resource depletion and/or greenhouse gas emissions, it is useful to evolve towards products greener chemicals.

Help to reduce environmental impacts comes from the use of energy from renewable sources, which has lower environmental loads than that from fossil sources. The energy mix influences both the manufacturing and use phases. It is therefore also useful to pay attention to the daily hours in which the battery is recharged. To promote the growth of renewable energies, innovative and flexible electricity distribution network systems, called "Smart-Grid", are indispensable, together with storage systems, with the aim of solving the problem linked to uncertainty, discontinuity, and non-programmability of renewable sources.

Another important aspect to consider is that of the specific energy of the battery. In fact, a high specific energy, for the same vehicle range, allows the use of lower quantities of materials and energy for manufacturing and it allows the reduction of losses associated with the transport of the battery itself.

Important to reduce environmental loads are also high battery durability and high efficiency of the battery pack (and, in general, of the vehicle), together with the ecological use of the car, obtainable thanks to the development of control strategies, managed by a control unit, and thanks to the will of the driver.

Recycling makes it possible to reduce some of the impacts introduced with the production phase, those relating to the materials and processes required, but not those strictly related to the use of energy for manufacturing. The research for new efficient recycling strategies must go hand in hand with the research for innovative and less impactful materials from an environmental point of view.

In addition to the environmental aspect, the economic aspect should also be considered: capital and maintenance costs associated with infrastructures suitable for the circulation of the growing number of electric vehicles, the purchasing power of people, and the different costs of the different battery chemistries and so on.

Finally, the transition to electric mobility would cause a non-negligible social impact: transition from petrol station to electric charging stations, from the thermal engine to the electric one, from mechanical to electrical connections, etc.

Therefore, many aspects should be taken into consideration in the transition towards electric mobility, since this has not only an environmental impact, but also social and economic ones. These last two aspects are beyond the aim of this article, but to properly assess the sustainability of electric mobility they should not be overlooked.

7 CONCLUSION

The goal of the work presented in this thesis was to identify energy management strategies on board electric and hybrid vehicles, in order to optimize energy management and thus allow for resource savings. In particular, strategies that allow energy savings, and a saving of resources necessary for the production of the latter, during use phase and also allow a saving of resources during the production phase of the vehicle, with particular reference to the realization of the battery pack. In fact, by optimizing the energy management in the operational phase of the vehicle, through appropriate logics to be implemented in the vehicle control unit and/or through the study of particular hybrid vehicle configurations, it is possible, with the same vehicle range, when sizing the battery pack, identify one with reduced dimensions and weight, thus saving resources in the production phase.

Initially a model (called TEST [10]) for simulating the longitudinal dynamics of electric and hybrid APU (Auxiliary Power Unit, with one or more generators suitable for recharging the battery pack) vehicles was created in MATLAB/Simulink®. This model allows to carry out consumption analysis and useful simulations for sizing the various components of the vehicle system, including sizing the battery pack.

The TEST model was the starting point for identifying energy management strategies, in particular, a regenerative braking logic (called RB logic [13]) and the possibility of simulating hybrid vehicles equipped with fuel cell were integrated into the TEST model.

The RB logic was created ad hoc to obtain the greatest possible regenerative recovery, avoiding vehicle instability. The logic is represented by a Simulink model, in which the code differs for three cases, for the case of front-wheel drive electric vehicles (FWD), rear-wheel drive (RWD) and, finally, all-wheel drive vehicles (AWD), with two electric motors, one for each axle. The integration of the RB logic in the TEST model was useful for estimating the energy savings guaranteed by the logic itself, compared to the consumption of an electric vehicle without regenerative braking and compared to a case of regenerative braking considered as "standard": a classic regenerative braking logic, commonly adopted on vehicles on the market according to [10]. The results obtained are interesting: for the FWD and RWD compact cars under consideration, the RB logic makes it possible to save around 30% in terms of energy consumption on the class 3b WLTP cycle compared to a vehicle without regenerative recovery and about 23.5% compared to a vehicle equipped with the

classic regenerative braking logic. On the US06 cycle, on the other hand, it made it possible to save 24.4% and 19.5%, respectively. Similar, promising results have been achieved with the AWD car.

An efficient regenerative braking logic can allow energy optimization on board full electric vehicles, increasing their range, but this increase may not be sufficient for certain categories of vehicles. To best solve this problem, it was therefore necessary to direct the study towards new vehicle technologies, in particular hybrids, without a traditional internal combustion engine, which, due to the increasingly stringent emission laws, is destined to disappear on newly registered cars of the next decades.

The first innovative technology analysed was that of hybrid vehicles equipped with hydrogen fuel cells. In particular, a PEMFC model (Proton Exchange Membrane Fuel Cell) and a power management logic (power split logic) on board the vehicle has been created [20]. The power split logic allows a combined use of fuel cell (which represents the primary energy source) and battery pack (which acts as peak power source) to supply the electric traction motor. These logics were created in Simulink and integrated within the TEST model.

Another technology under study was that of hybrid electric vehicles with fuel cells that can be powered by biomethane (or methane). The chemistry identified was that relating to SOFCs (Solid Oxide Fuel Cells), which allow, thanks to the reforming process, to be fed with fuels other than hydrogen, including methane. However, the SOFC cells are characterized by different problems, in particular by a high structural fragility, an aspect to be solved for the installation of the latter on a hybrid electric/SOFC vehicle, long ignition times and slow transients. For these reasons, the SOFC vehicle model that has been created, and integrated into the TEST model, is represented by a vehicle that operates in fleet (in the case in question a waste collection vehicle), with a predefined driving mission. Furthermore, the configuration is that of a full electric traction vehicle, with the electric motor (or motors) powered by the battery pack and with a solid oxide fuel cell stack that acts as a generator by recharging the batteries. A special feature of the system is that the SOFC, once switched on, when the vehicle has been put into operation for the first time, will not switch off for the rest of the vehicle's useful life. When the vehicle is not in operation and the battery pack does not need to be recharged, the vehicle must be connected to the electricity grid and the SOFC will supply power to the latter. Alternatively, it will be possible to recharge the battery pack of other electric vehicles in the fleet or to recharge a stationary energy storage system.

Finally, the thesis reports an in-depth analysis of the LCA (Life Cycle Assessment) studies relating to electric vehicles, with particular regard to the battery pack, to show the environmental criticalities associated with the different phases of the latter's life cycle. This latest study therefore highlights the importance of correct energy management and the importance of adopting hybrid electric strategies to minimize the environmental impact associated with energy consumption. Also allowing to size the battery pack with reduced mass in order to obtain a lower resources depletion during its production.

8 ACKNOWLEDGEMENT

Special thanks go to ENEA (Italian National Agency for New Technologies, Energy and Sustainable Economic Development) for supporting the research, in particular for the literature review of LCA studies relating to the traction battery of electric vehicles.

An important contribution to this thesis was also given by "BIOMASS HUB" project [ID 1165247, PORFESR 2014–2020, and Regione Lombardia (IT)].

9 NOMENCLATURE

Abbreviation	Description
A	Active cell area [1]
a	Longitudinal vehicle acceleration [3]
ABS	From the German: Antiblockiersystem. Anti-lock system. Avoid locking the vehicle's wheels when braking
A_f	Frontal area of the vehicle [1]
AFC	Alkaline Fuel Cell
a_{H_2}	Hydrogen activity [10]
a_{H_2O}	Water activity [10]
a_{O_2}	Oxygen activity [10]
AP	Acidification Potential
$A_{pistonF}$	Total area of the brake pistons, front callipers [1]
$A_{pistonR}$	Total action areas of the brake pistons of the rear callipers [1]
$a_{product}$	FC products activity [10]
APU	Auxiliary Power Unit
$a_{reactant}$	FC reactants activity [10]
a_{ref}	Reference vehicle acceleration (in TEST model) [4]
A_T	Coefficient as a function of temperature [10]
AWD	All-Wheel Drive vehicle
a_y	Lateral vehicle acceleration (of the centre of gravity), absolute value [8]
`BattChargeMax`	Rated capacity at nominal temperature, of a single cell or of the entire battery pack [1]
`Batt_Np`	Number of cells arranged in parallel inside the battery pack (N_p) [1]
`Batt_Np_2`	Number of battery pack cells in parallel (N_p) if the capacity is defined for the battery pack, equal to 1 if the capacity is defined for the single cell [2]
`Batt_Ns`	Number of cells arranged in series inside the battery pack (N_s) [1]
`Batt_Rint_table`	Table where the first column reports the temperature values, the first row the SOC values and at the centre the corresponding internal resistance data [1]
$BattSoc$	Battery State of Charge [4]
`Batt_SOC_Em`	Vector that reports the values of the open circuit voltage of the single cell of the battery pack as a function of the SOC [1]
BD	Optimal braking distribution (calculated in RB logic) [5]
BEV	Battery Electric Vehicle

Abbreviation	Description
$Bias_{brakeF}$	Pressure portion, compared to that of the master cylinder, which acts on the front brakes [1]
BMS	Battery Management System
$BrakeDemand$	Brake demand (from 0 to 1) [8]
B-V	Butler-Volmer equation
C_{batt}	Rated capacity at nominal temperature, of a single cell of the battery pack [2]
C_{batt_init}	Initial capacity of a single cell of the battery pack, expressed in Ah [2]
CeO_2	Ceric oxide, ceria
CG	Centre of gravity
CH_4	Molecule of methane
c_i	Stoichiometric coefficient of the i-th species [10]
c_j	Stoichiometric coefficient of the j-th species [10]
$c_N, \cdots, c_2, c_1, c_0$	Calibration coefficient of the calibration function y (in the TEST model) [1]
CO	Carbon monoxide
CO_2	Carbon dioxide
CO_2-eq	Equivalent carbon dioxide
$cos(\varphi)$	Power factor
$Crnt_{MAX}$	Maximum charging current of the battery pack (input of RB logic) [8]
$Crnt_{mot}$	Charging current of the battery pack generated by the motor or motors (calculated in RB logic) [5]
$Crnt_{refF}$	Current that the front motor sends to the battery pack when it produces a regenerative motor torque equal to T_{refF} (calculated in RB logic) [5]
$Crnt_{refR}$	Current that the rear motor sends to the battery pack when it produces a regenerative motor torque equal to T_{refR} (calculated in RB logic) [5]
$Crnt_{req}$	Total charging current generated by the motor or motors (calculated in RB logic) [5]
$Crnt_{reqF}$	Charging current generated by the front motor (calculated in RB logic) [5]
$Crnt_{reqR}$	Charging current generated by the rear motor (calculated in RB logic) [5]
C_x	Longitudinal aerodynamic coefficient [1]
DC	Direct Current
DMFC	Direct Methanol Fuel Cell

Abbreviation	Description
dx	The difference in distance travelled, between the current instant and the previous calculation instant (in the TEST model) [4]
dz	The difference between the altitude of the road at the point considered and the altitude of the point of the instant of calculation preceding that considered (in the TEST model) [4]
e^-	Electron
E_0	Reference standard electromotive force (standard EMF) [10]
E_0^0	Standard EMF at the standard temperature [10]
E_{act}	Activation energy [10]
EMF	Electromotive Force
EMS	Energy Management System
E_{Nernst}	Nernst voltage, reversible open circuit voltage of the FC [10]
EPA	Environmental Protection Agency
EU	European Union
EV	Electric vehicle
F	Faraday number [1,10]
f	Rolling resistance coefficient [3]
F_{aero}	Aerodynamic resistance, drag (calculated in the TEST model, using vehicle speed of the previous instant of calculation) [4]
F_{bfMAX}	Theoretical total maximum braking force that the front axle can unload on the ground (calculated in RB logic) [5]
F_{brake}	Force given by the traditional brakes (in the TEST model) [4]
F_{brake_max}	Maximum force that can be generated by the braking system (calculated in the TEST model) [4]
F_{brake_req}	Force required to traditional brakes (calculated in the TEST model) [4]
$F_{brakeReq}$	Total braking force request (calculated in RB logic) [5]
$F_{brakeReqF}$	Front braking force associated with the driver demand (calculated in RB logic) [5]
$F_{brakeReqR}$	Rear braking force associated with the driver demand (calculated in RB logic) [5]
F_{brMAX}	Theoretical total maximum braking force that the rear axle can unload on the ground (calculated in RB logic) [5]
FC	Fuel Cell
FCHEV	Fuel-Cell Hybrid Electric Vehicle
F_d	Aerodynamic resistance, drag [3]
FDP	Fossil Depletion Potential
FEP	Freshwater Eutrophication Potential
FETP	Freshwater Ecotoxicity Potential

Abbreviation	Description
$F_{inertiaF}$	Force lost due to inertia of the front wheels ("backward-facing" approach, in the TEST model) [4]
$F_{inertiaR}$	Force lost due to inertia of the rear wheels ("backward-facing" approach, in the TEST model) [4]
FLC	Fuzzy Logic Controllers
$F_{MAXbrake}$	Maximum braking force that the traditional brakes can unload on the ground (calculated in RB logic) [5]
$F_{MAXbrakeF}$	Maximum braking force that the traditional front brakes can unload on the ground (calculated in RB logic) [5]
$F_{MAXbrakeR}$	Maximum braking force that the traditional rear brakes can unload on the ground (calculated in RB logic) [5]
F_r	Rolling resistance [3]
f_r	Static rolling resistance coefficient [1]
f_{r_2}	Coefficient which allows to consider the rolling resistance coefficient as a linear function of vehicle speed [1]
F_{ref_wheels}	Total traction force required at the wheels (calculated in the TEST model) [4]
F_{reqF}	Braking force required from the front motor (calculated in RB logic) [5]
F_{reqR}	Braking force required from the rear motor (calculated in RB logic) [5]
F_{tr}	Traction force (calculated in the TEST model) [4]
F_{trF}	Portion of traction force which must be guaranteed by the front motor (calculated in the TEST model) [4]
F_{tr_motF}	Portion of traction force which must be guaranteed by the front motor (calculated in the TEST model) [4]
F_{trR}	Portion of traction force which must be guaranteed by the rear motor (calculated in the TEST model) [4]
FWD	Front-Wheel Drive vehicle
$F_{wheels\_inertia\_F}$	Force lost due to inertia of the front wheels ("forward-facing" approach, in the TEST model) [4]
$F_{wheels\_inertia\_R}$	Force lost due to inertia of the rear wheels ("forward-facing" approach, in the TEST model) [4]
F_θ	Additional force given by the presence of the slope of the ground [3]
g	Gravity acceleration [1]
GPS	Global Position System
GWP	Global Warming Potential
H^+	Hydrogen ion
H_2	Molecule of hydrogen
H_2O	Water molecule

Abbreviation	Description
h_{CRf}	Height of the front roll centre [1]
h_{CRr}	Height of the rear roll centre [1]
h_g	Height of the centre of gravity of the vehicle [1]
HTP	Human Toxicity Potential
I	Battery pack current [3]
i	Current density of FC [10]
i_0	Equilibrium exchange current density of FC [10]
ICE	Internal Combustion Engine
ICEV	Internal Combustion Engine Vehicle
I_{chrg_limit}	Charging limitation expressed as current [1]
$I_{dischrg\_limit}$	Discharging limitation expressed as current [1]
I_{FC}	Load current of a single cell of the FC stack [10]
I_{fc}	Fuel cell stack output current [6]
i_L	Limiting current density of FC [10]
In	Input
`init_SOC`	SOC of the battery pack at the start of the TEST simulation, in percentage [1]
I_{prev}	Battery current of the previous calculation instant (in the TEST model) [4]
I_{req}	Theoretically required battery current, if there are no limitations (calculated in the TEST model) [4]
ISO	International Organization for Standardization
j	Longitudinal vehicle deceleration (positive value) [8]
J	Fuel cell actual current density [6]
J_{inF}	Moment of inertia of the transmission after the front motor reducer [1]
J_{inR}	Moment of inertia of the transmission after the rear motor reducer [1]
J_{max}	Fuel cell maximum current density [1]
J_{motF}	Moment of inertia of the front electric motor [1]
J_{motR}	Moment of inertia of the rear electric motor [1]
J_{outF}	Moment of inertia of the transmission before the front motor reducer [1]
J_{outR}	Moment of inertia of the transmission before the rear motor reducer [1]
J_{wheelF}	Moment of inertia of a single front wheel [1]
J_{wheelR}	Moment of inertia of a single rear wheel [1]
k	Local k-point mean values for the moving mean of speed profile (in the TEST model) [1]
k_{ARBf}	Stiffness of the front anti-roll bar [1]

Abbreviation	Description
k_{ARBr}	Stiffness of the rear anti-roll bar [1]
K_{H_2}	Valve molar constant for hydrogen [10]
K_{H_2O}	Valve molar constant for water [10]
k_{heat}	Specific heat ratio [1]
K_{O_2}	Valve molar constant for oxygen [10]
KOH	Potassium hydroxide
K_r	Constant, $K_r = 1/4F$ [10]
k_{rollF}	The roll stiffness of the front axle [1]
k_{rollR}	The roll stiffness of the rear axle [1]
$k_{springF}$	Stiffness of the front suspension springs [1]
$k_{springR}$	Stiffness of the rear suspension springs [1]
L	Wheelbase [1]
L_a	Distance between the front axle and the centre of gravity of the vehicle [1]
L_b	Distance between the rear axle and the centre of gravity of the vehicle [2]
LCA	Life Cycle Assessment
L_{cableF}	Total length of the connection cables of the front motor [1]
L_{cableR}	Total length of the connection cables of the rear motor [1]
LCI	Life Cycle Inventory
LCIA	Life Cycle Impact Assessment
LCO	Lithium-cobalt oxide ($LiCoO_2$)
LFP	Lithium-iron-phosphate battery ($LiFePO_4$)
$Li_4Ti_5O_{12}$	Lithium-titanium oxide (LTO)
LIB	Lithium-ion Battery
$LiCoO_2$	Lithium-cobalt oxide (LCO)
$LiFePO_4$	Lithium-iron-phosphate battery (LFP)
$Limit_{batt\_acc}$	Binary control variable equal to 1 if there are limitations of the motors during traction due to the maximum performance of the batteries (in the TEST model) [4]
$Limit_{batt\_brak}$	Binary control variable equal to 1 if there are limitations of the motors under braking due to the maximum performance of the batteries (in the TEST model) [4]
$Limit_{gen}$	Binary control variable equal to 1 if there are limitations of the generators due to the maximum performance of the batteries (in the TEST model) [4]
$Limit_{mot\_acc}$	Binary control variable equal to 1 if there are limitations due to motors in acceleration (in the TEST model) [4]
$Limit_{mot\_brak}$	Binary control variable equal to 1 if there are limitations due to motors under braking (in the TEST model) [4]

Abbreviation	Description
$Limit_{trad\_brak}$	Binary control variable equal to 1 if there is a limitation of traditional braking (in the TEST model) [4]
$LiMn_2O_4$	Lithium-manganese oxide (LMO)
$LiNi_xCo_yAl_zO_2$	Lithium-nickel-cobalt-aluminium oxide (NCA)
$LiNi_xCo_yMn_zO_2$	Lithium-nickel-cobalt-manganese oxide battery (NMC or NCM)
$Li\text{-}O_2$	Lithium-oxygen
Li-S	Lithium-sulphur
l_M	Membrane thickness [1]
LMO	Lithium-manganese oxide ($LiMn_2O_4$)
LTO	Lithium-titanium oxide ($Li_4Ti_5O_{12}$)
M	Total vehicle mass (plus people and loads) [1](RB logic) [2](TEST model)
$\dot{m}_{air}$	Mass flow rate of air required for the PEMFC reaction [6]
m_{cargo}	Mass of the transported cargo [1]
MCFC	Molten Carbonate Fuel Cell
m_{conc}	Experimental constant [10]
MDP	Metal Depletion Potential
m_{driver}	Driver's mass (plus the mass of any passengers) [1]
MEP	Marine Eutrophication Potential
m_{fuel}	Mass of the fuel [1]
$\dot{m}_{H_2}$	Consumption of hydrogen mass flow, for FCHEV with PEMFC [6]
m_{nsF}	Half the front unsprung mass of the vehicle [1]
m_{nsR}	Half the rear unsprung mass of the vehicle [1]
$\dot{m}_{O_2}$	Mass flow rate of oxygen gas required for the PEMFC reaction [6]
MRC	Model Reference Controller
m_{RB_F}	Slope of regenerative braking torque curve of the front motor (in the TEST model) [1]
m_{RB_R}	Slope of regenerative braking torque curve of the rear motor (in the TEST model) [1]
m_{sF}	Front sprung mass of the vehicle [1]
m_{sR}	Rear sprung mass of the vehicle [1]
$m_{vehicle}$	Unloaded mass of the vehicle [1]
n	Number of FC cells [1]
N_2	Molecule of nitrogen
NCA	Lithium-nickel-cobalt-aluminium oxide ($LiNi_xCo_yAl_zO_2$)
NCM	Lithium-nickel-cobalt-manganese oxide battery ($LiNi_xCo_yMn_zO_2$ or NCM)
n_{conc}	Experimental constant [10]

Abbreviation	Description
n_e	Number of electrons [10]
N_{gen}	Number of generators [1]
Ni	Nickel
NiMH	Nickel-metal hydride
NMC	Lithium-nickel-cobalt-manganese oxide battery ($LiNi_xCo_yMn_zO_2$ or NCM)
NNC	Neutral Networks Controller
NOx	Oxides of nitrogen
N_p	Number of cells arranged in parallel inside the battery pack [1]
N_s	Number of cells arranged in series inside the battery pack [1]
$O^=$	Oxygen ion
O_2	Molecule of oxygen
O^{2-}	Oxygen ion
OCV	Open Circuit Voltage
Out	Output
p_0	Standard pressure [10]
$P_{absorbable}$	Maximum power that the battery pack can absorb, by the motors and generators (calculated in the TEST model) [4]
P_{acc}	Total power consumed by the vehicle accessories [1]
PAFC	Phosphoric Acid Fuel Cell
$P_{available}$	Available power which can be taken from the battery pack to power the motors (calculated in the TEST model) [4]
P_{AWDf}	Hypothetical power absorbed by the battery pack, coming from the front motor, in the case of an AWD vehicle, with battery limitations (calculated in RB logic) [5]
P_{AWD_HYPr}	Hypothetical charging power provided by the rear motor (calculated in RB logic) [5]
P_{AWD_NEWf}	Charging power provided by the front motor in case of approximation error in the calculation of T_{motR}, for AWD vehicles (calculated in RB logic) [5]
P_{AWDr}	Hypothetical power absorbed by the battery pack, coming from the rear motor, in the case of an AWD vehicle, with battery limitations (calculated in RB logic) [5]
P_{battF}	Available power which can be taken from the battery pack to power the front motor (calculated in the TEST model) [4]
$P_{battI2R}$	Total power of all cells, dissipated by Joule effect in the entire battery pack (calculated in the TEST model) [4]
P_{battR}	Available power which can be taken from the battery pack to power the rear motor (calculated in the TEST model) [4]
P_{batt_req}	The power which can be taken from the battery pack to power the front motor [6]

Abbreviation	Description
p_{brake_max}	Maximum pressure that can be generated inside the master cylinder of the brake system [2]
P_{buffer}	Constant power that is used to keep within the discharge and charge limits with a defined tolerance [1]
p_{CH_4}	Partial pressure of the methane [10]
P_{chrg_limit}	Charging limitation expressed as power [1]
p_{CO_2}	Partial pressure of the carbon dioxide [10]
P_{comp}	Power supply of the PEM fuel cell compressor [6]
$P_{dischrg\_limit}$	Discharging limitation expressed as power [1]
PEFC	Polymer Electrolyte Fuel Cell
PEM	Proton Exchange Membrane
PEMFC	Proton Exchange Membrane Fuel Cell
$Perc_{comp/acc}$	Percentage of the power consumed by the compressor of the FC compared to the power consumed by all the auxiliaries of the PEMFC itself [1]
P_{FC}	The output power of the fuel cell stack [6]
P_{FC_eff}	Effective FC output power [6]
P_{FCmax}	Maximum power of the fuel cell [2]
P_{FCmin}	Minimum power of the fuel cell [2]
P_{gen}	Power supplied to the batteries by the generators [4]
P_{gen_FC}	Effective FC power absorbed by the battery pack [6]
$P_{gen\_FC\_th}$	FC power that should be sent to charge the battery [6]
P_{gen_nom}	Nominal power of a generator [1]
P_{gen_th}	Total maximum power that the generators can supply as input to the battery pack [4]
p_{H_2}	Partial pressure of the hydrogen at the anode [1,10]
p_{H_2O}	Partial pressure of the water [10]
PI	Proportional–Integral controller
PID	Proportional–Integral–Derivative controller
PIDC	Proportional–Integral–Differential controllers
P_{in}	Inlet pressure of the PEMFC compressor [1]
PMFP	Particulate Matter Formation Potential
P_{mot_tot}	Total power that the motors absorb (calculated in the TEST model) [4]
p_{O_2}	Partial pressure of the oxygen at the cathode [1,10]
POCP	Photochemical Oxidant Creation Potential
P_{out}	Outlet pressure of the PEMFC compressor [1]
PPS	Peak Power Source
P_{reqF}	Power required to the battery pack by the front motor (calculated in the TEST model) [4]

Abbreviation	Description
P_{reqR}	Power required to the battery pack by the rear motor (calculated in the TEST model) [4]
$Pres_{brakeF}$	Front master cylinder brake pressure (calculated in RB logic) [9]
$Pres_{brakeR}$	Rear master cylinder brake pressure (calculated in RB logic) [9]
$Pres_{MAXbrakeF}$	Maximum pressure that can be generated inside the master cylinder of the front brake system (in RB logic) [1]
$Pres_{MAXbrakeR}$	Maximum pressure that can be generated inside the master cylinder of the rear brake system (in RB logic) [1]
PROPS	Powertrain ROad Performance Simulation
P_{SOFC}	Charging power that the SOFC system sends to the battery pack [11]
P_{SOFC_th}	Constant power supplied by SOFC [11]
P_{tot}	Sum of the traction power request (P_{tot_req}) and the power of the auxiliary systems [6]
P_{tot_req}	Total power required by the motors (calculated in the TEST model) [4]
PVDF	Polyvinylidene fluoride
R	Universal gas constant [1,10]
r	Ohmic resistance in the FC [10]
RB	Regenerative Braking
R_C	Fuel cell internal resistance due to the transport of electrons [1]
R_{cableF}	Electric resistance of the front connection cables [2]
R_{cableR}	Electric resistance of the rear connection cables [2]
R_{discF}	Average radius of application of the braking force on the front discs [1]
R_{discR}	Average radius of application of the braking force on the rear discs [1]
RES	Internal resistance of the battery pack
r_{HO}	Ratio between the inlet molar flow rates of hydrogen and oxygen [10]
R_i	Resistance of the single cell of the battery pack [4]
R_M	Fuel cell internal resistance due to the transport of ions [2]
R_{ohm}	Total resistance of the FC cell [2]
RPM	Revolutions per minute
RWD	Rear-Wheel Drive vehicle
R_{wheelF}	Nominal rolling radius of the front wheels [1]
R_{wheelR}	Nominal rolling radius of the rear wheels [1]
SAFC	Sulphuric Acid Fuel Cell

Abbreviation	Description
SC_F	Safety coefficient for the braking force guarantee by the front motor, for avoiding the locking of the front driving wheels (in the RB logic) [1]
SC_R	Safety coefficient for the braking force guarantee by the rear motor, for avoiding the locking of the rear driving wheels (in the RB logic) [1]
SFTP	Supplemental Federal Test Procedure
SI	International System of Units
SIB	Sodium-ion Battery
SMC	Sliding-Mode Controller
SOC	Battery State of Charge
SOC_{max}	Upper limit of the PEMFC "Power Split" logic [1]
SOC_{min}	Lower limit of the PEMFC "Power Split" logic [1]
SOFC	Solid Oxide Fuel Cell
SOFC-GT	Solid Oxide Fuel Cell / Gas Turbine
SPFC	Solid Polymer Fuel Cell
T	Fuel cell temperature [10]
T_0	Standard temperature [10]
T_{amb}	Ambient air temperature [1]
T_{AWD_HYPf}	Hypothetical front regenerative torque, minimum value between T_{AWD_MAXf} and T_{refF} (calculated in the RB logic) [5]
T_{AWD_HYPr}	Hypothetical rear regenerative torque, calculated starting from the power P_{AWD_HYPr} (calculated in the RB logic) [5]
T_{AWD_MAXf}	Maximum regenerative torque that can be obtained from the front motor, exploiting the absorbable power P_{AWDf} by the battery pack (calculated in the RB logic) [5]
TC	Threshold Controller
TEST	Target-speed EV Simulation Tool
TETP	Terrestrial Ecotoxicity Potential
T_{fc}	Fuel cell operating temperature [1]
T_{mot_F}	Front motor torque (calculated in the TEST model) [4]
T_{motF}	Regenerative torque of the front electric motor (calculated in the RB logic) [9]
T_{mot_R}	Rear motor torque (calculated in the TEST model) [4]
T_{motR}	Regenerative torque of the rear electric motor (calculated in the RB logic) [9]
$track_F$	Front track of the vehicle [1]
$track_R$	Rear track of the vehicle [1]

Abbreviation	Description
$TractRatio_{acc}$	Distribution of torque between the front and rear electric motors (towards the front) in the case of the accelerator pedal pressed (in the TEST model) [1]
$TractRatio_{brak}$	Distribution of torque between the front and rear electric motors (towards the front) in the case of the brake pedal pressed (in the TEST model) [1]
T_{RBmax_F}	Maximum regenerative braking torque of the front motor (in the TEST model) [1]
T_{RBmax_R}	Maximum regenerative braking torque of the rear motor (in the TEST model) [1]
T_{ref_F}	Front motor torques required (calculated in the TEST model) [4]
T_{refF}	Regenerative torque required from the front electric motor, respecting the limitations of the motor (calculated in the RB logic) [5]
T_{ref_R}	Rear motor torques required (calculated in the TEST model) [4]
T_{refR}	Regenerative torque required from the rear electric motor, respecting the limitations of the motor (calculated in the RB logic) [5]
T_{req_F}	Front motor request torque, considering the motor limitation (calculated in the TEST model) [4]
T_{reqF}	Regenerative torque required from the front electric motor, not considering any limitations (calculated in the RB logic) [5]
T_{req_R}	Rear motor request torque, considering the motor limitation (calculated in the TEST model) [4]
T_{reqR}	Regenerative torque required from the rear electric motor, not considering any limitations (calculated in the RB logic) [5]
t_s	Sampling time of the TEST simulation [1]
u	FC fuel usage ratio [10]
US06	Normed driving cycle, SFTP-US06
V	Voltage of the battery pack [4,8]
v	Longitudinal vehicle speed [4,8]
v_{act}	Activation potential loss [6,10]
V_{cell}	Output voltage of a single cell of the fuel cell stack [6]
v_{conc}	Concentration loss [6,10]
VCU	Vehicle Control Unit
V_{fc}	Fuel cell stack output voltage [6]
v_{ohm}	Ohmic loss [6,10]
v_{prev}	Vehicle speed of the instant of calculation preceding that considered (in the TEST model) [4]
V_r	Reversible open circuit voltage of the fuel cell [2,10]

Abbreviation	Description
v_{RBmin_F}	Minimum speed for the activation of the regenerative braking of the front electric motor (in the TEST model) [1]
v_{RBmin_R}	Minimum speed for the activation of the regenerative braking of the rear electric motor (in the TEST model) [1]
v_{ref}	Reference vehicle speed (in the TEST model) [7]
W_{air}	Molecular mass of the air in input in the PEMFC [1]
W_f	Load on the front axle, considering only the static weight and the longitudinal load transfer (calculated in the RB logic) [5]
WHF	Vertical aerodynamic coefficient [1]
W_{H_2}	Molecular mass of hydrogen [1]
WLTC	Worldwide harmonized Light-duty vehicles Test Cycles
WLTP	Worldwide harmonized Light-duty vehicles Test Procedure
W_{O_2}	Molecular mass of oxygen [1]
W_r	Load on the rear axle, considering only the static weight and the longitudinal load transfer (calculated in the RB logic) [5]
W_{refF}	Reference load on the front axle (calculated in the RB logic) [5]
W_{refR}	Reference load on the rear axle (calculated in the RB logic) [5]
x	Space travelled by the vehicle (in the TEST model) [4]
x_{prev}	Space covered by the vehicle from the start of the simulation until the calculation step preceding the one considered (in the TEST model) [4]
y	Calibration function, ratio between the TEST total motor torque and the "real" total motor torque [4]
Y_2O_3	Yttrium oxide
Y^{3+}	Ion of yttrium
YSZ	Yttria-Stabilized Zirconia
Zr^{4+}	Zirconium ion
ZrO_2	Zirconium oxide
α_1	Reduction coefficient [10]
α_2	Oxidation coefficient [10]
α_r	Constant coefficient [10]
β	Parametric coefficient of concentration loss [1]
β_r	Constant coefficient [10]
β_V	Symmetry factor [10]
ΔF_{zF}	Front-load transfer due to lateral acceleration (calculated in the RB logic) [5]
ΔF_{zR}	Rear-load transfer due to lateral acceleration (calculated in the RB logic) [5]
ΔP_{acc}	Power missing for the power supply of the accessories [3]
Δs	Entropy variation [10]

Abbreviation	Description
$\frac{\Delta}{\Delta t}$	Time derivative
η_{AWDf}	Electrical efficiency of the front motor at the operating point characterized by the parameters P_{AWDf} and ω_{motF} (in the RB logic) [5]
η_{AWD_HYPr}	Electrical efficiency of the rear motor at the operating point characterized by the parameters P_{AWD_HYPr} and ω_{motR} (in the RB logic) [5]
η_{AWD_NEWf}	Electrical efficiency of the front motor at the operating point characterized by the parameters P_{AWD_NEWf} and ω_{motF} (in the RB logic) [5]
η_{comp}	Total efficiency of the PEMFC compressor system [6]
$\eta_{DC/DC}$	Efficiency of the SOFC DC/DC converter [11]
η_{FWD}	Electrical efficiency of the front motor, for FWD vehicles (in the RB logic) [5]
η_{inv_ch}	Efficiency of the inverter in charge [1]
η_{inv_disch}	Efficiency of the inverter in discharge [1]
η_{mot_F}	Electrical efficiency of the front motor (in the TEST model) [4]
η_{motF}	Electrical efficiency of the front motor, before considering possible battery limitations (in the RB logic) [5]
η_{mot_R}	Electrical efficiency of the rear motor (in the TEST model) [4]
η_{motR}	Electrical efficiency of the rear motor, before considering possible battery limitations (in the RB logic) [5]
$\eta_{mot\_ref\_F}$	Reference electrical efficiency of the front motor (in the TEST model) [4]
$\eta_{mot\_ref\_R}$	Reference electrical efficiency of the rear motor (in the TEST model) [4]
η_{refF}	Electrical efficiency of the front motor at the operating point characterized by the parameters T_{refF} and ω_{motF} (in the RB logic) [5]
η_{refR}	Electrical efficiency of the rear motor at the operating point characterized by the parameters T_{refR} and ω_{motR} (in the RB logic) [5]
η_{RWD}	Electrical efficiency of the rear motor, for RWD vehicles (in the RB logic) [5]
η_{transF}	General efficiency of the entire front transmission [1]
η_{transR}	General efficiency of the entire rear transmission [1]
θ	Road slope angle [7]
θ_{H_2/O_2}	Stoichiometry ratio of oxygen and hydrogen [1]
θ_{ROLL}	Roll angle of the vehicle [5]
λ	The humidity of the fuel cell membrane [1]

Abbreviation	Description
μ	Road-tire friction coefficient (in the RB logic) [1]
μ_{padF}	Dynamic coefficient of friction between front brake pads and brake callipers [1]
μ_{padR}	Dynamic coefficient of friction between rear brake pads and brake callipers [1]
$\xi_1, \xi_2, \xi_3, \xi_4$	Parametric coefficients of activation loss [1]
ρ	Air density [1]
ρ_{Cu}	Electric resistivity of copper (or in any case of the conductive material of the electric cables) [1]
ρ_M	Membrane resistivity of the fuel cell [6]
τ_{diffF}	Reduction ratio of the front differential [1]
τ_{diffR}	Reduction ratio of the rear differential [1]
τ_{redF}	Reduction ratio of the front motor reductor [1]
τ_{redR}	Reduction ratio of the rear motor reductor [1]
Φ_{cableF}	Diameter of the front motor cables [1]
Φ_{cableR}	Diameter of the rear motor cables [1]
ω_{gen}	Angular velocity of the generator/s [1]
ω_{motF}	Angular velocity of the front electric motor [4,8]
$\omega_{mot\_prev\_F}$	Angular velocity of the front motor relative to the previous instant of calculation (in the TEST model) [4]
$\omega_{mot\_prev\_R}$	Angular velocity of the rear motor relative to the previous instant of calculation (in the TEST model) [4]
ω_{motR}	Angular velocity of the rear electric motor [4,8]
$\omega_{mot\_ref\_F}$	Reference angular velocity of the front motor (in the TEST model) [4]
$\omega_{mot\_ref\_R}$	Reference angular velocity of the rear motor (in the TEST model) [4]
$\omega_{mot\_req\_F}$	Angular velocity of the front motor request, considering the motor limitation (in the TEST model) [4]
$\omega_{mot\_req\_R}$	Angular velocity of the rear motor request, considering the motor limitation (in the TEST model) [4]
ω_{wheelF}	Angular velocity of the front wheels [4,8]
ω_{wheelR}	Angular velocity of the rear wheels [4,8]
$\omega_{wheel\_ref\_F}$	Reference angular velocity of the front wheels (in the TEST model) [4]
$\omega_{wheel\_ref\_R}$	Reference angular velocity of the rear wheels (in the TEST model) [4]
Ø	Percentage of oxygen in the air mixture [1]

[1] Constant value.

[2] Constant calculated parameter.

[3] Variable.

[4] "TEST model" calculated variable.

[5] "RB logic" calculated variable.

[6] "PEMFC" calculated variable.

[7] "TEST model" input.

[8] "RB logic" input.

[9] "RB logic" output.

[10] SOFC modelling theory.

[11] SOFC model.

10 REFERENCES

1. Sandrini G, Có B, Tomasoni G, Gadola M, Chindamo D. The Environmental Performance of Traction Batteries for Electric Vehicles from a Life Cycle Perspective. Environmental and Climate Technologies. 2021;25. doi:10.2478/rtuect-2021-0053

2. Automotive World. An ICE-y Road to an Electric Future. [cited 30 Aug 2022]. Available: https://www.automotiveworld.com/articles/anice-y-road-to-an-electric-future/

3. European Council, Council of the European Union. Stricter CO2 Emission Standards for Cars and Vans Signed Off by the Council. [cited 30 Aug 2022]. Available: https://www.consilium.europa.eu/en/press/press-releases/2019/04/15/stricter-co2-emissionstandards-for-cars-and-vans-signed-off-by-the-council/

4. European Law. Brussels, 3 April 2019. PE-CONS 6/19. Regulation of the European Parliament and of the council setting CO2 emission performance standards for new passenger cars and for new light commercial vehicles, and repealing Regulations (EC) No 443/2009 and (EU) No 510/2011 (recast). [cited 30 Aug 2022]. Available: https://data.consilium.europa.eu/doc/document/PE-6-2019 -INIT/en/pdf

5. Official Journal of the European Union. REGULATION (EU) 2021/1119 OF THE EUROPEAN PARLIAMENT AND OF THE COUNCIL of 30 June 2021. [cited 21 Dec 2021]. Available: https://eur-lex.europa.eu/legal-content/EN/TXT/PDF/?uri=CELEX:32021R1119&from=EN

6. Ehsani M, Gao Y, Longo S, Ebrahimi K. Modern Electric, Hybrid Electric, and Fuel Cell Vehicles. Third Edition. Third Edition. Boca Raton, FL, USA: CRC Press, Taylor & Francis Group; 2018. pp. 1–11.

7. Bonera E, Gadola M, Chindamo D, Morbioli S, Magri P. Integrated Design Tools for Model-Based Development of Innovative Vehicle Chassis and Powertrain Systems. 2020. pp. 118–128. doi:10.1007/978-3-030-31154-4_11

8. Wu T, Lin S, Ji X. Research on ecological environment quality management technology model based on the sustainable development of ecological theory. Fresenius Environ Bull. 2020;29: 10575–10580.

9. Liu A, Zhu J, Yue D, Liu G. Design of multi-scale expression model of ecological environment data based on wavelet transform. Fresenius Environ Bull. 2020;29: 9775–9781.

10. Sandrini G, Gadola M, Chindamo D. Longitudinal dynamics simulation tool for hybrid apu and full electric vehicle. Energies (Basel). 2021;14. doi:10.3390/en14041207

11. Zhang Y-J, Yang P-P. Modeling and simulation of regenerative braking system for pure electric vehicle. Wuhan Ligong Daxue Xuebao/Journal of Wuhan University of Technology. 2010;32: 90–94. doi:10.3963/j.issn.1671-4431.2010.15.022

12. Biao J, Xiangwen Z, Yangxiong W, Wenchao H. Regenerative Braking Control Strategy of Electric Vehicles Based on Braking Stability Requirements. International Journal of Automotive Technology. 2021;22: 465–473. doi:10.1007/s12239-021-0043-1

13. Sandrini G, Chindamo D, Gadola M. Regenerative Braking Logic That Maximizes Energy Recovery Ensuring the Vehicle Stability. Energies (Basel). 2022;15: 5846. doi:10.3390/en15165846

14. United Nations. Adoption of the Paris Agreement - Paris Agreement. Available: https://unfccc.int/sites/default/files/english_paris_agreement.pdf

15. BP. Energy Outlook: 2020 Edition. BP: London, UK, 2020. [cited 29 Sep 2022]. Available: https://www.bp.com/content/dam/bp/business-sites/en/global/corporate/pdfs/energy-economics/energy-outlook/bp-energy-outlook-2020.pdf

16. de Angelis E, Carnevale C, Marcoberardino G di, Turrini E, Volta M. Low Emission Road Transport Scenarios: An Integrated Assessment of Energy Demand, Air Quality, GHG Emissions, and Costs. IEEE Transactions on Automation Science and Engineering. 2022;19: 37–47. doi:10.1109/TASE.2021.3073241

17. Glenk G, Reichelstein S. Reversible Power-to-Gas systems for energy conversion and storage. Nat Commun. 2022;13: 2010. doi:10.1038/s41467-022-29520-0

18. Das V, Padmanaban S, Venkitusamy K, Selvamuthukumaran R, Blaabjerg F, Siano P. Recent advances and challenges of fuel cell based power system architectures and control – A review. Renewable and Sustainable Energy Reviews. 2017;73: 10–18. doi:10.1016/j.rser.2017.01.148

19. Olabi AG, Wilberforce T, Abdelkareem MA. Fuel cell application in the automotive industry and future perspective. Energy. 2021;214: 118955. doi:10.1016/j.energy.2020.118955

20. Zecchi L, Sandrini G, Gadola M, Chindamo D. Modeling of a Hybrid Fuel Cell Powertrain with Power Split Logic for Onboard Energy Management Using a Longitudinal Dynamics Simulation Tool. Energies (Basel). 2022;15: 6228. doi:10.3390/en15176228

21. Ehsani M, Gao Y, Longo S, Ebrahimi K. Chapter 19: Powertrain Optimization. Third Edition. Modern Electric, Hybrid Electric, and Fuel Cell Vehicles. Third Edition. Boca Raton, FL, USA: CRC Press, Taylor & Francis Group; 2018. pp. 473–497.

22. Chindamo D, Gadola M, Romano M. Simulation tool for optimization and performance prediction of a generic hybrid electric series powertrain. International Journal of Automotive Technology. 2014;15: 135–144. doi:10.1007/s12239-014-0015-9

23. Chindamo D, Economou JT, Gadola M, Knowles K. A neurofuzzy-controlled power management strategy for a series hybrid electric vehicle. Proceedings of the Institution of Mechanical Engineers, Part D: Journal of Automobile Engineering. 2014;228: 1034–1050. doi:10.1177/0954407014522777

24. Chindamo D, Gadola M. What is the Most Representative Standard Driving Cycle to Estimate Diesel Emissions of a Light Commercial Vehicle? IFAC-PapersOnLine. 2018;51: 73–78. doi:10.1016/j.ifacol.2018.06.213

25. Trigui R, Badin F, Jeanneret B, Harel F, Coquery G, Lallemand R, et al. Hybrid light duty vehicles evaluation program. International Journal of Automotive Technology. 2003;4: 65–75.

26. Wang L, Zhang Y, Yin C, Zhang H, Wang C. Hardware-in-the-loop simulation for the design and verification of the control system of a series–parallel hybrid electric city-bus. Simul Model Pract Theory. 2012;25: 148–162. doi:10.1016/j.simpat.2012.02.010

27. Xiaohua Z, Qingnian W, Weihua W, Liang C. Analysis and Simulation of Conventional Transit Bus Energy Loss and Hybrid Transit Bus Energy Saving. 2005. doi:10.4271/2005-01-1173

28. Tremblay O, Dessaint L-A, Dekkiche A-I. A Generic Battery Model for the Dynamic Simulation of Hybrid Electric Vehicles. 2007 IEEE Vehicle Power and Propulsion Conference. IEEE; 2007. pp. 284–289. doi:10.1109/VPPC.2007.4544139

29. Johnson VH. Battery performance models in ADVISOR. J Power Sources. 2002;110: 321–329. doi:10.1016/S0378-7753(02)00194-5

30. Sarathkumar T v, Poornanand M, Goswami AK. Modelling and Simulation of Electric Vehicle Drive Through SAEJ227 & EUDC Cycles. 2020 IEEE Students Conference on Engineering & Systems (SCES). IEEE; 2020. pp. 1–5. doi:10.1109/SCES50439.2020.9236717

31. Dubey M, Bhardwaj S, Harish R, Shyam Kumar MB. Simulation of Electric Vehicle using Scilab for Formula Student Application. IOP Conf Ser Earth Environ Sci. 2020;573: 012026. doi:10.1088/1755-1315/573/1/012026

32. Wipke KB, Cuddy MR, Burch SD. ADVISOR 2.1: a user-friendly advanced powertrain simulation using a combined backward/forward approach. IEEE Trans Veh Technol. 1999;48: 1751–1761. doi:10.1109/25.806767

33. Ehsani M, Gao Y, Longo S, Ebrahimi K. Modern Electric, Hybrid Electric, and Fuel Cell Vehicles. Third Edition. Third Edition. Boca Raton, FL, USA: CRC Press, Taylor & Francis Group; 2018. pp. 95–98.

34. Chan CC, Chau KT. Modern Electric Vehicle Technology. New York: Oxford University Press; 2001.

35. Chindamo D. Lectures of the course “Veicoli ibridi ed elettrici” ("Hybrid and Electric Vehicles), Department of Mechanical and Industrial Engineering, University of Brescia, Brescia, Italy. 2022.

36. Guiggiani M. Dinamica del Veicolo. Turin, Italy: Città Studi Edizioni; 1998.

37. Ehsani M, Gao Y, Longo S, Ebrahimi K. Modern Electric, Hybrid Electric, and Fuel Cell Vehicles. Third Edition. Third Edition. Boca Raton, FL, USA: CRC Press, Taylor & Francis Group; 2018. pp. 18–20.

38. COMMISSION REGULATION (EU) 2017/1151.

39. Bonera E, Gadola M, Chindamo D, Morbioli S, Magri P. On the Influence of Suspension Geometry on Steering Feedback. Applied Sciences. 2020;10: 4297. doi:10.3390/app10124297

40. Gadola M, Chindamo D. Experiential learning in engineering education: The role of student design competitions and a case study. International Journal of Mechanical Engineering Education. 2019;47: 3–22. doi:10.1177/0306419017749580

41. Crema C, Depari A, Flammini A, Vezzoli A, Benini C, Chindamo D, et al. Smartphone-based system for the monitoring of vital parameters and stress conditions of amatorial racecar drivers. 2015 IEEE SENSORS. IEEE; 2015. pp. 1–4. doi:10.1109/ICSENS.2015.7370521

42. Zhou W, Chen Y, Zhai H, Zhang W. Predictive energy management for a plug-in hybrid electric vehicle using driving profile segmentation and energy-based analytical SoC planning. Energy. 2021;220: 119700. doi:10.1016/j.energy.2020.119700

43. Li P, Jin DF, Luo YG. Regenerative braking control strategy for a mild HEV. Automotive Engineering. 2005;27: 570–574. doi:10.1007/s12239–021–0043–1

44. Regulation No 13 of the Economic Commission for Europe of the United Nations (UN/ECE) — Uniform provisions concerning the approval of vehicles of categories M, N and O with regard to braking [2016/194]. Available: http://www.unece.org/trans/main/wp29/wp29wgs/wp29gen/wp29fdocstts.html

45. He L, Ye W, He Z, Song K, Shi Q. A combining sliding mode control approach for electric motor anti-lock braking system of battery electric vehicle. Control Eng Pract. 2020;102: 104520. doi:10.1016/j.conengprac.2020.104520

46. Guo J, Wang J, Cao B. Brake-Force Distribution Strategy for Electric Vehicle Based on Maximum Energy Recovery. Hsi-An Chiao Tung Ta Hsueh/Journal of Xi'an Jiaotong University. 2008;42: 607–611.

47. Li YF, Tian YT, Hu LL, Yin C. A study on control algorithm of regenerative braking for EV/HEV. Automotive Engineering. 2007;29: 1059–1063.

48. Kim J, Ko S, Lee G, Yeo H, Kim P, Kim H. Development of co-operative control algorithm for parallel HEV with electric booster brake during regenerative braking. 2011 IEEE Vehicle Power and Propulsion Conference, VPPC 2011. 2011. doi:10.1109/VPPC.2011.6043151

49. Ko JW, Ko SY, Kim IS, Hyun DY, Kim HS. Co-operative control for regenerative braking and friction braking to increase energy recovery without wheel lock. International Journal of Automotive Technology. 2014;15: 253–262. doi:10.1007/s12239-014-0026-6

50. He H, Xiong R, Guo H. Online estimation of model parameters and state-of-charge of $LiFePO_4$ batteries in electric vehicles. Appl Energy. 2012;89: 413–420. doi:10.1016/j.apenergy.2011.08.005

51. Tjoønnäs J, Johansen TA. Stabilization of automotive vehicles using active steering and adaptive brake control allocation. IEEE Transactions on Control Systems Technology. 2010;18: 545–558. doi:10.1109/TCST.2009.2023981

52. Lian Y-F, Tian Y-T, Hu L-L, Yin C. A new braking force distribution strategy for electric vehicle based on regenerative braking strength continuity. J Cent South Univ. 2013;20: 3481–3489. doi:10.1007/s11771-013-1872-5

53. Vodovozov V, Raud Z, Petlenkov E. Review on braking energy management in electric vehicles. Energies (Basel). 2021;14. doi:10.3390/en14154477

54. Vodovozov V, Raud Z, Aksjonov A, Petlenkov E. Fuzzy Logic Control of Electric Vehicles in Changing Braking Conditions. 2020 XI International Conference on Electrical Power Drive Systems (ICEPDS). IEEE; 2020. pp. 1–6. doi:10.1109/ICEPDS47235.2020.9249083

55. Acosta M, Kanarachos S, Blundell M. Road friction virtual sensing: A review of estimation techniques with emphasis on low excitation approaches. Applied Sciences (Switzerland). MDPI AG; 2017. doi:10.3390/app7121230

56. Wang Y, Hu J, Wang F, Dong H, Yan Y, Ren Y, et al. Tire Road Friction Coefficient Estimation: Review and Research Perspectives. Chinese Journal of Mechanical Engineering (English Edition). Springer; 2022. doi:10.1186/s10033-021-00675-z

57. Mechichi O, Trigui R, el Amraoui L. Adaptive λ-Control Strategy for Plug-In HEV Energy Management Using Fast Initial Multiplier Estimate. Applied Sciences. 2022;12: 10543. doi:10.3390/app122010543

58. Zecchi L. MODELLAZIONE E SIMULAZIONE DI UN SISTEMA PROPULSIVO BASATO SU FUEL CELL AD IDROGENO. Università degli Studi di Brescia. 2021.

59. Gimba ID, Abdulkareem AS, Jimoh A, Afolabi AS. Theoretical Energy and Exergy Analyses of Proton Exchange Membrane Fuel Cell by Computer Simulation. Journal of Applied Chemistry. 2016;2016: 1–15. doi:10.1155/2016/2684919

60. S. Menesy A, Sultan HM, Korashy A, Banakhr FA, G. Ashmawy M, Kamel S. Effective Parameter Extraction of Different Polymer Electrolyte Membrane Fuel Cell Stack Models Using a Modified Artificial Ecosystem Optimization Algorithm. IEEE Access. 2020;8: 31892–31909. doi:10.1109/ACCESS.2020.2973351

61. Daud WRW, Rosli RE, Majlan EH, Hamid SAA, Mohamed R, Husaini T. PEM fuel cell system control: A review. Renew Energy. 2017;113: 620–638. doi:10.1016/j.renene.2017.06.027

62. Ehsani M, Gao Y, Longo S, Ebrahimi K. Chapter 15: Fuel Cells. Third Edition. Modern Electric, Hybrid Electric, and Fuel Cell Vehicles. Third Edition. Boca Raton, FL, USA: CRC Press, Taylor & Francis Group; 2018. pp. 397–420.

63. Hoogers G. Fuel Cell Technology Handbook. Boca Raton, FL, USA: CRC Press; 2003.

64. Lü X, Qu Y, Wang Y, Qin C, Liu G. A comprehensive review on hybrid power system for PEMFC-HEV: Issues and strategies. Energy Convers Manag. 2018;171: 1273–1291. doi:10.1016/j.enconman.2018.06.065

65. Sulaiman N, Hannan MA, Mohamed A, Ker PJ, Majlan EH, Wan Daud WR. Optimization of energy management system for fuel-cell hybrid electric vehicles: Issues and recommendations. Appl Energy. 2018;228: 2061–2079. doi:10.1016/j.apenergy.2018.07.087

66. Sulaiman N, Hannan MA, Mohamed A, Majlan EH, Wan Daud WR. A review on energy management system for fuel cell hybrid electric vehicle: Issues and challenges. Renewable and Sustainable Energy Reviews. 2015;52: 802–814. doi:10.1016/j.rser.2015.07.132

67. Gao J, Li M, Hu Y, Chen H, Ma Y. Challenges and developments of automotive fuel cell hybrid power system and control. Science China Information Sciences. 2019;62: 51201. doi:10.1007/s11432-018-9690-y

68. Işıklı F, Sürmen A, Gelen A. Modelling and Performance Analysis of an Electric Vehicle Powered by a PEM Fuel Cell on New European Driving Cycle (NEDC). Arab J Sci Eng. 2021;46: 7597–7609. doi:10.1007/s13369-021-05469-y

69. Ahsan N, al Rashid A, Zaidi AA, Imran R, Abdul Qadir S. Performance analysis of hydrogen fuel cell with two-stage turbo compressor for automotive applications. Energy Reports. 2021;7: 2635–2646. doi:10.1016/j.egyr.2021.05.007

70. Iora PG. Tecnologie per la mobilità sostenibile - Veicoli elettrici, ibridi e a fuel cell. First Edition. Esculapio; 2016.

71. Brtka E, Jotanovic G, Stjepanovic A, Jausevac G, Kosovac A, Cvitić I, et al. Model of Hybrid Electric Vehicle with Two Energy Sources. Electronics (Basel). 2022;11: 1993. doi:10.3390/electronics11131993

72. Du C, Huang S, Jiang Y, Wu D, Li Y. Optimization of Energy Management Strategy for Fuel Cell Hybrid Electric Vehicles Based on Dynamic Programming. Energies (Basel). 2022;15: 4325. doi:10.3390/en15124325

73. Xin W, Xu E, Zheng W, Feng H, Qin J. Optimal energy management of fuel cell hybrid electric vehicle based on model predictive control and on-line mass estimation. Energy Reports. 2022;8: 4964–4974. doi:10.1016/j.egyr.2022.03.194

74. Mounica V, Obulesu YP. Hybrid Power Management Strategy with Fuel Cell, Battery, and Supercapacitor for Fuel Economy in Hybrid Electric Vehicle Application. Energies (Basel). 2022;15: 4185. doi:10.3390/en15124185

75. Pukrushpan JP, Stefanopoulou AG, Peng H. Control of Fuel Cell Power Systems: Principles, Modeling, Analysis and Feedback Design. London, UK: Springer; 2004.

76. Ehsani M, Gao Y, Longo S, Ebrahimi K. Chapter 16: Fuel Cell Hybrid Electric Drivetrain Design. Third Edition. Modern Electric, Hybrid Electric, and Fuel Cell Vehicles. Third Edition. Boca Raton, FL, USA: CRC Press, Taylor & Francis Group; 2018. pp. 421–430.

77. Riemersma I. Development of a World-Wide Worldwide Harmonized Light Duty Driving Test Cycle (WLTC). In: Final version. Dec 2015.

78. Tonola A. STUDIO E MODELLAZIONE DI UN SISTEMA PROPULSIVO BASATO SU FUEL CELL A METANO E INCIDENZA DEL COMPRESSORE SULLA RICHIESTA ENERGETICA. Università degli Studi di Brescia. 2021.

79. Mangifesta P. SEMICELLE SOFC: STUDIO E PRODUZIONE DI ELETTROLITI CON PROCESSI A BASSO IMPATTO AMBIENTALE. Ph.D. Thesis, Università degli Studi di Bologna - Facoltà di Chimica Industriale. 2009. Available: http://amsdottorato.unibo.it/1493/1/Mangifesta_Patrizia_Tesi.pdf

80. Mellone R. Il mondo delle SOFC, o celle a combustibile ad ossidi solidi (The world of SOFCs, or solid oxide fuel cells). 14 Feb 2020. Available: https://energycue.it/mondo-sofc-celle-combustibile-ossidi-solidi/17825/. Accessed 10 Oct 2022.

81. Gür TM. Comprehensive review of methane conversion in solid oxide fuel cells: Prospects for efficient electricity generation from natural gas. Prog Energy Combust Sci. 2016;54: 1–64. doi:10.1016/j.pecs.2015.10.004

82. In-Hyung M, Ji-Soon K, Yung-Lip K. The effect of the doping method on the sinterability of nickel-doped tungsten compacts. Journal of the Less Common Metals. 1984;102: 219–226. doi:10.1016/0022-5088(84)90318-7

83. Ng KH, Rahman HA, Somalu MR. Review: Enhancement of composite anode materials for low-temperature solid oxide fuels. Int J Hydrogen Energy. 2019;44: 30692–30704. doi:10.1016/j.ijhydene.2018.11.137

84. Navarra MA, Scrosati B. Celle a combustibile. Enciclopedia della Scienza e della Tecnica. 2008.

85. Minh NQ. Ceramic Fuel Cells. Journal of the American Ceramic Society. 1993;76: 563–588. doi:10.1111/j.1151-2916.1993.tb03645.x

86. Escudero MJ, Yeste MP, Cauqui MÁ, Muñoz MÁ. Performance of a Direct Methane Solid Oxide Fuel Cell Using Nickel-Ceria-Yttria Stabilized Zirconia as the Anode. Materials. 2020;13: 599. doi:10.3390/ma13030599

87. Zhu Y, Tomsovic K. Development of models for analyzing the load-following performance of microturbines and fuel cells. Electric Power Systems Research. 2002;62: 1–11. doi:10.1016/S0378-7796(02)00033-0

88. Lakshmi TVVS, Geethanjali P, Krishna PS. Mathematical modelling of solid oxide fuel cell using Matlab/Simulink. 2013 Annual International Conference on Emerging Research Areas and 2013 International Conference on Microelectronics, Communications and Renewable Energy. IEEE; 2013. pp. 1–5. doi:10.1109/AICERA-ICMiCR.2013.6576016

89. Tuyen ND, Fujita G, Yokoyama R, Koyanagi K, Funabashi T, Nomura M. Using Simulink Simulation to Evaluate Load Following Characteristics of SOFC Generator with Heat Exchanger Considering Heat Balance. IEEJ Transactions on Power and Energy. 2010;130: 501–509. doi:10.1541/ieejpes.130.501

90. Padullés J, Ault GW, McDonald JR. An integrated SOFC plant dynamic model for power systems simulation. J Power Sources. 2000;86: 495–500. doi:10.1016/S0378-7753(99)00430-9

91. Singh BK, Gaonkar DN, Aithal RS, Sharma G. Modeling and Performance Analysis of Solid Oxide Fuel Cell Based Distributed Generation System. International Energy Journal. 2012;12: 123–134.

92. Chakraborty U. Reversible and Irreversible Potentials and an Inaccuracy in Popular Models in the Fuel Cell Literature. Energies (Basel). 2018;11: 1851. doi:10.3390/en11071851

93. El-Sharkh MY, Rahman A, Alam MS, Byrne PC, Sakla AA, Thomas T. A dynamic model for a stand-alone PEM fuel cell power plant for residential applications. J Power Sources. 2004;138: 199–204. doi:10.1016/j.jpowsour.2004.06.037

94. Jurado F, Valverde M. Multiobjective Genetic Algorithms for Fuzzy Inverter in Solid Oxide Fuel Cell System. Proceedings of the IEEE International Symposium on Industrial Electronics, 2005 ISIE 2005. IEEE; 2005. pp. 145–150. doi:10.1109/ISIE.2005.1528902

95. Jurado F, Valverde M. Genetic fuzzy control applied to the inverter of solid oxide fuel cell for power quality improvement. Electric Power Systems Research. 2005;76: 93–105. doi:10.1016/j.epsr.2005.05.007

96. Li YH, Choi SS, Rajakaruna S. An Analysis of the Control and Operation of a Solid Oxide Fuel-Cell Power Plant in an Isolated System. IEEE Transactions on Energy Conversion. 2005;20: 381–387. doi:10.1109/TEC.2005.847998

97. Li YH, Rajakaruna S, Choi SS. Control of a Solid Oxide Fuel Cell Power Plant in a Grid-Connected System. IEEE Transactions on Energy Conversion. 2007;22: 405–413. doi:10.1109/TEC.2005.853756

98. Wang C, Nehrir MH, Shaw SR. Dynamic Models and Model Validation for PEM Fuel Cells Using Electrical Circuits. IEEE Transactions on Energy Conversion. 2005;20: 442–451. doi:10.1109/TEC.2004.842357

99. Caisheng Wang, Nehrir MH. A Physically Based Dynamic Model for Solid Oxide Fuel Cells. IEEE Transactions on Energy Conversion. 2007;22: 887–897. doi:10.1109/TEC.2007.895468

100. Huo H-B, Zhong Z-D, Zhu X-J, Tu H-Y. Nonlinear dynamic modeling for a SOFC stack by using a Hammerstein model. J Power Sources. 2008;175: 441–446. doi:10.1016/j.jpowsour.2007.09.059

101. Wu X-J, Zhu X-J, Cao G-Y, Tu H-Y. Predictive control of SOFC based on a GA-RBF neural network model. J Power Sources. 2008;179: 232–239. doi:10.1016/j.jpowsour.2007.12.036

102. Chakraborty UK. Static and dynamic modeling of solid oxide fuel cell using genetic programming. Energy. 2009;34: 740–751. doi:10.1016/j.energy.2009.02.012

103. Chakraborty UK. An error in solid oxide fuel cell stack modeling. Energy. 2011;36: 801–802. doi:10.1016/j.energy.2010.12.038

104. Nayeripour M, Hoseintabar M, Niknam T. A new method for dynamic performance improvement of a hybrid power system by coordination of converter's controller. J Power Sources. 2011;196: 4033–4043. doi:10.1016/j.jpowsour.2010.11.156

105. Nayeripour M, Hoseintabar M, Niknam T, Adabi J. Power management, dynamic modeling and control of wind/FC/battery-bank based hybrid power generation system for stand-alone application. European Transactions on Electrical Power. 2012;22: 271–293. doi:10.1002/etep.558

106. Radisavljevic V. On controllability and system constraints of the linear models of proton exchange membrane and solid oxide fuel cells. J Power Sources. 2011;196: 8549–8552. doi:10.1016/j.jpowsour.2011.06.034

107. Torreglosa JP, Garcia P, Fernandez LM, Jurado F. Predictive Control for the Energy Management of a Fuel-Cell–Battery–Supercapacitor Tramway. IEEE Trans Industr Inform. 2014;10: 276–285. doi:10.1109/TII.2013.2245140

108. Fedakar S, Bahceci S, Yalcinoz T. Modeling and simulation of grid connected solid oxide fuel cell using PSCAD. Journal of Renewable and Sustainable Energy. 2014;6: 053118. doi:10.1063/1.4897936

109. Taghizadeh M, Hoseintabar M, Faiz J. Frequency control of isolated WT/PV/SOFC/UC network with new control strategy for improving SOFC dynamic response. International Transactions on Electrical Energy Systems. 2015;25: 1748–1770. doi:10.1002/etep.1925

110. Chettibi N, Mellit A, Sulligoi G, Pavan AM. Fuzzy-based power control for distributed generators based on solid oxide fuel cells. 2015 International Conference on Clean Electrical Power (ICCEP). IEEE; 2015. pp. 580–585. doi:10.1109/ICCEP.2015.7177550

111. Barelli L, Bidini G, Ottaviano A. Solid oxide fuel cell modelling: Electrochemical performance and thermal management during load-following operation. Energy. 2016;115: 107–119. doi:10.1016/j.energy.2016.08.107

112. Vigneysh T, Kumarappan N. Autonomous operation and control of photovoltaic/solid oxide fuel cell/battery energy storage based microgrid using fuzzy logic controller. Int J Hydrogen Energy. 2016;41: 1877–1891. doi:10.1016/j.ijhydene.2015.11.022

113. Pan L, Xue Y, Sun L, Li D, Wu Z. Multiple Model Predictive Control for Solid Oxide Fuel Cells. Volume 9: 13th ASME/IEEE International Conference on Mechatronic and Embedded Systems and Applications. American Society of Mechanical Engineers; 2017. doi:10.1115/DETC2017-67122

114. Wu G, Sun L, Lee KY. Disturbance rejection control of a fuel cell power plant in a grid-connected system. Control Eng Pract. 2017;60: 183–192. doi:10.1016/j.conengprac.2016.12.010

115. Sun L, Hua Q, Shen J, Xue Y, Li D, Lee K. A Combined Voltage Control Strategy for Fuel Cell. Sustainability. 2017;9: 1517. doi:10.3390/su9091517

116. Darjat, Sulistyo, Triwiyatno A, Thalib H. The Design of Connection Solid Oxide Fuel Cell (SOFC) Integrated Grid with Three-Phase Inverter. IOP Conf Ser Mater Sci Eng. 2018;316: 012057. doi:10.1088/1757-899X/316/1/012057

117. Sun L, Wu G, Xue Y, Shen J, Li D, Lee KY. Coordinated Control Strategies for Fuel Cell Power Plant in a Microgrid. IEEE Transactions on Energy Conversion. 2018;33: 1–9. doi:10.1109/TEC.2017.2729881

118. Chettibi N, Mellit A. Intelligent control strategy for a grid connected PV/SOFC/BESS energy generation system. Energy. 2018;147: 239–262. doi:10.1016/j.energy.2018.01.030

119. Safari A, Shahsavari H, Salehi J. A mathematical model of SOFC power plant for dynamic simulation of multi-machine power systems. Energy. 2018;149: 397–413. doi:10.1016/j.energy.2018.02.068

120. Noren DA, Hoffman MA. Clarifying the Butler–Volmer equation and related approximations for calculating activation losses in solid oxide fuel cell models. J Power Sources. 2005;152: 175–181. doi:10.1016/j.jpowsour.2005.03.174

121. Windisch CF, Stevenson JW, Simner SP, Williford RE, Chick LA. Experimentally-Calibrated, Spreadsheet-Based SOFC Unit-Cell Performance Model. In 2002 Fuel Cell Seminar: Fuel Cells - Reliable, Clean Energy for the World. 2002. pp. 383–386.

122. Sedghisigarchi K, Feliachi A. Dynamic and Transient Analysis of Power Distribution Systems With Fuel Cells—Part I: Fuel-Cell Dynamic Model. IEEE Transactions on Energy Conversion. 2004;19: 423–428. doi:10.1109/TEC.2004.827039

123. Al M, Van J, Gualous H. DC/DC Converters for Electric Vehicles. Electric Vehicles - Modelling and Simulations. InTech; 2011. doi:10.5772/17048

124. Brett DJL, Aguiar P, Brandon NP, Bull RN, Galloway RC, Hayes GW, et al. Concept and system design for a ZEBRA battery–intermediate temperature solid oxide fuel cell hybrid vehicle. J Power Sources. 2006;157: 782–798. doi:10.1016/j.jpowsour.2005.12.054

125. Cò B. Le prestazioni ambientali delle batterie per la trazione di veicoli elettrici nella prospettiva del ciclo di vita. Università degli Studi di Brescia. 2021.

126. Arshad F, Li L, Amin K, Fan E, Manurkar N, Ahmad A, et al. A Comprehensive Review of the Advancement in Recycling the Anode and Electrolyte from Spent Lithium Ion Batteries. ACS Sustain Chem Eng. 2020;8: 13527–13554. doi:10.1021/acssuschemeng.0c04940

127. Zhang R, Xia B, Li B, Cao L, Lai Y, Zheng W, et al. State of the Art of Lithium-Ion Battery SOC Estimation for Electrical Vehicles. Energies (Basel). 2018;11: 1820. doi:10.3390/en11071820

128. Casals LC, Amante García B, Canal C. Second life batteries lifespan: Rest of useful life and environmental analysis. J Environ Manage. 2019;232: 354–363. doi:10.1016/j.jenvman.2018.11.046

129. European Environment Agency. Electric vehicles from life cycle and circular economy perspectives. TERM 2018: Transport and Environment Reporting Mechanism (TERM) report. Copenhagen; 2018. Available: https://www.eea.europa.eu/publications/electric-vehicles-from-life-cycle

130. Ehsani M, Gao Y, Longo S, Ebrahimi K. Chapter 1: Environmental Impact and History of Modern Transportation. Third Edition. Modern Electric, Hybrid Electric, and Fuel Cell Vehicles. Third Edition. Boca Raton, FL, USA: CRC Press, Taylor & Francis Group; 2018. pp. 1–16.

131. Attualità Parlamento europeo. Emissioni di CO2 delle auto: i numeri e i dati. Infografica. (News European Parliament. CO2 emissions from cars: numbers and data. Infographic.). Available: https://www.europarl.europa.eu/news/it/headlines/society/20190313STO31218/emissioni-di-co2-delle-auto-i-numerie-i-dati-infografica

132. Attualità Parlamento europeo. Auto e inquinamento: i nuovi obiettivi (News European Parliament. Cars and pollution: the new goals). [cited 4 Feb 2021]. Available: https://www.europarl.europa.eu/news/it/headlines/society/20180920STO14027/auto-e-inquinamento-i-nuoviobiettivi-per-le-emissioni

133. Petrauskienė K, Skvarnavičiūtė M, Dvarionienė J. Comparative environmental life cycle assessment of electric and conventional vehicles in Lithuania. J Clean Prod. 2020;246: 119042. doi:10.1016/j.jclepro.2019.119042

134. European Environmental Agency. Number of Europeans exposed to harmful noise pollution expected to increase. [cited 18 Oct 2022]. Available: https://www.eea.europa.eu/highlights/number-of-europeans-exposed-to

135. Cecchel S, Chindamo D, Collotta M, Cornacchia G, Panvini A, Tomasoni G, et al. Lightweighting in light commercial vehicles: cradle-to-grave life cycle assessment of a safety-relevant component. Int J Life Cycle Assess. 2018;23: 2043–2054. doi:10.1007/s11367-017-1433-5

136. Jolliet O, Saade-Sbeih M, Shaked S, Jolliet A, Crettaz P. Environmental Life Cycle Assessment. CRC Press; 2015. doi:10.1201/b19138

137. van den Berg NW, Dutilh CE, Huppes G. Beginning LCA - A guide into environmental Life Cycle Assessment. Centrum voor Milieukunde, NOH National Reuse of Waste Research Programme; 1995.

138. Sun X, Luo X, Zhang Z, Meng F, Yang J. Life cycle assessment of lithium nickel cobalt manganese oxide (NCM) batteries for electric passenger vehicles. J Clean Prod. 2020;273: 123006. doi:10.1016/j.jclepro.2020.123006

139. Mohr M, Peters JF, Baumann M, Weil M. Toward a cell-chemistry specific life cycle assessment of lithium-ion battery recycling processes. J Ind Ecol. 2020;24: 1310–1322. doi:10.1111/jiec.13021

140. Wang F, Deng Y, Yuan C. Life cycle assessment of lithium oxygen battery for electric vehicles. J Clean Prod. 2020;264: 121339. doi:10.1016/j.jclepro.2020.121339

141. Deng Y, Li J, Li T, Gao X, Yuan C. Life cycle assessment of lithium sulfur battery for electric vehicles. J Power Sources. 2017;343: 284–295. doi:10.1016/j.jpowsour.2017.01.036

142. Peters J, Buchholz D, Passerini S, Weil M. Life cycle assessment of sodium-ion batteries. Energy Environ Sci. 2016;9: 1744–1751. doi:10.1039/C6EE00640J

143. Wang L, Hu J, Yu Y, Huang K, Hu Y. Lithium-air, lithium-sulfur, and sodium-ion, which secondary battery category is more environmentally friendly and promising based on footprint family indicators? J Clean Prod. 2020;276: 124244. doi:10.1016/j.jclepro.2020.124244

144. Peters J, Weil M. A Critical Assessment of the Resource Depletion Potential of Current and Future Lithium-Ion Batteries. Resources. 2016;5: 46. doi:10.3390/resources5040046

145. Oliveira L, Messagie M, Rangaraju S, Sanfelix J, Hernandez Rivas M, van Mierlo J. Key issues of lithium-ion batteries – from resource depletion to environmental performance indicators. J Clean Prod. 2015;108: 354–362. doi:10.1016/j.jclepro.2015.06.021

146. Yu Y, Chen B, Huang K, Wang X, Wang D. Environmental Impact Assessment and End-of-Life Treatment Policy Analysis for Li-Ion Batteries and Ni-MH Batteries. Int J Environ Res Public Health. 2014;11: 3185–3198. doi:10.3390/ijerph110303185

147. Unterreiner L, Jülch V, Reith S. Recycling of Battery Technologies – Ecological Impact Analysis Using Life Cycle Assessment (LCA). Energy Procedia. 2016;99: 229–234. doi:10.1016/j.egypro.2016.10.113

148. Tao Y, You F. Comparative life cycle assessment of three recycling approaches for electric vehicle lithium-ion battery after cascaded use. Chem Eng Trans. 2020;81: 1123–1128. doi:10.3303/CET2081188

149. Ellingsen LA-W, Majeau-Bettez G, Singh B, Srivastava AK, Valøen LO, Strømman AH. Life Cycle Assessment of a Lithium-Ion Battery Vehicle Pack. J Ind Ecol. 2014;18: 113–124. doi:10.1111/jiec.12072

150. Zackrisson M, Avellán L, Orlenius J. Life cycle assessment of lithium-ion batteries for plug-in hybrid electric vehicles – Critical issues. J Clean Prod. 2010;18: 1519–1529. doi:10.1016/j.jclepro.2010.06.004

151. Burchart-Korol D, Jursova S, Folęga P, Pustejovska P. Life cycle impact assessment of electric vehicle battery charging in European Union countries. J Clean Prod. 2020;257: 120476. doi:10.1016/j.jclepro.2020.120476

152. Pero F del, Delogu M, Pierini M. Life Cycle Assessment in the automotive sector: a comparative case study of Internal Combustion Engine (ICE) and electric car. Procedia Structural Integrity. 2018;12: 521–537. doi:10.1016/j.prostr.2018.11.066

153. Faria R, Marques P, Garcia R, Moura P, Freire F, Delgado J, et al. Primary and secondary use of electric mobility batteries from a life cycle perspective. J Power Sources. 2014;262: 169–177. doi:10.1016/j.jpowsour.2014.03.092

154. Majeau-Bettez G, Hawkins TR, StrØmman AH. Life cycle environmental assessment of lithium-ion and nickel metal hydride batteries for plug-in hybrid and battery electric vehicles. Environ Sci Technol. 2011;45: 4548–4554. doi:10.1021/es103607c

155. Badino V, Baldo GL. LCA: istruzioni per l'uso (LCA: instructions for use). Progetto Leonardo; 1998.

156. Alliance. Effective and affordable automobile lightweighting. [cited 17 Mar 2022]. Available: http://lightweight-alliance.eu/project/

157. Sandrini G, Có B, Tomasoni G, Gadola M, Chindamo D. The Environmental Performance of Traction Batteries for Electric Vehicles from a Life Cycle Perspective. Environmental and Climate Technologies. Sciendo; 2021. pp. 700–716. doi:10.2478/rtuect-2021-0053

158. Blagoeva DT, Dias PA, Marmier A, Pavel CC. Assessment of potential bottlenecks along the materials supply chain for the future deployment of low-carbon energy and transport technologies in the EU. 2016.

159. Dolganova I, Rödl A, Bach V, Kaltschmitt M, Finkbeiner M. A Review of Life Cycle Assessment Studies of Electric Vehicles with a Focus on Resource Use. Resources. 2020;9: 32. doi:10.3390/resources9030032

160. Patry G, Romagny A, Martinet S, Froelich D. Cost modeling of lithium-ion battery cells for automotive applications. Energy Sci Eng. 2015;3: 71–82. doi:10.1002/ese3.47

161. Nordelöf A, Poulikidou S, Chordia M, Bitencourt de Oliveira F, Tivander J, Arvidsson R. Methodological Approaches to End-Of-Life Modelling in Life Cycle Assessments of Lithium-Ion Batteries. Batteries. 2019;5: 51. doi:10.3390/batteries5030051

162. Hendrickson TP, Kavvada O, Shah N, Sathre R, D Scown C. Life-cycle implications and supply chain logistics of electric vehicle battery recycling in California. Environmental Research Letters. 2015;10: 014011. doi:10.1088/1748-9326/10/1/014011

163. Ciez RE, Whitacre JF. Examining different recycling processes for lithium-ion batteries. Nat Sustain. 2019;2: 148–156. doi:10.1038/s41893-019-0222-5